Institute for Materials Research
SCHOOL OF CHEMICAL
AND PROCESS ENGINEERING

UNIVERSITY OF LEEDS

Lead-free Dielectric and Piezoelectric Ceramics

By

Aurang ZEB

Submitted in accordance with the requirements for the degree of
Doctor of Philosophy

The University of Leeds
Institute for Materials Research
School of Chemical and Process Engineering

December, 2015

The candidate confirms that the work submitted is his own, except where work which has formed part of jointly-authored publications has been included. The contribution of the candidate and the other authors to this work has been explicitly indicated below. The candidate confirms that appropriate credit has been given within the thesis where reference has been made to the work of others.

Sample preparation, 95% data collection and analysis was performed by me. Dr S.J Milne whose name appears in each article as a co-author, is my academic supervisor. He guided me time to time and edited each draft before submission to different Journals. The contribution of other co-authors is mentioned below each article.

The last section of chapter 2 is based on the publication below;

Aurang Zeb and S. J. Milne "High temperature dielectric ceramics: a review of temperature-stable high-permittivity perovskites" J Mater Sci: Mater Electron, 26:9243-9255 (2015).

Chapter 4 is based on the publications:

Aurang Zeb and S. J. Milne, Large Electromechanical Strain in Lead-Free Binary $K_{0.5}Bi_{0.5}TiO_3$–$Bi(Mg_{0.5}Ti_{0.5})O_3$ System, J. Am. Ceram. Soc.,**97** [8]; 2413-2415 (2014).

Aurang Zeb, D.A Hall and S. J. Milne, "Lead-free Piezoelectric $K_{0.5}Bi_{0.5}TiO_3$-$Bi(Mg_{0.5}Ti_{0.5})O_3$ Ceramics with Depolarisation Temperatures up to ~ 220 °C, J Mater Sci: Mater Electron, 26:9516-9521 (2015).

In this article, Dr DA Hall is co-author, who contributed for thermally stimulated charge decay measurement for two samples and temperature based P-E loops.

The content of chapter 5 is based on the article;

Aurang Zeb and S. J. Milne, Dielectric and Piezoelectric Properties of $(1–x)K_{0.5}Bi_{0.5}TiO_3–xBa(Ti_{0.8}Zr_{0.2})O_3$ Ceramics, J. Am. Ceram. Soc.,**96** [10]; 3089-3093 (2013).

Chapter 6 is based on the article;

Aurang Zeb and S. J. Milne, Stability of High-Temperature Dielectric Properties for $(1-x)Ba_{0.8}Ca_{0.2}TiO_3–xBi(Mg_{0.5}Ti_{0.5})O_3$ Ceramics, J. Am. Ceram. Soc., **96**[9]; 2887-2892 (2013).

Chapter 7 include the content of the two published articles;

Aurang Zeb and S. J. Milne, Dielectric Properties of $Ba_{0.8}Ca_{0.2}TiO_3–Bi(Mg_{0.5}Ti_{0.5})O_3–NaNbO_3$ Ceramics, J. Am. Ceram. Soc., **96** [12]; 3701-3703 (2013).

Aurang Zeb, Yang Bai, Tim Button and S. J. Milne, Temperature-Stable Relative Permittivity from −70 °C to 500 °C in $(Ba_{0.8}Ca_{0.2})TiO_3–Bi(Mg_{0.5}Ti_{0.5})O_3–NaNbO_3$ Ceramics, J. Am Ceram. Soc., **97** [8]; 2479-2483 (2014).

In this article, Yang Bai and Tim Button are the co-authors and contributed for low temperature relative permittivity measurements for two samples.

Chapter 8 is based on the article;

Aurang Zeb and S. J. Milne, Temperature-stable dielectric properties from −20 °C to 430 °C in the system $BaTiO_3–Bi(Mg_{0.5}Zr_{0.5})O_3$, J. Eur. Ceram. Soc., **34** [13]; 3159-3166 (2014).

Chapter 9 include the content of the published article;

Aurang Zeb and S. J. Milne, Low variation in relative permittivity over the temperature range 25–450 °C for ceramics in the system $(1-x)[Ba_{0.8}Ca_{0.2}TiO_3-xBi(Zn_{0.5}Ti_{0.5})O_3]$, J. Eur. Ceram. Soc., **34** [7]; 1727-1734 (2014).

List of publications

1. **Aurang Zeb** and S. J. Milne, High temperature dielectric ceramics: a review of temperature-stable high-permittivity perovskites, J Mater Sci: Mater Electron, **26** [12]: 9243-9255 (2015).
2. **Aurang Zeb** and S. J. Milne, Large Electromechanical Strain in Lead-Free Binary System $K_{0.5}Bi_{0.5}TiO_3$-$Bi(Mg_{0.5}Ti_{0.5})O_3$, J. Am. Ceram. Soc., **97** [8]: 2413-2415 (2014).
3. **Aurang Zeb,** D. A. Hall and S. J. Milne, Lead-free piezoelectric $K_{0.5}Bi_{0.5}TiO_3$-$Bi(Mg_{0.5}Ti_{0.5})O_3$ ceramics with depolarisation temperatures up to ~ 220 ºC, J Mater Sci: Mater Electron, **26** [12]: 9516-9521 (2015).
4. **Aurang Zeb** and S. J. Milne, Stability of High-Temperature Dielectric Properties for $(1-x)Ba_{0.8}Ca_{0.2}TiO_3$-$xBi(Mg_{0.5}Ti_{0.5})O_3$ Ceramics, J. Am. Ceram. Soc., **96** [9]: 2887-2892 (2013).
5. **Aurang Zeb** and S. J. Milne, Dielectric and Piezoelectric Properties of $(1-x)K_{0.5}Bi_{0.5}TiO_3$-$xBa(Ti_{0.8}Zr_{0.2})O_3$ Ceramics, , J. Am. Ceram. Soc., **96** [10]: 3089-3093 (2013).
6. **Aurang Zeb** and S. J. Milne, Dielectric Properties of $Ba_{0.8}Ca_{0.2}TiO_3$-$Bi(Mg_{0.5}Ti_{0.5})O_3$-$NaNbO_3$ Ceramics, J. Am. Ceram. Soc., **96** [12]: 3701-3703 (2013).
7. **Aurang Zeb** and S. J. Milne, Low variation in relative permittivity over the temperature range 25-450 ºC for ceramics in the system $(1-x)[Ba_{0.8}Ca_{0.2}TiO_3$-$xBi(Zn_{0.5}Ti_{0.5})O_3]$, J. Eur. Ceram. Soc., **34** [7]: 1727-1734 (2014).

8. **Aurang Zeb** and S. J. Milne, Temperature-stable dielectric properties from -20 ºC to 430 ºC in the system $BaTiO_3$-$Bi(Mg_{0.5}Zr_{0.5})O_3$, J. Eur. Ceram. Soc., **34** [13] 3159-3166 (2014).
9. **Aurang Zeb,** Yang Bai, Tim Button and S. J. Milne, Temperature-Stable Relative Permittivity from -70 ºC to 500 ºC in $(Ba_{0.8}Ca_{0.2})TiO_3$-$Bi(Mg_{0.5}Ti_{0.5})O_3$-$NaNbO_3$ Ceramics, J. Am Ceram. Soc., **97** [8] 2479-2483 (2014).
10. **Aurang Zeb**, D.A Hall, T.P. Comyn and S. J. Milne, Phase Stability and Piezoelectric Properties of $K_{0.5}Bi_{0.5}TiO_3$-$Bi(Mg_{0.5}Ti_{0.5})O_3$ solid solutions, Submitted.

Acknowledgements

First of all, I would like to thank my Supervisor Dr. Steve J Milne by continuous guidance, support and valuable suggestions throughout my PhD research. With his experience and knowledge, he greatly contributed for this research with a lot of patience. Thanks are expressed to HEC and Islamia College for financial support.

I am also thankful to Professor Gin Jose and Dr. Tim P Comyn for their valuable instructions and advices at different occasions during experimental work. During this research work, I would like also to express my gratitude to Dr. David A Hall, University of Manchester for his insight advice and guidance.

Also, I would like to thank the administration team, especially Mrs. Marie Gray and the LEMAS team, Dr. Michael B. Ward, Mr. John P. Harrington, and Stuart Micklethwaite for their extended help during SEM, TEM samples preparation and operations.

Most of all, I am very thankful to my wife who encourage me a lot and sacrifices throughout my research studies to look after my daughters Manahil Zeb, Saroosh Zeb and my naughty son Muhammad Tayyab Zeb. She really managed everything in a nice way during this period of time.

Sincere thanks go to my parents, teachers, brothers, sisters and my friends who supported me in all aspects and encourage me at every step of my life particularly my grandfather Taj Muhammad Khan (Late) for his extended support and encouragement during my whole education.

Furthermore, I would like to thank all other PhD students who I have worked with during my studies at the University of Leeds for their friendship and help in difficult times, in particular to Saeed ullah Jan, Dr. Fangyuan Zhu, Kamran Khan and Laura Stoica.

Abstract

A goal in the search for lead-free piezoelectrics is to discover solid solutions with temperature insensitive morphotropic phase boundaries, as this is likely to enhance piezoelectric properties and promote temperature-stability. Furthermore, there is a high drive for developments of temperature stable dielectric ceramics which can operate at temperatures > 200 ºC, well above the limit of existing high volumetric efficiency capacitor materials.

A new family of novel lead-free piezoelectric perovskite solid solutions in the binary systems $(1\text{-}x)K_{0.5}Bi_{0.5}TiO_3\text{-}xBi(Mg_{0.5}Ti_{0.5})O_3$, $(1\text{-}x)$KBT-xBMT and $(1\text{-}x)K_{0.5}Bi_{0.5}TiO_3\text{-}xBa(Zr_{0.2}Ti_{0.8})O_3$, $(1\text{-}x)$KBT-xBZT were fabricated. In the examination of $(1\text{-}x)$KBT-xBMT ceramic system, a phase boundary (MPB) between tetragonal and mixed phase tetragonal+cubic (pseudocubic) was identified at $0.025 < x < 0.03$. Compositions $0.03 \leq x < 0.08$ were mixed, tetragonal and cubic phase. Compositions close to MPB exhibited favourable piezoelectric properties, for example, the piezoelectric charge coefficient, d_{33}, was 150 pC/N for composition $x = 0.03$, and 133 pC/N for $x = 0.04$. A high bipolar electric field-strain was exhibited by MPB compositions with strains of 0.25%-0.35%. Values of temperature dependent unipolar strain for the $(1\text{-}x)$KBT-xBMT ($x = 0.03$ and 0.04) were retained ~ 0.18% at a temperature ≥ 185 ºC. Thermally stimulated charge decay and k_p-T measurements revealed full depolarisation at T_d ~ 220 ºC. The overall properties are very promising for electromechanical actuator applications.

In the binary $(1\text{-}x)$KBT-xBZT system, the mixed phase (tetragonal+cubic) composition $x = 0.1$, demonstrated a piezoelectric charge coefficient, $d_{33} = 130$ pC/N, bipolar strain ~ 0.13% (60 kV/cm) and high depolarisation-temperature ~ 220 ºC.

Temperature stable dielectric systems; (1-x)$Ba_{0.8}Ca_{0.2}TiO_3$-xBi($Mg_{0.5}Ti_{0.5}$)O_3, (1-x)BCT-xBMT), 0.45$Ba_{0.8}Ca_{0.2}TiO_3$-(0.55-x)Bi($Mg_{0.5}Ti_{0.5}$)O_3-$x$$NaNbO_3$, 0.45BCT-(0.55-$x$)BMT-$x$NN, and (1-$x$)[0.5$K_{0.5}Bi_{0.5}TiO_3$-0.5Ba($Zr_{0.2}Ti_{0.8}$)$O_3$]-$x$Bi($Zn_{2/3}Nb_{1/3}$)$O_3$, (1-$x$)[0.5KBT-0.5BZT]-$x$BZN were synthesised with near plateau in relative permittivity-temperature response (ε_r-T), giving a ±15%, or better, consistency in ε_r across a wide temperature range, coupled with optimum dc resistivities. The composition: 0.5BCT-0.5BMT indicated a temperature stability, ε_r = 800±15% from 40-550 ºC, with tanδ ≤ 0.02 over the temperature range 100-400 ºC. For a slightly higher BMT content, the dielectric properties were superior to 0.5BMT, with ε_r = 950±15% from 70 to 600 ºC and tanδ ≤ 0.02 from 160-550 ºC. Achieving temperature-stability down to -55 ºC and below was accomplished in the 0.45BCT-0.55BMT ceramic materials by the incorporation of $NaNbO_3$ at a level $x \geq 0.2$. Modification with x = 0.3, led to the temperature stability in relative permittivity, with ε_r = 550±15% across the temperature range -70 ºC-300 ºC and tanδ ≤ 0.02 from -60 ºC to 300 ºC, thus achieving the goal of producing a temperature-stable relaxor dielectric to operate in a range of harsh environments down to < -55 ºC. Similarly, a near flat dielectric response was exhibited by the ceramic system (1-x)[0.5KBT-0.5BZT]-xBZN ceramic system (x = 0.2BZN) with ε_r = 805±15% across a wide temperature range, from -20 ºC to 600 ºC; with tanδ ≤ 0.02 across from 50 ºC to 450 ºC. These temperature stable dielectric materials were comparable to the best temperature stable dielectric materials for example; 50$BaTiO_3$-25Bi($Zn_{0.5}Ti_{0.5}$)O_3-25$BiScO_3$, ε_r = 1100±15% (80-500 ºC), 0.85[0.6$Na_{0.5}Bi_{0.5}TiO_3$-0.4$K_{0.5}Bi_{0.5}TiO_3$]-0.15$K_{0.5}Na_{0.5}NbO_3$, ε_r = 2167±10% (54-400 ºC) and highly attractive for the high temperature capacitor applications.

Contents

List of Figures

List of Tables

Abbreviations and Symbols

BT – Barium Titanate, $BaTiO_3$

PZT – Lead Zirconate Titanate, $Pb(Zr,Ti)O_3$

KBT – Potassium Bismuth Titanate, $K_{0.5}Bi_{0.5}TiO_3$

BMT – Bismuth Magnesium Titanate, $Bi(Mg_{0.5}Ti_{0.5})O_3$

BZT – Barium Zirconium Titanate, $Ba(Zr_{0.2}Ti_{0.8})O_3$

BZT – Bismuth Zinc Titanate, $Bi(Zn_{0.5}Ti_{0.5})O_3$

BMZ – Bismuth Magnesium Zirconate, $Bi(Mg_{0.5}Zr_{0.5})O_3$

BZN – Bismuth Zinc Niobate, $Bi(Zn_{2/3}Nb_{1/3})O_3$

BCT – Barium Calcium Titanate, $Ba_{0.8}Ca_{0.2}TiO_3$

NBT – Sodium Bismuth Titanate, $Na_{0.5}Bi_{0.5}TiO_3$

NN – Sodium Niobate, $NaNbO_3$

KNN – Potassium Sodium Niobate, $K_{0.5}Na_{0.5}NbO_3$

E_a – Activation energy

C – Capacitance

ε_r' – Real part of relative permittivity

ε_r'' – Imaginary part of relative permittivity

ε_r – Relative permittivity

$\varepsilon_{r\,max}$ – Maximum relative permittivity

$\varepsilon_{r\,mid}$ – Normalized relative permittivity

T_m – Temperature of maximum relative permittivity

T_c – Curie temperature

T_d – Depolarization temperature

$\tan\delta$ – Loss tangent

θ – Diffraction angle

EDX – Energy dispersive X-ray spectroscopy

MPB – Morphotropic Phase Boundary

PPT – Polymorphic Phase Transition

P – Electric polarization

P_{max} – Maximum electric polarization

P_r – Remanent polarization

P–E – Polarization-electric field

S–E – Strain-electric field

S – Mechanical Strain

S_{max} – Maximum Strain

E_c – Coercive field

EIA – Electronic Industries Alliance

d_{33} – Piezoelectric charge coefficient

d_{33}^* – Normalized strain (S_{max}/E_{max})

K_p – Planar electromechanical coupling factor

PNRs – Polar nanoregions

SEM – Scanning Electron Microscopy

TEM – Transmission Electron Microscopy

XRD – X-ray Diffraction

Chapter 1 : Introduction

This thesis encompasses two important categories of electroceramics: lead-free piezoelectrics and lead-free high temperature dielectrics.

1.1 Piezoelectric Materials

Piezoelectricity refers to the conversion of mechanical energy into electrical energy and vice versa. Piezoelectric materials have diverse uses and applications; examples includes high voltage generators, actuators, sensors, transducers, capacitors and fuel injectors in automobile industries [Leontsev and Eitel (2010), Zhou et al. (2012)]. The market-leading high performance piezoelectric, lead zirconate titanate, PZT, is a perovskite solid solution between $PbZrO_3$ and $PbTiO_3$ in which a morphotropic phase boundary, MPB, exists between rhombohedral and tetragonal phase fields at around 52 mol% $PbZrO_3$; compositions at this boundary have enhanced electromechanical properties [Jaffe (1971), Noheda et al. (1999)]. For undoped PZT at MPB, the reported piezoelectric properties were: Curie temperature, T_c = 390 ºC, relative permittivity, ε_r = 1600 at room temperature, piezoelectric charge coefficient, d_{33} = 233 pC/N and planar electromechanical coupling factor, k_p = 0.52 [Ansell et al. (2014)].

A range of chemical dopants, commonly classified as donors (*soft* PZT) or acceptors (*hard* PZT), have been used to optimise the piezoelectric properties of PZT for specific applications. However, health and environmental concerns surrounding the use of toxic lead oxide pose the threat of global restrictions under European Union and other legislations [(Directive 2003a), (Directive 2003b)]. Therefore, an intensive search is underway for lead-free alternatives to replace PZT-based materials.

Numerous lead free barium titanate-based ($BaTiO_3$) ferroelectric materials with improved piezoelectric properties have been developed. Liu and Ren (2009) reported excellent piezoelectric properties of the $0.5Ba(Zr_{0.2}Ti_{0.8})O_3$-$0.5Ba_{0.7}Ca_{0.3}TiO_3$ ceramic system. A high value of d_{33} ~ 620 pC/N was obtained due to the coexistence of rhombohedral and tetragonal polymorphs at temperatures close to the cubic paraelectric phase transition. However, because the Curie point T_c (depolarisation temperature) is ≤ 100 ºC, these properties are highly temperature sensitive and degrade as temperature increases above room temperature. A closely related piezoelectric properties with high piezoelectric constant, d_{33} ~ 530 pC/N was achieved in the binary system $0.7Ba(Sn_{0.2}Ti_{0.8})O_3$-$0.3Ba_{0.7}Ca_{0.3}TiO_3$ but at a phase convergence temperature close to T_c ~ 20 ºC [Xue et al. (2011a)].

A number of other lead-free piezoelectrics have been proposed, for example potassium sodium niobate ($K_{0.5}Na_{0.5}NbO_3$) based systems, a relatively high value of d_{33} ~ 230 pC/N and k_p ~ 0.44 because of phase co-existence at a polymorphic phase transition PPT rather than a temperature-invariant MPB [Guo et al. (2004), Skidmore et al. (2009)]. More recent developments have further improved properties and improved temperature stability, for example; the reported piezoelectric properties were for $0.92K_{0.5}Na_{0.5}NbO_3$-$0.02Bi_{0.5}Li_{0.5}TiO_3$-$0.06BaZrO_3$, d_{33} = 348 pC/N and k_p = 0.57 at room temperature and retained up to ~ 200 ºC [Wang et al. (2015)]. Similarly, in the ternary system: $0.955K_{0.48}Na_{0.52}NbO_3$-$0.005BiScO_3$-$0.04Bi_{0.5}(Na_{0.7}K_{0.2}Li_{0.1})_{0.5}ZrO_3$, a high value of d_{33} ~ 366 pC/N was reported at room temperature and retained (~ 319 pC/N) up to ~ 300 ºC [Xiaojing Cheng et al. (2014)].

Piezoelectrics based on sodium bismuth titanate ($Na_{0.5}Bi_{0.5}TiO_3$) solid solutions are another important class of material. Leading examples are the binary systems, $Na_{0.5}Bi_{0.5}TiO_3$-$BaTiO_3$ and $Na_{0.5}Bi_{0.5}TiO_3$-$K_{0.5}Bi_{0.5}TiO_3$. These materials develop large electromechanical strains, up to 0.3-0.45%, upon application of a high electric field (~

80 kV/cm) and are of interest for actuator applications [Takenaka et al. (1991a), Chu et al. (2002)]. The d_{33} values were reported to be in the range 122-176 pC/N for the MPB compositions in $Na_{0.5}Bi_{0.5}TiO_3$-$BaTiO_3$ system, and 140-190 pC/N in $Na_{0.5}Bi_{0.5}TiO_3$-$K_{0.5}Bi_{0.5}TiO_3$, but relatively low depolarisation temperatures, T_d of ~ 100 ºC and ≤ 170 ºC respectively, are drawbacks since the temperature limit as a working piezoelectric would be well below these T_d values [Rödel et al. (2009)].

A variety of chemical modifications to $Na_{0.5}Bi_{0.5}TiO_3$-$BaTiO_3$ and $Na_{0.5}Bi_{0.5}TiO_3$-$K_{0.5}Bi_{0.5}TiO_3$ solid solutions have been investigated as means to enhance the piezoelectric properties; examples includes $Na_{0.5}Bi_{0.5}TiO_3$-$K_{0.5}Bi_{0.5}TiO_3$-$BaTiO_3$ [Nagata et al. (2003)] typically with d_{33} ~ 170 pC/N and T_d ~ 162 ºC (determined from the ε_r-T plot), and $Na_{0.5}Bi_{0.5}TiO_3$-$BaTiO_3$-$K_{0.5}Na_{0.5}NbO_3$ which develops giant electromechanical strains, up to ~ 0.45%, at MPB compositions. This is reported to be a consequence of an electric field-induced relaxor-ferroelectric phase transformation [Zhang et al. (2007)]. This field-induced transformation gives rise to a characteristic discontinuity and wide hysteresis in strain-electric field plots [Daniels et al. (2010), Glaum et al. (2013)]. However, depolarisation temperatures for $Na_{0.5}Bi_{0.5}TiO_3$-compositions with the best piezoelectric properties are modest.

1.2 High Temperature Dielectrics

There is a high impetus for the development of high permittivity dielectrics for use in capacitors operating at higher temperatures than current commercial products. The main predicted growth market is in power electronics due to advances made in increasing the temperature limits of wide band gap semiconductors for transistors. The lack of passive components capable of operating at 300 ºC and above has restricted developments in high temperature electronic systems [Watson and Castro (2012), Zeb and Milne (2015), Turner et al. (1994), Dittmer et al. (2012)]. Capacitors for power conditioning, such as inverters for integrating renewable electricity generation with the national grid are examples where higher temperature capacitors are required capable of reliable operation at > 200 ºC (due to heat generation and dissipation from high voltage electronics).

Other application areas are for electronics operating in harsh environments includes: distributed control and sensing systems in aviation, and aerospace. Electronic controls placed close to the engine, at temperatures of 200-300 ºC reduce weight by removing the need for cabling. Deep well-drilling and space applications are other technologies where high temperature electronics are required.

Examples of materials resulting from research into high temperature stable dielectrics include: $BaTiO_3$-$BiScO_3$ [Ogihara et al. (2009a)]; $K_{0.5}B_{0.5}TiO_3$-$BiScO_3$ [Kruea-In et al. (2012)]; $BiScO_3$-$BaTiO_3$-$(K_{1/2}Bi_{1/2})TiO_3$ [Lim et al. (2009)]; and $BaTiO_3$-$Bi(Zn_{1/2}Ti_{1/2})O_3$-$BiScO_3$ [Raengthon et al. (2012)]. These offer temperature-stability (defined as a variation in relative permittivity within ±15%) to a maximum temperature of ~ 300-450 ºC, but the performance fails to extend to the lower limit of -55 ºC required for commercial capacitors to satisfy military specifications. It should be noted that Sc_2O_3 content in these material leads to high costs. Many of these materials are relaxor dielectrics in which accepted knowledge of structure-property relationships indicates a disruption of long range polar order (of a ferroelectric) due to substitution of host ions by ions of different charge and radii to form polar nanoregions (PNRs).

Other complex solid solution perovskites with minimal temperature variation in relative permittivity include: $Na_{0.5}Bi_{0.5}TiO_3$-$BaTiO_3$-$K_{0.5}Na_{0.5}NbO_3$ [Dittmer et al. (2011)]; $Na_{0.5}Bi_{0.5}TiO_3$-$K_{0.5}Bi_{0.5}TiO_3$-$K_{0.5}Na_{0.5}NbO_3$ [Dittmer et al. (2012)] with optimum dielectric properties ε_r = 2151±10%, from temperatures 43 ºC to 319 ºC and ε_r = 2167±10%, from 54 ºC to 400 ºC respectively. The lower limiting temperature was decreased to well below the room temperature in the solid solution; $Na_{0.5}Bi_{0.5}TiO_3$-

$BaTiO_3$-$CaZrO_3$ [Acosta et al. (2012)]; and $Na_{0.5}Bi_{0.5}TiO_3$-$BaTiO_3$-$K_{0.5}Na_{0.5}NbO_3$-$CaZrO_3$ [Acosta et al. (2012)]. However, the dielectric losses substantially increased above ~ 300 ºC for this family of materials suggesting a practical working limit up to ~ 300 ºC.

1.3 Aims and Objectives

The aim of this research work was to develop new and improved lead-free piezoelectrics, and to investigate compositional systems that may yield new and improved high temperature dielectrics.

1.3.1 Objectives

1.3.1.1 Piezoelectrics

- Explore novel perovskite titanate solid solution systems involving tetragonal and rhombohedral end-members in the search for a morphotropic phase boundary akin to that of lead zirconate titanate.
- Measure dielectric, ferroelectric and piezoelectric properties as a function of composition and temperature.
- Study phase stability as a function of temperature.
- Investigate microstructure using scanning and transmission electron microscopy.
- Consider structure-property relationships.
- Compare performance of new lead-free piezoelectrics with the best materials from other research laboratories.

1.3.1.2 High Temperature Dielectrics

- Fabricate novel relaxor dielectrics with high levels of charge and size disorder on the perovskite lattice.

- Measure relative permittivity and dielectric loss tangent as a function of temperature and different set of frequencies.
- Determine temperature limits of ±15% stability in relative permittivity; estimate dielectric breakdown strength.
- Establish effects of dc bias fields on relative permittivity values.
- Investigate ceramic microstructures using scanning and transmission microscopy.
- Compare properties to other high temperature dielectric ceramics reported by other research groups.

Chapter 2

Background Science and Literature Review

2.1 Summary

This chapter outlines the basic concepts of dielectric and piezoelectric ceramic materials. The early sections of this chapter describe the crystal structures, dielectric properties and polarisation mechanisms, followed by the basics of ferroelectrics and piezoelectrics. Later sections review published research literature on lead-free dielectric and piezoelectric materials.

2.2 Crystal Structure

The physical properties of solids are closely related to their internal atomic arrangement. Many solids possess a crystalline structure in which the atoms have long range periodic arrangement in three dimensions [Stock and Cullity (2001)]. The three dimensional periodic array of atoms is known as a lattice, and the simplest repetitive portion of the lattice, is called the unit cell (which represents the overall lattice symmetry). Unit cells are classified into seven crystal systems based on the shape of the unit cell (cubic, tetragonal, orthorhombic, rhombohedral, hexagonal, monoclinic and triclinic). The geometrical parameters that describe unit cells of different crystal systems are: the three axial lengths (a, b c) and angles (α, β, γ) including the location of the body or face centred atom, Figure 2.1.

Lattices may be further classified according to the number of lattice points and their distribution in a unit cell (each lattice point represents a repeating atom group-the motif of the 3D patterns). In total there are 14 combinations of crystal system and lattice type that describe all crystal structures. These are the 14 Bravais lattices, named after the French crystallographer Bravais in 1848, shown in Figure 2.2 [Stock and Cullity (2001)]. In addition to this, based on different symmetry operations (e.g. mirror, transitional, inversion), the fourteen Bravais lattices are further characterized into 32 crystallographic point groups, 11 of which are centrosymmetric and exhibit no piezoelectricity due their non-polarity. The 21 crystal noncentrosymmetric point groups demonstrate piezoelectricity with the exception of one, which does not exhibit a piezoelectric effect due to combined symmetry elements [Moulson and Herbert (2003)].

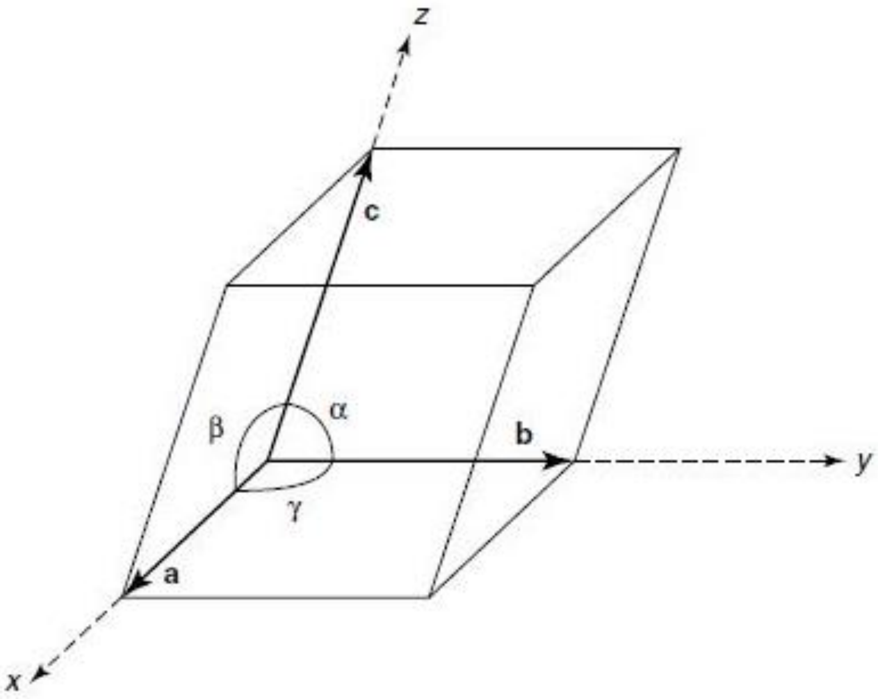

Figure 2.1 Illustration of the three axial lengths (a, b, c) and angle (α, β, γ) of the unit cell [Mitchel (2003)].

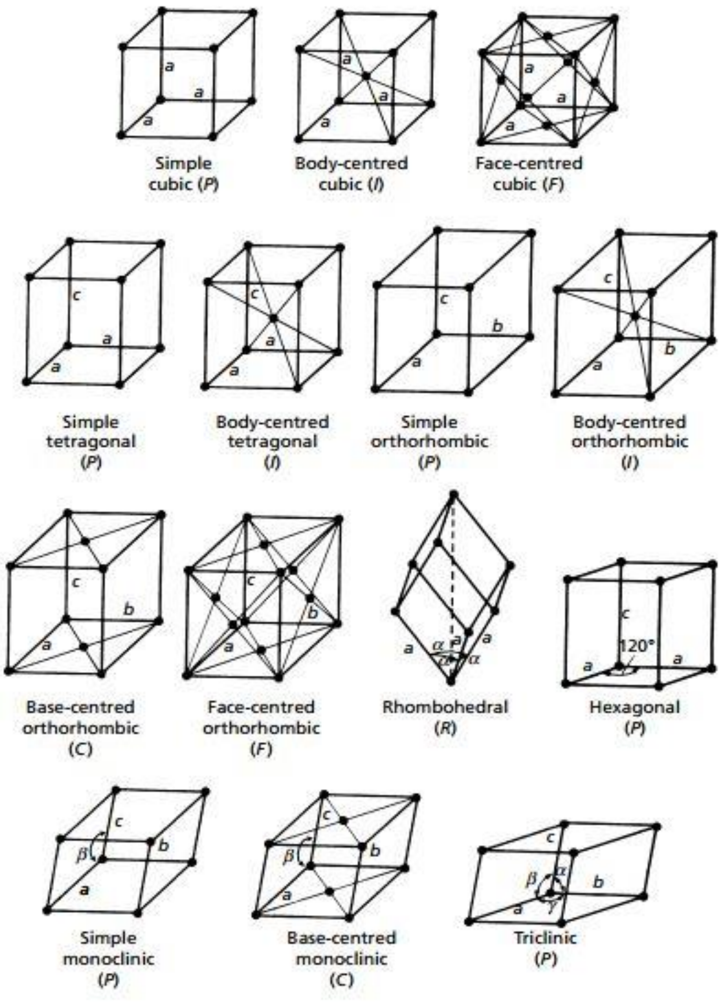

Figure 2.2 The Fourteen Bravais lattices types [Hammond (2001)].

2.2.1 Perovskite Structure

Perovskite is the most widely investigated structure which displays ferroelectric and piezoelectric properties [Paik et al. (1999)]. A perovskite structure has a general formula of the form of ABX_3, where A, B are cations and X is an anion (O^{-2}, Cl^{-2}, F^{-2}, Br^{-1}) [Feng et al. (2008)]. The unit cell of the oxide perovskite ABO_3 typified by $CaTiO_3$, is cubic and usually represented with large A cations at the corners, small B cation in the body centre and oxygen on the face centres, Figure 2.3. Alternatively, the unit cell for perovskite structure may be described with small B cations at the corners, large A cation in the body centre and oxygen at the midpoint of edges [Jaffe (1971)].

The structure of perovskite can be visualized as a network of corner sharing BO_6 octahedra (oxygen octahedra) with the small B cation in the centre of the oxygen octahedral cage and large A cations occupying dodecahedral (12 co-ordinate) sites [Ramadass (1978)]. It is also useful to consider perovskite as being related to cubic close packing of atoms with O and the relatively large A ions in a pseudo close packed array, and with B ions occupying a quarter of the available octahedral voids of cubic close packing [West (2007)].

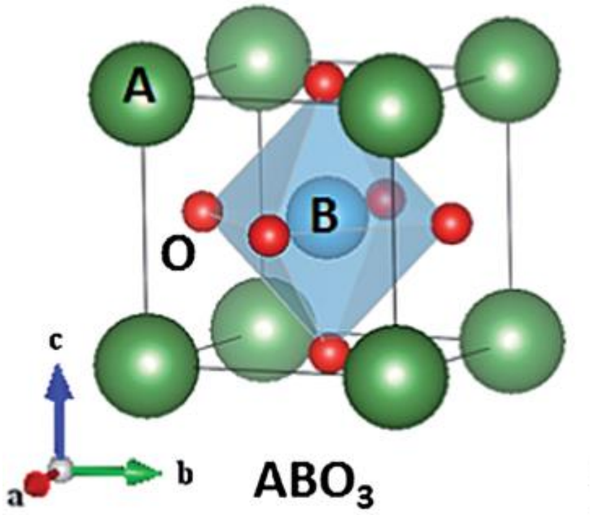

Figure 2.3 Perovskite structure with highlighted BO_6 octahedral cage [Cheng et al. (2014)].

Although the idealized perovskite structure is cubic, many perovskite compounds deviate from this high symmetry over certain ranges of temperature, undergoing a transition to a lower symmetry phase with decreasing temperature [Reaney et al. (1994)]. For example, $BaTiO_3$, above a temperature of ~ 130 ºC is cubic perovskite, transforming to a lower symmetry tetragonal (non-symmetric) structure below ~ 130 ºC. Below ~ 0 ºC a transition to orthorhombic (with monoclinic primary cell, derived from the cubic parent cell) occurs, and below -90 ºC a rhombohedral form is thermodynamically stable. The non-cubic forms contain a Ti ion which is displaced from its standard central position in the BO_6 octahedra. This creates a charge displacement in the unit cell, and a permanent or spontaneous dipole results (in practice O and B ions may also be displaced relative to the parent cubic perovskite), Figure 2.4. The position of the Ti ion, and dipole direction can be altered by applying an external electric fields. The existence of spontaneous polarisation, switchable by an electric field is the definition of a ferroelectric crystal. Hence, below ~ 130 ºC $BaTiO_3$ is ferroelectric. Above 130 ºC it is paraelectric (non-ferroelectric).

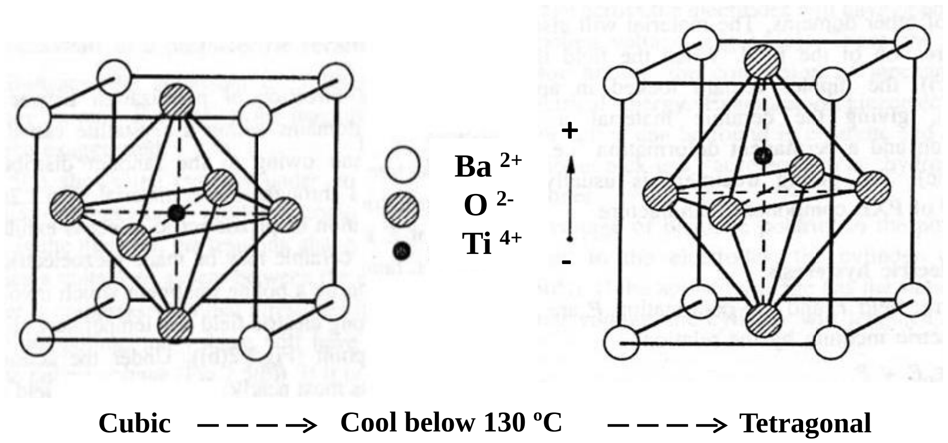

Figure 2.4 Crystal structure of $BaTiO_3$, cubic above the Curie temperature (~ 130 ºC) and ferroelectric below the curie temperature with Ti ion displacement relative to Ba and O ions [modified as Damjanovic (1998)].

The perovskite structure can accommodate a variety of substituent ions of different valence and ionic radii to the host structure. This allows electrical properties to be manipulated. However, the stability of the structure depends on the ionic radii and often this is explained on the basis of a tolerance factor (τ) introduced by Goldschmidt, given by a relation [Eitel et al. (2001)]:

$$\tau = \frac{(R_A + R_O)}{\sqrt{2}(R_B + R_O)} \qquad \text{Equation 2.1}$$

where R_A, R_B and R_o indicates the ionic radii of the A, B cations and oxygen anion respectively. Based on the Shannon ionic radii, for stable perovskite structures, a perovskite structure may exist for a tolerance factor in the range of $0.88 < \tau < 1.09$ [Lee et al. (2009)]. It has been found that the tolerance factor for ideal cubic perovskite structure is unity. If the tolerance factor is slightly greater than unity ($\tau > 1$), the structure of perovskite is stabilized in tetragonal or hexagonal symmetry. However, if the tolerance factor is smaller than one ($\tau < 1$), the structure is often considered as rhombohedral or monoclinic [Snel et al. (2005)]. Table 2.1 illustrates some examples of tolerance factor for different perovskite materials. It is noted that the tolerance factor is a very basic tool, arising from geometric considerations.

Table 2.1 The tolerance factor (τ) for some perovskite compounds [Bengagi et al. (2012), Lee et al. (2009), Jarupoom et al. (2011)].

Perovskite Compounds	Tolerance Factor (τ)	Structure
$BaTiO_3$	1.06	Tetragonal
$K_{0.5}Bi_{0.5}TiO_3$	1.03	Tetragonal
$PbTiO_3$	1.02	Tetragonal
$SrTiO_3$	1.00	Cubic
$Na_{0.5}Bi_{0.5}TiO_3$	0.98	Rhombohedral
$Bi(Mg_{0.5}Ti_{0.5})O_3$	0.94	Rhombohedral

2.3 Dielectrics

A dielectric is an electrically insulating material in which there is no appreciable long range movement of charge carriers. An insulator can acquire a polarised structure in the presence of external electric field [Moulson and Herbert (2003)]. The polarised structure of dielectric material is the result of separation of negative and positive charge centres. These charge displacements are known as dipole moments (see section 2.3.1 for details). Due to this electric polarisation phenomena, dielectric materials acquire opposite charges across their surfaces and are utilized for charge storage in capacitor applications. The electric dipole moment per unit volume of a dielectric material, is known as electric polarisation and is proportional to the external applied electric field for linear dielectrics [Moulson and Herbert (2003)]:

$$\vec{P} = \chi_e \varepsilon_\circ \vec{E} \qquad \text{Equation 2.2}$$

where χ_e is the electric susceptibility, $\varepsilon_\circ$ is the permittivity of free space or air (8.85×10^{-12} F/m) and E is the electric field magnitude. Placing a dielectric between the plates of a capacitor enhances the charge storage capabilities and supports an electrostatic field. If ε is the permittivity of the dielectric medium then the ability of the dielectric material to store the electric charges, is known as relative permittivity (ε_r) given by the following relation [Zhang and Yu (2011)]:

$$\varepsilon_r = \frac{\varepsilon}{\varepsilon_\circ} \qquad \text{Equation 2.3}$$

where ε_r is a dimensionless quantity depending on temperature, frequency and material characteristics (polarisability). If a slab of dielectric is layered as an insulating material between the two conducting plates of a capacitor, then the dielectric material becomes polarized in the external electric field, this enhances the capacitance and reduces the loss of charge on the plates, Figure 2.5, and Equation 2.4.

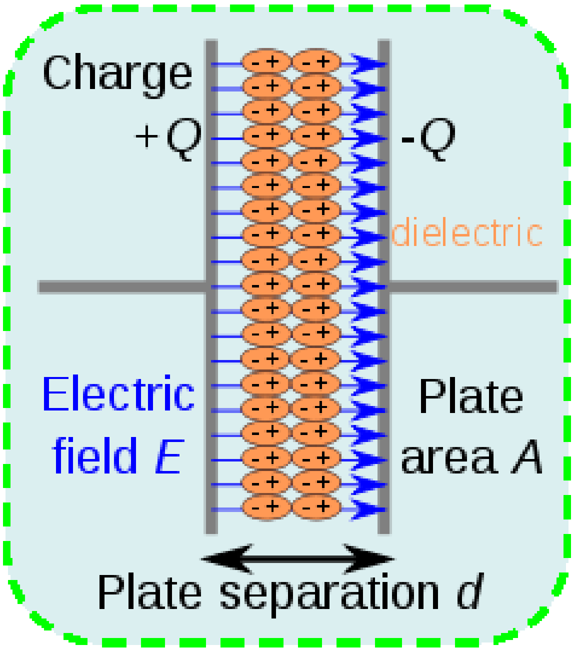

Figure 2.5 Polarisation of dielectric in parallel plate capacitor [Hao (2013)].

The capacitance value of a capacitor depends on geometrical factors and the relative permittivity (ε_r) given by the relation [Hao (2013)]:

$$C = \varepsilon_r \varepsilon_\circ \frac{A}{d} \qquad \text{Equation 2.4}$$

where C is the capacitance, A is the area of the electrode plate; d is the separation of the plates/thickness of the dielectric material. The different polarisation mechanisms of a dielectric are described in the following section.

2.3.1 Polarisation Mechanisms

In dielectrics, there are mainly four types of polarisation mechanisms contributing to relative permittivity; these are atomic, ionic, dipolar and space charge polarisation, Figure 2.6 [Moulson and Herbert (2003)].

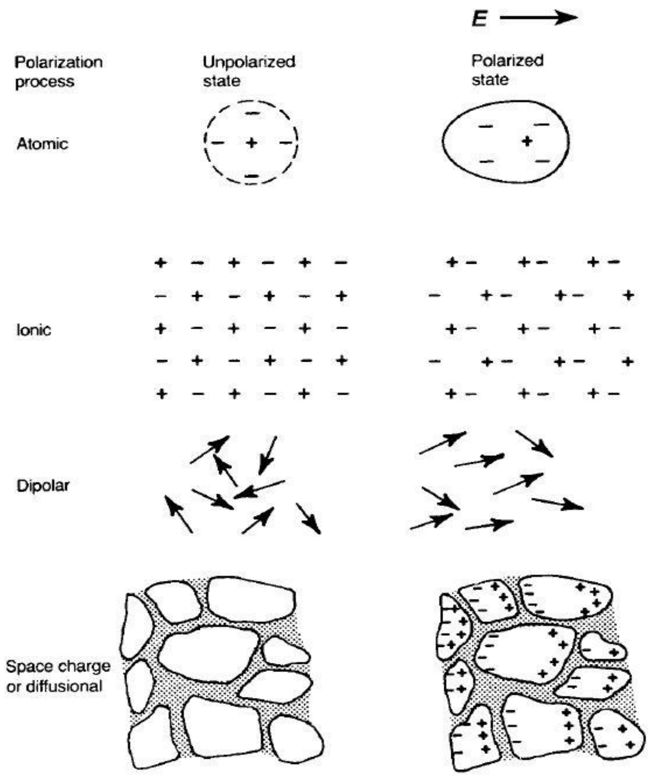

Figure 2.6 Illustration of different polarisation mechanisms in dielectrics [Moulson and Herbert (2003)].

2.3.1.1 Atomic Polarisation

Atomic or electronic polarisation is based on the relative shift of negative charges (electron cloud) and positively charged nucleus of the atom in the external electric field. This type of polarisation occurs up to a frequency of ~ 10^{17} Hz.

2.3.1.2 Ionic Polarisation

In ionic materials, ionic polarisations frequently take place by the relative displacement of positive and negative ions in the presence of an applied electric field. This ionic polarisation responds to a frequency up to the order of ~ 10^{13} Hz. Both atomic and ionic polarisation mechanisms have are the main contributions to most dielectrics [Zhang and Yu (2011)].

2.3.1.3 Dipolar Polarisation

There are many dielectric materials found having permanent dipole moments with random orientations, resulting zero net polarisation in the absence of electric field. Ferroelectric materials (described below) are an example of this type of polarisation mechanism. When such dielectric materials are subjected to an external applied electric field, the dipoles tend to align in the direction of electric field, giving net polarization. Dipolar polarization is temperature dependent and contributes to the dielectric and ferroelectric properties at a frequency of up to ~ 10^{10} Hz [Barsoum and Barsoum (2003), Zhang and Yu (2011)].

2.3.1.4 Space Charge Polarisation

In space charge polarisation, the charge carriers displaced by an electric field are stopped (blocked) at the surfaces or grain boundaries of the material, Figure 2.6. This movement of charge carriers to the surfaces creates dipoles. Space charge polarisation mechanism is relevant at low frequency up to ~ 10^3 Hz.

These electric field induced polarisation mechanisms in dielectric materials are highly frequency dependent on the applied field: their contribution to relative permittivity occurs over different ranges of frequencies [Hass and Wadley (2011)]. In summary, polarisability of atoms occurs up to ~ 10^{17} Hz and ionic polarisation up to ~ 10^{13} Hz respectively, Figure 2.7. Dipole realignment occurs up to ~ 10^{10} Hz, and for space charge the limit is ~ 10^3 Hz

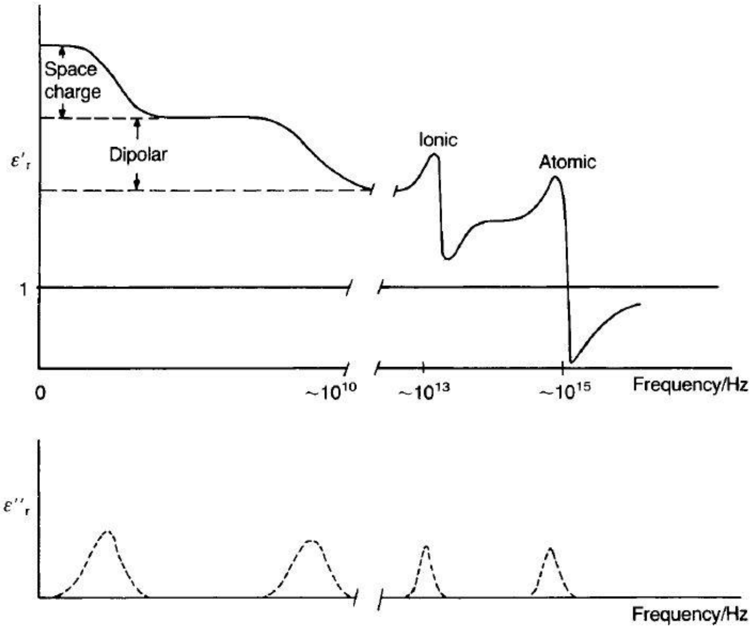

Figure 2.7 Variation of real part (εr′) and imaginary part (εr″) of relative permittivity with frequency [Moulson and Herbert (2003)].

2.3.1.5 Dielectric Loss

Dielectric losses are common alongside polarisation mechanism under an applied alternating electric field. In case of ideal dielectric material (capacitor), the phase angle between alternating current and voltage is 90°, Figure 2.8(a). But in real dielectric case, the current has two components (i) capacitive, out phase by 90° with voltage and (ii) lossy component, in phase with voltage, Figure 2.8(b). Therefore, the relative permittivity (ε_r) of the dielectric material is generally expressed in complex form; the real part (ε_r') and the imaginary part (ε_r'') represented by a relation [Hass and Wadley (2011)];

$$\varepsilon_r = \varepsilon_r' - j\varepsilon_r'' \qquad \text{Equation 2.5}$$

where ε_r' is the real part and ε_r'' is the imaginary part of relative permittivity. The real part corresponds to the charge storage ability while the imaginary part measures the energy loss. The dielectric loss tangent (tanδ) is the ratio of the energy lost to the energy stored in the electric field, given by a relation [Hass and Wadley (2011)];

$$\tan\delta = \frac{\varepsilon_r''}{\varepsilon_r'}$$ Equation 2.6

Low dielectric loss tangent (tanδ) and high relative permittivity (ε_r) of dielectric materials are of primary interest for many capacitor applications (for miniaturization and integrated components).

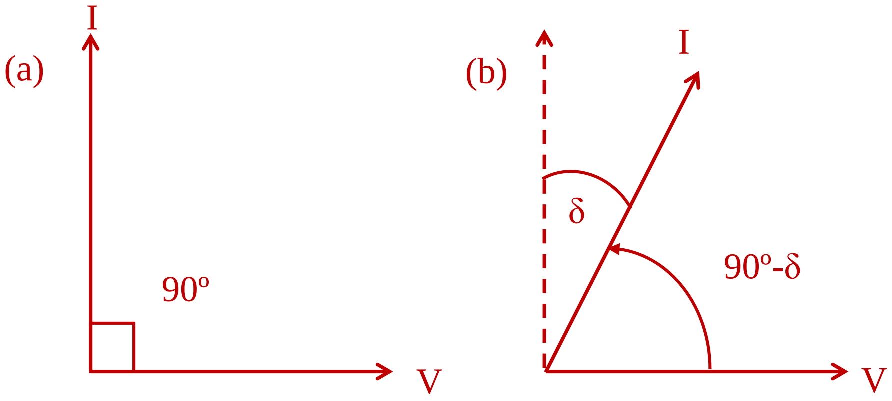

Figure 2.8 Phasor diagram indicating the phase angle between alternating current and voltage in case of: (a) ideal dielectric and (b) real dielectric [modified as Moulson and Herbert (2003)].

2.4 Ferroelectricity

Ferroelectricity is characterized by the existence of at least two spontaneous polarisation directions in the absence of an external field and their reversibility along their polar axis parallel to the direction of an applied field [Damjanovic (1998)]. The ability of polarisation reorientation of materials can experimentally be demonstrated by a polarisation-electric field (P-E) curve, ferroelectrics give rise to a characteristic ‘S’ shape response showing broadening, it is known as a hysteresis loop as shown in Figure 2.10 (section 2.4.1).

Ferroelectric materials above their Curie point (T_c) possess no spontaneous polarisation and are in a paraelectric phase, as in case of barium titanate the structure is highly symmetric (paraelectric) above ~ 130 ºC. Cooling below the Curie point (~ 130 ºC), ferroelectric phase(s) exist in $BaTiO_3$ which have of lower symmetry and possess spontaneous polarisation due to the relative displacement of Ti ion from its centrosymmetric position in the unit cell and result a creation of electric dipole, Figure 2.9 [Smith et al. (2008)]. A simple perovskite structure of $BaTiO_3$ with tetragonal symmetry, Figure 2.9, indicates the reversibility of the polarization caused by the relative displacement of Ti ion in the octahedra. Ceramic materials of perovskite structures like $BaTiO_3$ and $Pb(Ti,Zr)O_3$ are the common examples regarded as the foundation stone of ferroelectric science.

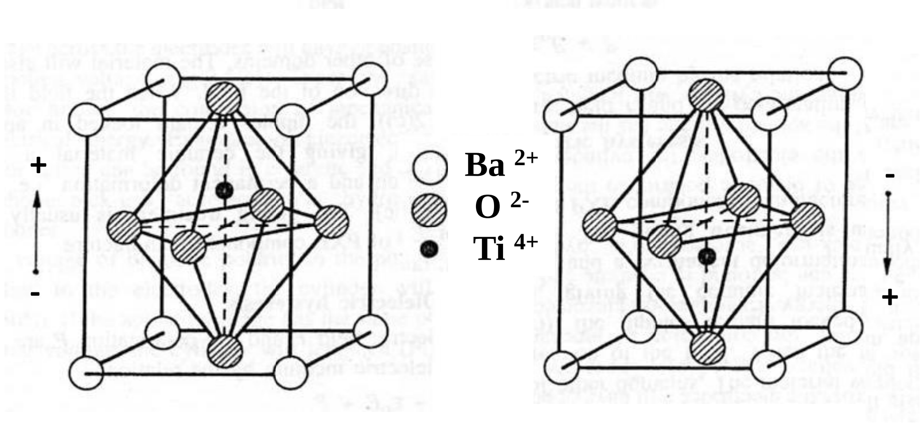

Figure 2.9 Ferroelectric tetragonal distortion of perovskite structure with polarisation switching [modified as Ahn et al. (2004)].

2.4.1 Ferroelectric Hysteresis

In ferroelectric materials, regions of aligned dipoles are referred to domains and the boundary separating these domains is known as domain wall. The formation of domains as a result of shifting of B cations according to allowed equivalent orientation states in the absence of external field. Domains in ferroelectric materials are mainly 180º corresponding to lattice deformation and non 180º due to mechanical strain, and can be switched to another state by an electric field [Gang Liu et al. (2015)].

When ferroelectric materials are subjected to an alternating electric field at a temperature below the Curie point, the domains start aligning in the direction of the field, Figure 2.10. For small magnitude of electric field, the effect is linear due to non-alignment of all domains. As the field strength is increased, a nonlinear increase in polarisation occurs until it becomes saturated. At the saturated stage the polarisation is known as saturation polarization (P_{sat}). The spontaneous polarization (P_s) at this stage is usually taken as an intercept on the polarization axis extrapolating from the tangent on saturation polarisation [Damjanovic (1998)].

When the magnitude of the field is decreased gradually to zero, the polarization starts to decline but polarization is not zero due to locking of some domains in the direction of the field, termed as remanent polarisation (P_r). To get zero polarization, a field of opposite polarity with specific strength is required, called coercive field (E_c). Further increase of field strength in the negative direction initiates a new alignment of domains in this direction and the cycle is completed reducing the field and reversing the direction once again. Thus, the curve traced out as a result of the alignment and disalignment of domains in positive and negative directions of field is known as Hysteresis curve or P-E curve, Figure 2.10. Ideally, the polarisation-electric field response (P-E loop) is symmetrical but the shape depends on the electric field, temperature and field frequency.

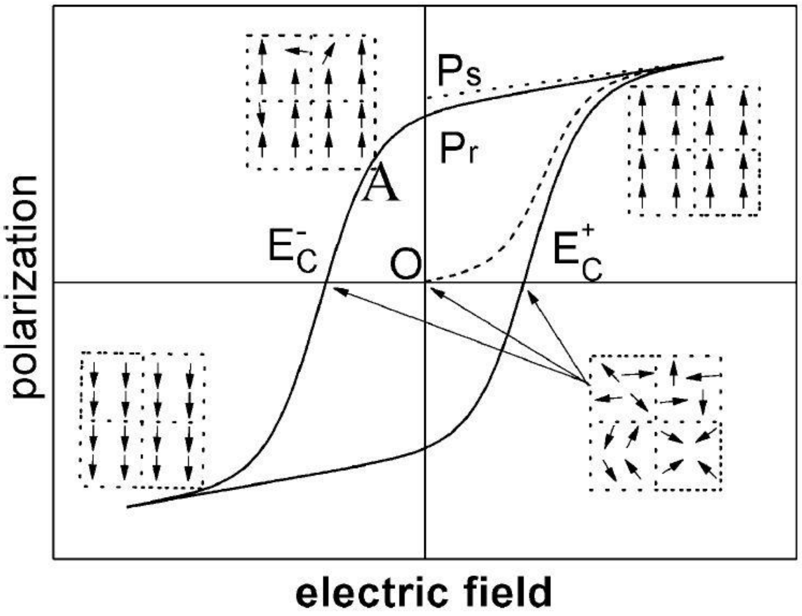

Figure 2.10 Polarisation-electric hysteresis loop [Yu et al. (2005)].

2.4.2 Ferroelectric phase transitions and Curie-Weiss law

The high symmetric polymorph for barium titanate ($BaTiO_3$) is cubic and paraelectric. It is stable at a temperature above T_c ~ 130 ºC [Shvartsman and Lupascu (2012)], up to the onset of the hexagonal polymorph at > 1400 ºC [Lee et al. (2007)]. A transition from cubic to ferroelectric tetragonal occurs below ~ 130 ºC. The other ferroelectric phases are orthorhombic and rhombohedral at a temperature of ~ 0 ºC and ~ -90 ºC respectively, Figure 2.11. All these ferroelectric phase transitions are attributed to the displacement of Ti^{4+} along different polar axes. The direction of spontaneous polarization in $BaTiO_3$, of tetragonal, orthorhombic and rhombohedral symmetry is along the direction of the edge, face diagonal and body diagonal unit cell respectively.

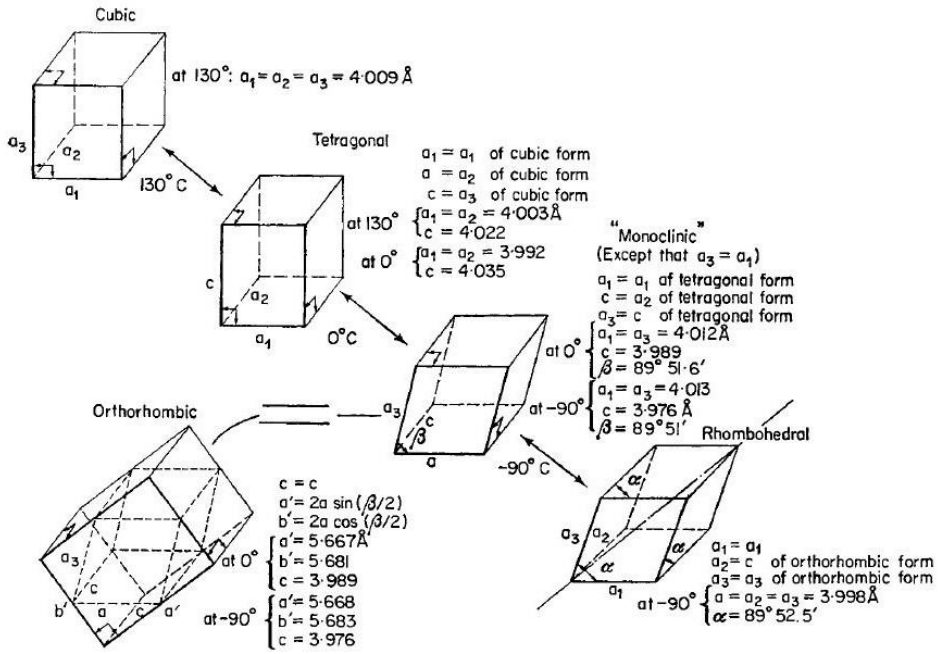

Figure 2.11 Illustration of ferroelectric phase transitions in $BaTiO_3$ [Jaffe (1971)].

The relative permittivity of most ferroelectric materials is changed considerably with changes in temperature and frequency [Moulson and Herbert (2003)]. As the temperature changes, most ferroelectric materials show dielectric anomalies with maxima at a certain temperatures corresponding to crystallographic phase transition temperatures. The temperature corresponding to the maximum relative permittivity, at the ferro-paraelectric transition is known as the Curie point (T_c). In the case of $BaTiO_3$, T_c ~ 130 °C. A decrease in relative permittivity take place above the Curie point (T_c) in accordance with the Curie-Weiss law [Zhu et al. (2011a)];

$$\varepsilon_r = \frac{C}{T - T_o} \qquad \text{Equation 2.12}$$

where C is the Curie constant for a given material, T_o is the Curie-Weiss temperature, T is the temperature at which relative permittivity is measured ($T > T_o$).

2.4.3 Relaxor Ferroelectrics

In contrast to classic ferroelectrics, another group of dielectric materials display broad frequency dependent relative permittivity-temperature peaks. These materials are known as relaxors [Ravez and Simon (2001), Zeb and Milne (2014b)]. The distinctive features of relaxors are broad dielectric peaks in the relative permittivity versus temperature plots and strong frequency dispersion of both real and imaginary parts of the relative permittivity close to the peak temperature, T_m, Figure 2.12. Relaxor characteristics were first explored by Smolenskii and co-worker in lead magnesium niobate (PMN) and this material received considerable attention due to favourable dielectric and electromechanical properties [Smolenskii (1984), Zeb and Milne (2014b)].

Several theories have been proposed to account for this relaxor behaviour, based on concepts of compositional fluctuations and the formation of polar nanoregions/domains [Bokov and Ye (2000), Badapanda et al. (2009)].

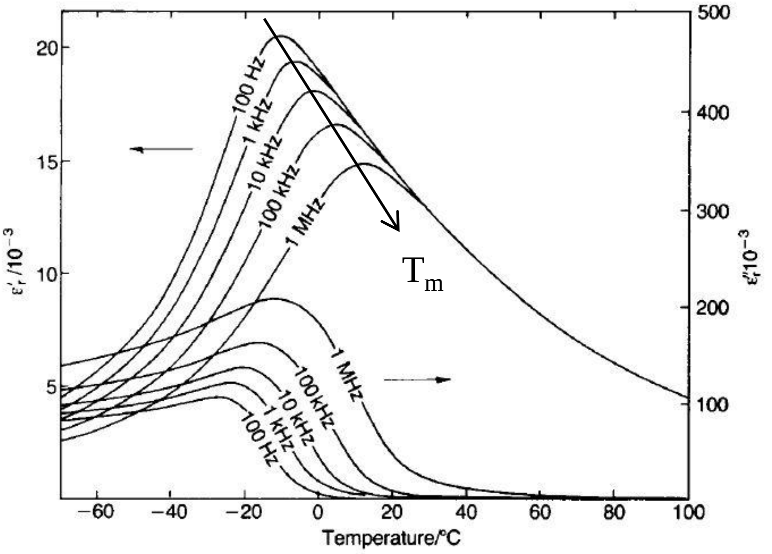

Figure 2.12 Illustration of frequency dispersion in temperature-dependent real and imaginary relative permittivity plot for PMN [Moulson and Herbert (2003)].

Different relaxation times of the PNRs give rise to the broad dielectric peak and frequency dispersion. In many relaxors, there are mixed valence multiple cation site occupancies on the B sites of the perovskite ABO_3 [Bokov and Ye (2007), Bokov (1992)]. This creates fluctuating electrostatic and stress fields which are thought to perturb long range polar domains (of a ferroelectric), instead short range order exists (PNRs). However, a number of perovskites have emerged in recent years, involving both A and B site mixed valence occupancies. These complex perovskites display relaxor-like frequency dependent decreases in ε_r at $T < T_m$ but for some solid solution compositions the dielectric peak is supressed and the material shows little variation in relative permittivity (ε_r) over a wide temperature range, $T > T_m$.

For relaxor systems, the decrease in relative permittivity above the T_m does not conform to the standard Curie-Weiss law, and is more effectively described by a modified Curie-Weiss equation [Yiliang Wang et al. (2013)];

$$\frac{1}{\varepsilon_r} - \frac{1}{\varepsilon_{r\max}} = \frac{(T - T_{\varepsilon_r \max})^{\gamma}}{C} \qquad \text{Equation 2.13}$$

For classic ferroelectric material, the γ coefficient is equal to unity, increasing to ~ 2 for a typical relaxor [Wang et al. (2013)]. These types of relaxor dielectric materials are of particular interest for high permittivity (Class 2) dielectrics operating at > 200 ºC for applications in power electronics and in control and sensing systems for deep-well drilling and aerospace [Zeb and Milne (2014b)].

2.5 Piezoelectricity

Piezoelectricity is the capability of some materials to develop proportional electric charges (potential difference) across it surfaces when subjected to mechanical stress, termed as the direct piezoelectric effect. In effect, the polarity of the potential difference produced depends on the nature of the applied stress (e-g compressive or tensile). Conversely, a mechanical deformation is produced in the same material with the application of electric field, is known as the converse piezoelectric effect [Damjanovic (1998)]. The sign of deformation in the material depends on the polarity of the electric field. The generation of bipolar S-E loop (butterfly like loop) is the result of the converse piezoelectric effect [Damjanovic (1998)]. Materials exhibiting both these types of phenomena are considered piezoelectric materials and widely used for variety of applications. The piezoelectric effects can be described by the following relations [Moulson and Herbert (2003)];

$P = dX$ (direct effect) Equation 2.7

where P is the polarisation, X is the mechanical stress (compression or extension). The converse piezoelectric effect in terms of applied field (E) and strain (*x*) produced in the material is given by;

$x = dE$ (converse effect) Equation 2.8

The piezoelectric charge coefficient, d, used in the above two equations (2.7 and 2.8) have identical numerical equivalence and is the ratio of electric polarisation produced to stress applied or the strain produced to the applied field. However, the direct and converse piezoelectric effects are usually expressed with different units pC/N and pm/V, respectively. Both direct and converse effects are illustrated in Figure 2.13.

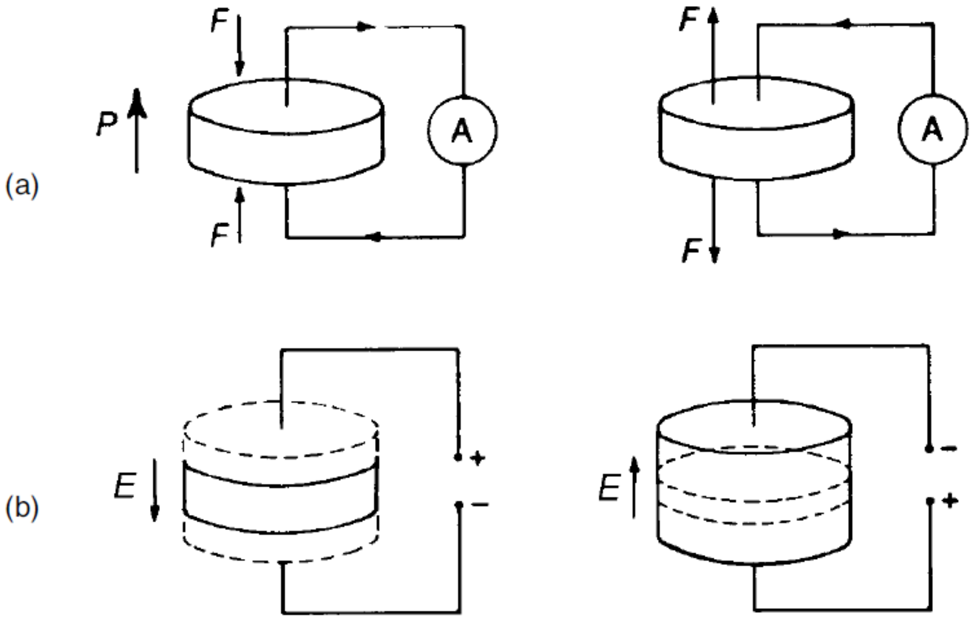

Figure 2.13 Illustration of (a) direct and (b) converse piezoelectric effect [Moulson and Herbert (2003)].

The piezoelectric charge coefficient is a directional dependent quantity due to anisotropic nature of materials [Haertling (1999)]. Therefore, usually, they are assigned with two subscripts indices to indicate their directional characteristics of the two related quantities (field and strain or stress and polarisation). For example, the piezoelectric constant, d_{33} represents the induced polarization per unit applied stress in direction 3 or the induced strain per unit electric field whilst d_{31} is the induced polarization in direction 3 per unit stress in direction 1.

For the piezoelectric constant which relates the electric and mechanical quantities, the first subscript indicates the electric quantity (electric field or electric polarisation) while the second, for the mechanical (strain or stress) [Jaffe (1971)].

Conventionally, the three mutual orthogonal axes x, y and z are labelled as 1, 2 and 3 respectively, Figure 2.14. Another convention used for the direction of positive polarization (Poling direction) which coincide with along 3-axis. The shear stress about these axes are represented by 4, 5 and 6 which are perpendicular to directions 1, 2 and 3 respectively, Figure 2.14 [Moulson and Herbert (2003)].

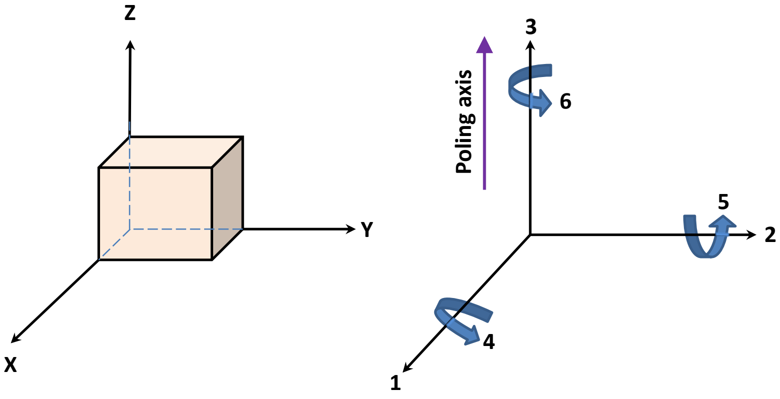

Figure 2.14 Poling axis and their orthogonal axes for strain [modified as Moulson and Herbert (2003)].

2.5.1 Electrostriction

In piezoelectricity, the strain effect produced in a material is proportional to the applied electric field and sign of deformation depends on the polarity of the applied field. Electrostriction, is another electromechanical effect closely related to piezoelectricity but the strain produced is proportional to the square of field and sign of deformation is independent of the polarity of the field [Haertling (1999)]. Although all dielectric materials exhibit a minimal electrostriction behaviour with the applied field, this becomes more significant in dielectrics of high relative permittivity. In terms of electrostriction, the relation of strain and the applied electric field can be expressed by the following relation [Haertling (1999)];

$$x = mE^2 \qquad \text{Equation 2.9}$$

where m is electrostrictive coefficient, x is the strain and E is the magnitude of the applied electric field.

2.5.2 Electromechanical Coupling Factor (k_p)

As mentioned above, piezoelectric materials couple the electric and mechanical energies e.g. convert electrical energy into mechanical energy and vice versa. Thus to represent this conversion strength, an electromechanical coupling factor is used. This coupling factor is always less than unity and defined as [Jaffe (1971)];

$$k_p^{\,2} = \frac{\text{electrical energy converted into mechanical energy}}{\text{input electrical energy}} \qquad \text{Equation 2.10}$$

or

$$k_p^{\,2} = \frac{\text{mechanical energy converted into electrical energy}}{\text{input mechanical energy}} \qquad \text{Equation 2.11}$$

A high coupling factor is often desirable in piezoelectric materials for different applications, which are constantly required in new materials. The coupling factor is dimensionless quantity, whose typical values of the order of ~ 0.4 for $BaTiO_3$ and for $Pb(Ti,Zr)O_3$ is ~ 0.5-0.7 [Jaffe (1971)].

2.6 Morphotrophic Phase Boundary(MPB) and Lead Zirconate Titanate (PZT)

The term morphotrophic phase boundary (MPB) is usually specified as a vertical or near vertical (temperature insensitive) phase boundary on the phase diagram of a solid solution system. The phase content in the vicinity of a MPB varies with the change in composition, but if a true vertical MPB, not with temperature up to the maximum temperature of the MPB [Ahart et al. (2008)]. In perovskites, the coexistence of ferroelectric phases with different symmetries at the MPB results in enhancement of piezoelectric properties which allow for easy re-alignment of spontaneous polarisation directions.

For example in PZT, six spontaneous polarisations from tetragonal coupled with eight of rhombohedral symmetry during poling. The market-leading piezoelectric material, lead zirconate titanate, PZT, is a solid solution between $PbZrO_3$ and $PbTiO_3$ in which a phase boundary exists between rhombohedral and tetragonal phase fields at around ~ 52 mol% $PbZrO_3$. This phase boundary is almost vertical on the $PbZrO_3$-$PbTiO_3$ phase diagram over a wide temperature range, and for this reason it is referred to as a morphotropic phase boundary (MPB), Figure 2.15 [Jaffe (1971), Noheda et al. (1999)]. Other examples of solid solutions which possess a MPB includes; $Na_{0.5}Bi_{0.5}TiO_3$-$BaTiO_3$, $Na_{0.5}Bi_{0.5}TiO_3$-$K_{0.5}Bi_{0.5}TiO_3$, and the ternary $Na_{0.5}Bi_{0.5}TiO_3$-$BaTiO_3$-$K_{0.5}Bi_{0.5}TiO_3$ [Leontsev and Eitel (2010)].

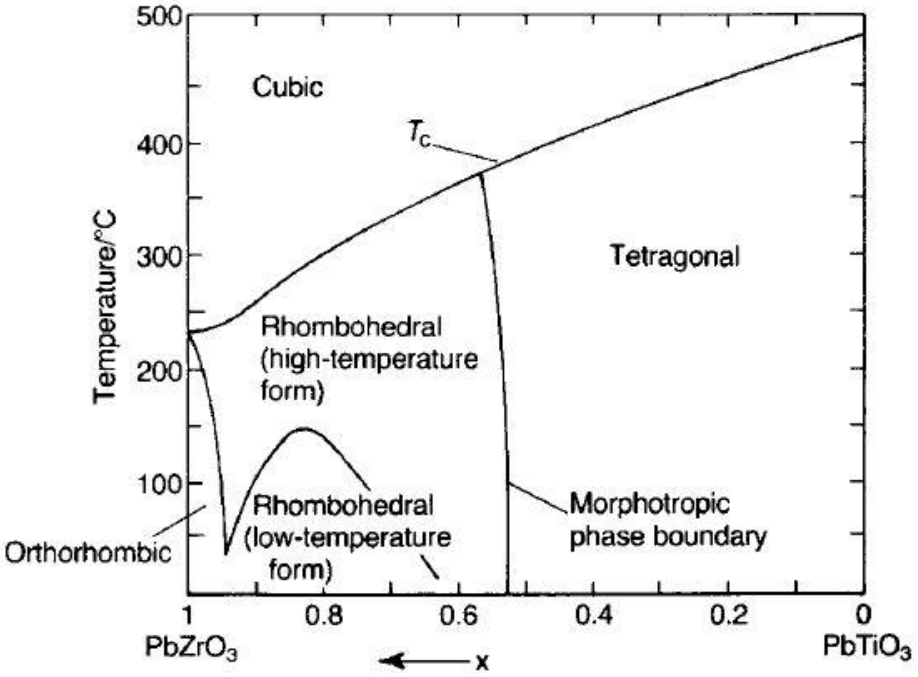

Figure 2.15 Illustration of MPB in PZT [Moulson and Herbert (2003)].

Piezoelectric ceramic materials based on lead zirconate titanate, PZT, are well known due to the very favourable electromechanical properties. The high electromechanical performance of lead zirconate titanate (PZT), is the result of coexistence of ferroelectric phases (MPB) [as discussed above] between rhombohedral $PbZrO_3$ and tetragonal $PbTiO_3$ at around 52 mol% $PbZrO_3$ [Jaffe (1971)]. The reported piezoelectric properties at the MPB for undoped PZT are; T_c = 390 ºC, ε_r = 1600 at room temperature, d_{33} = 233 pC/N and k_p = 0.52 [Ansell et al. (2014)].

A range of chemical dopants, commonly classified as donors (soft PZT) or acceptors (hard PZT), have been used to tailor the properties of PZT for specific applications. In donor doping higher valence ions for example; La^{3+} on the A site and Nb^{5+} on the B site whereas for acceptor doping, a lower valence ions such as K^{1+} on the A site and Fe^{3+} on the B site were employed. Soft PZT exhibit high piezoelectric constant (d_{33}) with low coercive field due to cation vacancy and facilitate easy domain wall motion. In contrast, in hard PZT, the observed loss tangent is low and they show low piezoelectric performance along with high a poling field due to difficulty in domain wall motion caused by oxygen vacancies [Damjanovic (1998), Ansell et al. (2014), Panda and Sahoo (2015)].

Despite high piezoelectric performance and relatively high Curie temperature (T_c), PZT based piezoelectric materials are facing global restrictions; owing to serious environmental and health concerns regarding Pb toxicity [RoHS Directive (2003), Saito et al. (2004)]. These global restrictions constantly drive in a search for lead-free material systems.

2.6.1 Applications of Piezoelectricity

Piezoelectric materials have diverse uses and applications. The direct and converse piezoelectric effects can be used for many practical applications ranging from high voltage generators (transducers), electromechanical actuators, sensors, diesel fuel injectors (actuators) and sonar [Haertling (1999), Aksel and Jones (2010)]. These applications can be mainly classified into three categories: (i) generators (direct effect) (ii) motors (converse effect) and (iii) generator and motor combined. A summary of each group applications is given in the flow chart, Figure 2.16.

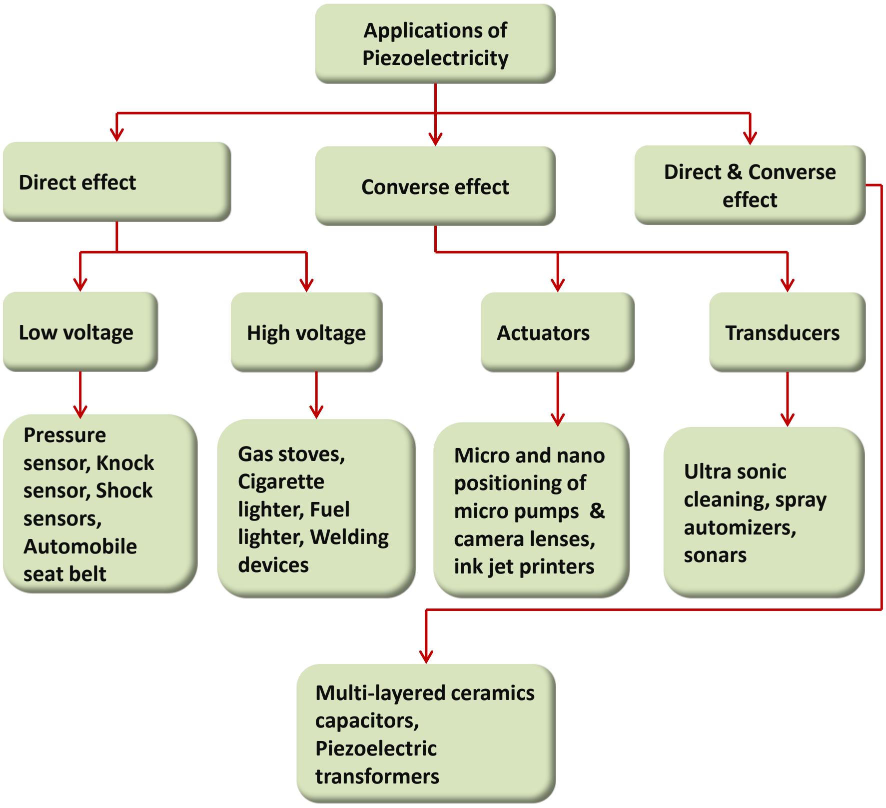

Figure 2.16 Flow chart represents the applications of piezoelectricity.

2.7 Lead-free piezoelectric ceramics

Piezoelectric ceramics having no lead oxide (PbO) content are referred to as lead free piezoelectric ceramics. Common examples includes; barium titanate ($BaTiO_3$), sodium bismuth titanate ($Na_{0.5}Bi_{0.5}TiO_3$), potassium sodium niobate ($K_{0.5}Na_{0.5}NbO_3$) and potassium bismuth titanate ($K_{0.5}Bi_{0.5}TiO_3$). The regulations on the PZT-based or PMN-based materials have motivated researchers to search for lead free piezoelectric materials to replace the toxic Pb-containing materials. At the time of writing this thesis the European Union has granted exemptions from relevant health and safety regulations surrounding lead and lead oxide to permit the ongoing use of Pb-containing piezoelectrics.

2.7.1 Barium Titanate ($BaTiO_3$)

Barium titanate, $BaTiO_3$ (BT) was the first ferroelectric perovskite to be used as a piezoelectric, and was employed in sonar applications in the 1940s. The reported piezoelectric constant (d_{33}) for pure $BaTiO_3$ by solid state processing route is ~ 190 pC/N with an electromechanical coupling factor k_p ~ 0.35-0.4 [Moulson and Herbert (2003), Coondoo et al. (2013)]. Intensive research and efforts have been made for improving dielectric and piezoelectric performance of $BaTiO_3$-based materials and its applications in a wide working temperature range.

2.7.2 $BaTiO_3$-based piezoelectric ceramics

Numerous barium titanate-based ferroelectric materials with improved piezoelectric properties have been developed. Liu and Ren (2009) reported excellent piezoelectric properties of $0.5Ba(Zr_{0.2}Ti_{0.8})O_3$-$0.5Ba_{0.7}Ca_{0.3}TiO_3$ ceramic system. A high d_{33} ~ 620 pC/N was obtained for ceramic composition at $x = 0.5$ based on the coexistence of rhombohedral and tetragonal polymorphs combining with the cubic paraelectric phase (tri critical point), Figure 2.17. These piezoelectric properties were attributed to the enhanced polarisation rotation in the vicinity of triple point at room temperature. However, these properties are temperature sensitive and the depolarisation temperature is low, below 100 ºC [Liu and Ren (2009)]. A similar result of high piezoelectric constant, d_{33} ~ 530 pC/N was achieved in the binary system $0.7Ba(Sn_{0.2}Ti_{0.8})O_3$-$0.3Ba_{0.7}Ca_{0.3}TiO_3$ in the vicinity of room temperature [Xue et al. (2011a)]. Other workers reported the composition $Ba_{0.93}Ca_{0.07}Ti_{0.95}Zr_{0.05}O_3$ exhibited d_{33} ~ 387 pC/N and k_p ~ 0.44. However, the working temperature was again limited to below 100 ºC [Li et al. (2011)]. These findings further drive research to achieve high electromechanical properties coupled with the stability in properties over a wider working temperature range.

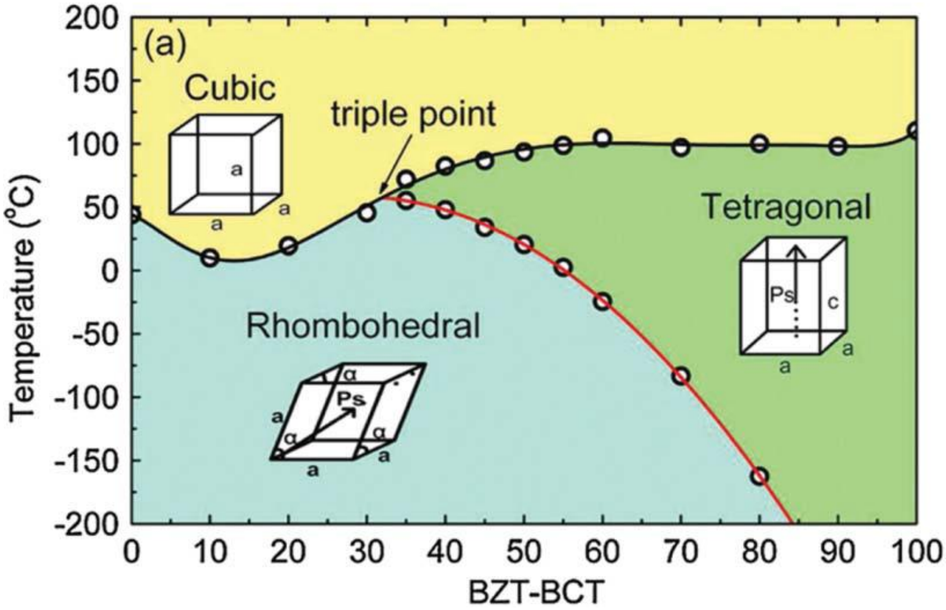

Figure 2.17 Illustration of phase diagram for lead free 0.5BZT-0.5BCT piezoelectric ceramic system [Liu and Ren (2009)].

2.7.3 $Na_{0.5}Bi_{0.5}TiO_3$-based lead-free piezoelectric ceramics

2.7.3.1 Sodium bismuth titanate ($Na_{0.5}Bi_{0.5}TiO_3$)

Sodium bismuth titanate, $Na_{0.5}Bi_{0.5}TiO_3$ (NBT) is a ferroelectric perovskite first reported by Smolenskii and co-workers in 1960s [Smolenskii et al. (1961), Hiruma et al. (2009)]. The structure of NBT is complex and still under debate. Based on the neutron diffraction experiments, NBT is rhombohedral at room temperature while high resolution synchrotron X-ray diffraction study proposed a monoclinic phase for NBT [Li et al. (2015)]. NBT has relatively high remanent polarisation, P_r ~ 38 μC/cm^2, coercive field, E_c ~ 73 kV/cm and low piezoelectric charge coefficient, d_{33} ~ 73 pC/N. For NBT, the phase transition temperature from rhombohedral to cubic paraelectric phase takes place at T_c ~ 320 ºC [Hiruma et al. (2009)]. Relative permittivity versus temperature plots demonstrate relaxor character and an additional inflection peak appears in ε_r-T plots at ~ 200 ºC [Dorcet et al. (2008)]. Numerous research studies have been focussed on modifications to NBT. These NBT-based solutions have attracted much attention over the past decade. Leading examples are the binary systems, $Na_{0.5}Bi_{0.5}TiO_3$-$BaTiO_3$ (NBT-BT) and $Na_{0.5}Bi_{0.5}TiO_3$-$K_{0.5}Bi_{0.5}TiO_3$ (NBT-KBT), and the ternary $Na_{0.5}Bi_{0.5}TiO_3$-$BaTiO_3$-$K_{0.5}Na_{0.5}NbO_3$ (NBT-BT-KNN).

The solid solution of NBT-BT was studied by many research groups and a MPB is reported between the rhombohedral and tetragonal solid solution phase at 6-7 mol% BT [Takenaka et al. (1991b), Xu et al. (2008)]. The reported piezoelectric properties for NBT-BT at the MPB are, d_{33} ~ 122-176 pC/N, P_r ~ 37-40 μC/cm^2, k_p ~ 0.21-0.36, T_d ~ 90-105 ºC and T_m ~ 225-288 ºC [Rödel et al. (2009), Leontsev and Eitel (2010)].

In solid solution of NBT-KBT a MPB was found at ~ 20 mol% KBT, exhibiting piezoelectric properties: d_{33} ~ 140-192 pC/N, P_r ~ 20-38 μC/cm^2, k_p ~ 0.27-0.35, T_m ~

280-300 ºC and depolarisation temperature T_d ~ 140 ºC [Leontsev and Eitel (2010), Rödel et al. (2009), Coondoo et al. (2013)].

A variety of chemical modifications to NBT-BT and NBT-KBT have been made as means to enhance the piezoelectric properties. The promising pseudoternary systems include; NBT-KBT-BT, typically with d_{33} ~ 170 pC/N, k_p ~ 0.35 and T_d ~ 162 ºC (determined from the ε_r-T plot) [Nagata et al. (2003)]. The ternary system NBT-BT-KNN demonstrated 'giant' electromechanical strains, up to ~ 0.45%, in the MPB region. This is reported to be a consequence of electric field-induced phase transformation from ferroelectric to relaxor [Zhang et al. (2007)]. This field-induced transformation gives rise to a characteristic discontinuity and wide hysteresis in strain-electric field plots.

However, NBT-based piezoelectrics exhibit relatively low depolarisation temperatures at MPB compositions: T_d ~ 90-105 ºC, and the lossy S-E response (wide hysteresis in S-E plots, ~ 69%) risks self-heating induced depolarisation making the materials unsuitable for high power applications [Rödel et al. (2009)].

2.7.4 $K_{0.5}Na_{0.5}NbO_3$-based lead free ceramic systems

Potassium sodium niobate, $K_{0.5}Na_{0.5}NbO_3$ (KNN) is formed as a result of a solid solution between potassium niobate ($KNbO_3$) and sodium niobate ($NaNbO_3$). KNN is orthorhombic/monoclinic at room temperature and exhibits modest piezoelectric properties, d_{33} ~ 92-117 pC/N; and k_p ~ 0.32-0.44 [Egerton and Dillon (1959), Zuo et al. (2006)]. To enhance piezoelectric properties, KNN has been modified by many dopants, Table 2.2. Modification by $LiTaO_3$ and $LiSbO_3$ leads to a relatively high value of d_{33} ~ 300 pC/N, which arises because of phase co-existence at a polymorphic phase transition PPT (an inclined boundary on the phase diagram) rather than a temperature-invariant MPB [Skidmore et al. (2009)]. The PPT between orthorhombic and tetragonal phases occurs near room temperature for a narrow band of KNN-LT compositions, and hence d_{33} values of these compositions measured at room temperature are enhanced, but properties degrade as the temperature is raised above room temperature.

Recent research has demonstrated a promising combination of high d_{33} ~ 263-321 pC/N, k_p ~ 0.40 and good temperature stability up to temperature ~ 200 ºC in the ceramic system KNN-$BaZrO_3$-$(Bi,Li)TiO_3$ due to development of a tetragonal/rhombohedral MPB [Zushi et al. (2013), Shi et al. (2016)]. More recent developments have further improved properties and improved temperature stability, for example; the reported piezoelectric properties for $0.92K_{0.5}Na_{0.5}NbO_3$-$0.02Bi_{0.5}Li_{0.5}TiO_3$-$0.06BaZrO_3$, d_{33} = 348 pC/N and k_p = 0.57 at room temperature and retained up to ~ 200 ºC [Wang et al. (2015)]. Similarly, in the ternary system: $0.955K_{0.48}Na_{0.52}NbO_3$-$0.005BiScO_3$-$0.04Bi_{0.5}(Na_{0.7}K_{0.2}Li_{0.1})_{0.5}ZrO_3$, a high value of d_{33} ~ 366 pC/N was reported at room temperature and retained (~ 319 pC/N) up to ~ 300 ºC [Xiaojing Cheng et al. (2014)].

Table 2.2 Piezoelectric properties of KNN-based ceramic materials [Panda and Sahoo (2015)].

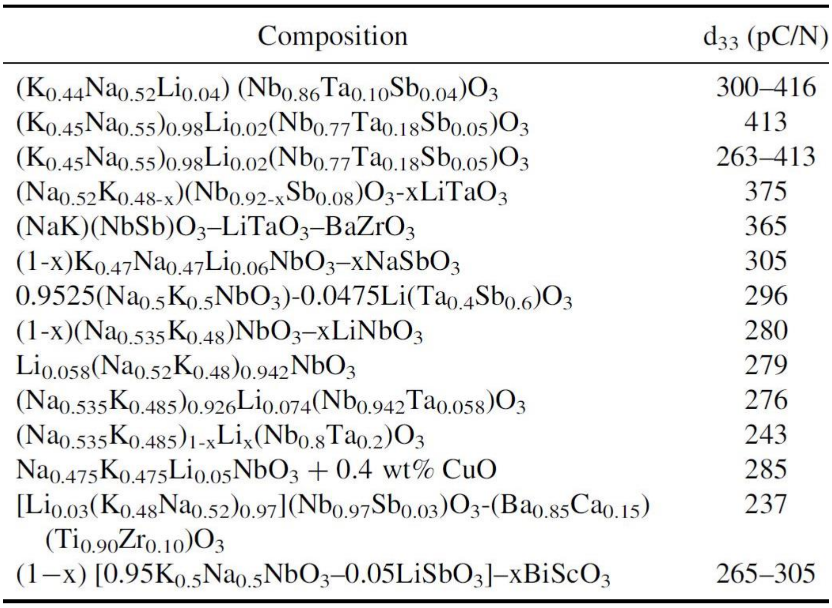

Composition	d_{33} (pC/N)
$(K_{0.44}Na_{0.52}Li_{0.04})\ (Nb_{0.86}Ta_{0.10}Sb_{0.04})O_3$	300–416
$(K_{0.45}Na_{0.55})_{0.98}Li_{0.02}(Nb_{0.77}Ta_{0.18}Sb_{0.05})O_3$	413
$(K_{0.45}Na_{0.55})_{0.98}Li_{0.02}(Nb_{0.77}Ta_{0.18}Sb_{0.05})O_3$	263–413
$(Na_{0.52}K_{0.48-x})(Nb_{0.92-x}Sb_{0.08})O_3$-$xLiTaO_3$	375
$(NaK)(NbSb)O_3$–$LiTaO_3$–$BaZrO_3$	365
$(1-x)K_{0.47}Na_{0.47}Li_{0.06}NbO_3$–$xNaSbO_3$	305
$0.9525(Na_{0.5}K_{0.5}NbO_3)$-$0.0475Li(Ta_{0.4}Sb_{0.6})O_3$	296
$(1-x)(Na_{0.535}K_{0.48})NbO_3$–$xLiNbO_3$	280
$Li_{0.058}(Na_{0.52}K_{0.48})_{0.942}NbO_3$	279
$(Na_{0.535}K_{0.485})_{0.926}Li_{0.074}(Nb_{0.942}Ta_{0.058})O_3$	276
$(Na_{0.535}K_{0.485})_{1-x}Li_x(Nb_{0.8}Ta_{0.2})O_3$	243
$Na_{0.475}K_{0.475}Li_{0.05}NbO_3 + 0.4$ wt% CuO	285
$[Li_{0.03}(K_{0.48}Na_{0.52})_{0.97}](Nb_{0.97}Sb_{0.03})O_3$-$(Ba_{0.85}Ca_{0.15})(Ti_{0.90}Zr_{0.10})O_3$	237
$(1-x)\ [0.95K_{0.5}Na_{0.5}NbO_3$–$0.05LiSbO_3]$–$xBiScO_3$	265–305

2.7.5 $K_{0.5}Bi_{0.5}TiO_3$-based lead free ceramic systems

2.7.5.1 Potassium bismuth titanate ($K_{0.5}Bi_{0.5}TiO_3$)

Potassium bismuth titanate, $K_{0.5}Bi_{0.5}TiO_3$ (KBT) is ferroelectric perovskite fabricated first by Popper et al. in 1957 [Popper et al. (1957), Rödel et al. (2009)]. KBT is tetragonal at room temperature and dielectric data has revealed a relatively broad peak in ε_r-T plots with phase transition temperature at T_c ~ 380 ºC with room temperature relative permittivity, $\varepsilon_r \leq 800$ [Hiruma et al. (2005), Otoničar et al. (2010)]. The reported value of piezoelectric charge coefficient, d_{33} is ~ 31 pC/N and k_p ~ 0.18 for ceramics prepared by a conventional processing route.

Generally, KBT is less studied than NBT because it can be difficult to fabricate dense ceramics by conventional solid state methods due to weight loss of volatile constituents during sintering processing [Isupov (2005), Wada et al. (2002)]. However, hot pressing techniques and Bi-excess are reported to enhance the densification of KBT ceramics which led to promising ferroelectric and piezoelectric properties [Hiruma et al. (2007a)]. Dielectric, ferroelectric and piezoelectric properties of KBT, KBT hot pressed (HP) and Bi-excess KBT are summarized in Table 2.3.

Table 2.3 Dielectric (1 MHz), ferroelectric and piezoelectric properties of the KBT ceramics [Kim et al. (2010), Sasaki et al. (1999)] KBT-HP and KBT-Bi-excess [Hiruma et al. (2007a)].

Properties	KBT	KBT-HP	KBT (Bi-excess)
ε_r at RT	800	520	764
T_{max} (°C)	380	410	391
P_r ($\mu C/cm^2$), E_{max}=150 kV/cm	-	22.2	28
d_{33} (pC/N)	31	82	101
k_p	0.18	-	-
S_{max} (%) (E_{max} = 80 kV/cm)	-	0.1	0.13

2.7.5.2 $K_{0.5}Bi_{0.5}TiO_3$-$BaTiO_3$

Buhrer (1962) first reported the solid solution of $(1-x)K_{0.5}Bi_{0.5}TiO_3$-$xBaTiO_3$. It was found that the Curie temperature and the tetragonality decreased with the increase of $BaTiO_3$ content. Later, the dielectric and piezoelectric properties in $(1-x)K_{0.5}Bi_{0.5}TiO_3$-$xBaTiO_3$ has been reported by Hiruma et al. (2004). A solid solution between the two tetragonal end members was formed across the whole compositional range. X-ray diffraction data revealed the decrease in tetragonality (***c/a***) in the BT-rich compositions. Values of piezoelectric constant, d_{33} were modest, ~ 60 pC/N similar to unmodified KBT, increasing to ~ 100 pC/N for a composition with minor levels of doping of manganese oxide [Hiruma et al. (2004)]. There are also reports about $(1-x)$KBT-xBT solid solutions fabricated by textured and grain oriented techniques. An improved piezoelectric constant, d_{33} of ~ 85 pC/N and 121 pC/N was achieved by textured and grain oriented techniques respectively at 10 mol% of BT content [Nemoto et al. (2008), Nemoto et al. (2009)].

2.7.5.3 $K_{0.5}Bi_{0.5}TiO_3$-$Bi(Zn_{0.5}Ti_{0.5})O_3$

Huang et al. (2009) synthesised the solid solution of KBT and $Bi(Zn_{0.5}Ti_{0.5})O_3$ (BZT). A single phase of $(1\text{-}x)K_{0.5}Bi_{0.5}TiO_3\text{-}xBi(Zn_{0.5}Ti_{0.5})O_3$ was obtained at ≤ 20 mol% of BZT content. It was found that the tetragonality was supressed while the cell volume increased with the addition of BZT content. The reported dielectric data indicated broad peaks in the ε_r-T plots, with a linear decrease of T_m. A peak value of remanent polarisation, $P_r \sim 12$ μC/cm^2 (E_{max} = 80 kV/cm) was observed for composition $x = 0.1$. It was also found that composition $x = 0.1$ exhibited a bipolar strain of ~ 0.18% (E_{max} = 80 kV/cm) and a value of coupling factor, $k_p = 0.18$.

2.7.5.4 $K_{0.5}Bi_{0.5}TiO_3$-$BiFeO_3$

The solid solution of $(1\text{-}x)K_{0.5}Bi_{0.5}TiO_3\text{-}xBiFeO_3$ was studied by a number of research groups. Kim et al. (2010) investigated the dielectric and piezoelectric properties in binary system $(1\text{-}x)K_{0.5}Bi_{0.5}TiO_3\text{-}xBiFeO_3$. It was shown that relative permittivity ε_r-T plots displayed broad peaks for $x = 0.6$. The piezoelectric constant, d_{33} increased from 31 pC/N at $x = 0$ to a peak value of 64 pC/N for $x = 0.06$ [Kim et al. (2010)]. Matsuo et al. (2010) reported a large remanent polarisation, $P_r = 52$ μC/cm^2 (E_{max} = 100 kV/cm) in $(1\text{-}x)K_{0.5}Bi_{0.5}TiO_3\text{-}xBiFeO_3$ for the $BiFeO_3$ rich region ($x = 0.6$). There are also some reports about large electric field induced bipolar strain ~ 0.18% (E_{max} = 50 kV/cm) for composition $x = 0.25$ [Morozov et al. (2012)].

2.7.5.5 $K_{0.5}Bi_{0.5}TiO_3$-$BiScO_3$

KBT modified with $BiScO_3$, $(1\text{-}x)K_{0.5}Bi_{0.5}TiO_3\text{-}xBiSO_3$ was studied by [Kruea-In et al. (2012)]. Incorporation of $BiScO_3$ effectively induced relaxor behaviour with strong frequency dispersion in ε_r-T plots. Compositions $x = 0.15$ and $x = 0.2$ presented a flat ε_r-T response: for example $x = 0.15$ exhibited a ±3% variation in relative permittivity about ε_r = 2880 across the temperature range 227 ºC to 427 ºC. Independently, Martín-Arias et al., reported a similar temperature stable dielectric response for composition $x = 0.2$ [Martín-Arias et al. (2012)].

2.7.5.6 $K_{0.5}Bi_{0.5}TiO_3$-$(K_{0.5}Bi_{0.5})ZrO_3$

The structural and electrical properties of KBT-modified with $K_{0.5}Bi_{0.5}ZrO_3$ (KBZ) were investigated by Bengagi et al. (2012). XRD data revealed a single phase over the entire compositional range, changing from tetragonal to pseudocubic at $x > 0.05$. Addition of KBZ resulted a relaxor behaviour in the ε_r-T plots. The reported value of piezoelectric constant, d_{33} was 31 pC/N for $x = 0$ and decreased to d_{33} ~ 2 pC/N for composition $x = 0.1$.

2.7.5.7 $K_{0.5}Bi_{0.5}TiO_3$-$Bi(Ni_{0.5}Ti_{0.5})O_3$

Zhao and Zuo studied KBT modified with the $Bi(Ni_{0.5}Ti_{0.5})O_3$ [Zhao and Zuo (2013)]. In this binary $(1-x)K_{0.5}Bi_{0.5}TiO_3$-$xBi(Ni_{0.5}Ti_{0.5})O_3$ ceramic system, a single phase solid solution was obtained up to 20 mol% of $Bi(Ni_{0.5}Ti_{0.5})O_3$. Based on the XRD data, a coexistence of tetragonal and rhombohedral phases (MPB) was identified at compositional range of $x = 0.05$-0.07.

Plots of relative permittivity versus temperature exhibited broad frequency dependent peaks. Values of T_m were found to decrease with the addition of $Bi(Ni_{0.5}Ti_{0.5})O_3$. Among all these compositions of this system, sample $x = 0.06$ displayed a high piezoelectric constant with value of d_{33} = 126 pC/N and k_p = 0.18.

2.7.5.8 $K_{0.5}Bi_{0.5}TiO_3$-$LiNbO_3$

Zuo et al. (2013) synthesised the relaxor solid solution of $(1-x)K_{0.5}Bi_{0.5}TiO_3$-$xLiNbO_3$. A MPB between the tetragonal KBT and rhombohedral $LiNbO_3$ was found in the compositional range at $0.015 < x < 0.03$. All compositions of this binary system were characterized with diffuse, frequency dependent dielectric peaks. Values of remanent polarisation for KBT ($x = 0$) were ~ 5 μC/cm^2 increasing to a maximum value of ~ 7.1 μC/cm^2 at $x = 0.015$ (E_{max} = 60 kV/cm). It was also shown that composition $x = 0.015$ exhibited enhanced piezoelectric properties of d_{33} ~ 75 pC/N and $k_p = 0.18$.

2.7.5.9 $K_{0.5}Bi_{0.5}TiO_3$-$(Bi_{0.5}Na_{0.5})ZrO_3$

The solid solution $(1-x)K_{0.5}Bi_{0.5}TiO_3$-$x(Bi_{0.5}Na_{0.5})ZrO_3$ was fabricated by Wefring et al. (2014) who studied the dielectric and ferroelectric properties. It was reported that the end member KBT ($x = 0$) was tetragonal and changed to pseudocubic at $x = 0.1$. The ceramic system exhibited relaxor dielectric behaviour evident from the broad dielectric peaks and frequency dispersion below T_m. From polarisation-electric field response, a maximum electric field induced remanent polarisation, P_r = 20.6 μC/cm^2 (E_{max} = 60 kV/cm) and bipolar strain of ~ 0.08% was reported for $x = 0.1$.

2.7.5.10 $K_{0.5}Bi_{0.5}TiO_3$-$Bi(Mg_{0.5}T_{0.5})O_3$-$BiFeO_3$

The ternary KBT-based ceramic system, $K_{0.5}Bi_{0.5}TiO_3$-$Bi(Mg_{0.5}T_{0.5})O_3$-$BiFeO_3$ was studied by Kamei et al. (2014). Dielectric data revealed broad peaks of relative permittivity and the peak temperature was higher than 300 ºC for all studied compositions. The room temperature reported electric field induced unipolar strain at E_{max} = 50 kV/cm was ~ 0.113% for 0.45KBT-0.1BMT-0.45BF and 0.07% for 0.85KBT-0.075BMT-0.075BF.

2.8 Lead-free temperature stable dielectrics

The term ‘temperature stable’ relates to a variability in capacitance or relative permittivity, ε_r within ±15% (for R-type) across a wide temperature range. The Electronic Industries Alliance, EIA, coding uses the letter R to designate ±15% specification (P ±10%, F ±7.5%); a lower working temperature of -55 ºC is represented by X; the upper temperature is represented by a number. For example, existing high-volumetric-efficiency capacitors based on ferroelectric barium titanate, such as X7R, X8R, X9R are specified to operate at temperatures from -55 to +125 ºC, +150 ºC and +175 ºC respectively [Zeb and Milne (2015)].

Numerous compositional systems have been reported to display near-flat relative permittivity over a wide temperature range. These are mostly based on relaxor dielectrics: classic relaxors such as lead magnesium niobate (PMN) exhibit broad frequency dependent $\varepsilon_r(T)$ peaks. The broad frequency dependent ε_r relaxor peak is thought to originate from temperature-dependent changes in the length scales and coupling dynamics of polar nanoregions. The diffuse ε_r relaxor peak can be further broadened and suppressed by additional cation substitutions on A and B sites to develop a temperature-insensitive $\varepsilon_r(T)$ plateau.

This section focusses on different lead-free polycrystalline ceramic compositional systems that offer promise as high volumetric efficiency Class II capacitor materials. Relative permittivity ε_r, loss tangent $\tan\delta$, electrical resistivity (ρ) versus temperature and capacitive time constant (RC) are described and compared. A comparison of temperature range of ±15% or better stability in ε_r and $\tan\delta \leq 0.02$ for potential temperature stable dielectrics are presented in Table 2.4 and a bar plot, Figure 11.10 [Chapter 11].

2.8.1 $BaTiO_3$-based dielectrics

2.8.1.1 $BaTiO_3$-$BiScO_3$

Ogihara et al. studied the binary system (1-x)$BaTiO_3$-$x$$BiScO_3$: samples were prepared with 3 mol% excess Bi_2O_3 [Ogihara et al. (2009b)]. The Curie peak for $x = 0$ ($BaTiO_3$) at ~ 130 ºC became diffuse as x increased to 0.02 and at $x = 0.05$ an additional lower temperature frequency-dependent peak appeared, associated with core-shell microstructures. The shell region of the grains was enriched in $BiScO_3$ and considered to be responsible for the frequency dependent dielectric anomaly. A single, very diffuse relaxor ε_r-T peak occurred around $x = 0.2$. This gave rise to near-stable ε_r values, 800-1000; over a wide temperature ~ 0-350 ºC (estimated). A similar dielectric behaviour had previously been reported for thin film samples [Tinberg and Trolier-McKinstry (2007)]. A ε_r value of ~ 1000 from 0 to 300 ºC was found for sample composition $x = 0.3$ with high electrical resistivity of 10^{12} Ω cm at 250 ºC. The energy density of bulk and tape-cast thick film $x = 0.03$ samples was investigated. A 15 µm dielectric layer has a room-temperature energy density of 6.1 J/cm^3 at 730 kV/cm (just below the breakdown field). Reasonably stable energy densities of 2-3 J/cm^3 were observed from 0 to 300 ºC (bias fields E = 30-40 kV/cm).

2.8.1.2 $BaTiO_3$-$Bi(Mg_{0.5}Ti_{0.5})O_3$

A solid solution in the binary system (1-x)$BaTiO_3$-$x$$Bi(Mg_{0.5}Ti_{0.5})O_3$, (1-$x$)BT-$x$BMT was studied by a number of research groups. Wada et al. focussed on the piezoelectric properties, but noted a changeover from ferroelectric to relaxor characteristics occurred at 0.1BMT. A plot of ε_r-T at 1 MHz showed a very diffuse dielectric response for compositions 0.2BMT and 0.3BMT, with ε_r-values of 600-1000 at temperatures from approximately 25 to 400 ºC. Dielectric loss tangent at 100 Hz was in the range 0.05-0.1 [Wada et al. (2010)].

Zhang et al., provided a detailed account of the temperature stability of dielectric properties [Zhang et al. (2011)]. Compositions x = 0.5BMT and 0.6BMT displayed a plateau in ε_r-T response: for $x = 0.5$, values of $\varepsilon_r \sim 2400 \pm 15\%$ (1 kHz) were observed for temperatures 167 to 400 ºC, with tanδ < 0.02 (100 kHz) for temperatures 238-400 ºC. For $x = 0.4$, $\varepsilon_r \sim 2200 \pm 15\%$ at temperatures of 175 to 400 ºC; low losses occurred over most of this temperature range, with tanδ ≤ 0.02 from 197-400 ºC (at 100 kHz).

Choi et al., investigated (1-x)BT-xBMT bulk ceramics and multilayer capacitors (20×129 μm layers) [Choi et al. (2013)]. They found the solubility limit of BMT to occur around x = 0.4-0.5. Highly diffuse relaxor-like behaviour was observed for compositions x = 0.1 to 0.4. Different compositions displayed distinctive temperature ranges of stable ε_r values, depending on the T_m for each specific composition. However, temperature ranges over which ε_r varied within ±15% were not commented upon in detail.

Xiong et al., examined the effect of Nb_2O_5 and Co_2O_3 co-dopants on the properties of (1-x)BT-xBMT: similar dopants are incorporated into BT to develop core-shell structures and X7R temperature-stable performance [Xiong et al. (2012), Xiong et al. (2011), Hao et al. (2012)]. These authors reported that composition x = 0.15BMT doped with 2 wt% Nb_2O_5 produced $\varepsilon_r \sim 1000 \pm 15\%$ over the temperature range -55 to +155 ºC: tanδ = 0.09 at room temperature. Microstructures were presented indicating core-shell characteristics.

2.8.1.3 $BaTiO_3$-$Bi(Mg_{2/3}Nb_{1/3})O_3$

Wang et al., examined the solid solution, $(1\text{-}x)BaTiO_3\text{-}xBi(Mg_{2/3}Nb_{1/3})O_3$, reporting basic dielectric properties and energy storage capabilities [Wang et al. (2014)]. Composition $x = 0.2$ exhibited temperature-stable dielectric response with ε_r

varying from 628-787 in the temperature range -50 to +300 ºC: tanδ ≤ 0.025 over the temperature range 0-150 ºC (estimated). Values of dc resistivity were of 7.4×10^{12} Ω cm at room temperature and an energy density of 0.74 J/cm^3 (E_{max} = 160 kV/cm) was recorded for $x = 0.2$. However, all compositions of this system showed a sharp increase in dielectric loss tangent at temperature ≥ 200 ºC.

2.8.1.4 $BaTiO_3$-$Bi(Mg_{2/3}Ta_{1/3})O_3$

Ma et al., studied the dielectric properties of the $(1-x)BaTiO_3$-$xBi(Mg_{2/3}Ta_{1/3})O_3$ ceramic system [Ma et al. (2015)]. Composition $x = 0.1$ exhibited dielectric stability across the temperature range 30 to 150 ºC (±15%), with $\varepsilon_{r\ max} = 1278$: tanδ ≤ 0.02 over the temperature range 30 ºC to 195 ºC. There was a sharp rise in dielectric loss tangent at a temperature of ≥ 200 ºC.

2.8.1.5 $BaTiO_3$-$Bi(Zn_{0.5}Ti_{0.5})O_3$

The $(1-x)BaTiO_3$-$xBi(Zn_{0.5}Ti_{0.5})O_3$ system, $(1-x)$BT-xBZT, was studied by Huang and Cann at Oregon State University, who determined the solid solution limit to occur at x = 0.33BZT [Huang and Cann (2008)]. The crystal system changed from tetragonal for $x < 0.1$ compositions to mixed tetragonal and rhombohedral at $x \sim 0.1$. The ferroelectric Curie peak became broad at $x = 0.05$, T_c decreased relative to BT, and the lower temperature ε_r discontinuities due to tetragonal-orthorhombic-rhombohedral polymorphic phase transitions disappeared. Further increases in the BZT content caused dielectric peaks to become increasingly diffuse, and relaxor behaviour was reported at x = 0.2BZT.

A subsequent study by Raengthon and Cann investigated the effect of introducing Ba vacancies (2-8 mol%) into 0.8BT-0.2BZT ceramics [Raengthon and Cann (2011)]. Compositions with 2 mol% Ba-deficiency were claimed to give improved temperature stability in ε_r, with a nearly flat response from temperatures of

100 ºC to 350 ºC. Designing compositions with Ba vacancies also increased electrical resistivity: for the optimum x = 0.2BZT composition (2 mol% Ba deficient) resistivity was of the order of ~ 7×10^{10} Ω cm at 270 ºC, decreasing to 5.78×10^{9} Ω cm at 335 ºC and with a RC time constant of 1.47 s (335 ºC). The same research group have proceeded to further characterise BT-BZT ceramics. They studied the effects of incorporating Zr and Mn excess into the BT-BZT based system, but found no significant improvements in temperature stability [Raengthon and Cann (2011)]. The group also reported the $(1-x)[0.5BaTiO_3-0.5Bi(Zn_{0.5}Ti_{0.5})O_3]-xK_{0.5}Bi_{0.5}TiO_3$ system: a relatively stable dielectric response was found for composition x = 0.6KBT. Approximate values (estimated by interpolation of diagrams) were $\varepsilon_{r\ mid}$ ~ 2400±15% in the temperature range from 150 to 450 ºC with tanδ ~ 0.02 from 200-350 ºC [Prasatkhetragarn et al. (2012)].

2.8.1.6 $BaTiO_3-Bi(Zn_{0.5}Zr_{0.5})O_3$

The dielectric properties of $(1-x)BaTiO_3-xBi(Zn_{0.5}Zr_{0.5})O_3$ [$(1-x)$BT-xBZZ] were studied by Yiliang Wang et al. (2013). Increasing the BZZ content induced relaxor behaviour in ε_r-T plots, with supressed values of $\varepsilon_{r\ max}$. Good temperature stability in ε_r was reported for x = 0.6, with $\varepsilon_{r\ mid}$ = 1000±15% from 200 to 450 ºC, with tanδ ≤ 0.25 from room temperature to 300 ºC (estimated).

2.8.1.7 $BaTiO_3-BiAlO_3$

Liu et al., fabricated the binary $(1-x)BaTiO_3-xBiAlO_3$ ceramic system by solid state and sol-gel processing routes [Mengying Liu et al. (2015)]. The temperature stability in ε_r-T plots increased with increases in the $BiAlO_3$ content. The best temperature stability in ε_r was demonstrated for ceramic samples fabricated using powders prepared by a sol-gel method. At x = $0.3BiAlO_3$, $\varepsilon_{r\ max}$ = 660±15% over the temperature range -55 to 440 ºC: tanδ ~ 0.012 at room temperature. However, conventional solid state methods for producing the starting powders failed to achieve this level of temperature range of stability. The reported relative permittivity for the solid state route for composition $x = 0.3$ was ε_r = 1558±15% across the temperature range, -55 to 124 ºC. These researchers also studied the effect of Nb incorporation to $0.8BaTiO_3$-$0.2BiAlO_3$ ($x = 0.2$) to try to extend the working temperature range. A sample composition containing 4 mol% Nb displayed ε_r = 925±15% from -55 to 178 ºC, and tanδ ~ 0.004 in the temperature range -20 to 200 ºC (estimated).

2.8.1.8 $BaTiO_3$-$BiScO_3$-$Bi(Zn_{0.5}Ti_{0.5})O_3$

The incorporation of $BiScO_3$ into the $BaTiO_3$-$Bi(Zn_{0.5}Ti_{0.5})O_3$ (BT-BZT) system further flattens the ε_r(T) response [Raengthon et al. (2012)]. The solid solution composition, $50BaTiO_3$-$25Bi(Zn_{0.5}Ti_{0.5})O_3$-$25BiScO_3$, compositionally engineered to have 2 mol% Ba-deficiency exhibited ε_r ~ 1100 from 80 to 500 ºC (estimated from published plot) with a temperature coefficient of permittivity TCε_r = -182 ppm/ºC [TCε_r = $1/\varepsilon_{r\ mid}\{\varepsilon_{r1/T1}$-$\varepsilon_{r2/T2}\}$] [Raengthon et al. (2012)] which corresponds to 5% variation (estimated). Dielectric losses were low, with tanδ = 0.007 at 335 ºC. High electrical resistivity was reported by Raengthon et al., for this temperature stable composition: 4.1×10^9 Ω cm at 335 ºC. However, a disadvantage of this material lies in the very high costs of Sc_2O_3 [Raengthon et al. (2012)].

2.8.1.9 $NaNbO_3$-doped $BaTiO_3$-$Bi(Zn_{0.5}Ti_{0.5})O_3$

Raengthon et al., found that incorporation of small amounts of $NaNbO_3$ into $BaTiO_3$-$Bi(Zn_{0.5}Ti_{0.5})O_3$ (BT-BZT) according to a compositional formula expressed in mol% terms as, $70BaTiO_3$-$(30-y)Bi(Zn_{0.5}Ti_{0.5})O_3$-$yNaNbO_3$, y = 5-25 shifted T_m to lower temperatures, thereby decreasing the lower temperature limit of stable ε_r to -103 ºC from a value of ~ 100 ºC without $NaNbO_3$ modification [Raengthon et al. (2013), Huang and Cann (2008)]. Dielectric properties (ε_r-T plots) were shown from -150 ºC to

+200 ºC: a number of $NaNbO_3$ modified compositions e.g. $70BaTiO_3$-$5Bi(Zn_{0.5}Ti_{0.5})O_3$-$25NaNbO_3$ displayed a temperature range of stable ε_r better than X9R (-55-175 ºC). The average ε_r values fell from ~ 1500 in BT-BZT to ≤ 700 for the $NaNbO_3$ modified compositions with the best low-temperature performance.

2.8.2 $Na_{0.5}Bi_{0.5}TiO_3$-based temperature stable dielectrics

2.8.2.1 $Na_{0.5}Bi_{0.5}TiO_3$-$NaNbO_3$

The system $(1\text{-}x)Na_{0.5}Bi_{0.5}TiO_3\text{-}xNaNbO_3$ (NBT-NN) was investigated for $NaNbO_3$ contents up to $x = 0.08$ [Li et al. (2004)]. The NBT end-member is a relaxor dielectric with a broad ε_r peak at ~ 300 ºC, and shoulder at ~ 180 ºC. Incorporation of $NaNbO_3$ in the range $x = 0.01$-0.03 shifts the peak and shoulder to lower temperatures; both features become increasingly diffuse for $NaNbO_3$ modified samples [Li et al. (2004)]. At $x = 0.08$, a broad $\varepsilon_r(T)$ plateau extends from ~ 200-400 ºC but with continued evidence of two distinct humps.

Bridger et al., patented a series of high temperature dielectric materials based on the relaxor sodium bismuth titanate (NBT) [Bridger et al. (2008)]. A variety of substituents and dopants were used to broaden and adjust the temperature of the $\varepsilon_r(T)$ shoulder and main peak. Example of minor substituents included Sr, Ca, Ba. A further flattening of the dielectric response, along with increases in electrical resistivity, was achieved through the use of dopants (Mn, Cu, Co). In agreement with earlier work by Li et al. (2004), the binary solid solution between $Na_{0.5}Bi_{0.5}TiO_3$ and $NaNbO_3$ was found to give a near flat dielectric response over a wide temperature range [Bridger et al. (2008)]. Optimum compositions gave $\varepsilon_r > 1000$, and $\tan\delta < 0.02$ over the temperature range -30 to +200 ºC: resistivity was $> 10^{10}\ \Omega$ m.

2.8.2.2 $Na_{0.5}Bi_{0.5}TiO_3$-$KTaO_3$

König et al., reported trends in $\varepsilon_r(T)$ peak temperatures and widths of ε_r peaks of various $(1-x)Na_{0.5}Bi_{0.5}TiO_3-xKTaO_3$ binary compositions [König et al. (2011)]. Increasing the $KTaO_3$ content resulted in a fatter ε_r-T response: for composition $x = 0.2$, $\varepsilon_{r\ mid} = 2000 \pm 15\%$, in the temperature range 80-300 ºC (estimated) with $\tan\delta \leq 0.02$ over a narrower temperature range, from 200 to 300 ºC. For composition $x = 0.05$ annealed at high temperatures, a broad dielectric maxima $\varepsilon_{r\ max} = 2700$, from 160 to 260 ºC was reported with $\tan\delta \leq 0.02$ spanning temperatures from 100 to 300 ºC (estimated).

2.8.2.3 $Na_{0.5}Bi_{0.5}TiO_3$-$BaTiO_3$-$K_{0.5}Na_{0.5}NbO_3$

Dittmer et al., Technical University Darmstadt, studied the ternary system, $(1-x)[0.94Na_{0.5}Bi_{0.5}TiO_3-0.06BaTiO_3]-xK_{0.5}Na_{0.5}NbO_3$, (NBT-BT-KNN) for compositions $x \leq 0.18$KNN [Dittmer et al. (2011)]. In a similar manner to NBT-based materials reported by Li et al., for the $Na_{0.5}Bi_{0.5}TiO_3$-$NaNbO_3$ system, and by Bridger et al., for complex compositions based on NBT [Li et al. (2004), Bridger et al. (2008)], Dittmer et al. (2011) observed a $\varepsilon_r(T)$ plateau which exhibited two broad humps originating from shoulder and broad ε_r peak in the base material. However, the width of the ε_r-T plateau was greater in the NBT-BT-KNN system. Optimum properties occurred at $x = 0.18$KNN, with $\varepsilon_r = 2151 \pm 10\%$, from temperatures of 43 ºC to 319 ºC: $\tan\delta \leq 0.025$ from ~ 50 to < 300 ºC (estimated from published plot). For $(1-x)$[NBT-BT]-xKNN at $x = 0.18$, electrical resistivity was $\rho = 10^8\ \Omega$ m at 300 ºC, and RC time constant ~ 1.13 s. For $x = 0.15$, the reported properties were, $\varepsilon_{r150} = 2349 \pm 10\%$ from 49 to 313 ºC, with $\tan\delta \leq 0.025$ from ~ 100-300 ºC (estimated) (150 = mid temperature), Table 2.4.

2.8.2.4 $Na_{0.5}Bi_{0.5}TiO_3$-$K_{0.5}Bi_{0.5}TiO_3$-$K_{0.5}Na_{0.5}NbO_3$

The Darmstadt group subsequently studied (1-x)[$0.6Na_{0.5}Bi_{0.5}TiO_3$-$0.4K_{0.5}Bi_{0.5}TiO_3$]-$xK_{0.5}Na_{0.5}NbO_3$, x = 0.08-0.015 ceramics, reporting ε_r = 2167±10%, from 54 to 400 ºC for the best composition, x = 0.15KNN. Compositions with the widest temperature range of stability in ε_r, namely x = 0.12 and 0.15KNN exhibited tanδ < 0.025 (1 kHz) over what appeared to be a narrow temperature span, ~ 100-250 ºC (estimated) [Dittmer et al. (2012)].

It appears that dielectric losses show a greater temperature fluctuation in NBT-KBT-KNN than for the leading $BaTiO_3$-$Bi(Mg_{0.5}Ti_{0.5})O_3$ or $BaTiO_3$-$Bi(Zn_{0.5}Ti_{0.5})O_3$ based dielectric ceramics. In NBT-KBT-KNN low loss occurs over a significantly narrower temperature range than the full range of the ε_r plateau. Hence, working temperature ranges may be more restricted that at first appears from ε_r stability data.

2.8.2.5 $CaZrO_3$-modified NBT-BT and NBT-BT-KNN

The effect of incorporating $CaZrO_3$ into NBT-BT and NBT-BT-KNN was to decrease the lower operating temperature and also to decrease ε_r values [Acosta et al. (2012), Zang et al. (2014)]. The ceramic materials were fabricated according to the solid solution formula: (1-x)[$0.94Na_{0.5}Bi_{0.5}TiO_3$-$0.06BaTiO_3$]-$xCaZrO_3$ and (1-x)[$0.82(0.94Na_{0.5}Bi_{0.5}TiO_3$-$0.06BaTiO_3)$-$0.18K_{0.5}Na_{0.5}NbO_3$]-$xCaZrO_3$, respectively. Ceramics with different $CaZrO_3$ [CZ] contents exhibited different combinations of $\varepsilon_{r\ max}$ and plateau temperature ranges. For the NBT-BT-CZ compositional series, the lower limiting temperature of near flat ε_r(T) decreased with increasing amounts of $CaZrO_3$ substitution, from 109 ºC at 0.05CZ to -97 ºC at 0.2CZ. For NBT-BT-KNN-CZ solid solutions, the variation was from -6 ºC to -69 ºC with increasing levels of $CaZrO_3$ incorporation. Dielectric losses (1 kHz) increased sharply at temperatures above 200-300 ºC in both NBT-BT-CZ and NBT-BT-KNN-CZ. The NBT-BT-CZ composition x =

$0.2CaZrO_3$ gave the flattest ε_r-T response, with a ±15% consistency in ε_r (550 mid) from -97 to +371 ºC, with tanδ = 0.7% at 300 ºC (1 kHz). Dielectric losses (deduced from ε_r''-T plots) increased substantially above 300 ºC, suggesting a practical upper working temperature (combination of stable ε_r and low loss) may be ~ 300 ºC.

In the NBT-BT-KNN-CZ system, the flattest ε_r-T response again occurred for $x = 0.2$CZ [Acosta et al. (2012)]. In this case, the temperature range of ±15% consistency in ε_r (467 mid) extended from -69 ºC to +468 ºC; dielectric loss at 1 kHz ($\tan\delta = \varepsilon_r''/\varepsilon_r'$) increased sharply above 300 ºC. An electrical resistivity of ~ 10^7 Ω m at 300 ºC was recorded for the NBT-BT-CZ composition $x = 0.2$ which had the most stable dielectric properties. For the NBT-BT-KNN-CZ compositions, the electrical resistivity was ~ 10^8 Ω m at 300 ºC for $x = 0.2$CZ: other compositions with less favourable ε_r-T response exhibited higher resistivity, up to 10^9 Ω m (e.g. NBT-BT-KNN-0.05CZ).

2.8.2.6 $Na_{0.5}Bi_{0.5}TiO_3$-$BaTiO_3$-$Bi_{0.2}Sr_{0.7}TiO_3$

Shi et al., reported the electrical properties for the Bi-deficient solid solution series ‘$(Na_{0.5}Bi_{0.5-y})_{0.94-x}Ba_{0.06}(Bi_{0.2}Sr_{0.7}\square_{0.1})_xTiO_3$’(where □ = A-site strontium vacancy) derived from a NBT-BT composition at the morphotropic phase boundary [Shi et al. (2015)]. The system demonstrated promising temperature stable dielectric properties with low loss tangent. A flat dielectric response with very high relative permittivity, $\varepsilon_r = 4884 \pm 10\%$ was reported for composition $x = 0.26$, $y = 0.07$ over the temperature span 50 ºC to 270 ºC: tanδ ≤ 0.02 from 100 to 300 ºC (estimated). A rapid decrease in ε_r occurred for temperatures outside this range. The value of time constant (RC) was 5.96 s at a temperature of 300 ºC.

Table 2.4 Comparison of temperature stability of relative permittivity within ±15% or less and tanδ ≤ 0.02 at 1 kHz for potential dielectric systems.

Material system	$\varepsilon_{r\ mid}$ (T-range, ºC)	T-range (ºC) tanδ ≤ 0.02	References
$0.7BaTiO_3$-$0.3BiScO_3$	1000±15% (0-300)	50-400	Ogihara et al. (2009a)
$0.5BaTiO_3$-$0.5Bi(Mg_{0.5}Ti_{0.5})O_3$	2400±15% (167-400)	238-400 (100 kHz)	Zhang et al. (2011)
$0.8BaTiO_3$-$0.2Bi(Zn_{0.5}Ti_{0.5})O_3$ (Ba-deficient)	1150±15% (100-350)	tanδ~0.05 (100-460)	Raengthon and Cann (2011)
$50BaTiO_3$-$25Bi(Zn_{0.5}Ti_{0.5})O_3$-$25BiScO_3$ (Ba-deficient)	1100±15% (80-500)	~100-450	Raengthon et al. (2012)
$0.9Na_{0.5}Bi_{0.5}TiO_3$-$0.1KTaO_3$	>2500±15% (80-340)	tanδ~0.05 (80-300)	Bridger et al. (2008), (2010)
$0.82(0.94Na_{0.5}Bi_{0.5}TiO_3$-$0.06BaTiO_3)$-$0.18K_{0.5}Na_{0.5}NbO_3$	2151±10% (43-319)	tanδ ≤ 0.025 (50-300)	Dittmer et al. (2011)
$0.85[0.6Na_{0.5}Bi_{0.5}TiO_3$-$0.4K_{0.5}Bi_{0.5}TiO_3]$-$0.15K_{0.5}Na_{0.5}NbO_3$	2167±10% (54-400)	~100-250	Dittmer et al. (2012)
$0.8[0.82(0.94Na_{0.5}Bi_{0.5}TiO_3$-$0.06BaTiO_3)$-$0.18K_{0.5}Na_{0.5}NbO_3]$-$0.2CaZrO_3$	467±15% (-69-+468)	-	Acosta et al. (2012)

2.8.2.7 $BiScO_3$-$BaTiO_3$-$(K_{1/2}Bi_{1/2})TiO_3$

Lim et al. investigated the ternary $(1-x)[0.4BiScO_3-0.6BaTiO_3]-xK_{0.5}Bi_{0.5}TiO_3$ series [Lim et al. (2009)]. The $x = 0.2$KBT material displayed a temperature-insensitive response with $\varepsilon_{r\,max} = 1750$, and $TC\varepsilon_r = -800$ ppm/ºC across the temperature range 200-400 ºC: tanδ < 0.02 for the equivalent temperature range. The energy density increased from 0.3 J/cm^3 at 50 kV/cm to 4.0 J/cm^3 at 220 kV/cm. An electrical resistivity of 10^9 Ω cm and RC constant of 0.8 s at 300 ºC were reported.

2.8.2.8 $K_{0.5}Na_{0.5}NbO_3$-$LiTaO_3$

Another approach to achieving wide-ranging temperature stability is not reliant on relaxor behaviour. Instead ferroelectrics with high T_c offer stable properties with moderate ε_r values below T_c. This is illustrated by the $(1-x)K_{0.5}Na_{0.5}NbO_3-xLiTaO_3$ solid solution series (KNN-LT), taking advantage of the high ferroelectric Curie temperature of KNN (T_c ~ 420 ºC). However, unmodified KNN displays an orthorhombic ↔ tetragonal polymorphic phase transition at ~ 200 ºC creating a ε_r discontinuity which prevents temperature stability in ε_r values at $T < T_c$. This transition can be shifted to much lower temperatures through appropriate levels of $LiTaO_3$ incorporation, as demonstrated by Skidmore [Skidmore (2009)]. The polymorphic phase transition can be shifted to below 0 ºC by incorporation of between 0.7LT and 0.1LT, thereby imparting improved temperature stability. A flat ε_r-T response was obtained for $x = 0.1LiTaO_3$ from temperatures -50 ºC to 350 ºC with ε_r ~ 480±15%: the upper temperature limit lies at the onset of the tail to the ferroelectric Curie peak (T_c ~ 450 ºC). For the composition $x = 0.07$, a slightly narrower temperature-stable range occurred, with ε_r = 630-700±15% from -15 ºC to +300 ºC. [Skidmore et al. (2009), Skidmore (2009)].

2.8.2.9 $K_{0.5}Na_{0.5}NbO_3$-$LiTaO_3$-$BiScO_3$

Skidmore et al., also studied dielectric and piezoelectric properties in the ternary compositional system $(1-x)[(K_{0.5}Na_{0.5}NbO_3)_{0.93}-(LiTaO_3)_{0.07}]-xBiScO_3$ [Skidmore et al. (2010)]. Addition of $BiScO_3$ led to a decrease in values of $\varepsilon_{r\,max}$ from ~ 3600 at $x = 0$ to ~ 1800 at $x = 0.02$ and the creation of a diffuse ε_r-T peak. The dielectric response become flatter at $x = 0.05$ with estimated ε_r values of ~ 1150±15% from ~ 20 ºC to 450 ºC, [Skidmore et al. (2010), Skidmore (2009)]: tanδ values were 0.03-0.05 for temperatures from 20-200 ºC, decreasing to < 0.025 at 200-350 ºC [Skidmore (2009)].

Zhu et al., studied dielectric and piezoelectric properties in the system, $(1-x)[0.98K_{0.5}Na_{0.5}NbO_3-0.02BiScO_3]-xLiTaO_3$ [Zhu et al. (2011a), Zhu et al. (2011b)]. Values of $\varepsilon_{r\,max}$ decreased from an estimated 7000 at $x = 0$, to 2600 at $x = 0.03LiTaO_3$. Composition $x = 0.02LiTaO_3$ showed consistent $\varepsilon_r(T)$ response with ε_r estimated at 1000±15% from 0-300 ºC. The $x = 0.03$ samples gave ε_r ~ 700±15% from approximately -55-200 ºC. Values of tanδ were ~ 0.03 over these temperature ranges. For certain compositions, the broad ε_r-T response showed two sub-peaks. Analysis by TEM-EDX indicated the origin of the sub-peaks in certain $K_{0.5}Na_{0.5}NbO_3$-$LiTaO_3$-$BiScO_3$ compositions, e.g. $0.98[0.95K_{0.5}Na_{0.5}NbO_3-0.05LiTaO_3]-0.02BiScO_3$, was due to core-shell segregation [Zhu et al. (2015)].

2.8.2.10 $K_{0.5}Na_{0.5}NbO_3$-$Bi(Zn_{0.75}W_{0.25})O_3$

The solid solution $(1-x)K_{0.5}Na_{0.5}NbO_3-xBi(Zn_{0.75}W_{0.25})O_3$, [KNN-BZW] was synthesised by Chen et al. (2015). The crystal structure was identified as having orthorhombic symmetry with no evidence of secondary phases. Plots of ε_r-T indicated two phase transitions above room temperature: orthorhombic-tetragonal and tetragonal-cubic. These transitions became more diffuse with increasing BZW content.

Composition x = 0.01BZW gave temperature-stable dielectric behaviour, with ε_r ~ 1300±15% from temperatures of 150 to 350 ºC; tanδ < 0.04 across this temperature range.

2.9 Conclusions

As mentioned above, a wide variety of compositionally complex perovskite solid solutions display near-stable relative permittivity over wide temperature ranges with upper temperature limits of ε_r ±15% at 300-500 ºC. The materials with the widest temperature range of stable and high relative permittivity (ε_r ~ 1000), low dielectric loss and high electrical resistivity were found in some materials; for example in $BaTiO_3$-$BiZn_{0.5}Ti_{0.5}O_3$-$BiScO_3$ system, exhibited ε_r = 1000±15% across the temperature range 80-500 ºC. However, the lower temperature limit lies above room-temperature. Moreover, the costly scandium content in these materials led to the limitation for commercial applications. Materials which achieve stability down to -55 ºC exhibit moderate relative permittivity values (ε_r ~ 500) and low loss occurs over a significantly narrower temperature range than the full range of the ε_r plateau. Hence, working temperature ranges may be more restricted that at first appears from ε_r stability data.

Therefore, despite these advances in high temperature dielectric ceramics, further improvements in basic dielectric properties and temperature ranges are required to bring the materials to a stage where they can be considered for further evaluation and implementation as practical high temperature capacitor materials.

Chapter 3

Experimental Methods

3.1 Introduction

The performance of ceramic materials for various applications strongly depends on the method of their processing. The production of a dense and chemically homogeneous ceramics is the basic requirement for tailoring electrical properties for different applications. This chapter outlines various steps used for processing raw materials, sample preparation and different experimental techniques for their analysis, conducted in this research. The flow chart, Figure 3.1, describes the key stages of processing of raw powders and shaping of samples by a conventional solid state route including sintering, grinding and electroding.

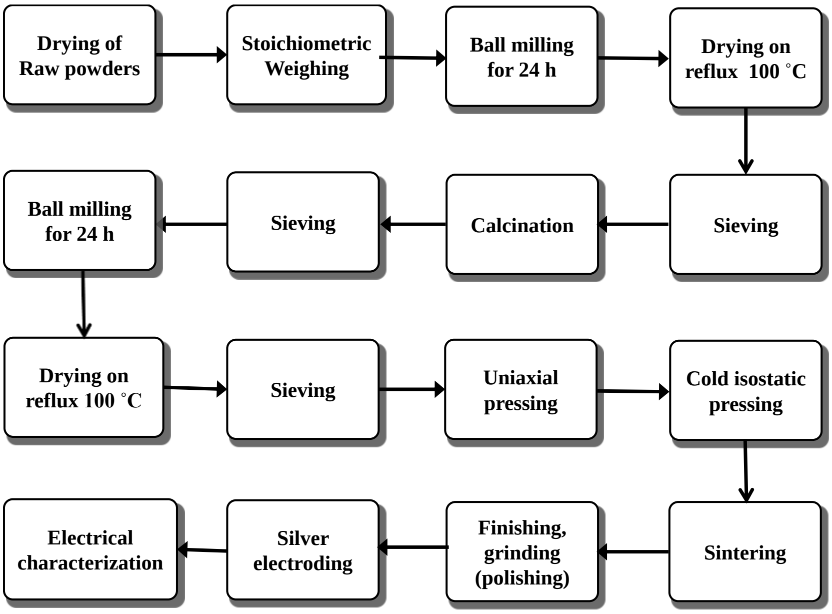

Figure 3.1 Flow chart describes the key steps for powder processing including shaping, sintering and electroding.

3.2 Ceramics Fabrication

3.2.1 Powder processing

The raw powders were processed by a conventional mixed oxide route using reagent grade carbonates and oxides. The details of starting reagents of the respective elements, suppliers and their purity are listed in the Table 3.1.

Table 3.1 Carbonate, oxide reagents, purity and suppliers.

Raw powders	Purity	Supplier	CAS Code
K_2CO_3	$\geq 99\%$	Sigma Aldrich	584-08-7
$BaCO_3$	$\geq 99\%$	Alfa Aeser	513-77-9
$CaCO_3$	$\geq 99\%$	Sigma Aldrich	471-34-1
Na_2CO_3	$\geq 99.5\%$	Sigma Aldrich	497-19-8
Bi_2O_3	99.9%	Sigma Aldrich	1304-76-3
TiO_2	99.9%	Sigma Aldrich	1317-80-2
Nb_2O_5	99.9%	Alfa Aeser	1313-96-8
ZnO	99.9%	Sigma Aldrich	1314-13-2
ZrO_2	99%	Sigma Aldrich	1314-23-4
MgO	99.9%	Alfa Aeser	1309-48-4

The raw powders were dried overnight in an oven at a temperature of 250 ºC to remove moisture owing to the hygroscopic nature of some precursors and then cooled to room temperature in a desiccator under reduced pressure. For each batch formulation, the powders were weighed according to their respective stoichiometric ratios, using a Sartorius electronic balance (Sartorius UK Ltd, UK) within the precision limit of ±0.001 g.

3.2.1.1 Ball Milling

The mixing of raw powders was performed by conventional ball milling, in a custom made plastic bottle (0.5 Litre) and yttria-stabilized zirconia (YSZ) cylindrical balls ~ 7.3×7.2 mm (length. diameter) as a grinding media. All compositions were milled for 24 hours using 2-propanol (Sigma Aldrich, purity 99.5%) as the milling media. The raw powders, grinding media and 2-propanol together filled 2/3 of the plastic bottle: this was then placed on the horizontal mechanical rollers for 24 hours with speed of ~ 100 rpm.

3.2.1.2 Drying of milled slurry

The milled slurry for each composition was dried by using the electrothermal reflux kit with magnetic stirrer at a temperature ~ 100 ºC. In order to break agglomerates and get finer particles size, the dried powders were sieved through 300 µm mesh size nylon, and then stored in air for further processing.

3.2.1.3 Calcination of powders

Before shaping and sintering, the milled powders were calcined at certain temperatures. The main purpose of calcination of the milled powders is to cause dehydration, removal of carbon in the form of carbon dioxide and thermo-chemical reaction to form a desired solid solution. The homogenized milled powders were placed in covered alumina crucibles with lids (Alsint, Fisher Scientific Ltd, UK) and calcined at optimised temperatures in a box digital programmable furnace in air. In this study, a heating, cooling ramp rate of 5 ºC/min, dwell time 3-4 hours and calcination temperature in the range of 800-1100 ºC was used for most of compositions of different systems, Figure 3.2 and Table 3.2. After calcination at appropriate temperature, the powders were passed through 300 µm mesh, re-milled for 24 hours and 1 wt% binder was introduced (Ciba Glascol HA4: Ciba speciality Chemicals, Bradford, UK). To facilitate compaction and shaping into pellets, re-milled powders were sieved again and stored in air.

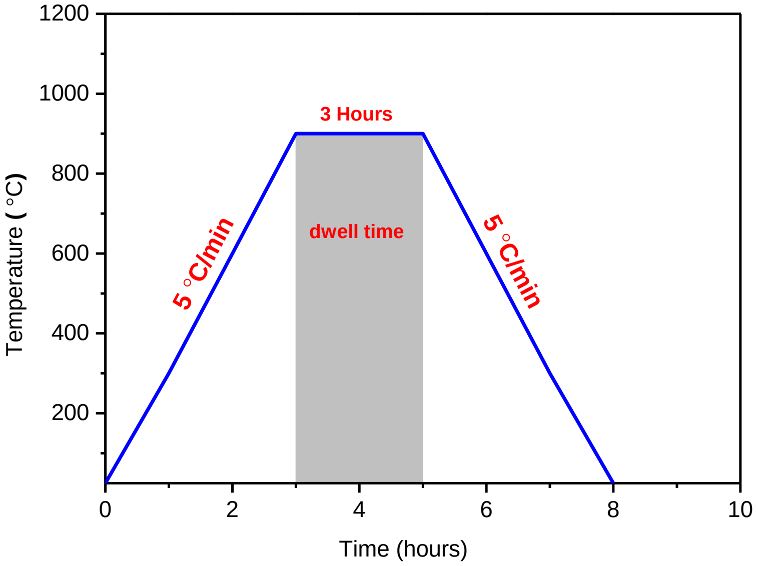

Figure 3.2 A general scheme for calcination of powders during this research.

Table 3.2 Detailed summary of calcination of powders for different systems.

Material System	Heating/ cooling rate	Calcination Temperature	Dwell time
$(1-x)K_{0.5}Bi_{0.5}TiO_3-xBi(Mg_{0.5}Ti_{0.5})O_3$	5 °C/min	850 °C	3 h
$(1-x)K_{0.5}Bi_{0.5}TiO_3-xBa(Zr_{0.2}Ti_{0.8})O_3$	5 °C/min	850-1000 °C	4 h
$(1-x)Ba_{0.8}Ca_{0.2}TiO_3-xBi(Mg_{0.5}Ti_{0.5})O_3$	5 °C/min	800-1100 °C	3 h
$(1-x)Ba_{0.8}Ca_{0.2}TiO_3-xBi(Zn_{0.5}Ti_{0.5})O_3$	5 °C/min	900 °C	3 h
$(1-x)BaTiO_3-xBi(Mg_{0.5}Zr_{0.5})O_3$	5 °C/min	900 °C	4 h
$0.45Ba_{0.8}Ca_{0.2}TiO_3-(0.55-x)Bi(Mg_{0.5}Ti_{0.5})O_3-xNaNbO_3$	5 °C/min	900 °C	3 h
$(1-x)[0.5K_{0.5}Bi_{0.5}TiO_3-0.5Ba(Zr_{0.2}Ti_{0.8})O_3]-xBi(Zn_{2/3}Nb_{1/3})O_3$	5 °C/min	900 °C	3 h

3.2.1.4 Shaping of Powders/Pelletization

The shaping of powders in the form of pellets was carried out by uniaxial pressing (Apex Construction Ltd, UK). Powders ~ 0.5 g were compacted into pellets of thickness ~ 1.5 mm and diameter ~ 10 mm using a highly polished steel die, with a uniaxial pressure of ~ 65 MPa. However, for full and uniform pressing, the green pellets were further subjected to cold isostatic pressure by using an Isostatic Press (Stanstead fluid power, Essex, UK). The green pellets were placed in finger pockets of flexible rubber gloves to protect them from oil contamination and pressed to ~ 200-300 MPa for ~ 10 minutes. The green pellets after isostatic pressing were fired at various temperatures for sintering.

3.2.1.5 Sintering

The most important and key stage of the ceramic processing is sintering, to accomplish pore-free ceramics and to achieve a high quality material for various applications.

In this work, the sintering of the green pellets was carried out in air in a closed alumina crucibles at different appropriate temperatures and dwell times for each composition of different systems using a box furnace. The green pellets were embedded in “atmosphere” powders of the same composition to reduce the loss of volatile substances and fired slowly with ramp rates of 50 ºC/h up to 550 ºC to burn out the organic binder. The temperature was then subsequently raised with ramp rate of 300 ºC/h to optimised high temperature limit with different dwell time hours for sintering and then cooled to room temperature at 300 ºC/h. The general scheme of the firing of green pellets in this research is shown in Figure 3.3. A detailed summary of the sintering temperature and dwell time after burning the binder at slow ramp rate of 50 ºC/h up to 550 ºC is given in Table 3.3.

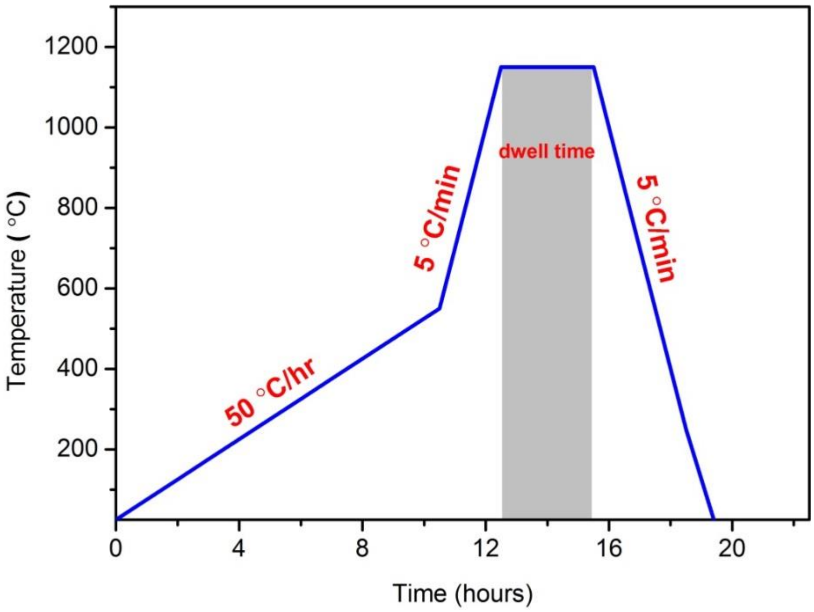

Figure 3.3 A general scheme for sintering of green pellets in this research.

Table 3.3 Summary of the heating/cooling rate, sintering temperature and dwell time after binder burn out at 550 ºC at slow ramp rate of 50 ºC/h of different system.

Chap No.	Material System	Heating/cooling rate	Sintering Temperature	Dwell time
4	$(1-x)K_{0.5}Bi_{0.5}TiO_3-xBi(Mg_{0.5}Ti_{0.5})O_3$	5 ºC/min	1050-1100 ºC	4 h
5	$(1-x)K_{0.5}Bi_{0.5}TiO_3-xBa(Zr_{0.2}Ti_{0.8})O_3$	5 ºC/min	1060-1350 ºC	4-6 h
6	$(1-x)Ba_{0.8}Ca_{0.2}TiO_3-xBi(Mg_{0.5}Ti_{0.5})O_3$	5 ºC/min	1000-1400 ºC	3 h
7	$(1-x)Ba_{0.8}Ca_{0.2}TiO_3-xBi(Zn_{0.5}Ti_{0.5})O_3$	5 ºC/min	1050-1400 ºC	6 h
8	$(1-x)BaTiO_3-xBi(Mg_{0.5}Zr_{0.5})O_3$	5 ºC/min	1000-1350 ºC	6 h
9	$0.45Ba_{0.8}Ca_{0.2}TiO_3-(0.55-x)Bi(Mg_{0.5}Ti_{0.5})O_3-xNaNbO_3$	5 ºC/min	1050-1150 ºC	3 h
10	$(1-x)[0.5K_{0.5}Bi_{0.5}TiO_3-0.5Ba(Zr_{0.2}Ti_{0.8})O_3]-xBi(Zn_{2/3}Nb_{1/3})O_3$	5 ºC/min	1040-1100 ºC	4 h

3.2.1.6 Finishing and Electroding

Before the electrical characterization of the ceramic sample, the pellets were ground to flat surfaces of ~ 1 mm in thickness with grinding discs at grit 500 and 1200 (MD Piano Stainless strips GmbH, Willich, Germany), using Motopol 2000 (Buehler, USA). The pellets were cleaned with acetone and dried at 200 ºC for 1 h. The densities of sintered ceramic pellets were determined geometrically for at least three pellets of each sample type; relative densities were obtained by comparing these results with the theoretical densities as estimated from unit cell parameters and the assumed cell contents (Table A4, Appendix).

For electrical measurements, a silver paste (Agar Scientific, Stanstead Essex, UK) was applied to opposite parallel faces of the ground pellets and then the pellets were heated in a furnace at 550 ºC for 10 min to form electrodes. After firing, the edges were cleaned by using silicon carbide paper (Buehler carbimet Grit 2500) to eliminate any short circuiting during electrical testing/characterization.

3.3 Characterization

The fabricated ceramic compositions were routinely characterized by X-ray diffraction (XRD) for determining phase purity and crystal system. Electrical characterization of the ceramics, including the measurement of relative permittivity, dielectric loss tangent, piezoelectric charge coefficients, polarization-electric field response and other electrical properties like dc resistivity, SEM and TEM were also used to investigate microstructure.

3.3.1 X-ray Diffraction (XRD)

The physical properties of the solids are strongly dependent on the internal arrangements of the atoms and their crystal structure. Therefore, the identification of the phase/crystal structure by XRD is the most commonly and widely used characterization technique in material science. The main advantage of XRD technique is that of the fast, non-destructive testing and small sample size required for the analysis as compared to other conventional chemical analysis [Cullity and Stock (2001)].

X-rays are electromagnetic radiation having wavelength of the order of ~ 1Å and of the same order as that of inter atomic planes distance of crystalline materials. X-rays are commonly generated when high energy electrons hit the metal target like cupper etc., ionise the K-shells electrons, Figure 3.4.

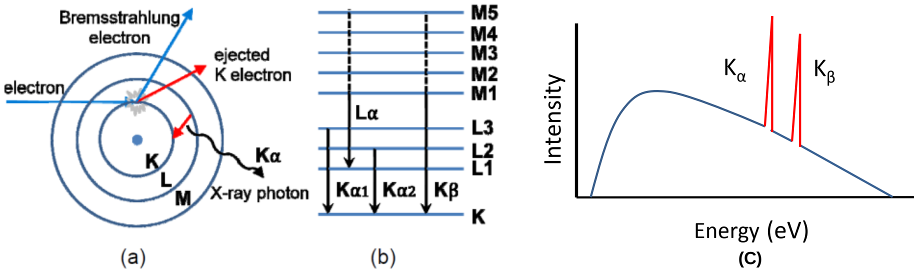

Figure 3.4 Characteristic X-rays production mechanism (a) electron interaction (b) electron shell transition and (c) continuous and characteristic X-rays spectra [modified as Stevenson (2010)].

Electrons from the outer shells (L, M, N) make transition to the K-shell vacancies and high energy X-ray photons are emitted, known as characteristic X-rays. The most probable transition is from outermost shells produce a K-series; K_{α}-radiation from L while K_{β} emission occurs from M-shell respectively [Cullity and Stock (2001)]. Due to sub energy levels of L-shell, K_{α}-consists of $K_{\alpha1}$ ($\lambda \sim 1.5406$ Å) and $K_{\alpha2}$ ($\lambda \sim 1.5443$ Å). Since monochromatic radiation is used for diffraction research, K_{β} is filtered by Nickel (Ni) while $K_{\alpha2}$ is stripped by X'pert high score plus software. In addition to this, the incident electrons when hitting the metal target, decelerate causing the emission of another types radiation, known as continuous X-rays. A collimated beam of X-rays incident on the crystalline material is diffracted by the crystal planes, Figure 3.5.

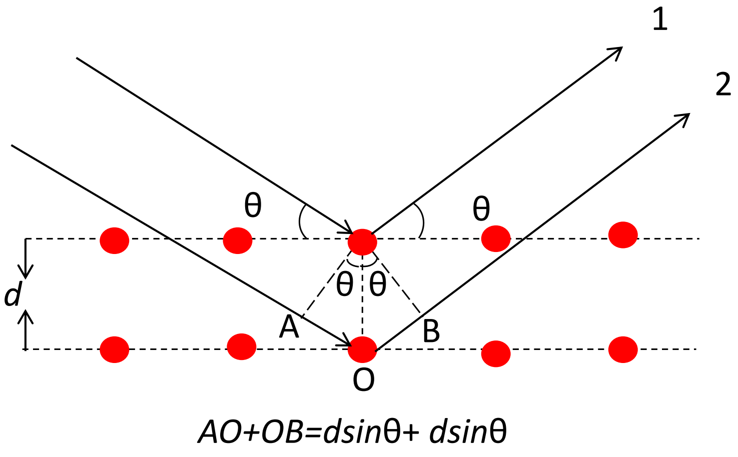

Figure 3.5 Bragg's reflection by crystal [modified from Cullity and Stock (2001)].

The diffracted rays from different planes in phase are superimposed with each other and resulting a diffraction pattern in the form of intense peaks. The intense peaks in the diffraction pattern are due to constructive superposition and occur only when Bragg's law is satisfied (in phase) given by equation as [Cullity and Stock (2001)];

$$2d\sin\theta = n\lambda \qquad \text{Equation 3.1}$$

where d is the inter planer distance, λ is the wavelength of X-rays, θ is the Bragg's angle and n is an integer which represents the order of diffraction. For constructive interference, the path difference, Figure 3.5, must be equal to integral multiple of wavelength of X-rays (nλ).

In this study, X-ray diffraction facilities were used to analyse the phase purity and structural transitions in the powders of sintered ceramic materials. Clean sintered ceramic pellets were grounded to fine powders in a mortar/pestle and then annealed at 300 ºC for 1 h to release any stress/strain or texture effects. The fine powders were then analysed by using X-ray powder diffractrometer Bruker D8 (Cu, Kα ~ 1.5406 Å, Karlsruhe, Germany) with scan speed, 1º/min and range of angles from 20-70º 2θ.

High temperature XRD analysis was carried out for specific compositions at a scan speed 1º/min over the temperature range 25 ºC to 400 ºC by using a PANalytical X'pert Pro MPD diffractrometer (Philips, Almelo, Netherlands) fitted with a HTK 1200 oven and TCU 1000 controller (Paar Physica). Internal standard was not used for these compositional comparison. The collected XRD patterns were analysed by using the PANalytical X'pert Highscore Plus software and the unit cell parameters were obtained by using WinPlotr (least square refinement method) and peak profile fit by X'pert Highscore Plus software (Figure A5 and A6, Appendix).

3.3.2 Permittivity-Temperature Measurement

To study the Curie temperature (T_c) and characteristics of structural phase transitions of a material, the temperature dependent relative permittivity (ε_r) and dielectric loss tangent (tanδ) is the common technique. The relative permittivity and dielectric loss tangent (tanδ) as a function of temperature at various frequencies (1 kHz-1 MHz) were measured by using an Impedance Analyser (HP Agilent, 4192A Hewlett Packard, Santa Clara, CA) powered by LabVIEW software. The relative permittivity is usually measured from the capacitance and dimensions of the ceramic discs using the formula [Cai et al. (2011)];

$$\varepsilon_r = \frac{C \times t}{\varepsilon_\circ \times A} \qquad \text{Equation 3.2}$$

where *C* is the capacitance measured in Farad (F), t is the thickness of the ceramic disc in meter (m), A is the area of the face of the disc (m^2) and $\varepsilon_\circ$ is permittivity of the free space/or air (~ 8.85×10^{-12} F/m).

The dielectric measurements were carried out on fired silver electroded pellets (thickness ~ 1 mm and diameter ~ 8 mm) with heating and cooling ramp rate of 2 ºC/min from room temperature to a maximum of 600 ºC. Different limits of high temperatures were set for some samples by using computer control programmable temperature oven (Eurotherm 847 programmable controller).

Low temperature dielectric measurements for some samples were conducted from -70 ºC to 20 ºC or 70 ºC by using an environmental chamber (TJR; Tenney Environmental-SPX, white Deer, CA) in University of Birmingham and Leeds.

The dc resistivity measurements were performed by applying a fixed voltage of 80 V, using a Keithley 617, programmable electrometer (Cleveland, OH) in the temperature range from 25 ºC to 550 ºC. For each measurement, the temperature was stabilised for at least 30 min and data was recorded with intervals of 20 ºC.

3.3.3 Ferroelectric measurements

The polarisation-electric field (P-E) and strain-electric field (S-E) response were studied simultaneously by an experimental setup consisting of an optical fibre displacement sensor (MTI-2100, Fotonic Instrument, Albany, NY), a 5 kV amplifier source (Model 5/80, Trek Inc., Medina, NY) and data aqusition hardware (Radiant Technologies Inc., Albuquerque, New Mexico) which was controlled by computer software package (Vision, Radiant Technologies, Albuquerque, New Mexico). The sample was placed in silicone oil and data was collected for samples of thickness ≤ 1 mm and area ~ 0.50 cm^2 at room temperature for a frequency of 1 Hz. The electric field was increased with 10 kV/cm steps to a maximum of 50-80 kV/cm.

Polarisation-electric field response from 25 ºC to 180 ºC was also conducted for some selected samples at the University of Manchester, using a custom made polarisation setup. The latter P-E measurements were performed with a temperature controlled silicone oil bath, using a computer-controlled Thurlby-Thandar TG1304 function generator in combination with a HVA1B high voltage (±50 kV/cm) amplifier (Chevin Research, Otley, UK).

3.3.4 Poling and Piezoelectric Charge Coefficient (d_{33}) measurement

For piezoelectric charge coefficient measurements d_{33}, the samples were poled by using a custom made poling rig, Figure 3.6. The electroded pellet of thickness ~ 1 mm with clean edges was clamped with the copper holder in the silicon oil bath at an optimised temperature provided by the hot plate (different level of temperature used for different systems). The temperature was checked by a K-type thermocouple before applying the electric field. An electric field of 30-60 kV/cm was applied at ramp rate of 50 V/s for 20 min. The temperature was lowered to room temperature and then the field reduced to zero for removal of the pellet.

After poling, the piezoelectric charge coefficient d_{33} was measured at room temperature after 24 h at a frequency of 110 Hz, using a PiezoMeter PM300, based on the oscillating force and induced charge per unit applied force (d_{33}).

The electromechanical planar coupling factor, k_p, as function of temperature was measured using an electrical impedance analyser Agilent 4192A (Agilent, USA) on poled discs (diameter: thickness ratio of 10:1) by the resonance method. Thermal depolarisation measurements were conducted by measuring the electric charge released during heating of a poled specimen at a ramp rate of 2 ºC/min., using a Keithley 6512 electrometer.

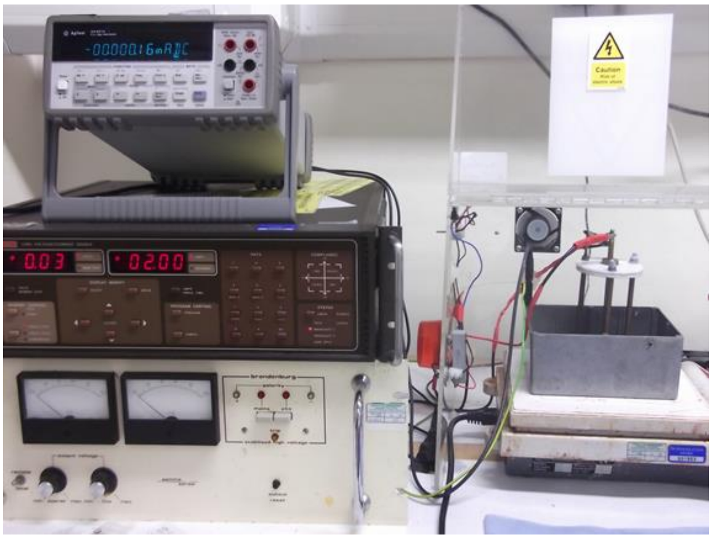

Figure 3.6 Custom made poling rig for poling of ceramic samples.

3.3.5 Scanning Electron Microscopy (SEM) and Energy Dispersive Spectroscopy (EDS/EDX)

Scanning Electron Microscopy is one of the most widely used tools for the analysis of surface topography of material. A scanning electron microscope produces magnified images with high resolution for studying the surface characteristics or topography of the bulk materials e.g. particle/grain size, porosity and possible existence of the second phases [Goodhew et al. (2001)].

A scanning electron microscope mainly consists of an electron gun, electromagnetic lens system (condenser and objective lens) and detectors. In the electron gun, the electrons are ejected by field emission (FEG SEM) or from the tungsten filament by thermionic emission and accelerated to the specimen with high energy (1-30 keV). The condenser lens de-magnifies the accelerated electrons to control the beam diameter (2-10 nm) before striking the sample. Below the condenser, the objective lens further focuses the electrons on the surface of the sample. SEM also consists of scanning coils which deflect the beam in opposite directions which allow the electrons always to pass through the optical centre of the objective, Figure 3.7. The electron beam scans the sample when striking the sample, the beam position on the sample and image is digitally controlled and displayed on the screen of the computer.

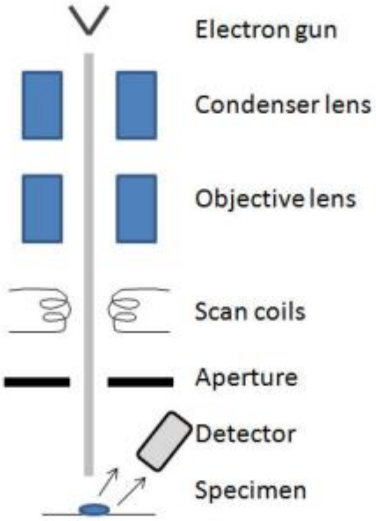

Figure 3.7 A block diagram for Scanning Electron Microscope [Prukop and Barron (2011)].

The interaction of incident electrons with the sample results in the emission of secondary electrons from the atoms of the sample. X-rays and some incident electrons are bounced back (back scattered electrons) after inelastic scattering from the nucleus of the sample atom. The secondary, backscattered electrons and X-rays signals are detected in all microscopes by a detector, produce a magnified image and displayed on the screen. Scanning electron microscopes give the magnified images with high resolution of the sample and provide information about their particle size and shapes.

The SEM with X-ray detector is also used for phase analysis which in turn gives the quantitative measurement of the amount of an element present in the sample [Goodhew et al. (2001)]. Whenever, highly accelerated electrons hit the sample and knock out the inner shell electrons of the sample atoms, characteristic X-rays are produced as a result of a vacancy filled by higher shell electrons (see Figure 3.4). These lines of characteristic X-rays correspond to particular wavelength depend on the atomic energy levels of the atom. The EDX (Energy Dispersive X-ray spectroscopy) X-ray detector measures the number of X-rays versus their energy and produces an energy distribution histogram which enables us to analyse the presence of elements and their amount [Argast (2004)].

In this research study, SEM was used to see grain morphology, grain size and composition analysis using EDX, from thermally and chemically etched polished surfaces. Samples were coated with a ~ 3-5 nm thin layer of platinum by using an Agar High Resolution Sputter Coater (Essex, UK), to minimize the charging effect of samples and then cleaned with ZONE$_{\text{SEM}}$ (Hitachi, Japan). The specimen were analysed by using LEO 1530 Gemini FEGSEM (Field Emission Gun Scanning Electron Microscope, Zeiss, Germany) and Hitachi SU 8230 cold FESEM (Field Emission Scanning Electron Microscope, Japan) in secondary electron and back scattered mode with voltage settings of ~ 2 kV-3 kV and a working distance of ~ 3-7 mm.

3.3.6 Transmission Electron Microscopy (TEM)

In Transmission Electron Microscopy, a magnification down to atomic scale is achieved when a highly focussed beam of electrons transmits through an ultra-thin specimen (≤ 500 nm). Due to high electron beam energy, Transmission Electron Microscopes (TEMs) generate magnified and highly resolved images in imaging and diffraction modes, unlike Scanning Electron Microscopes (SEMs). In TEM, images are built up from diffracted electrons (dark field, STEM) and undiffracted electrons (bright field electrons) due to elemental differences. The contrast of dark and bright fields gives the details of elemental differences and sample microstructure. For elemental mapping, EDX is used with STEM.

In this work, the sintered ceramic samples were cut down to ~ 3 mm in diameter by using a Disc Cutter (Model 601, Gatan, USA) and ground to ~ 70 µm by using 40, 15 and 5 µm grits. For electron transparency, the samples were dimpled and thin down further at the centre by using Dimple Grinder (Model 656, Gatan, USA) with alumina suspension polishing paste (~ 0.05 µm). The samples were further polished and etched using a Precision Ion Beam Polishing System (PIPS, Model 691, Gatan, USA). A Philips CM200 Field Emission Gun Transmission electron microscope (FEGTEM) was used to study microstructure structure and compositional variations. All TEM operations were conducted with the help of Dr. M. Ward, University of Leeds.

Chapter 4

Phase Stability and Properties of the $K_{0.5}Bi_{0.5}TiO_3$-$Bi(Mg_{0.5}Ti_{0.5})O_3$ Ceramic System

4.1 Summary

This chapter deals with the dielectric, ferroelectric and piezoelectric properties of the relaxor $(1-x)K_{0.5}Bi_{0.5}TiO_3$-$xBi(Mg_{0.5}Ti_{0.5})O_3$ ceramic system, abbreviated $(1-x)$KBT-xBMT.

Compositional disorder and the formation of polar nanoregions are the basis for most models of relaxor dielectric behaviour where mixed ion valence and size occupancy on A and/or B sites of the perovskite ABO_3 lattice are involved [Kleemann (2012), Bokov and Ye (2006)]. In contrast, classic ferroelectrics exhibit long range alignment of polar dipoles, forming microdomains.

X-ray powder diffraction, XRD, patterns exhibited single-phase perovskite for compositions $x < 0.1$, but precise phase analysis proved difficult. The interpretation reached from standard XRD data is that compositions $x \leq 0.025$ were tetragonal, and at $0.025 < x < 0.03$ there was a phase boundary between tetragonal and mixed tetragonal+cubic (or pseudocubic) phase fields. The high x limit of the mixed phase field occurred at $x \sim 0.08$. Uncertainty surrounds the true symmetry of the 'cubic' phase, it may be globally cubic but randomly oriented localised non-centrosymetric regions may exist and be responsible for its ferroelectric character (as evidenced for ferroelectric behaviour in $x = 0.08$) which was predominantly cubic with a very minor level of co-existing tetragonal phase. Future high resolution X-ray and neutron diffraction, and short range structural analysis would be invaluable in understanding the

structure of these materials. In-situ electric-field diffraction studies to investigate if any field induced transition takes place.

The compositional position of the tetragonal/mixed phase boundary varied only slightly with temperature up to the temperature of the transition to a high-temperature cubic single-phase (~ 280-260 ºC for $x = 0.03$-0.04). Hence, the boundary approximates to a morphotropic phase boundary, MPB, but in this case the boundary most probably represents the start of a transitional zone of phase coexistence of two relaxor phases, each differing in local structure. These MPB compositions exhibited favourable piezoelectric properties, for example, the piezoelectric charge coefficient, d_{33}, was 150 pC/N for composition $x = 0.03$. Large bipolar electromechanical strains of ~ 0.30% at fields of 50 kV/cm were recorded, with d_{33}^* (S_{max}/E_{max}) values of ~ 760 pm/V for composition $x = 0.04$. Room-temperature unipolar strains at fields of 80 kV/cm were ~ 0.30% for $x = 0.03$ and $x = 0.04$, with low hysteresis, which is of benefit for actuator applications. High strains (unipolar) were retained to temperatures of at least 185 ºC; a slight increase in strain with increasing temperature was observed such that S_{max} = 0.18% at 185 ºC for the MPB compositions.

The system's distinctive high depolarisation temperature (superior to many alternative Pb-free piezoelectric ceramics) was confirmed by thermally stimulated charge decay measurements, and piezoelectric coupling coefficient k_p versus temperature measurements, both techniques indicated a depolarisation (P = 0) temperature T_d ~ 220 ºC. At room temperature, values of k_p were ~ 0.16 for KBT ($x = 0$), increasing to a peak value of ~ 0.18 for $x = 0.03$. The $0.03 \leq x \leq 0.06$ materials sustained polarisation at low electric fields at room-temperature (no constriction being observed in P-E loops), with remnant polarisation ~ 18 µC/cm^2 for $x = 0.04$ and 0.06; the coercive fields were 28 kV/cm and 23 kV/cm for $x = 0.04$ and 0.06 respectively. On heating to maximum test temperatures of 180 ºC, P-E constriction became evident in $x = 0.04$ at 180 ºC.

4.2 Results and Discussion

4.2.1 Phase Relations

Figure 4.1 shows X-ray diffraction patterns obtained at room-temperature for crushed sintered pellets. XRD patterns indicated that (1-x)KBT-xBMT compositions with $0 \leq x < 0.03$ were tetragonal. For $x = 0.04$, comparisons of the peak profiles in the ~ 45-47 º2θ range ($002_T/200_T$) indicated a third peak was present between the tetragonal doublet, Figure 4.2. The third peak became more prominent as x increased to 0.07. Initially rhombohedral or other lower symmetry (single) phase was suspected (monoclinic) [Skidmore (2009)], but there was no associated splitting or broadening of the {111} peak. The conclusion is that compositions $0.03 \leq x \leq 0.08$ were mixed phase, tetragonal and cubic (there was only a hint of tetragonal in the $x = 0.08$ pattern). Close inspection of $x = 0.03$, showed evidence of a shoulder consistent with the presence of cubic phase coexisting with tetragonal phase, Figure 4.2(b).

A minor amount of secondary bismuth titanate ($Bi_4Ti_3O_{12}$) phase, along with a cubic KBT-BMT phase was evident for the $x = 0.1$ and 0.12 sample compositions (Figure A1, Appendix), implying the solid solution limit was at $x < 0.1$, but the equilibrium solid solution limit was not studied in detail as the best piezoelectric properties were found at $x = 0.03$ and 0.04.

The variation in lattice parameters for different samples is shown in Figure 4.3. For KBT ($x = 0$), the tetragonal lattice parameters were $\boldsymbol{a} = 3.907 \pm 0.002$ Å and $\boldsymbol{c} = 3.979 \pm 0.003$ Å changing to $\boldsymbol{a} = 3.914 \pm 0.003$ Å and $\boldsymbol{c} = 3.972 \pm 0.001$ Å at $x = 0.03$. The contraction in tetragonal ***c/a*** ratio with addition of BMT content into the solid solution is shown in Figure 4.3 (inset). For KBT ***c/a*** ~ 1.02, decreasing to 1.015 at $x = 0.03$. The observation that lattice parameters vary across the two phase region shows the region is not a typical equilibrium two-phase zone. Instead it implies the compositions of each phase change progressively.

The classic relaxor $Pb(Mg_{1/3}Nb_{2/3})O_3$ (PMN) also diffracts as cubic (in PMN the space group is Pm3m). Randomly oriented polar nanoregions form by cation displacements from standard crystallographic positions [Bonneau et al. (1989), Bonneau et al. (1991)].

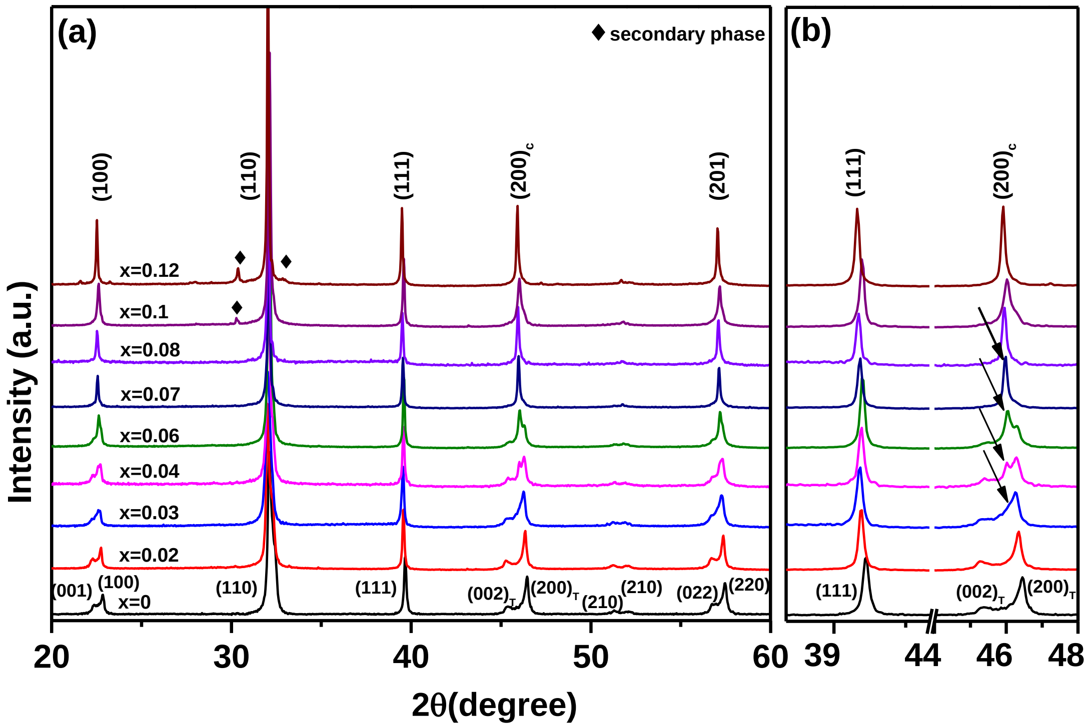

Figure 4.1(a) Room temperature XRD patterns for (1-*x*)KBT-*x*BMT ceramic system; (b) highlighted {111} and {200} reflections (arrows indicate the cubic phase coexisting with tetragonal phase).

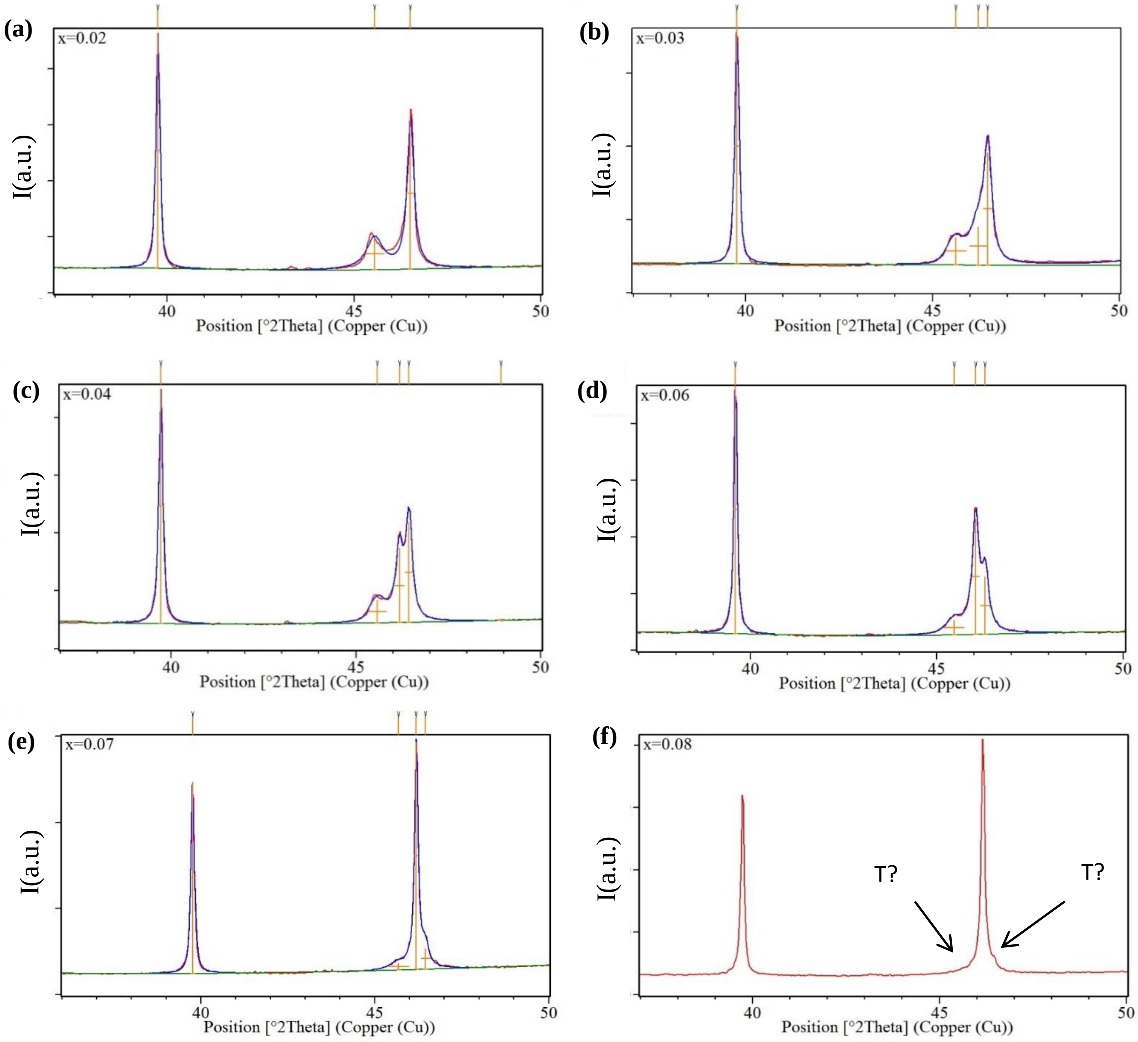

Figure 4.2 XRD profiles and peak fitting for (1-*x*)KBT-*x*BMT: (a) *x* = 0.02; (b) *x* = 0.03; (c) *x* = 0.04; (d) *x* = 0.06 (e) *x* = 0.07 (f) *x* = 0.08 (without profile fit) (highlighted {111} and {200} reflections).

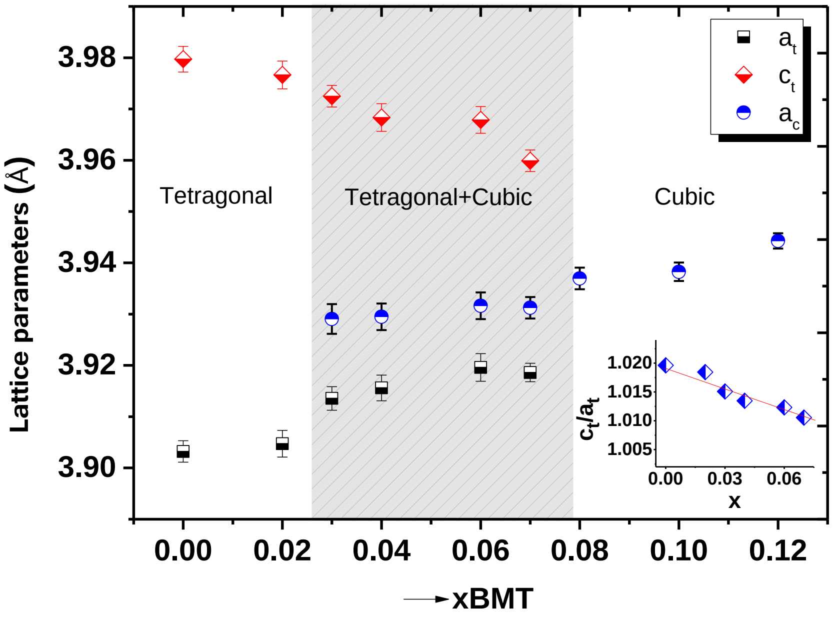

Figure 4.3 Variation of room temperature lattice parameters (by least square refinement) as function of *x*BMT, shading highlights the mixed phase tetragonal+cubic (inset shows *c/a* ratios).

4.2.2 High Temperature XRD and Phase Diagram

High temperature X-ray powder diffraction data are presented on an expanded scale for {111} and {200} reflections in the 38-48 º2θ range in Figure 4.4. These data were used to construct a phase stability diagram, as shown in Figure 4.6. The variation of unit cell parameters and their ***c/a*** ratios for compositions x = 0-0.07 measured over the temperature range 25-400 ºC are shown in Figure 4.5.

The temperature variable XRD was conducted on the Philips X'pert Pro MPD diffractrometer, while the room-temperature data reported in Section 4.2.1 on the Bruker D8. Comparisons indicated an offset of ~ 0.15 º2θ between the two instruments. Internal standards were not used: key samples should be re-run using a standard in future to obtain highly accurate lattice parameters. However, the existing data is considered sufficient to highlight trends with changing composition or temperature.

The phase diagram showed the existence of a phase boundary between tetragonal and mixed tetragonal+cubic phase with only a slight deviation from vertical. Overall, the boundary position varies by ≤ 1 mol% for temperatures from 25 ºC to 300 ºC, Figure 4.6, and thus it can be considered to approximate to a MPB which is a prime goal in developing new piezoelectric solid solution systems. However, it is not a MPB between two ferroelectric phases of different polarisation directions, as in PZT, since the (1-x)KBT-xBMT system may show co-existence of two different relaxor phases, one which diffracts as tetragonal, the other showing no deviation from cubic diffraction patterns (the other boundary between mixed and cubic was also reasonably temperature insensitive).

The ferroelectric and piezoelectric properties were enhanced at the MPB, but the mechanisms are not known; arguments of polarisation rotation used for PZT at its MPB are unlikely to apply. Local structure analysis (nanoscale) is required. For whatever reason, experimentally it is demonstrated that ferro- and piezoelectric properties are enhanced near the KBT-BMT MPB, showing that the specific local structure or co-existence of two different local structures (one diffracting as tetragonal, the other cubic) enhances the polarisability of the bulk structure. It is thought this is because of the beneficial effects in reducing coercive field by reductions in ***c/a*** ratio from 1.02 in KBT to ≤ 1.015 at x = 0.03 (so energy barriers to dipole switching are reduced) as well as easier re-orientation of dipoles due to the presence of a small amount of cubic phase (polar tetragonal regions may move more easily in the biphasic structure).

The relaxor end member KBT (x = 0) was tetragonal at room temperature and retained its tetragonal symmetry up to temperature ≤ 260 ºC. A mixed phase tetragonal+cubic appeared at temperature of ≥ 280 ºC and became cubic at 320 ºC.

Composition x = 0.02 remained single-phase tetragonal from room temperature up to 300 ºC above which single phase cubic patterns appeared**.** Composition x = 0.03 showed a mixed-phase tetragonal+cubic from room temperature (25 ºC) to 260 ºC, transforming to single phased cubic at ~ 280 ºC**.** Composition x = 0.04 exhibited a mixed phase from room temperature to 240 ºC, above which it existed as single phase cubic. The mixed phase temperature span reduced to 25-220 ºC at x = 0.06 and 25-160 ºC for x = 0.07.

A significant variation in the tetragonal lattice parameters $\boldsymbol{a}$ and $\boldsymbol{c}$ were observed as a function of temperature for all studied samples, Figure 4.5. The tetragonal distortion contracted as the temperature of the high temperature cubic phase was reached (insets to Figure 4.5). Measurements became more difficult as peak overlap increased and/or peak intensities decreased.

The mixed phase tetragonal+cubic are highlighted with shaded regions in Figure 4.5. For the KBT end member (x = 0) the lattice parameters were $\boldsymbol{a}$ = 3.907 Å and $\boldsymbol{c}$ = 3.979 Å at room temperature, decreasing to values of $\boldsymbol{a}$ = 3.928 Å and $\boldsymbol{c}$ = 3.944 Å at a temperature of 300 ºC. A similar trend occurred for compositions x = 0.02 and 0.03, where the tetragonal lattice parameters converged to cubic at a temperature of 300 ºC and 260 ºC, respectively.

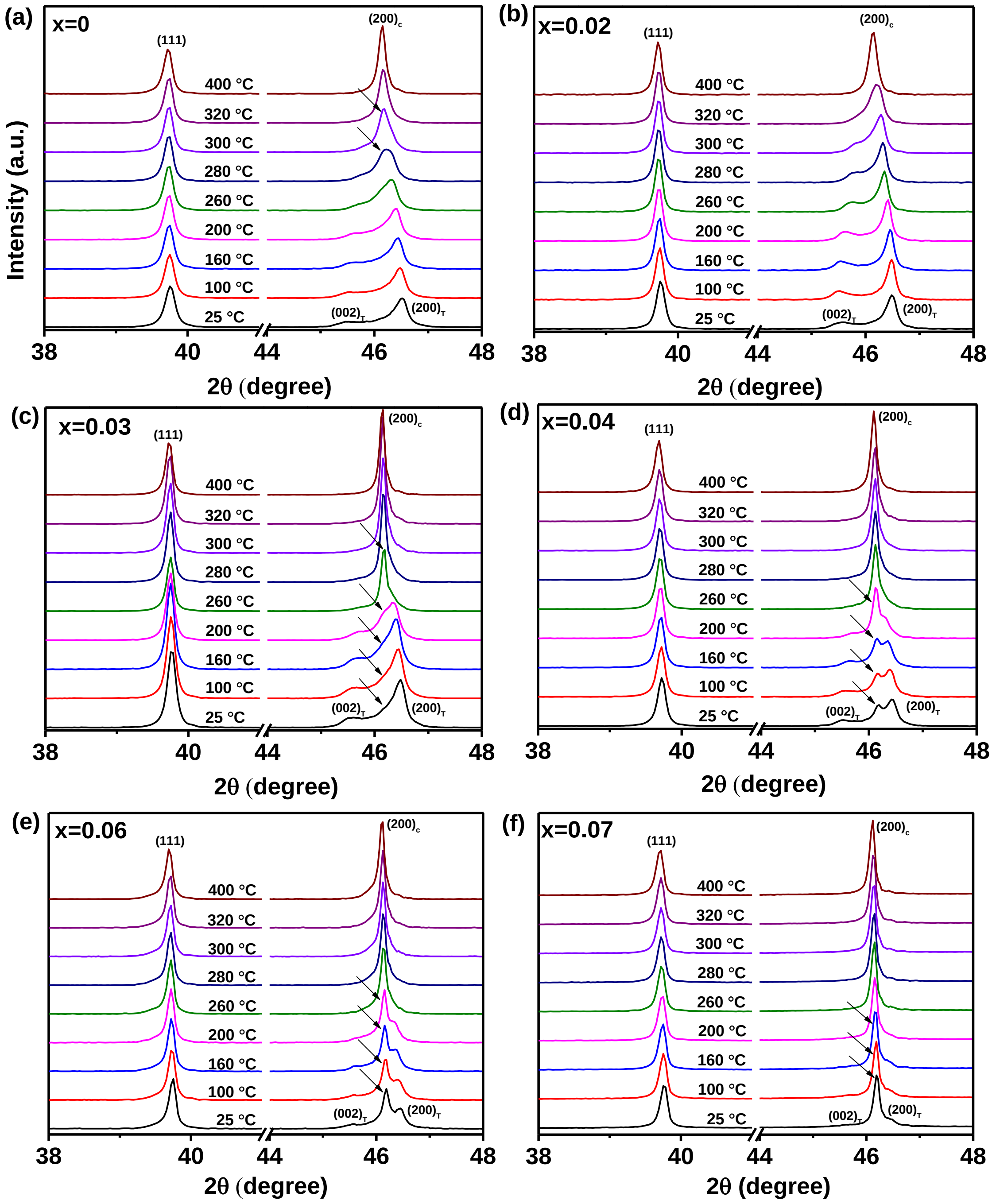

Figure 4.4 High temperature XRD patterns from 25 °C to 400 °C for (1-*x*)KBT-*x*BMT: (a) *x* = 0, (b) *x* = 0.02, (c) *x* = 0.03, (d) *x* = 0.04, (e) *x* = 0.06, and (f) *x* = 0.07 at 38-48 °2θ range (arrows indicate cubic phase coexisting with tetragonal phase).

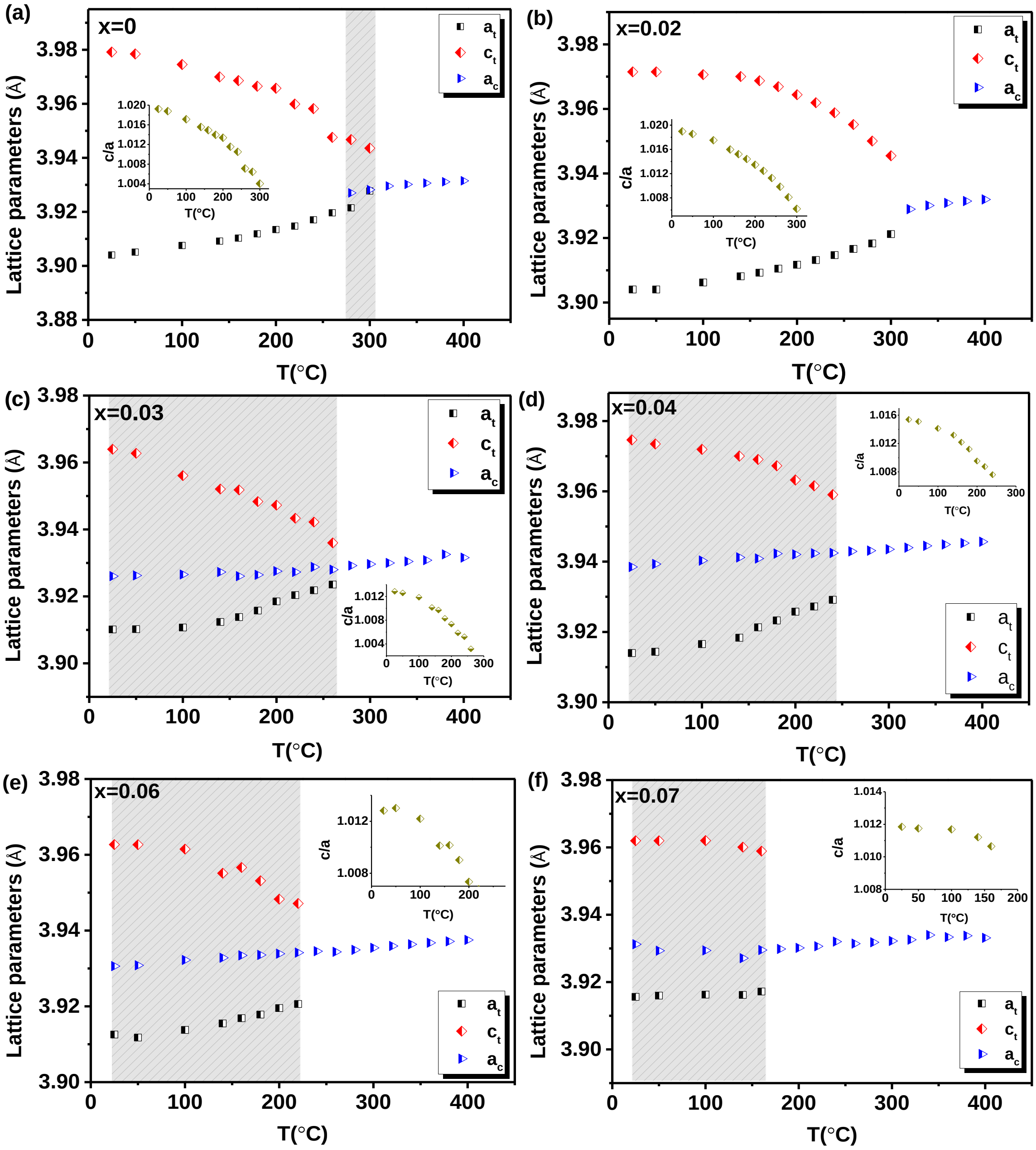

Figure 4.5 Variation of estimated lattice parameters versus temperature for (1-*x*)KBT-*x*BMT system: (a) *x* = 0 (b) *x* = 0.02 (c) *x* = 0.03 (d) *x* = 0.04 (e) *x* = 0.06 and (f) *x* = 0.07 (inset displays *c/a* ratios). For *x* = 0 and *x* = 0.04, six peaks were used with least square refinement (WinPlotr) to calculate lattice parameters. For other samples lattice parameters were simply estimated from 111 (for cubic) and 002/200 peaks (tetragonal)-hence error statistics are not available.

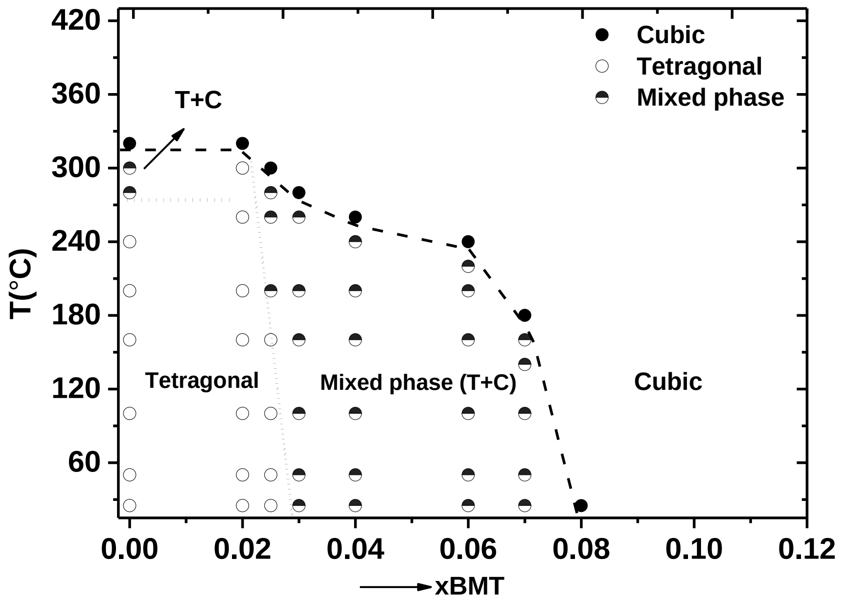

Figure 4.6 Phase diagram for (1-*x*)KBT-*x*BMT ceramic system based on high temperature XRD data.

A summary of the dielectric, ferroelectric and piezoelectric data presented in the following sections is given in Table 4.2 (page 112).

4.2.3 Dielectric properties

Plots of temperature-dependent relative permittivity, ε_r and loss factor (tanδ) at different frequencies are presented in Figure 4.7. The dielectric response of unmodified KBT, with peak temperature T_m ~ 380 ºC (1 kHz) is shown in Figure 4.7(a). The (1-*x*)KBT-*x*BMT solid solutions also exhibited broad frequency-dependent peaks in the ε_r-T plots and dispersion in tanδ at T ~ T_m, characteristic of a relaxor. For (1-*x*)KBT-*x*BMT, the dielectric peak temperature T_m decreased from ~ 380 ºC for KBT ($x = 0$) to ~ 330 ºC-340 ºC for compositions in the range $0.02 \leq x \leq 0.08$. There was no correlation between T_m values and the boundary temperature of the high temperature cubic phase for $x < 0.08$ in the phase diagram (Figure 4.6).

A discontinuity or inflection at ≥ 260 ºC (heating onset) appeared in ε_r-T plots of KBT unpoled (onset temperature on heating), Figure 4.7(a), but not in the BMT-modified samples. A similar inflection to unpoled KBT exists in alternative lead-free piezoelectric $Na_{0.5}Bi_{0.5}TiO_3$-$BaTiO_3$ (NBT-BT), where samples of NBT-BT near the MPB (6 mol% BT) have ε_r(T) inflections in the range 90-105 ºC; the inflection temperature is reported to correspond to the depolarisation temperature T_d [Rödel et al. (2009)].

Plots of tanδ gave a clear indication of a discontinuity below T_m in the unpoled KBT- a broad peak onset temperature was similar to the ε_r inflection temperature; the peak centre was ~ 300 ºC (1 kHz) which may signify the end of any atom rearrangements that cause the dielectric discontinuity in KBT, Figure 4.8. A correlation exists between the temperature of the discontinuities in tanδ at $T < T_m$, for KBT and the cubic boundary temperatures on the phase diagram exist (this aspect is considered further in Section 4.2.7, Figure 4.20).

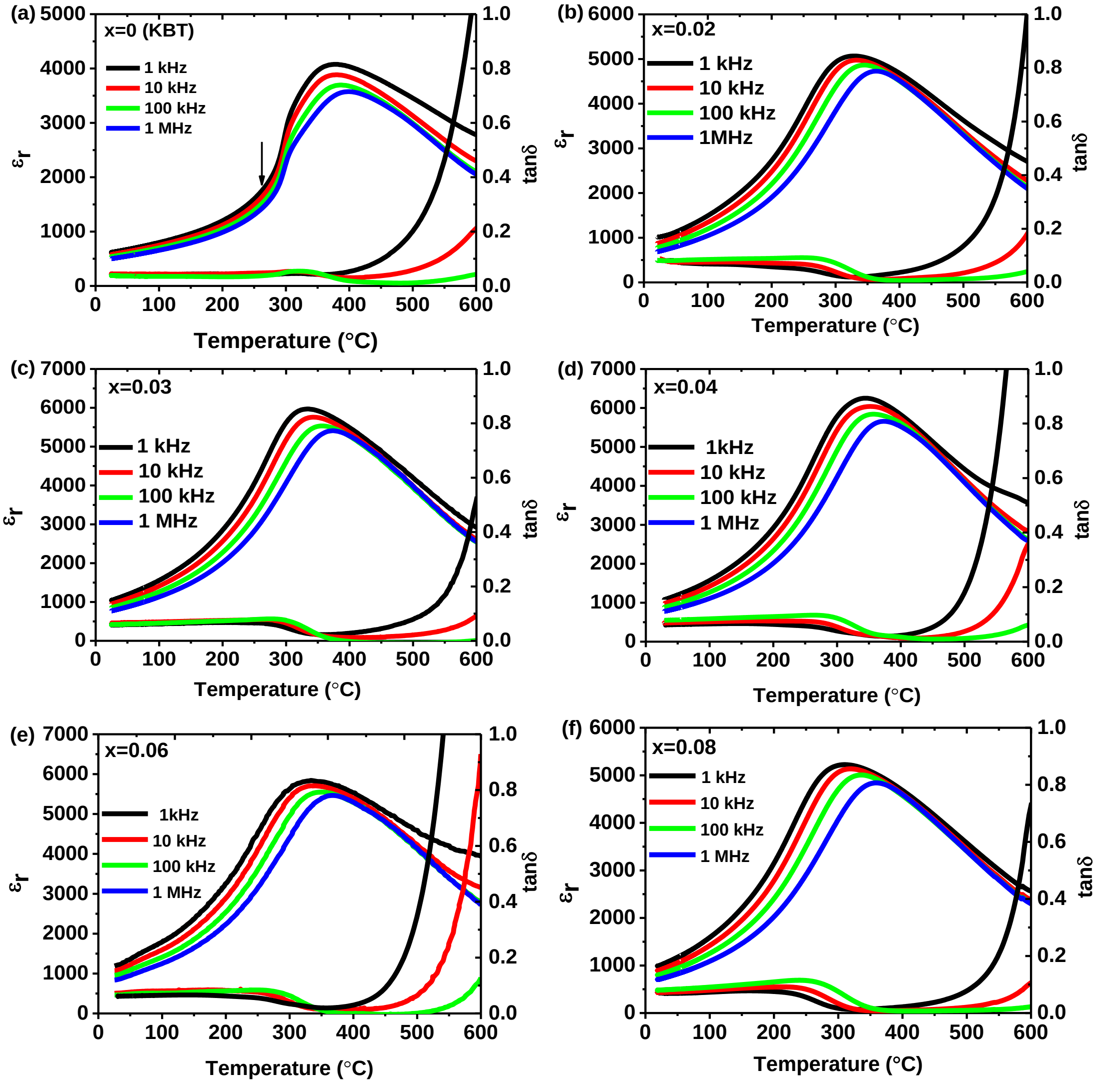

Figure 4.7 Relative permittivity and loss tangent versus temperature at different frequencies for: (a) *x* = 0 (KBT), (b) *x* = 0.02, (c) *x* = 0.03, (d) *x* = 0.04 (e) *x* = 0.06 and (f) *x* = 0.08 (arrow indicates the onset temperature of the inflection in KBT).

The temperature of dielectric inflections in poled KBT shifted by ~ 50 ºC toward lower temperatures ~ 200 ºC, with tanδ peak at moving ~ 250 ºC in poled KBT, Figure 4.8. In KBT-BMT unpoled samples, there was no inflection, but a faint ε_r-T discontinuity appeared in poled samples. For poled *x* = 0.03, there was a discontinuity at 180-200 ºC (1 kHz data), Figure 4.8.

For (1-*x*)KBT-*x*BMT ceramic samples, values of tanδ were ≤ 0.07 (1 kHz) at ≤ 350 ºC and increased sharply above ~ 400 ºC, this increase may relate to the loss of some bismuth oxide and potassium oxide during high temperature calcination/sintering and consequent changes to defect chemistry, resulting in ionic or electronic conduction which gives rise to high measured values of dielectric loss [Ranjan and Dviwedi (2005)]. A similar sharp rise in tanδ values was also reported for NBT-BT at the MPB composition (6 mol% BT), where tanδ > 0.25 at ≥ 400 ºC (at a frequency of 10 kHz) [Wang et al. (2003)].

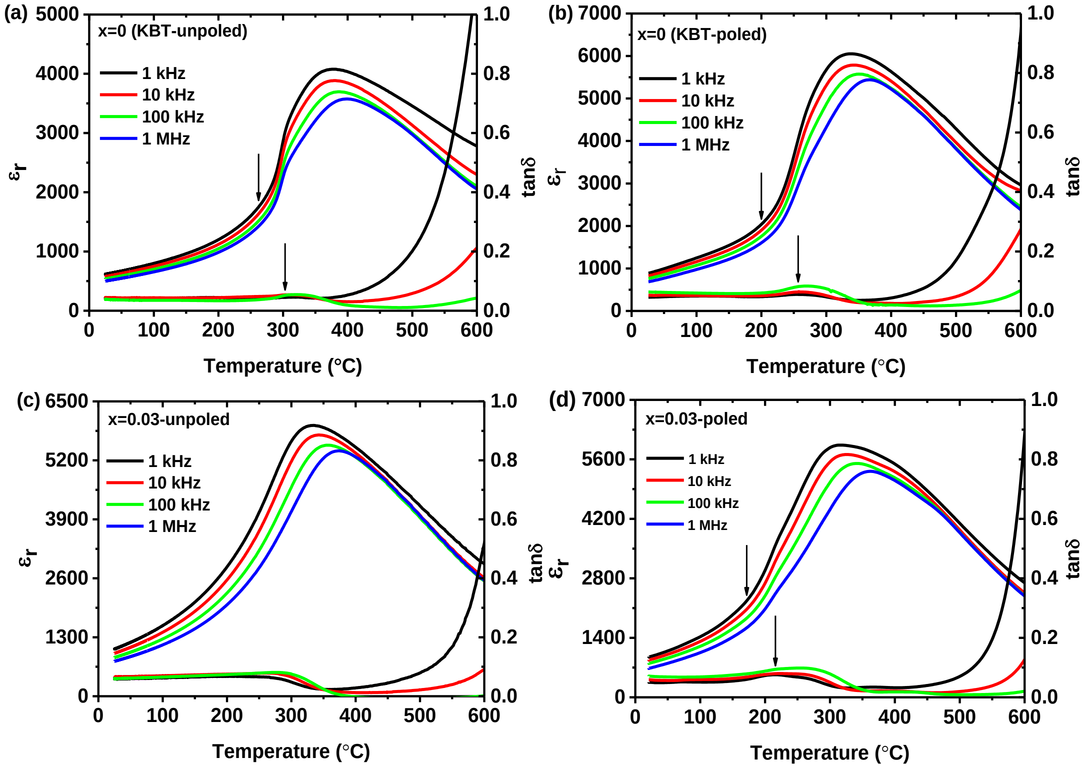

Figure 4.8 Relative permittivity and loss tangent versus temperature for: (a) *x* = 0 (KBT-unpoled), (b) *x* = 0 (KBT-poled), (c) *x* = 0.03-unpoled and (d) *x* = 0.03-poled (arrow indicates the onset temperature of the inflection in ε_r and tanδ.

4.2.4 Ferroelectric Properties

4.2.4.1 Room Temperature Ferroelectric Properties

Figure 4.9 shows the P-E response for the (1-*x*)KBT-*x*BMT system measured at room temperature ($E_{max} \leq 50$ kV/cm, 1 Hz). There was no clear evidence of ferroelectric switching in KBT ($x = 0$) or in single-phase tetragonal $x = 0.02$ ceramics. The ellipsoid loops were typical of a lossy dielectric. However, for $x \geq 0.03$ samples the shape of the P-E loops indicated ferroelectric behaviour, Figure 4.9.

Values of remnant polarisation were $P_r \sim 14$ μC/cm^2 for $x = 0.03$, increasing to ~ 18 μC/cm^2 for $x = 0.04$, with coercive fields ~ 25 kV/cm and 28 kV/cm, respectively. In the example of the $x = 0.06$ composition, the remnant polarisation, P_r, was ~ 18 μC/cm^2 and coercive field, $E_c \sim 23$ kV/cm. One possible explanation for the evolution of ferroelectric P-E loops with increasing BMT content is that the coercive field of the tetragonal phase (co-existing with cubic) decreases with increasing BMT content due to a contraction in the ***c/a*** ratio (Figure 4.3 inset). However, the reason may be more complicated as the true, or local symmetry, of the low-temperature phase, which appears cubic by standard XRD, is not known: a slight distortion from true cubic symmetry may exist and/or may develop on application of an electric field, as for example during P-E measurements. But many relaxors including lead magnesium niobate (PMN), diffract as cubic despite containing polar (and non polar) regions due to the short polar length scales. Thus KBT-BMT may be similar in this regard. Others have reported that ‘tails’ on diffraction peaks of PMN are indicative of the existence of polar nanoregions, arising from disordering of cations [Bonneau et al. (1989), Bonneau et al. (1991)].

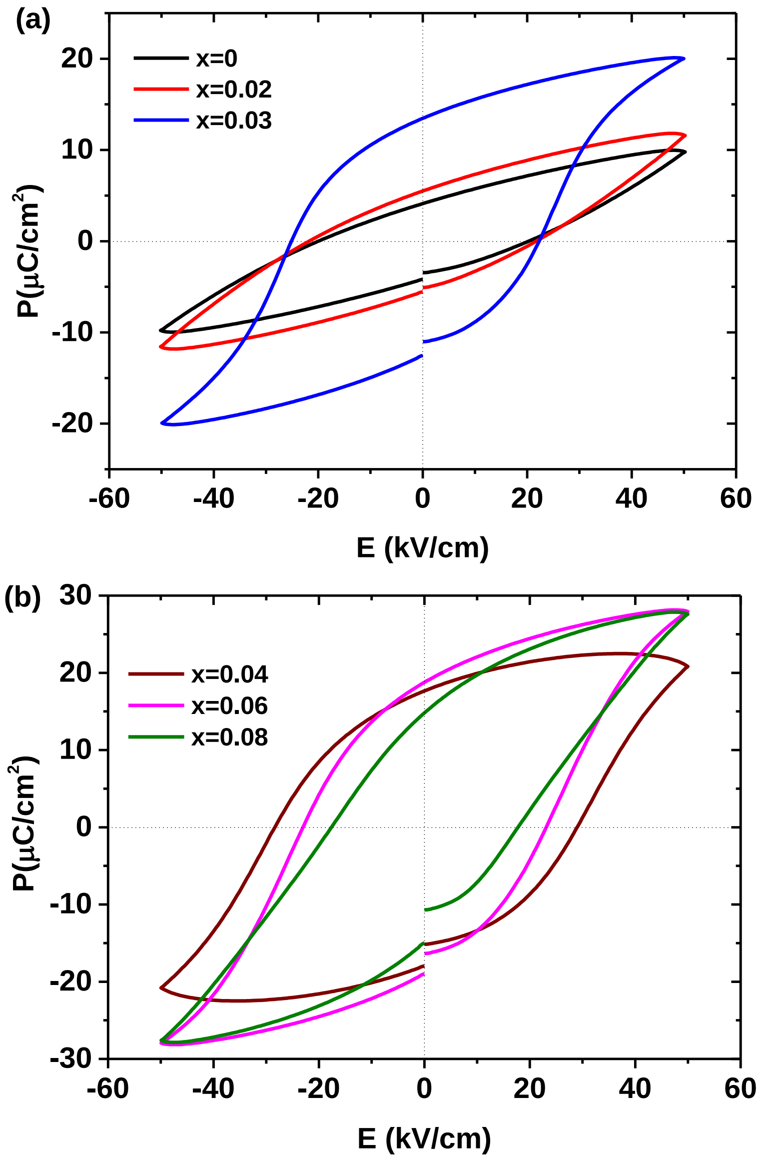

Figure 4.9 Room-temperature polarisation-electric field hysteresis loops for (1-*x*)KBT-*x*BMT: (a) $x \leq 0.03$ and (b) $x \geq 0.04$ (at 1 Hz).

4.2.4.2 Effect of Temperature on P-E Response

Polarisation-electric field response was also studied as a function of temperature (50, 100, 150, 180 ºC in a silicone oil bath) for selected samples, x = 0, 0.03, 0.04 and 0.06, Figure 4.10. These high temperature experiments were conducted with D A Hall’s help at Manchester University.

For KBT (x = 0), there was no ferroelectric switching at 50 ºC (E_{max} = 50 kV/cm), but at 100 ºC-180 ºC, typical ceramic ferroelectric P-E loops were observed, with P_r ~ 14 µC/cm^2 and $E_c \leq 20$ kV/cm at 100 ºC, Figure 4.10(a). Composition x = 0.03 displayed standard ferroelectric P-E loops up to 180 ºC; loops became narrower (less lossy) as the temperature increased in this range consistent with easier nanodomain mobility/reorientation as temperature rises. For composition x = 0.03, values of remanent polarisation, P_r were ~ 14 µC/cm^2 at 25 ºC increasing to 18 µC/cm^2 at temperature 150 ºC, with a decrease in coercive field from 28 kV/cm to 17 kV/cm.

Possibly KBT is a ferroelectric below the ε_r inflection temperature but coercive field at < 100 ºC is too high to show ferroelectric P-E loops (***c/a*** ~ 1.02 at 25 ºC) but as temperature rises to ~ 100 ºC and ***c/a*** decreases to ~ 1.015 switching is possible under the measurement condition (E_{max} = 50 kV/cm). The ε_r-T inflection temperature is 260-300 ºC for KBT- possibly above this temperature the P-E loops would constrict (see below for KBT-BMT). It is noted that 260 ºC-300 ºC corresponds to a narrow mixed phase tetragonal+cubic region for KBT on the phase diagram.

Compositions x = 0.04 and 0.06 each exhibited normal (non-saturated) ferroelectric loops to temperatures of 150 ºC, but the 180 ºC loops for x = 0.04 showed pinching or constriction, Fig 4.10(c), (d), suggesting proximity to the onset temperature of depolarisation. The reason this was more obvious in x = 0.04 than 0.06 is not clear (T_d values of x = 0.06 were not recorded) but experimental variations in the oil bath temperatures close to T_d may be responsible.

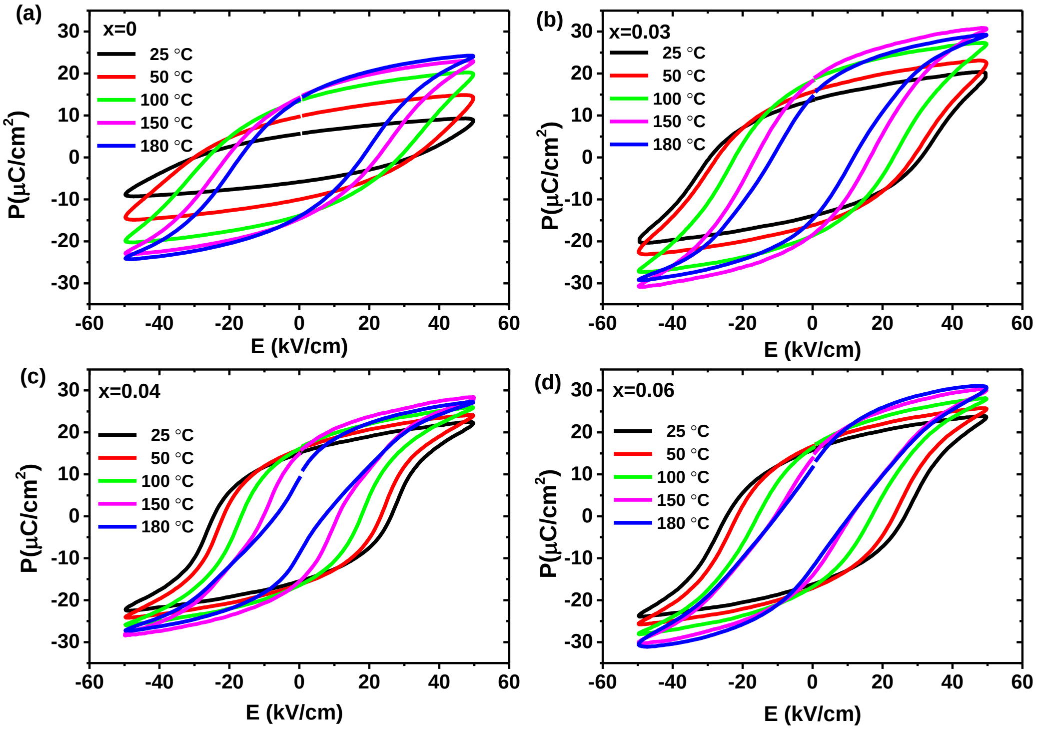

Figure 4.10 Polarisation-electric field loops as a function of temperature for: (a) *x* = 0, (b) *x* = 0.03 (c) *x* = 0.04 and *x* = 0.06 at 50 kV/cm.

4.2.5 Electromechanical Properties

4.2.5.1 Strain-Feld Response

Bipolar strain-electric field, S-E, loops for the (1-*x*)KBT-*x*BMT system measured at room temperature are presented in Figure 4.11. For unmodified KBT the maximum electric field-induced bipolar strain values were < 0.05% (50 kV/cm, 1 Hz), and for *x* = 0.02 BMT, S_{max} ~ 0.07% (from electroconstriction). Butterfly loops showing positive and negative strains of a piezoelectric were recorded for *x* > 0.02. Strains (positive strains) were ~ 0.25% for *x* = 0.03; ~ 0.35% for *x* = 0.04 and ~ 0.30% for *x* = 0.06. Peak-to-peak strains were up to ~ 0.45%, Figure 4.11. The d_{33}* (S_{max}/E_{max}) values from bipolar S-E loops were ~ 760 pm/V and 660 pm/V for *x* = 0.04 and *x* =

0.06 respectively. The *x* = 0.08 which was near-single phase cubic also gave a strong piezoelectric S-E response, Figure 4.11.

These strain values at moderate drive fields are comparable to the best NBT-BT MPB compositions [Guo et al. (2010)] and ternary $Na_{0.5}Bi_{0.5}TiO_3$-$K_{0.5}Bi_{0.5}TiO_3$-$Bi(M'_{0.5}Ti_{0.5})O_3$ systems [Hiruma et al. (2007b), Ma et al. (2010), Maurya et al. (2013)]. But lower than the ‘giant’ strains of 0.45-0.48% developed (80 kV/cm, 50 mHz) in $Na_{0.5}Bi_{0.5}TiO_3$-$BaTiO_3$-$K_{0.5}Na_{0.5}NbO_3$ and $Na_{0.5}Bi_{0.5}TiO_3$-$K_{0.5}Bi_{0.5}TiO_3$-$K_{0.5}Na_{0.5}NbO_3$ ceramics, which arise from an electric field-induced phase transition that gives a different shape of S-E loop [Zhang et al. (2007)].

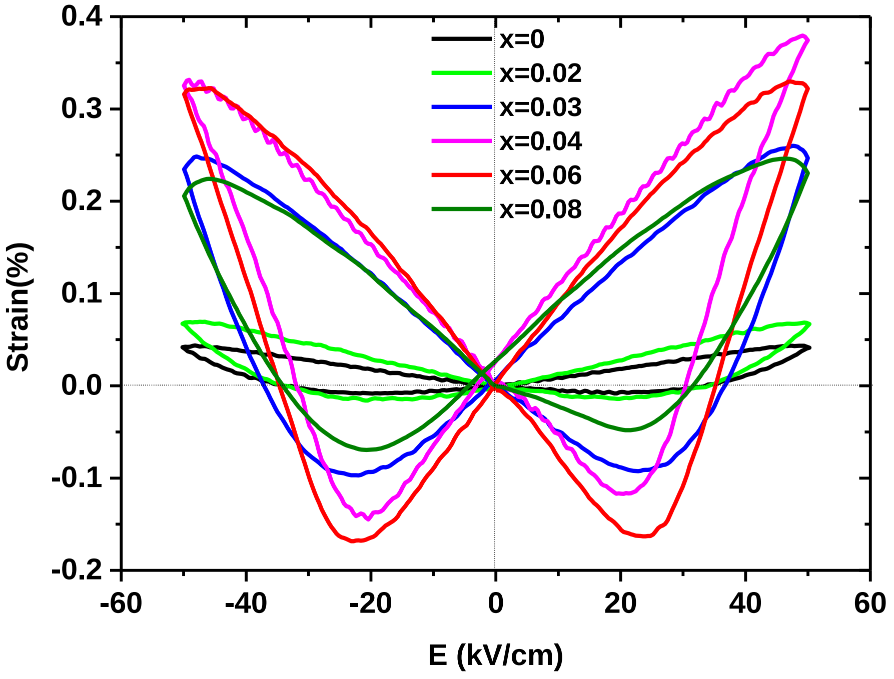

Figure 4.11 Electromechanical bipolar strain versus electric field for (1-*x*)KBT-*x*BMT ceramic system.

Unipolar strains-field plots for compositions *x* = 0-0.06 at progressively increasing fields (E_{max}) from 10 kV/cm to 80 kV/cm are shown in Figure 4.12 and 4.13 (different presentational styles). The maximum strain obtained for *x* = 0 was ~ 0.15% at 80 kV/cm, 1 Hz. For composition *x* = 0.03 and 0.04, the strain level was ~ 0.30% at fields of ~ 80 kV/cm, Figure 4.13(b) and (c). In all cases standard deviation calculated from 10 repeat in-situ measurements was ~ 0.02% (without removing the sample from the sample holder). In another set of experiment, unipolar strain for $x = 0.03$ was tested by removing the pellet from the rig and placing back, then re-measuring 3 times. The variation in maximum unipolar strain was about ~ 0.03%; the lowest strain in the set of three was ~ 0.14%. Hence, the relative error was ~ 25%, Figure 4.15. The corresponding d_{33}* values (S_{max}/E_{max}) from unipolar S-E loops were from 370-280pm/V for $x = 0.03$ (see Figure 4.16 and Table 4.2).

Unipolar strains at 50 kV/cm were in the range 0.14-0.17 % for $x = 0.03$ (measured in Leeds), and 0.11 % for samples sent to Tsinghua. Ageing studies (below) showed little variation (other than standard scatter) over a 6 week period, Figure 4.25.

The unipolar S-E loops were relatively narrow, with hysteresis of ~ 7% at 20 kV/cm and 13% at 50 kV/cm (% hysteresis defined as width at $1/2S_{max}$ divided by S_{max}×100%) [Zhang et al. (2008)]. Independent researchers have commented that strain hysteresis of > 60% occurs for ternary NBT-BT-KNN ‘giant’ strain materials [Zheng and Zuo (2015)]. Self-heating leading to possible depolarisation may result from wide hysteretic S-E response.

The low S-E hysteresis values are in some ways similar to hard PZT (Chapter 11) which has low dielectric losses but for KBT-BMT, the dielectric losses were moderately high (Figure 4.7). The reasons for this are uncertain but it is noted that loss values were measured routinely at 1 kHz and strain at 1 Hz. Future work should include the study of frequency effects. The variation in room-temperature strains in (1-x)KBT-xBMT, $x = 0.03$ versus drive field (≤ 80 kV/cm, 1 Hz) is presented in Figure 4.14, suggesting a discontinuity at $E \geq 60$ kV/cm.

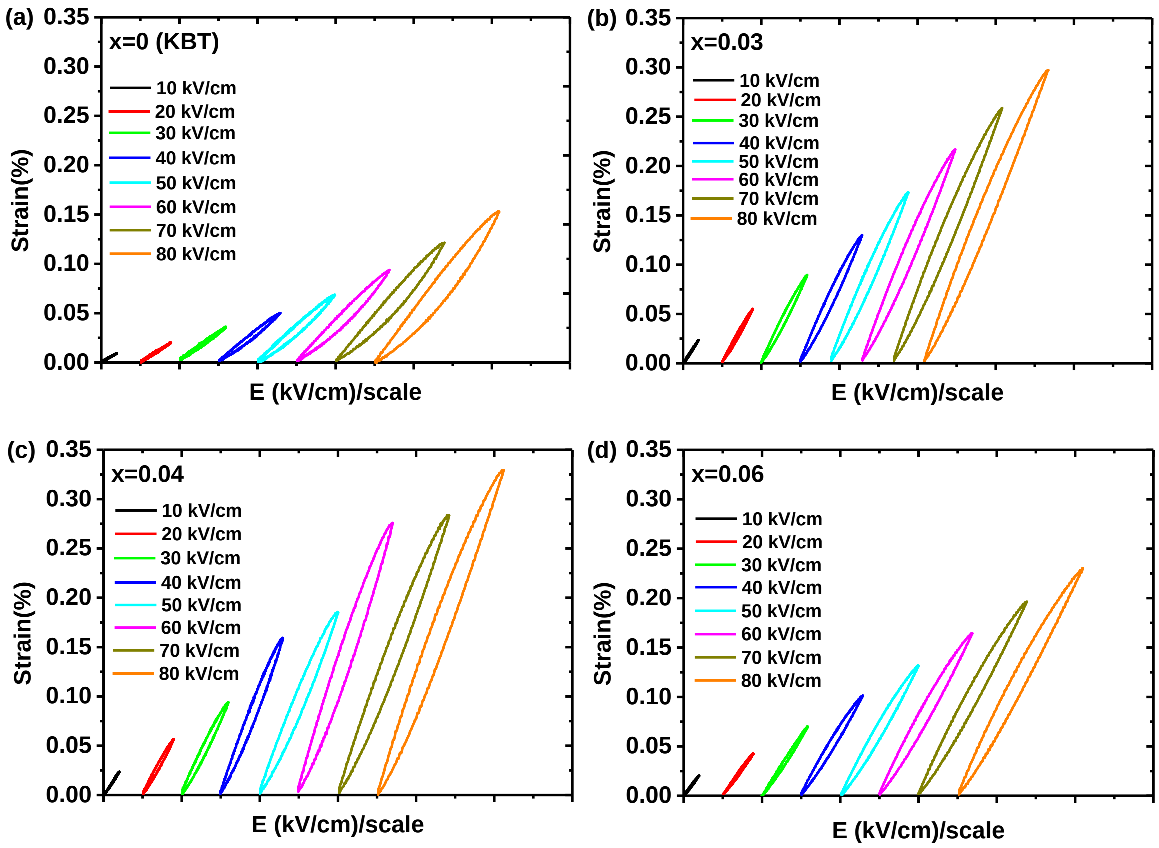

Figure 4.12 Evolution of unipolar electric field induced strain for (1-*x*)KBT-*x*BMT ceramic system: (a) *x* = 0, (b) *x* = 0.03, (c) *x* = 0.04 and (d) *x* = 0.06.

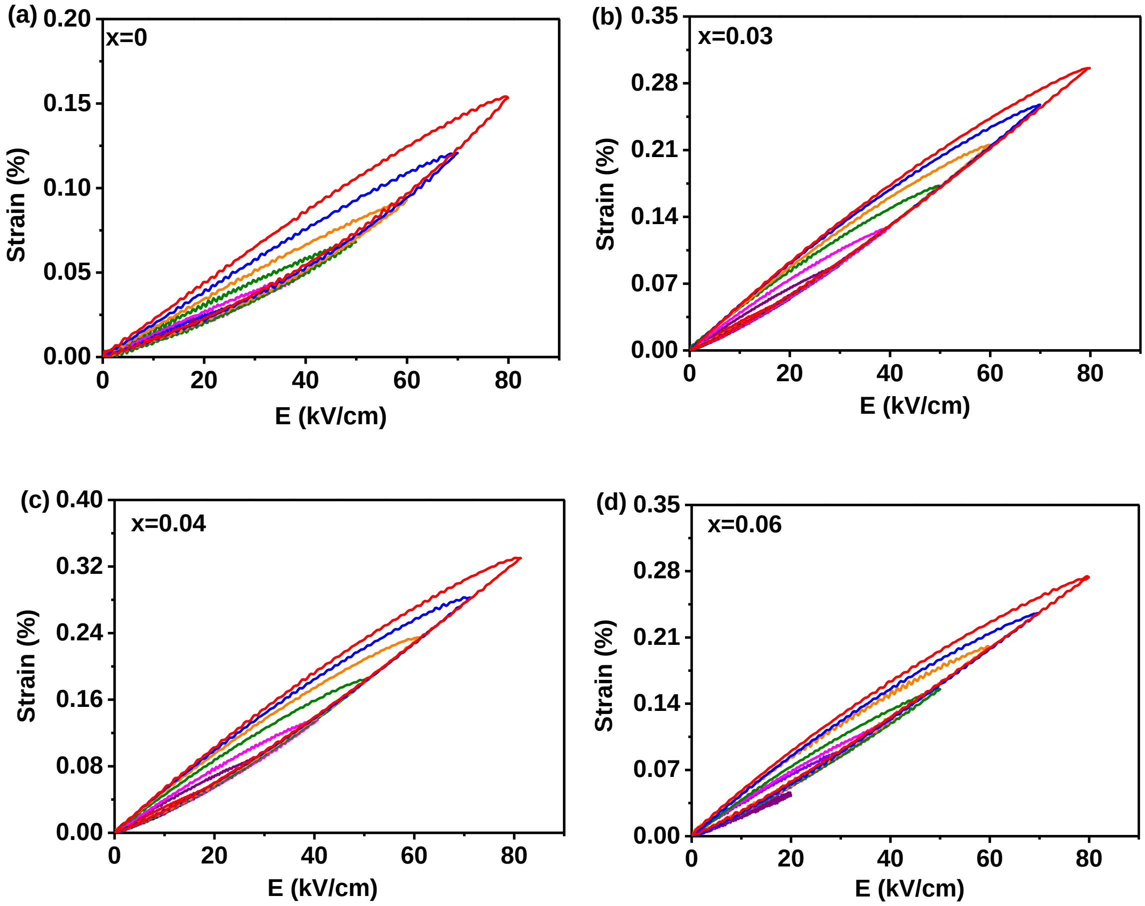

Figure 4.13 Unipolar electric field induced strain for (1-*x*)KBT-*x*BMT ceramic system: (a) *x* = 0, (b) *x* =0.03, (c) *x* = 0.04 and (d) *x* = 0.06.

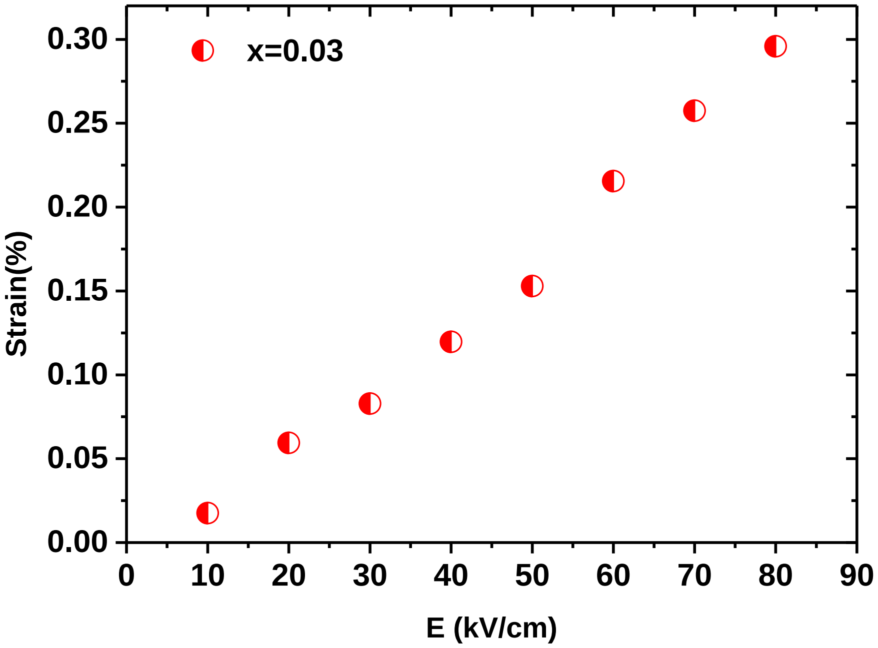

Figure 4.14 Variation of unipolar strain versus electric field for *x* = 0.03.

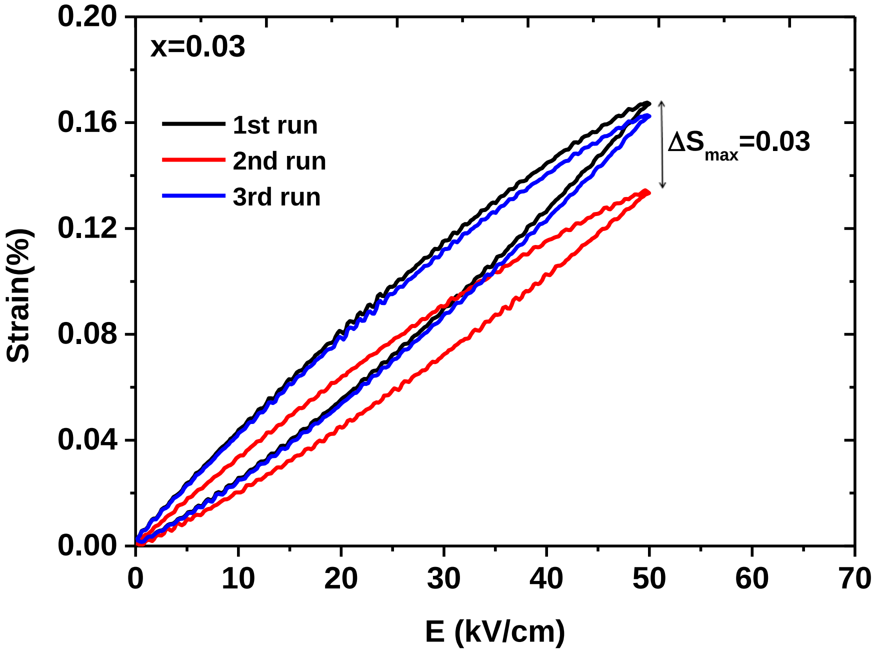

Figure 4.15 Variation of unipolar strain (*x* = 0.03) by repeating measurement 3 times under the same conditions but by taking out the sample from the rig and placing back.

4.2.6 Measurement of Piezoelectric Charge Coefficient (d_{33})

The measurement of piezoelectric charge coefficient, d_{33}, was carried out using the Berlincourt method. The poling conditions (electric field and temperature) were optimized for composition *x* = 0.03, Table 4.1. The samples were poled at a temperature of ~ 80 ºC at an applied field of 60 kV/cm for 20 min, this condition was used for other compositions except *x* = 0 and 0.02 which were poled at ~ 40 kV/cm due their breakdown at higher fields. For poling, the pellets were heated on a hotplate, a field was then applied at a ramp rate of ~ 50 V/s to a maximum value. After 20 min the temperature was then reduced to room temperature whilst the field was still applied.

Sample *x* = 0 had a piezoelectric charge coefficient, d_{33} of 44 pC/N (poled at 40 kV/cm); *x* = 0.02 was similar. Values of d_{33} reached a maximum of 150 pC/N for *x* = 0.03 (poling field, 60 kV/cm). Compositions with high BMT content had a piezoelectric charge coefficient, d_{33} of 133 pC/N for *x* = 0.04 and 100 pC/N for *x* = 0.06. A progressive decrease in d_{33} was observed with the further addition of BMT. The effective d_{33} values (d_{33}^*) for the converse piezoelectric effect, determined as S_{max}/E_{max} (bipolar and unipolar) are also presented in Figure 4.16 and Table 4.2 (bipolar and unipolar data).

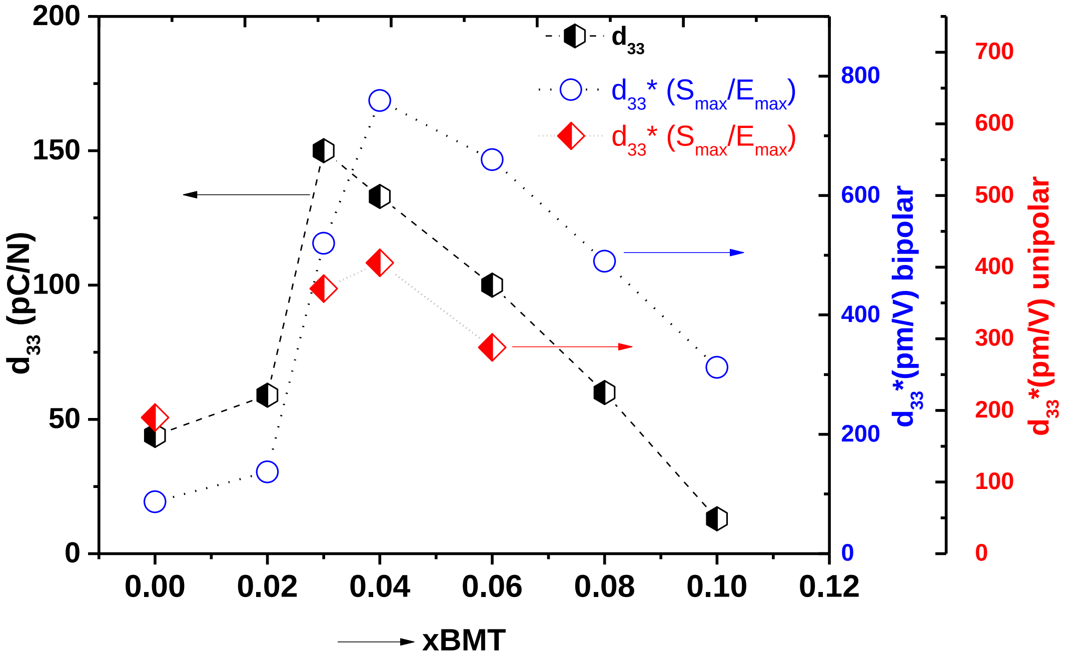

Figure 4.16 Variation of piezoelectric charge coefficient, d_{33} and effective d_{33}^* (bipolar, S_{max}/E_{max}) and d_{33}^* (unipolar, S_{max}/E_{max}) versus *x*BMT for the (1-*x*)KBT-*x*BMT system.

Table 4.1 Optimum poling conditions for composition *x* = 0.03.

Temperature	d_{33} (pC/N) at 50 kV/cm	d_{33} (pC/N) at 60 kV/cm	d_{33} (pC/N) at 70 kV/cm	d_{33} (pC/N) at 80 kV/cm
25 ºC	134	137	139	143
60 ºC	137	142	140	140
80 ºC	**140**	**150**	**145**	Breakdown
100 ºC	138	140	Breakdown	Breakdown

4.2.7 High Temperature Performance

Many lead-free piezoelectric systems with interesting properties at room temperature undergo a severe degradation in piezoelectric properties on heating, for example (Ba,Ca)(Zr,Ti)O_3 with high d_{33} ~ 620 pC/N is reported to undergo thermal depolarisation at temperatures below 100 ºC [Xue et al. (2011b)]. The MPB displayed by (1-*x*)KBT-*x*BMT system (Figure 4.6) suggests that consistent ferroelectric and piezoelectric performance may be possible over a relatively wide temperature range. The high temperature P-E loops (Figure 4.10) were evidence that polarisation without loss of remnance was retained to ~ 180 ºC for $x = 0.03$. Systems such as NBT-BT show P-E constriction linked to depolarisation at ≤ 100 ºC.

4.2.7.1 Coupling coefficient k_p versus temperature

Both KBT ($x = 0$) and $x = 0.03$ and $x = 0.04$ (1-*x*)KBT-*x*BMT exhibited similar trends in k_p as a function of temperature, Figure 4.17. Researcher at Tokyo University have selected KBT for development of lead-free actuators, despite its modest strain, due to its T_d value being higher than alternative materials [Nagata et al. (2013)].

At room temperature, values of k_p were: ~ 0.16 for KBT ($x = 0$); 0.18 for $x = 0.03$; and 0.15 for $x = 0.04$. On heating all samples exhibited similar trends in k_p values, with a slight increase up to ~ 100 ºC, Figure 4.17. Above 100 ºC, k_p began to decrease, the rate of decrease increasing above 150 ºC. Values approached zero at ~ 210-220 ºC, (signifying T_d) Figure 4.17 for all three samples. The similarity in T_d to KBT is very promising for the KBT-BMT system, since strains are up to ~ 2-3 times higher than KBT (depending on drive field), would be attractive for actuator devices.

A rapid drop in k_p values in the NBT-BT system (6 mol% BT) was reported to take place below 100 ºC [Xu et al. (2008)]. The values of k_p at room temperature for $x = 0.03$-0.06 are comparable to a number of other KBT-based ceramics $K_{0.5}Bi_{0.5}TiO_3$-$Bi(Ni_{0.5}Ti_{0.5})O_3$ and $K_{0.5}Bi_{0.5}TiO_3$-$LiNbO_3$ ($k_p = 0.18$) [Zhao and Zuo (2013), Zuo et al. (2013)], but lower than for $94Na_{0.5}Bi_{0.5}TiO_3$-$6BaTiO_3$ (k_p ~ 0.36) [Xu et al. (2008)],

$80Na_{0.5}Bi_{0.5}TiO_3$-$20K_{0.5}Bi_{0.5}TiO_3$ (k_p ~ 0.27) [Yoshii et al. (2006)] and $93Na_{0.5}Bi_{0.5}TiO_3$-$5BaTiO_3$-2KNN (k_p ~ 0.27) [Zhang et al.(2008a), Rödel et al. (2009)].

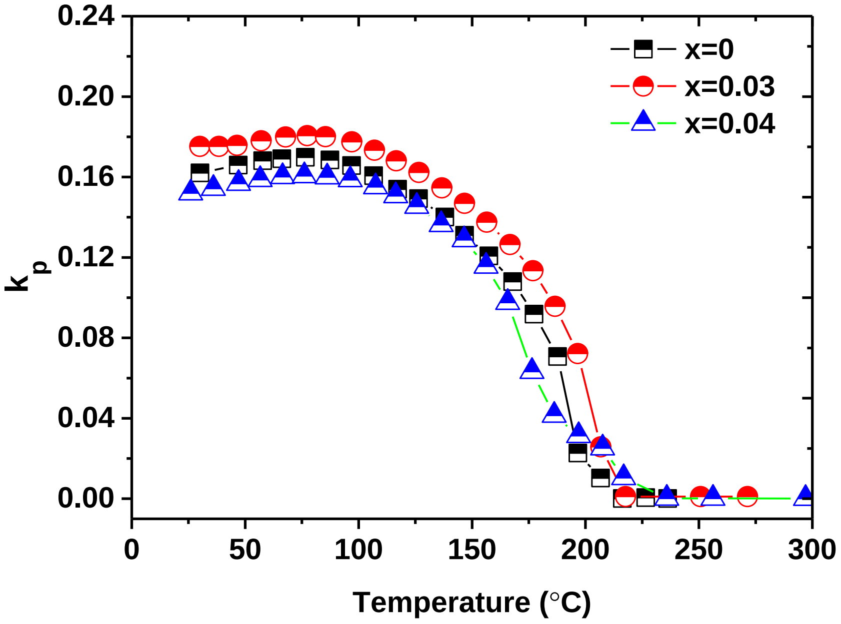

Figure 4.17 Variation of electromechanical coupling factor, k_p vs temperature for *x* = 0-0.04.

4.2.7.2 Thermally Stimulated Charge Decay Measurements

The thermal charge decay data (obtained at Manchester University) for *x* = 0.03 and 0.04 are shown in Figure 4.18. These samples had been poled under a static electric field of 60 kV/cm, at a temperature of 80 ºC for a period of 20 min. The poled *x* = 0.03 sample had lost all polarisation by ~ 220 ºC (T_d). For *x* = 0.04, the T_d value was slightly lower, ~ 200 ºC, in agreement with trends in k_p data. The maximum rate of temperature-induced depolarisation, -dP/dT, for *x* = 0.03 occurred at ~ 190 ºC, Figure 4.18(a) (inset), but by this temperature the sample had lost ~ 75% of its original polarisation. The corresponding maximum rate of thermal de-poling occurred at ~ 170 ºC for sample *x* = 0.04. In contrast, the 94NBT-6BT sample, had lost its polarisation at a temperature ~ 60 ºC, Figure 4.19, although k_p-T data from other laboratories suggest T_d could be ~ 100 ºC [Xu et al. (2008)].

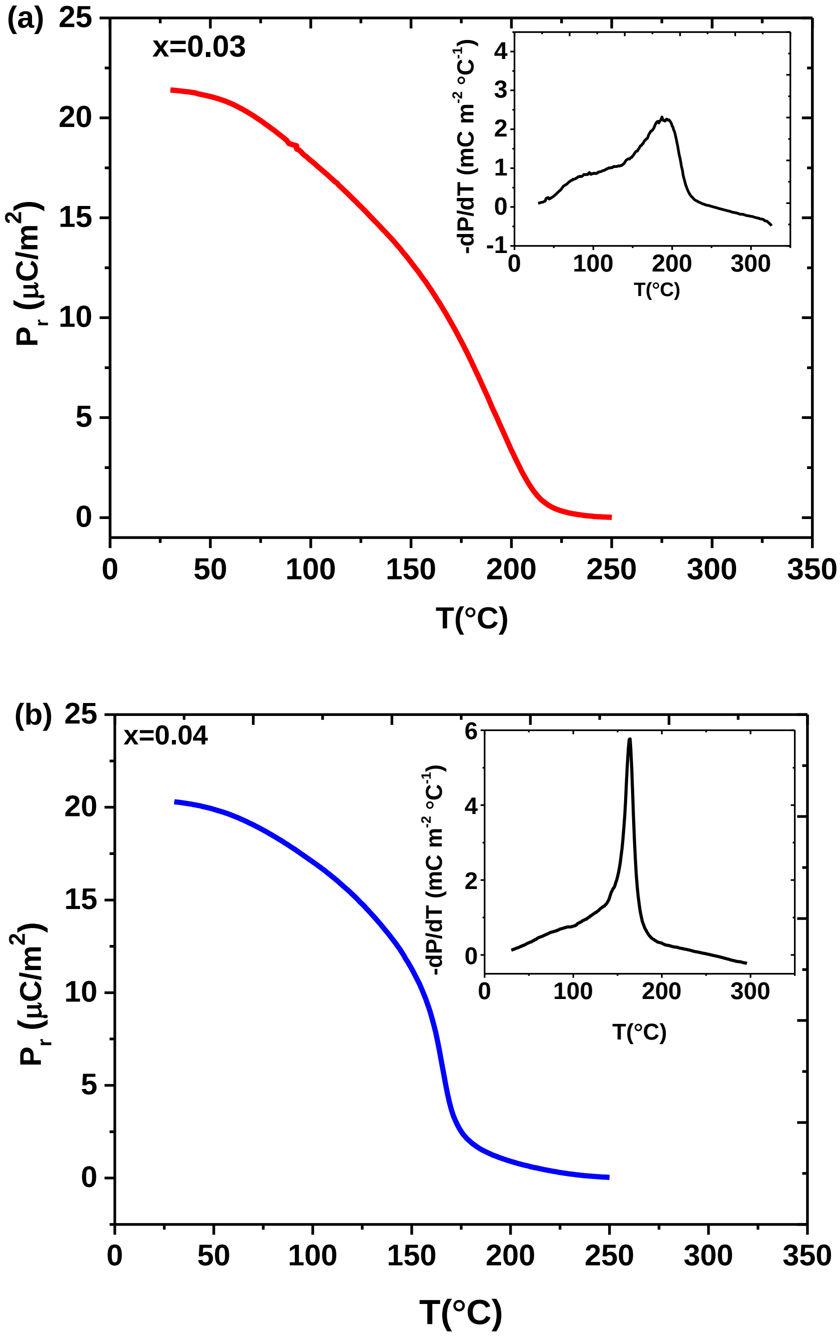

Figure 4.18 Thermally stimulated depolarisation as a function of temperature for: (a) *x* = 0.03 and (b) 0.04 (inset shows the differential plots vs temperature).

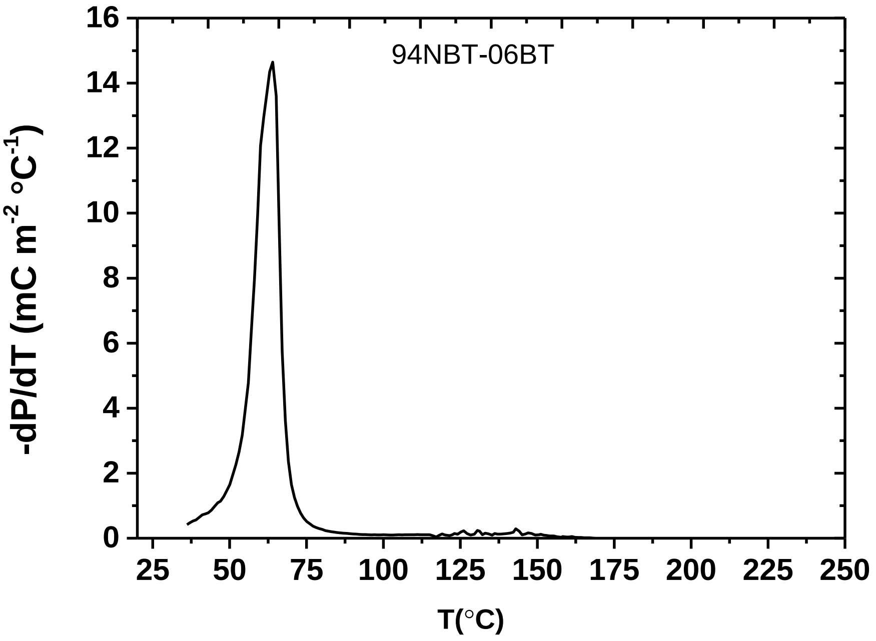

Figure 4.19 Differential plots of polarisation versus temperature for 94NBT-6BT indicating maximum rate of depolarisation at ~ 60 °C [Courtesy D.A Hall and Ge Wang, University of Manchester).

Depolarisation temperature, T_d can also be derived from the inflection in the ε_r-T plots (below the ε_r peak temperature), although this method of determining T_d can led to an overestimate [Anton et al. (2011)]. There was no inflection in unpoled KBT-BMT samples (Figure 4.7), but a faint ε_r-T discontinuity appeared in poled samples, Figure 4.20. For $x = 0.03$, there is some suggestion of a discontinuity at 180-200 °C (1 kHz data), but it is difficult to accurately determine the onset temperature. A similar profile occurred for poled $x = 0.04$. A well-defined inflection has been reported in the literature in ε_r-T plots for the NBT-BT ceramic system at a temperatures ~ 100 °C for MPB compositions [Xu et al. (2008)].

A corresponding discontinuity in tanδ data can also signify T_d of polar materials. For KBT-BMT this proved more useful, and temperatures of the loss anomaly below T_m were in general agreement with T_d values from thermal charge decay measurements. Comparing poled tanδ-T plots to unpoled plots, the poled plots for $x = 0.03$ showed a hump, with a maximum at ~ 200 ºC (1 kHz). The $x = 0.04$ plot gave a less-defined hump, around the same temperature as $x = 0.04$. The start temperature of the anomaly ('hump') was ~ 150-170 ºC (1 kHz). Further analysis appears in Appendix, Figure A7.

The start temperature of the broad hump in tanδ-T (on heating) and ε_r inflection approximate to the to the onset of a rapid decrease in k_p (Figure 4.17) and the onset of the -dP/dT peak (Figure 4.18).

There are also correlations between the dielectric discontinuity temperatures and the onset of constriction in P-E loops ($x = 0.04$, 180 ºC and predicted constriction in $x = 0.03$ at just above 180 ºC, Figure 4.10). Hence, a common mechanism links these effects- presumably atoms rearrange and the sample loses polarisation (long range ferroelectric) at these temperatures and becomes a relaxor (short range polar order) at temperatures above the ε_r inflection and P-E pinching onset ($x = 0.03$-0.04).

The phase diagram shows a correlation to the dielectric anomaly temperatures in unpoled KBT at ~ 260 ºC, Figure 4.8 (2-phase boundary starts at ~ 260 ºC; single cubic phase starts ~ 300 ºC) but in poled KBT the dielectric anomalies are 50 ºC lower than in unpoled and the fit to the (unpoled) phase diagram is not obvious. Likewise, in KBT-BMT there is no obvious correlation between temperature of dielectric and ferroelectric anomalies in poled samples and the phase diagram (dielectric and ferroelectric change at ~ 180 ºC in $x = 0.03$-0.04 but no phase boundary is located near this temperature-the cubic boundary occurs at 260-280 ºC for $x = 0.03$-0.04). The high-temperature phase diagram for poled samples was not determined but is recommended in future work.

In this work, the T_d ($P \rightarrow 0$) of KBT was not tested by charge decay (there were problems with this sample's connections experimentally, this should be carried out in future). However, from k_p-T data the KBT poled inflection occurred at ~ 200 ºC and T_d from k_p appeared similar in temperature to $x = 0.03$-0.04 ~ 220 ºC. For KBT-BMT the onset inflection temperatures in ε_r and tanδ plots were slightly lower than T_d obtained from k_p and charge decay data.

Reference to the phase diagram shows that the depolarisation temperatures for $x = 0.03$ and 0.04 are ~ 100 ºC lower than the phase boundary temperature between mixed and high temperature cubic phase. Reasons are not understood but mechanisms may be different, especially since inflections (weak) in ε_r were only observed after poling KBT-BMT in contrast to strong inflections in KBT unpoled.

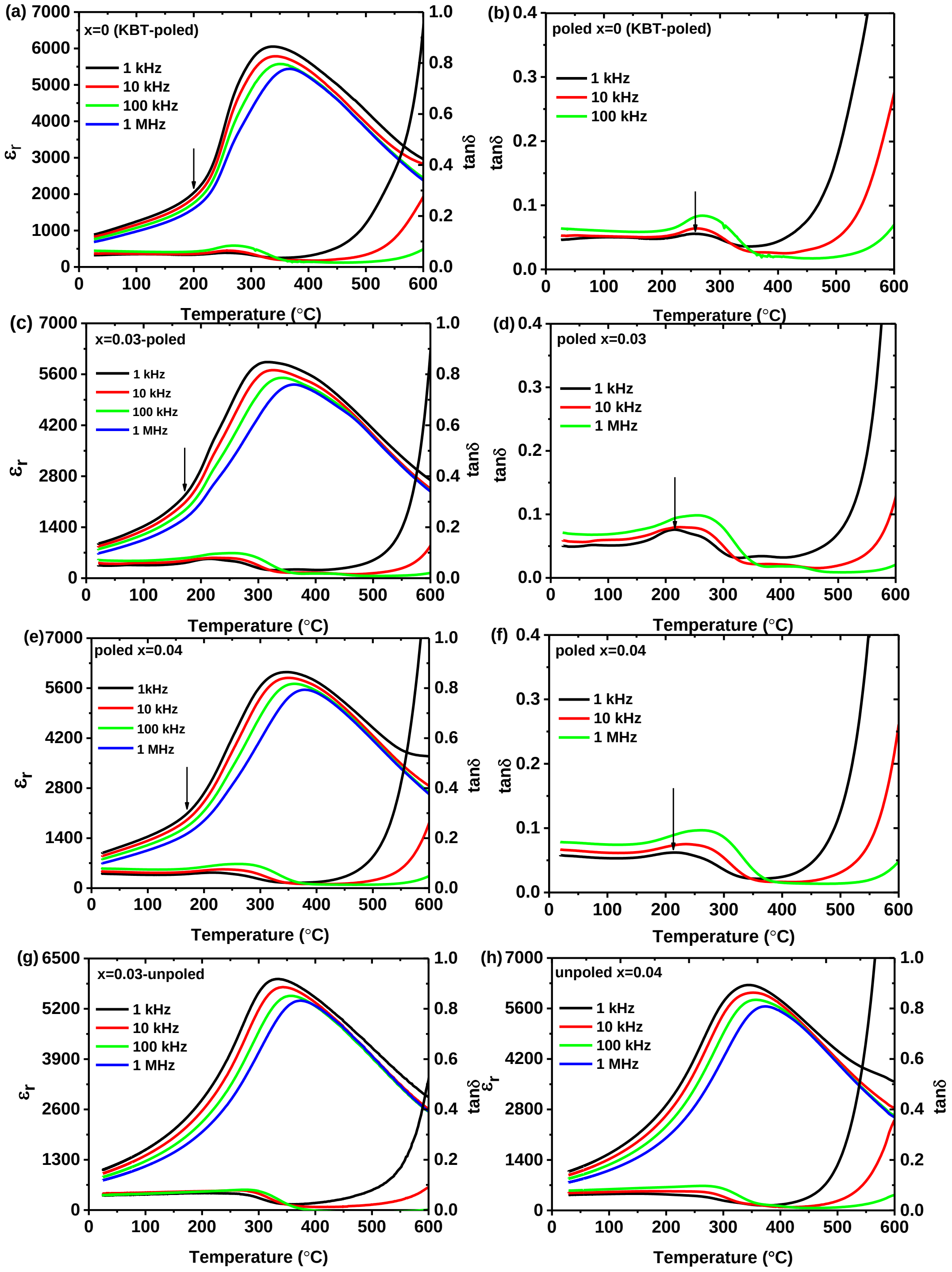

Figure 4.20 Temperature dependent relative permittivity for poled samples: (a) *x* 0.03 and (b) tanδ for *x* = 0.03 (c) *x* = 0.04 and (d) tanδ for *x* = 0.04 (arrows indicate inflection in ε_r and hump in tanδ on heating) (e) unpoled *x* = 0.03; (f) unpoled *x* = 0.04.

4.2.8 Piezoelectric Measurements: Temperature Effects

The thermal stability of piezoelectric properties was first of all studied by measuring d_{33} before and after heat treatment (annealing) sample compositions $x = 0.03$ and 0.04, Figure 4.21. Pellets were annealed in a box furnace for 20 min at 25 ºC increments. The percentage loss in d_{33} values was ~ 10% up to a temperature of ~ 150 ºC, and ~ 20% from 25 ºC to 190 ºC. On increasing temperature further > 190 ºC, d_{33} decreased sharply. The observation of a d_{33} ~ 70 pC/N at 225 ºC is inconsistent with T_d measurement, as is the modest but finite d_{33} value after heating to 275 ºC. This implies reversibility in polarisation on cooling. However, it is noted that the temperature reading from the furnace was not checked independently by a separate thermocouple, so there could be a large error in actual temperature. More rigorous testing was carried out by in-situ S-E measurements at Tsinghua University, China courtesy of Dr F JY Zhu and Prof J-F Li.

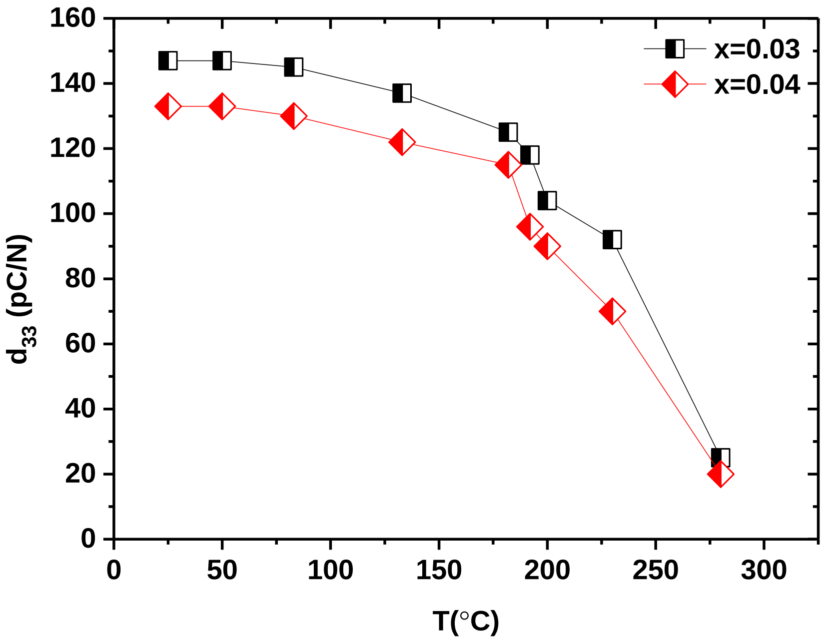

Figure 4.21 Variation of piezoelectric charge coefficient, d_{33} versus temperature after thermal depoling for $x = 0.03$ and 0.04.

Unipolar electric field induced strain curves were examined as a function of temperature at 50 kV/cm (1 Hz) for poled samples $x = 0.03$ and $x = 0.04$ (fabricated in Leeds) in the temperature range from 25-185 ºC are shown in Figure 4.22. At room temperature, both samples had similar values of unipolar strain ~ 0.11%, but this is slightly lower than equivalent value obtained at room-temperature in Leeds, ~ 0.14% (Figure 4.12, 4.13). The results for $x = 0.03$ indicate strains increase in a linear manner between temperatures of 25 ºC to 150 ºC (S_{max} ~ 0.11% at 25 ºC and 0.15% at 150 ºC), increasing more steeply above 150 ºC, reaching 0.18% at 185 ºC, Figure 4.22(a) and 4.23(a). The variation in corresponding d_{33}* is shown in Figure 4.23(b), along with values normalised against room-temperature.

Low S-E hysteresis was retained across the full temperature range, but evidence of differences in strain-field behaviour were observed at ≥150 ºC, Figure 4.24; at 175 ºC and 185 ºC tear-drop S-E loops with curvature at high fields were observed, but with relatively low hysteresis, Figure 4.24. This type of S-E loop, albeit usually with much greater hysteresis, has been observed in NBT- based piezoelectrics and is attributed of a field induced phase change. In KBT-BMT at 175 ºC and 185 ºC, it is assumed to represent a relaxor (low field) to ferroelectric (high field transition): the dielectric anomaly and P-E pinching temperatures were ~ 160 ºC and ≥ 180 ºC: given deviations in temperature measurements in different tests this seems self-consistent findings. Presumably the 175 ºC and 185 ºC S-E test samples were above the changeover temperature at zero and low fields < 20 kV/cm approximately.

The interpretation of this change in S-E loop at > 150 ºC, and the changes to dielectric and ferroelectric properties is that a transition from relaxor to ferroelectric phase occurs in (1-x)KBT-xBMT, $x = 0.03$ at temperatures ≥ 150 ºC with increasing field. The thinking is that applied field aligns dipoles to form longer range domains similar to a ferroelectric.

For sample *x* = 0.04, the unipolar strain-temperature data showed more scatter than for *x* = 0.03. Strain increased from ~ 0.1% at 25 ºC to a peak value of ~ 0.17% at 175 ºC and then slightly decreased to a value of 0.16% with further increase of temperature to 185 ºC. The latter decrease may be due to the lower T_d (dP/dT) for *x* = 0.04 as described above.

This retention of high strain compares well to other Pb-free piezoelectrics, including a number of KNN-based materials, as discussed in Chapter 11.

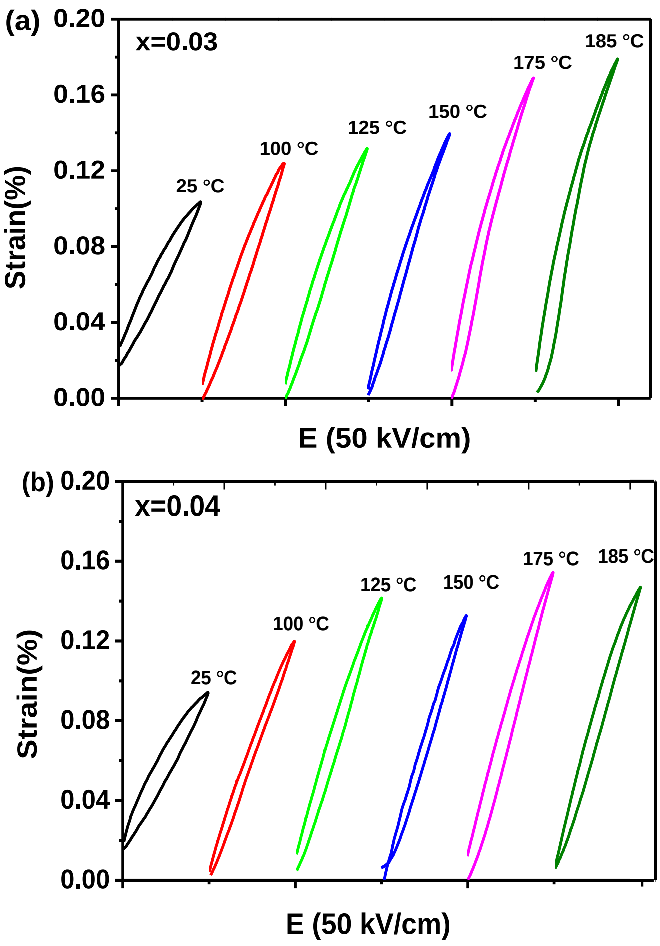

Figure 4.22 Unipolar strain curves versus temperature measured at 50 kV/cm (1 Hz) for poled samples: (a) *x* = 0.03 and (b) *x* = 0.04.

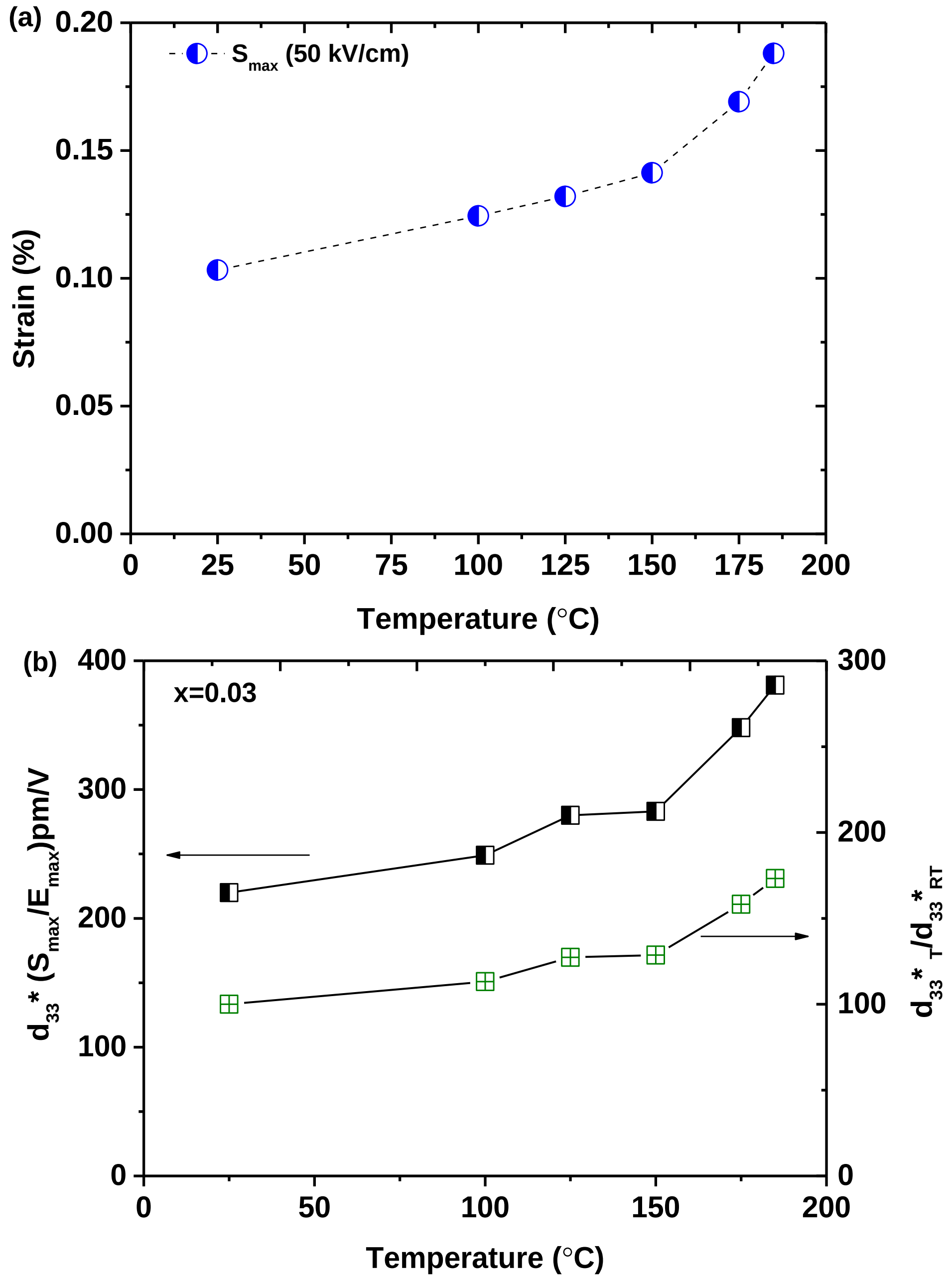

Figure 4.23 (a) Temperature dependent unipolar strain, S_{max}(%) at 50 kV/cm (1 Hz), (b) variation of effective d_{33}* (S_{max}/E_{max}) and normalized, $d_{33}*T/d_{33}*RT$ versus temperature for *x* = 0.03.

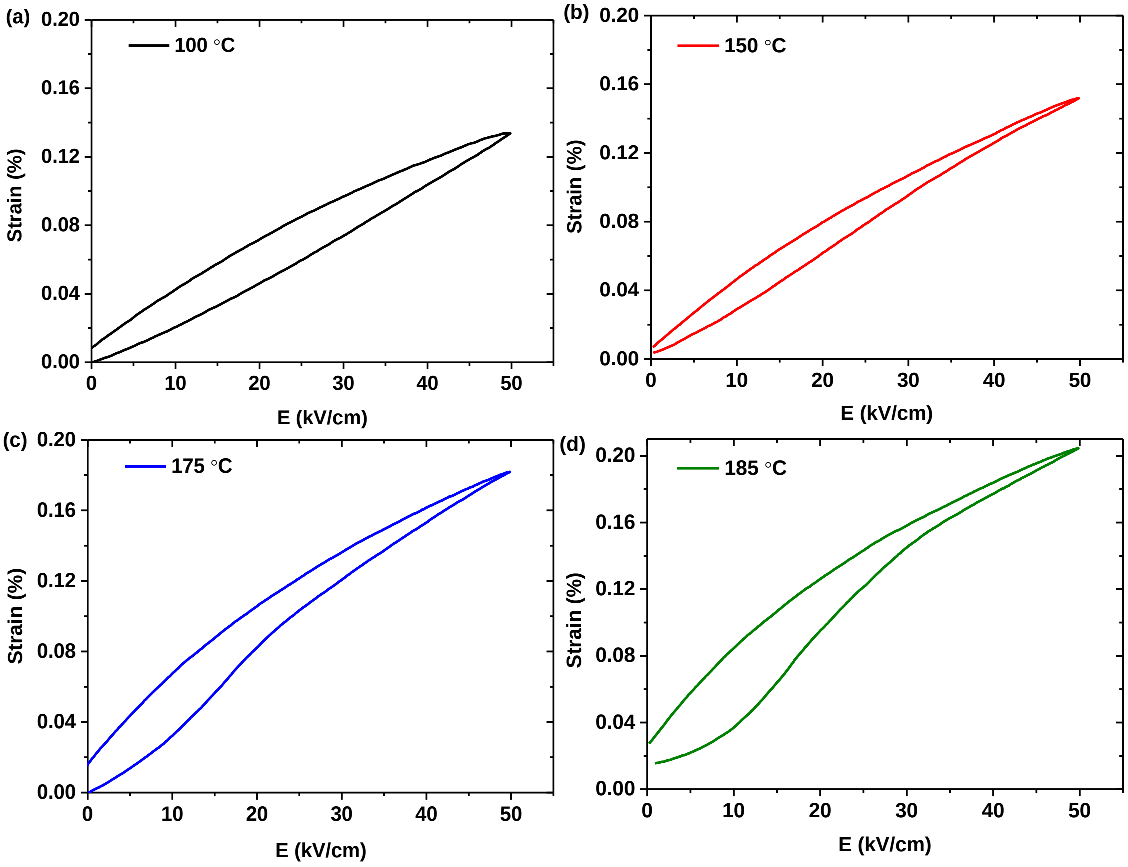

Figure 4.24 Unipolar strain versus temperature for *x* = 0.03 indicating a tear-drop like behaviour at temperature ≥ 175 °C.

4.2.9 Aging Study (room-temperature)

The effect of aging-time (room-temperature in air) was studied by measuring the unipolar strains for *x* = 0.03 and 0.04 over the time period 0-45 days (where 0 represents the normal measurement 24 h after poling). For composition *x* = 0.03, the value of unipolar strain was ~ 0.12% (50 kV/cm) at un-aged condition (0 day). As the project developed it became apparent that the equipment occasionally gave unreliable readings. This was also noted by colleagues working with other materials. A 0.02% relative error mentioned earlier in this chapter relates to repeat measurements whilst the pellets remains in the rig. It is possible that extra error occurs by inconsistency in locating pellets in the rig, or by inconsistencies concerning the electromechanical linkage used to measure dimensional changes. The plots shown in Figure 4.25(b) and (d) show scatter but no falling trend. Longer term ageing tests would be important in future, as would multicycle fatigue testing. The latter could not be carried out due to software problems.

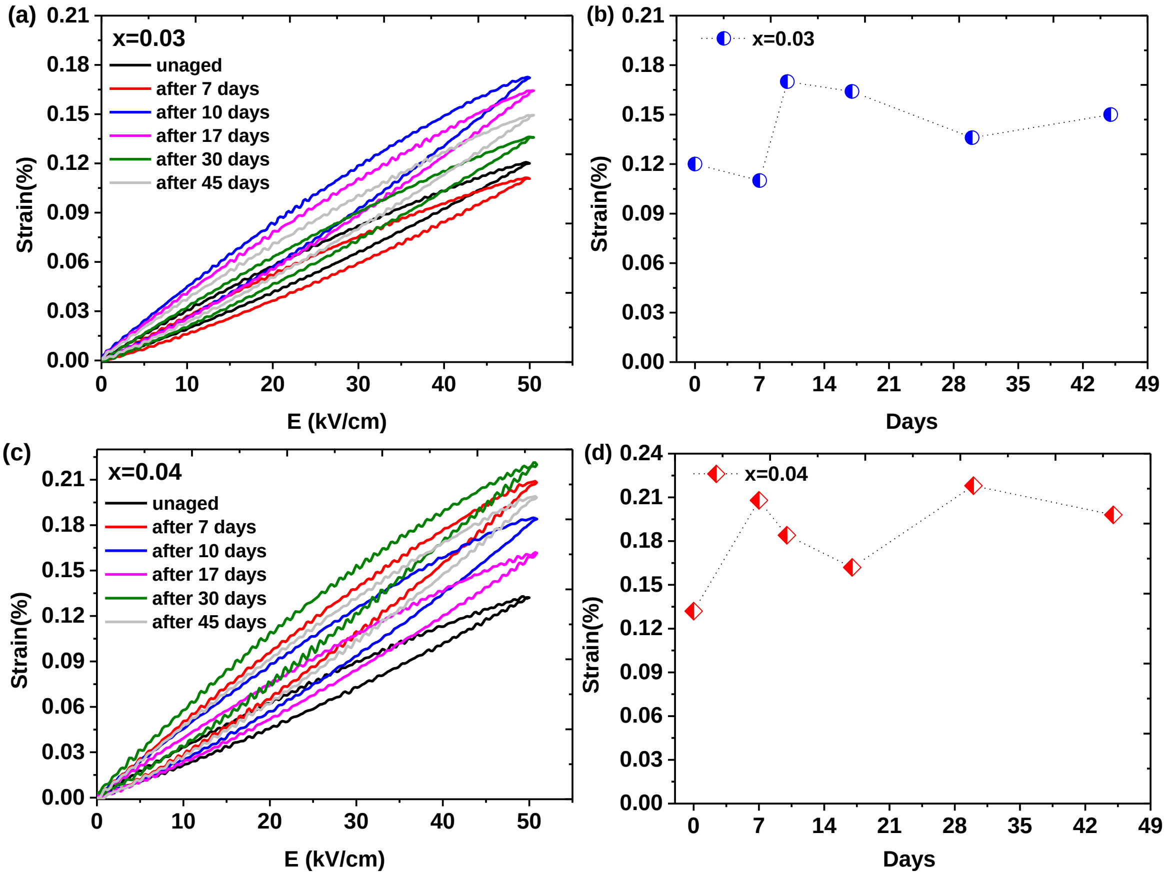

Figure 4.25 Electric field induced unipolar strain for unaged and aged ceramic samples: (a-b) x = 0.03 and (c-d) x = 0.04.

4.2.10 XRD of Poled Samples

For this experiment pellets were electroded using air-drying silver paint, so the electrode could be removed without grinding after poling. Grinding to remove normal fired-on silver introduces strain which changes the diffraction patterns. Instead acetone was used to remove the air-dried electrodes. The results are shown in Figure 4.26.

There was peak broadening due to strain in poled ceramic samples. Poling relative increase in intensity of {002} tetragonal peaks confirmed the effectiveness of poling. The position of the MPB did not appear to change in poled samples (although broadening prevented accurate analysis).

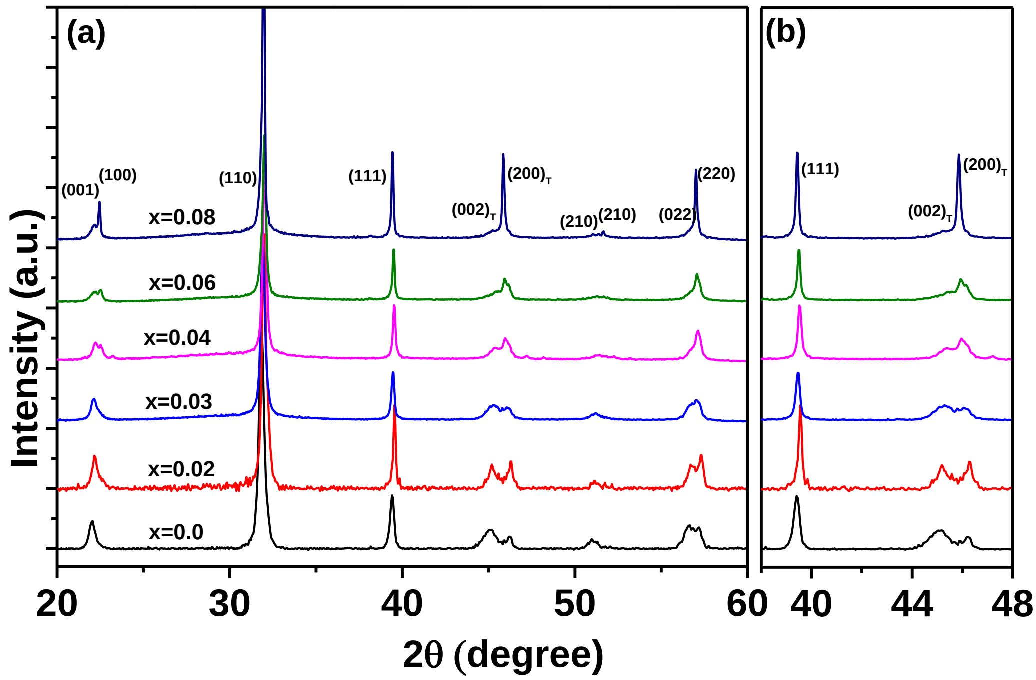

Figure 4.26 (a) Room temperature XRD patterns for poled ceramic samples of (1-*x*)KBT-*x*BMT (*x* = 0-0.08) with (b) highlighted 111 and 002/200 peaks.

Table 4.2 Summary Table of Dielectric, Ferroelectric and Piezoelectric properties of (1-*x*)KBT-*x*BMT system.

Parameters	$x = 0$	0.02	0.03	0.04	0.06	0.08
T_m (ºC, 1 kHz)	380	330	334	336	333	308
ε_r (20 ºC, 1 kHz)	620	1020	1050	1050	1190	1015
$\varepsilon_{r\ max}$ (1 kHz)	4080	5070	5970	6240	5840	5220
tanδ (20 ºC, 1 kHz)	0.04	0.07	0.06	0.06	0.07	0.07
P_r (µC/cm^2)	4.1	5.5	13.5	18	18	11
E_c (kV/cm)	-	-	25	28	23	20
d_{33} (pC/N)	44	59	147	133	100	60
k_p	0.16	0.16	0.18	0.15	0.11	-
T_d (ºC) from k_p-T		-	220	200	-	-
Bipolar strain (%, 50 kV/cm)	0.04	0.07	0.25	0.35	0.32	0.23
d_{33}^*(pm/V)	87	137	520	760	660	490
Unipolar strain (%, 80 kV/cm)	0.15	-	0.30	0.32	0.23	-
d_{33}^*(pm/V) unipolar	190	-	370	406	288	-

4.2.11 Microstructural analysis

Microstructural information was obtained for polished and thermally etched samples. The grain size was estimated by the linear intercept method. Figure 4.27 shows the SEM micrographs for samples x = 0, 0.04, 0.06 and 0.08. Average grain size (estimated) increased from ~ 0.5 µm for x = 0 (KBT) to ~ 1 µm for solid solutions $x \geq 0.02$. The geometric densities were 5.1 g/cm^3 for KBT, and 5.6-5.8 g/cm^3 for the x = 0.03-0.08 samples, Table 4.3, representing ~ 90-94% of theoretical density (estimate based on assumed unit cell contents, Table A3 and A4, Appendix).

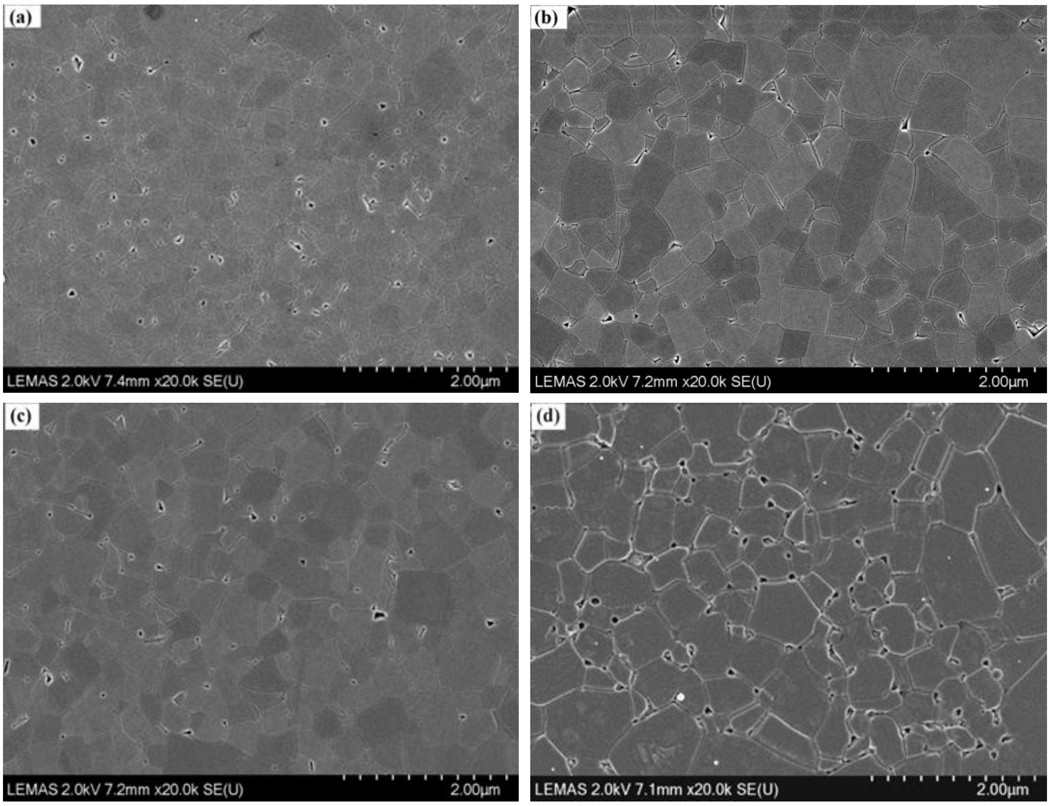

Figure 4.27 Microstructure from SEM micrographs for (1-*x*)KBT-*x*BMT:(a) *x* = 0, (b) *x* = 0.04, (c) *x* = 0.06 and (d) *x* = 0.08.

Table 4.3 The average grain size and geometrical densities for (1-*x*)KBT-*x*BMT system.

Composition(x)	Ave. grain size (µm)	Density (g/cm^3)
$x = 0$	0.5	5.13
$x = 0.02$	1	5.52
$x = 0.03$	1	5.64
$x = 0.04$	1	5.78
$x = 0.06$	1	5.86
$x = 0.07$	1	5.80
$x = 0.08$	1	5.84

4.2.12 Conclusions

The novel solid solution system (1-*x*)KBT-*x*BMT offers very favourable piezoelectric properties with high depolarisation temperature. The phase diagram based on the high temperature XRD revealed a morphotropic phase boundary, MPB, for $x \sim 0.03$, between tetragonal and mixed tetragonal+pseudocubic phase fields.

The highest values of piezoelectric charge coefficient, d_{33} and electric field-induced strains were found in biphasic compositions located close to the MPB. The speculative reason for this may be that the contraction in ***c/a*** ratio of the tetragonal phase (from 1.020 in KBT, $x = 0$ to 1.015 for $x = 0.03$) brings a decrease in coercive field which facilitates polar reorientation; also it seems the presence of a small amount of cubic phase may allow easier realignment of tetragonal polar regions (domains) i.e. increases extrinsic contribution to piezoelectric properties. In combination these factors enhance measured d_{33} and strain values. At $x > 0.04$ ***c/a*** decreases further, as does the amount of tetragonal phase, so piezoelectric properties decline.

The MPB between tetragonal and biphasic is almost vertical, varying from $0.025 < x < 0.03$ (room temperature) and $0.02 < x < 0.025$ at ~ 300 ºC. The boundary between mixed and cubic phase at $x \sim 0.08$ is also nearly vertical. Maximum d_{33} values were 150 pC/N for $x = 0.03$, with bipolar positive strains of 0.25% (E_{max} = 50 kV/cm, 1 Hz), and unipolar strains of 0.30% (Leeds, E_{max} = 80 kV/cm, 1 Hz). At 50 kV/cm the strain was ~ 0.14% (Leeds data) and 0.11% (Tsinghua). The $x = 0.04$ composition gave d_{33} = 133 pC/N, bipolar strain of 0.35% and unipolar strains of 0.30%. These values are competitive with other lead-free piezoceramics.

It became apparent during the research and from discussions with other users of the strain measurement equipment, there was a large variation in strain values between repeat measurements, Multiple repeat measurements suggested a variation of 25%

(relative error). The duplicate measurements in Tsinghua were ~ 25% below Leeds' maximum values. Hence, the lowest repeat values from Leeds is quoted as a reliable value.

The temperature stability of properties was determined using a variety of techniques. Unipolar strain values of ~ 0.18% were measured for x = 0.03 at a temperature of 185 ºC (maximum temperature tested). The depolarisation temperature, T_d obtained from k_p-T and thermally stimulated charge decay measurements was ~ 220 ºC for x = 0.03 and ~ 200 ºC for x = 0.04. These depolarisation temperatures are ~ 100 ºC higher than for the widely cited NBT-BT morphotropic phase boundary system, and 50 ºC higher than NBT-KBT lead-free piezoceramics. The high T_d and retention of piezoelectric properties to > 150 ºC is potentially useful for lead-free actuator and sensor devices.

Chapter 5

Dielectric, Ferroelectric and Piezoelectric Properties of the $K_{0.5}Bi_{0.5}TiO_3$-$Ba(Zr_{0.2}Ti_{0.8})O_3$ Ceramic System

5.1 Summary

This chapter focusses on the dielectric, ferroelectric and piezoelectric properties in the ceramic system, $(1\text{-}x)K_{0.5}Bi_{0.5}TiO_3\text{-}xBa(Zr_{0.2}Ti_{0.8})O_3$. The properties of relaxor ceramics in the compositional series $(1\text{-}x)K_{0.5}Bi_{0.5}TiO_3\text{-}xBa(Zr_{0.2}Ti_{0.8})O_3$, abbreviated as (1-*x*)KBT-*x*BZT have been investigated. Composition $x = 0$ was tetragonal; changed to mixed phase (tetragonal+cubic) at $0.05 \leq x \leq 0.4$ and then single phase cubic for compositions $x \geq 0.5$.

Values of T_m, the temperature of maximum relative permittivity, decreased from ~ 380 ºC at $x = 0$ to below room-temperature, -10 ºC, for $x = 0.8$. Compositions $x = 0.1$ and 0.2 were piezoelectric and ferroelectric. The maximum value of d_{33} piezoelectric charge coefficient, 130 pC/N, and bipolar strain, 0.13%, occurred at $x = 0.1$.

Values of k_p were 0.16 at room temperature for compositions $x = 0$ and 0.1. The variation of k_p versus temperature suggested a depolarisation-temperature ~ 220 ºC for $x = 0.1$, consistent with results from high-temperature X-ray diffraction indicating a transition to single-phase cubic at ≥ 250 ºC.

5.2 Results and discussion

5.2.1 Phase analysis

X-ray diffraction patterns for the crushed sintered pellets of the (1-*x*)KBT-*x*BZT compositional series are shown in Figure 5.1. All studied compositions in the solid solution were single phase perovskites. Composition $x = 0$ (KBT) was tetragonal at room temperature. A close analysis for composition $x = 0.05$ revealed a cubic phase coexistence with tetragonal phase. For compositions $0.1 \leq x \leq 0.4$, an extra reflections in ~ 45 °2θ range signified a phase coexistence region of tetragonal and cubic phases. The (1-*x*)KBT-*x*BZT solid solution, for compositions $0.5 \leq x \leq 1$ had single-phase cubic.

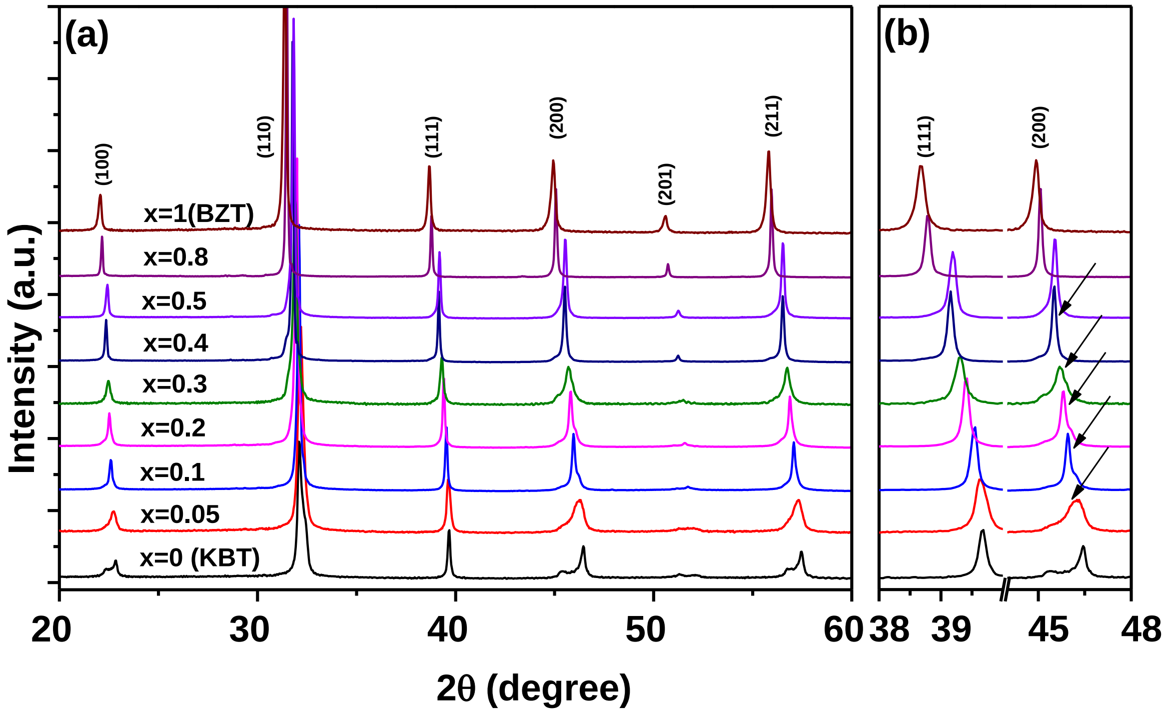

Figure 5.1 (a) X-rays diffraction patterns for the (1-*x*)KBT-*x*BZT ceramic system at room temperature (b) {111} and {200} peaks highlighted (arrows indicate the cubic phase coexisted with tetragonal phase).

Lattice parameters of the (1-*x*)KBT-*x*BZT ceramic system were deduced from the XRD patterns by least square refinement method are plotted as *x*BZT, Figure 5.2. The tetragonal lattice parameters changed from ***a*** = 3.907±0.002 Å and ***c*** = 3.979±0.003 Å for *x* = 0 [Chapter 4], to ***a*** = 3.911±0.003 Å and ***c*** = 3.986±0.002 Å for *x* = 0.05. Adding BZT content from 10 mol% to 40 mol% led to further decrease of ***c/a*** ratios. Compositions of cubic structure, 0.5 ≤ *x* ≤ 1 had lattice parameter ***a*** increasing linearly from 3.999±0.004 Å for *x* = 0.5 to 4.033±0.002 Å for *x* = 1.

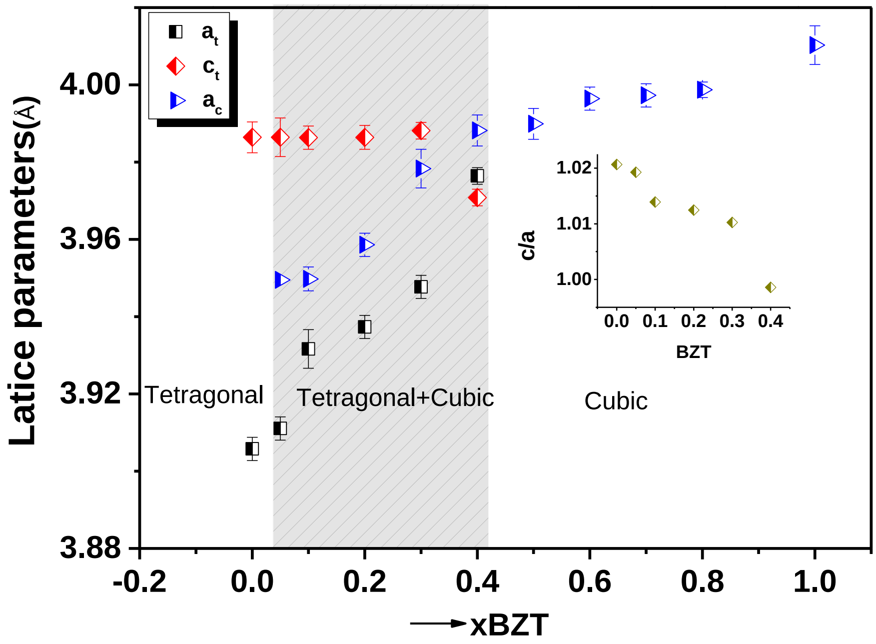

Figure 5.2 Variation of room temperature lattice parameters as a function of *x*BZT for (1-*x*)KBT-*x*BZT ceramic system (inset show *c/a* ratios).

5.2.2 High Temperature XRD and Phase Diagram

Figure 5.3 indicate the high temperature X-ray diffraction patterns for compositions *x* = 0-0.2. The end member KBT (*x* = 0) retained its tetragonal structure from room temperature up to < 280 ºC, then changed to mixed phase tetragonal+cubic at temperature ≥ 280 ºC and become cubic at ≥ 320 ºC, Figure 5.3(a) [as discussed in

Chapter 4]. Composition x = 0.05 was mixed phase tetragonal+cubic at room temperature and change to cubic at a temperature ≥ 250 ºC. Samples x = 0.1 and 0.2 indicated mixed phase tetragonal+cubic from room temperature to a temperature of < 250 ºC.

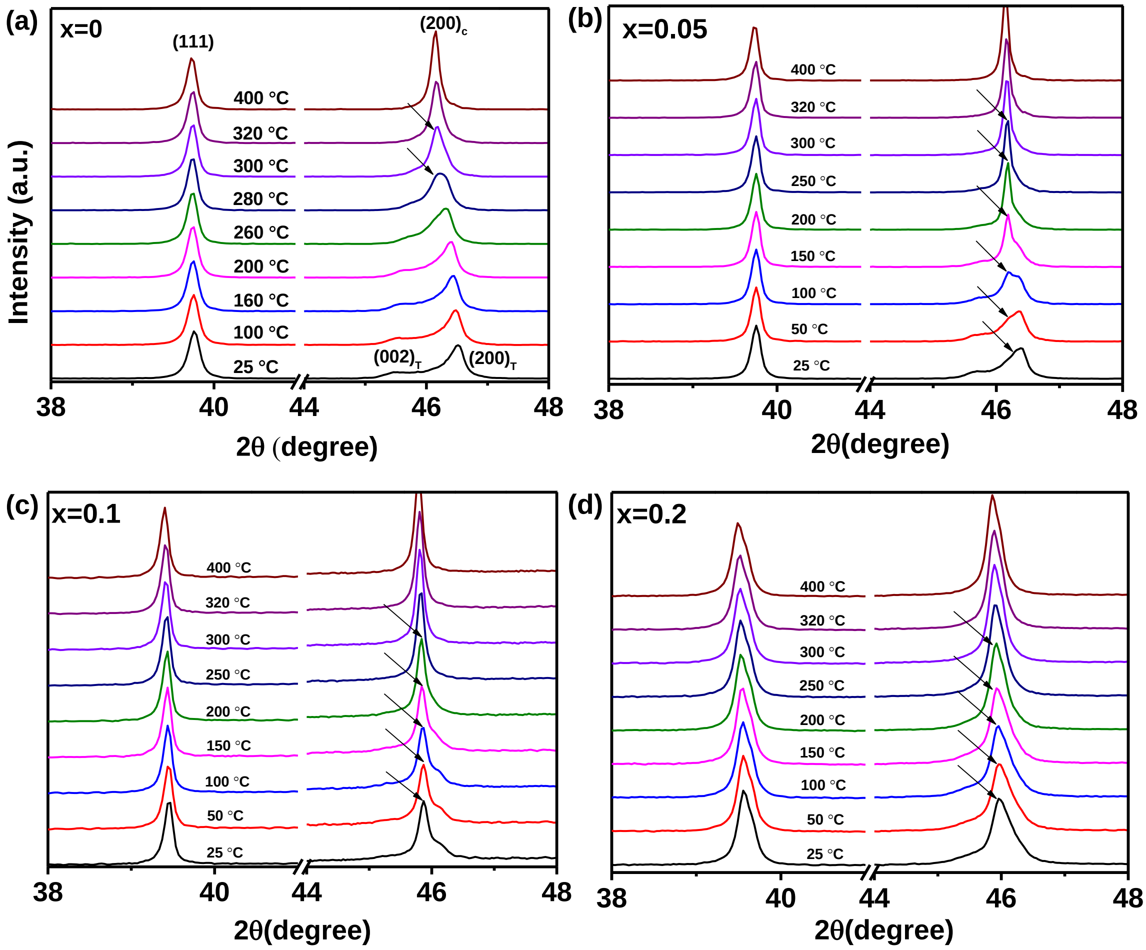

Figure 5.3 High temperature XRD patterns in 38-48 º2θ range for (a) x = 0 (b) x = 0.05 (c) x = 0.1 and (d) x = 0.2 (arrows indicating cubic phase between tetragonal peaks).

Lattice parameters as function of temperature for samples x = 0-0.2 are presented in Figure 5.4. The measured lattice parameters for x = 0 were $\boldsymbol{a}$ = 3.907±0.002 Å and $\boldsymbol{c}$ = 3.979±0.003 Å at room temperature changed to $\boldsymbol{a}$ = 3.928±0.003 Å, $\boldsymbol{c}$ = 3.944±0.002 Å at 300 ºC [as discussed in Chapter 4]. For composition x = 0.05, the tetragonal lattice parameters converged from $\boldsymbol{a}$ =

3.926±0.001 Å and ***c*** = 3.987±0.002 Å at room temperature to ***a*** = 3.939±0.003 Å and ***c*** = 3.970±0.001 Å at ~ 250 ºC. Similar trend was observed for *x* = 0.1, with tetragonal contraction (***c/a*** ratio) from ~ 1.014±0.002 at room temperature to ~ 1.006±0.003 at ~ 200 ºC.

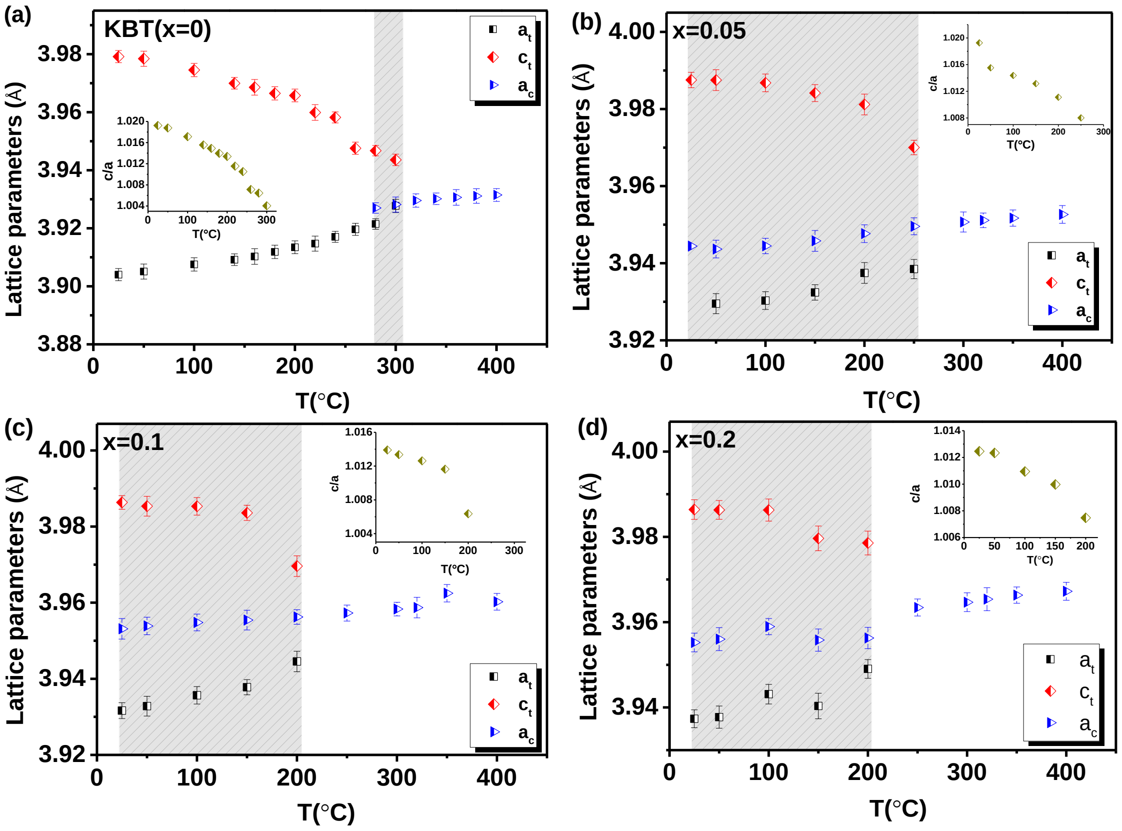

Figure 5.4 Variation of lattice parameters as a function of temperature for KBT-*x*BZT: (a) *x* = 0, (b) *x* = 0.05 (c) *x* = 0.1 and (d) *x* = 0.2 (shaded regions indicate mixed phase tetragonal+cubic phase and insets show *c/a* ratio).

Based on the high temperature XRD data, phase diagram have been constructed for (1-*x*)KBT-*x*BZT, *x* ≤ 0.2. Figure 5.5 displays temperature-composition dependence phase transitions from tetragonal to mixed phase tetragonal+cubic and then cubic for compositions *x* ≤ 0.2. The phase transition from tetragonal to mixed phase tetragonal+cubic take place at ~ 280 ºC for composition *x* = 0 and at room temperature for *x* = 0.05. Other compositions *x* = 0.1 and 0.2 also exhibited mixed phase tetragonal+cubic from room temperature up to ~ 200 ºC. Therefore, the phase boundary between the tetragonal and mixed phase tetragonal+cubic was nearly vertical and varies only by ≤ 0.05% over the temperature range from 25 ºC to ~ 280 ºC. The compositions (*x* = 0.1 and 0.2) located at this phase boundary exhibited favourable electromechanical properties.

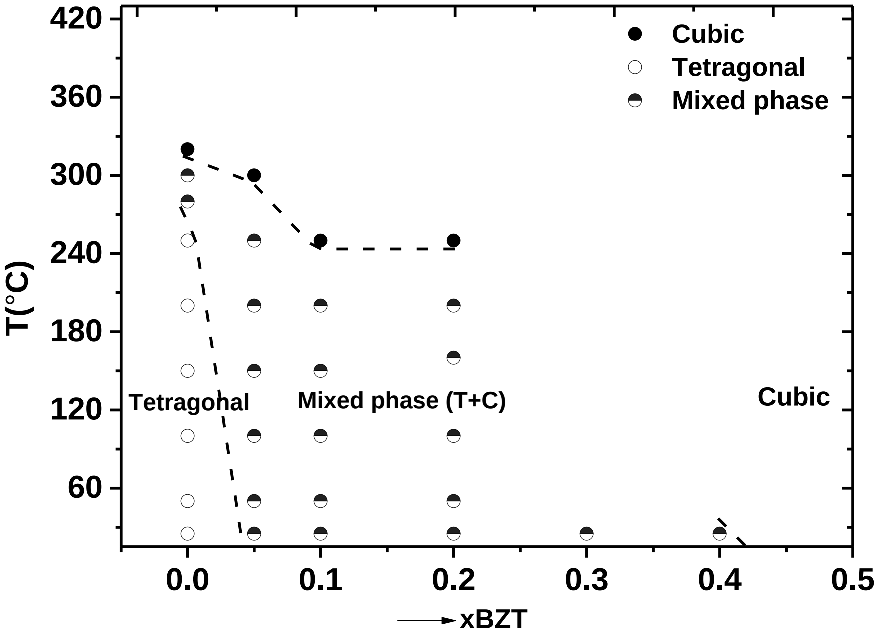

Figure 5.5 Temperature-composition dependent phase transitions for (1-*x*)KBT-*x*BZT, *x* ≤ 0.2 based on high temperature XRD data.

The data of the following sections is summarised in Table 5.1.

5.2.3 Dielectric properties

Plots of relative permittivity, ε_r, and tanδ versus temperature at different frequencies for the (1-*x*)KBT-*x*BZT system are shown in Figure 5.6 and 5.7. The ε_r-T plot for KBT (*x* = 0) showed diffuse peaks, with T_m ~ 380 ºC, (1 kHz) [as discussed in chapter 4]. The ε_r-T plot for *x* = 0.05 was similar to KBT, but T_m was slightly lower, 370 ºC, Figure 5.6(b). A much stronger frequency-dependence in T_m values was observed for compositions *x* ≥ 0.1, Figure 5.8. This, together with the relaxation in tanδ at temperatures around T_m, is typical of a relaxor dielectric. The change in frequency-dependence of T_m as the BZT constituent increased from $x = 0.05$ to 0.1 correlates to the emergence of the cubic phase as the dominant phase in XRD patterns (Figure 5.1).

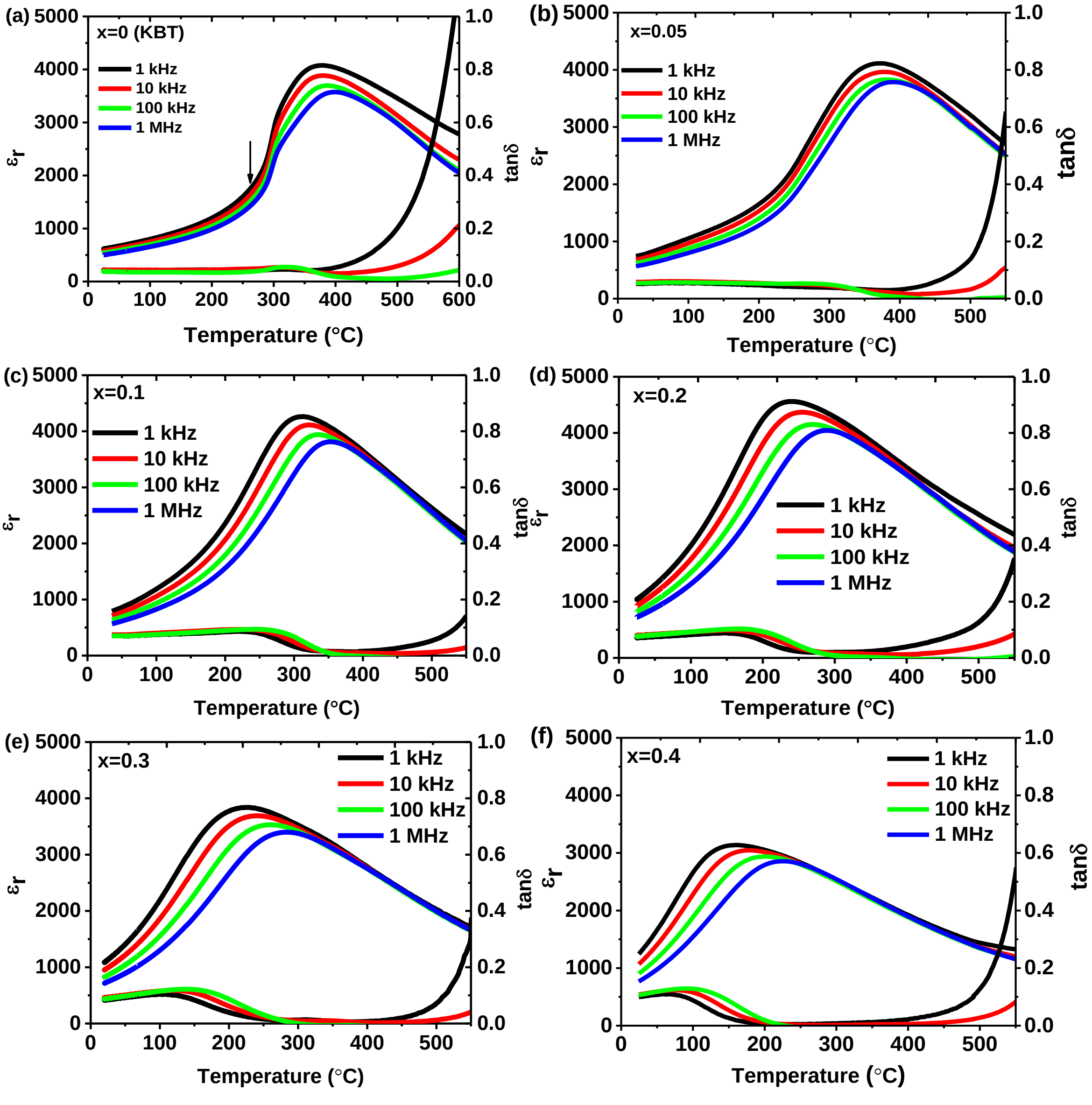

Figure 5.6 Relative permittivity and loss tangent as a function of temperature at different frequencies for (a) $x = 0$ (arrow indicate inflection), (b) $x = 0.05$, (c) $x = 0.1$, (d) $x = 0.2$, (e) $x = 0.3$ and (f) $x = 0.4$ (continued over leaf).

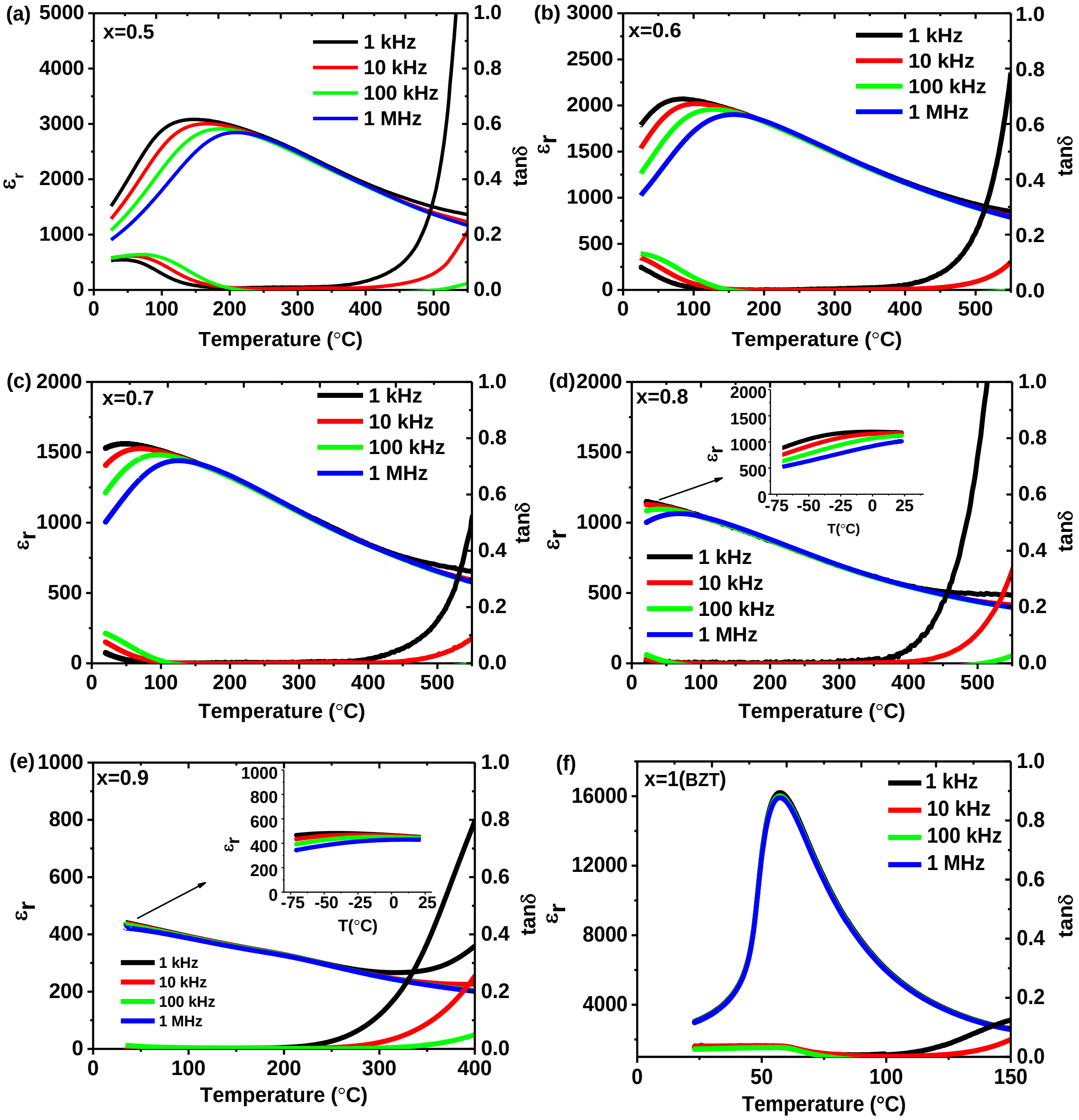

Figure 5.7 Relative permittivity and loss tangent as a function of temperature at different frequencies for: (a) *x* = 0.5, (b) *x* = 0.6, (c) *x* = 0.7, (d) *x* = 0.8, (e) *x* = 0.9 and (f) *x* = 1 (insets show ε_r-T from -70 ºC to 25 ºC).

Room temperature relative permittivity was ~ 700 for *x* = 0.1, and ~ 1000 for *x* = 0.2 (1 kHz); with tanδ (25 ºC) values of 0.06-0.07 (1 kHz). Higher values of tanδ ~ 0.1, were recorded for compositions $0.4 \leq x \leq 0.6$: this is due to the effects of the relaxor loss tangent dispersion peak as T_m decreased. Peak values of relative permittivity decreased from $\varepsilon_{r\ max}$ ~ 4000 (1 kHz) for $x \leq 0.2$, to ~ 3000 for $0.3 \leq x \leq 0.5$, and then to ≤ 1500 at $x \geq 0.6$, Figure 5.6 and 5.7. The trend of falling T_m with increasing *x*BZT was such that T_m decreased to -10 °C for $x = 0.8$, Figure 5.9. Plot of relative permittivity versus temperature for the BZT ($x = 1$) displayed a broad peak at 50 °C with no frequency dispersion; behaves as a diffuse ferroelectric (T_c ~ 50 °C).

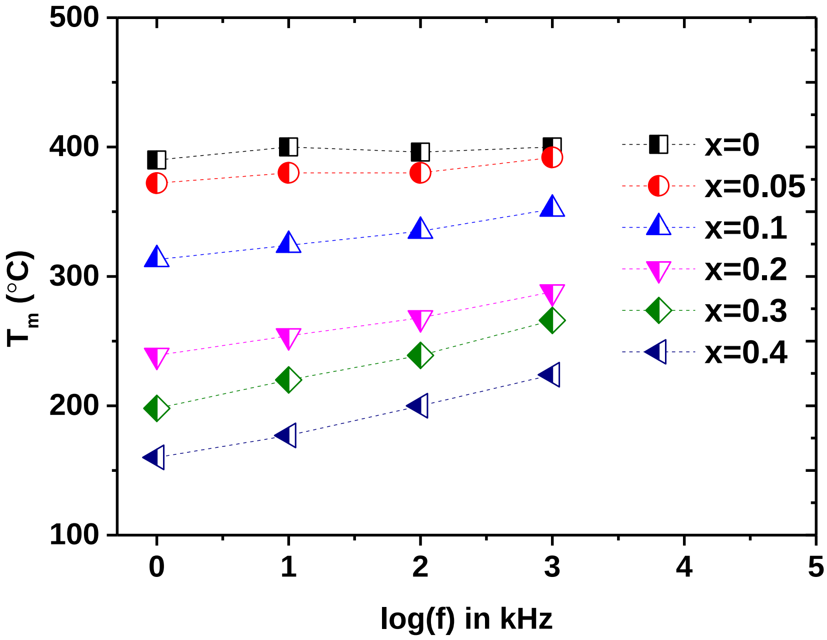

Figure 5.8 Temperature of maximum relative permittivity, T_m versus log frequency for x = 0-0.4BZT.

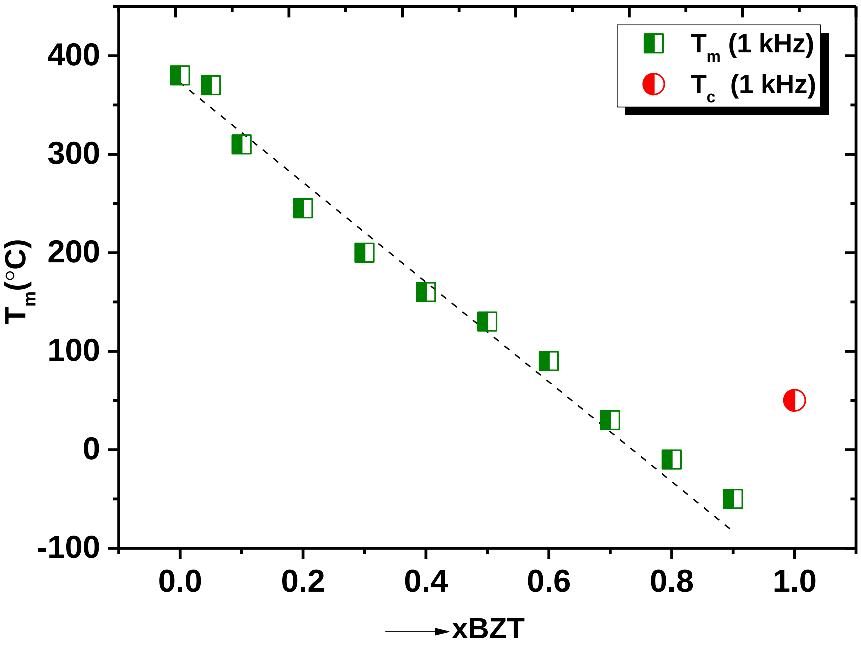

Figure 5.9 Temperature of maximum relative permittivity as a function of *x*BZT.

5.2.4 Ferroelectric Properties

Polarisation hysteresis loops versus electric field of the (1-*x*)KBT-*x*BZT system measured at room temperature (60 kV/cm, 1 Hz), Figure 5.10. Sample x = 0 and 0.05, exhibited no polarisation switching at field of 60 kV/cm. Compositions x = 0.1 and 0.2 were ferroelectric; remanent polarization, P_r, values were ~ 12 μC/cm^2 and ~ 14 μC/cm^2 with coercive fields, E_c ~ 30 kV/cm and ~ 20 kV/cm respectively, Table 5.1. Compositions $0.3 \leq x \leq 0.5$ exhibited slim P-E loops with little evidence of ferroelectric character. Linear P-E response of typical of dielectric capacitor was observed for samples x = 0.6-0.9. The BZT (x = 1) showed a P-E response like a pinch shape with remanent polarisation, P_r ~ 8 μC/cm^2 at coercive field of 50 kV/cm, Figure 5.10(d).

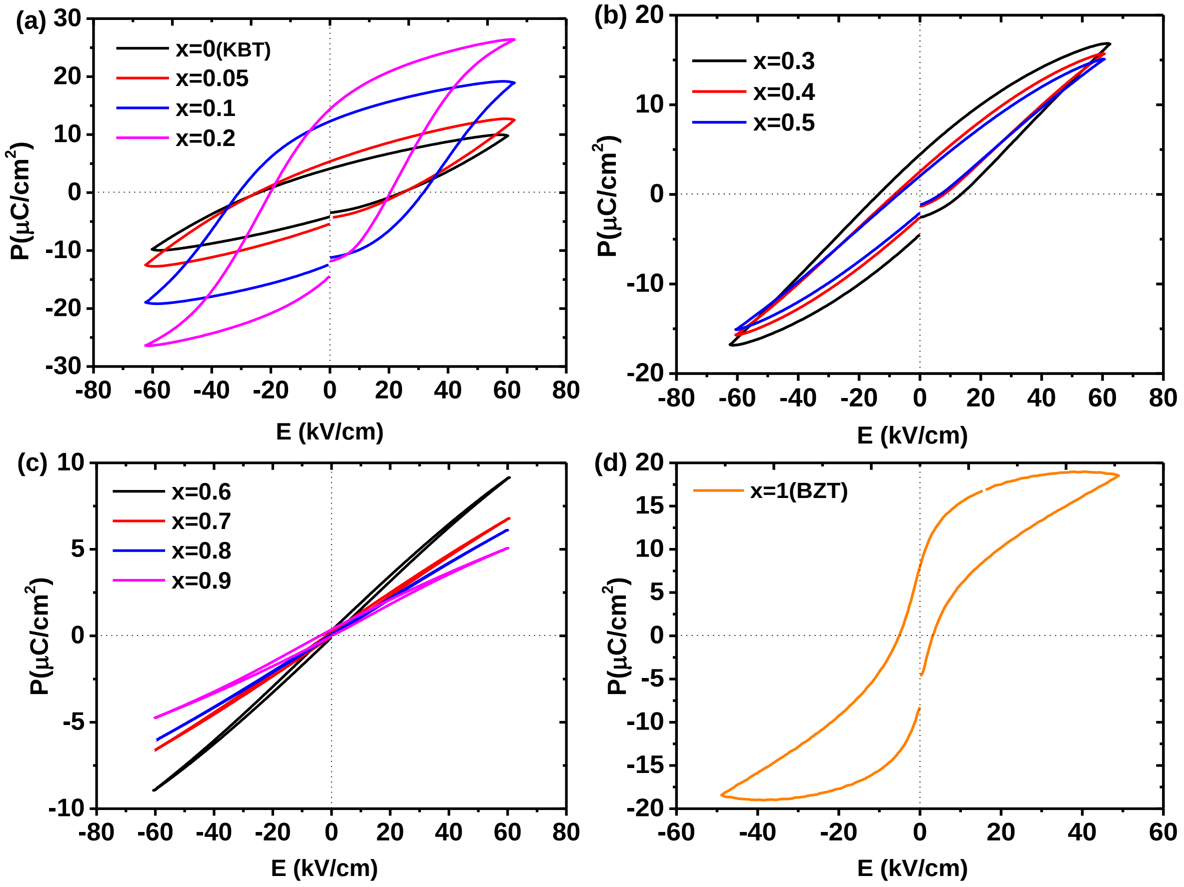

Figure 5.10 Polarisation-electric field response for (a) *x* = 0-0.2, (b) *x* = 0.3-0.5, (c) *x* = 0.6-0.9 and (d) *x* = 1 (BZT).

5.2.5 Electromechanical Properties

Figure 5.11 shows the bipolar electromechanical strain curves for the (1-*x*)KBT-*x*BZT ceramic system. Sample *x* = 0 and 0.05 exhibited a negative strain but with no classic butterfly shape like loops with strain of ~ 0.05% at 60 kV/cm. A typical butterfly loops were observed for compositions *x* = 0.1 and 0.2. Composition *x* = 0.1 had maximum strain value ~ 0.13%, with d_{33}^* ~ 200 pC/N (S_{max}/E_{max}) and 0.14%, and d_{33}^* ~ 230 pC/N (S_{max}/E_{max}) for *x* = 0.2, Figure 5.11(a). Negative strains recorded for *x* = 0.1 and 0.2 samples, were of the order of ~ 0.07% and 0.05% respectively consistent with piezoelectric behaviour. Other compositions $0.3 \leq x \leq 0.9$ were non-piezoelectric, displayed an electrostrictive behaviour with strain values ≤ 0.08%, Figure 5.11(b).

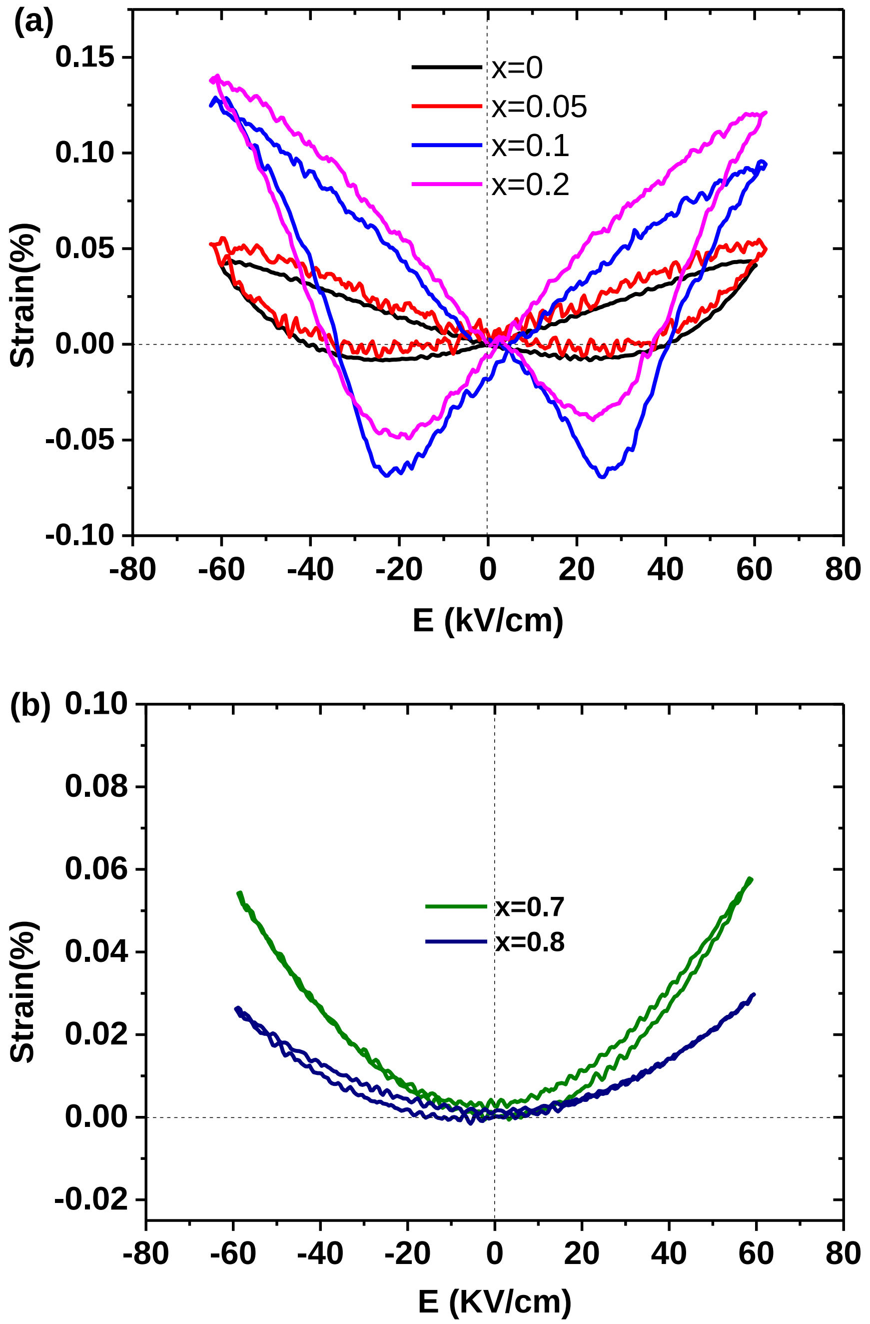

Figure 5.11 Electromechanical strain response for: (a) *x* = 0-0.2 and (b) *x* = 0.7-0.8.

5.2.6 Measurement of Piezoelectric Charge Coefficient(d_{33})

Samples of the (1-*x*)KBT-*x*BZT ceramic system were poled in silicon oil at a temperature of ~ 50 ºC at an applied field of ~ 40 kV/cm. Poling at high fields > 40 kV/cm and temperature (> 50 ºC) led to the breakdown of the samples. Trends in measured d_{33} values from composition *x* = 0 to *x* = 0.5 are shown in Figure 5.12.

Values of piezoelectric charge coefficients, d_{33} were increased from 44 pC/N for $x = 0$ (KBT) to a peak of 130 pC/N for $x = 0.1$, Table 5.1. For composition $x = 0.2$, value of piezoelectric charge coefficient, d_{33} was ~ 100 pC/N and then dropped sharply to $\leq$ 10 pC/N for compositions $x \geq 0.3$. Hence, the optimum ferroelectric and piezoelectric properties in (1-x)KBT-xBZT occurred around the changeover in phase content from tetragonal to mixed phase (tetragonal+cubic) for $x = 0.1$.

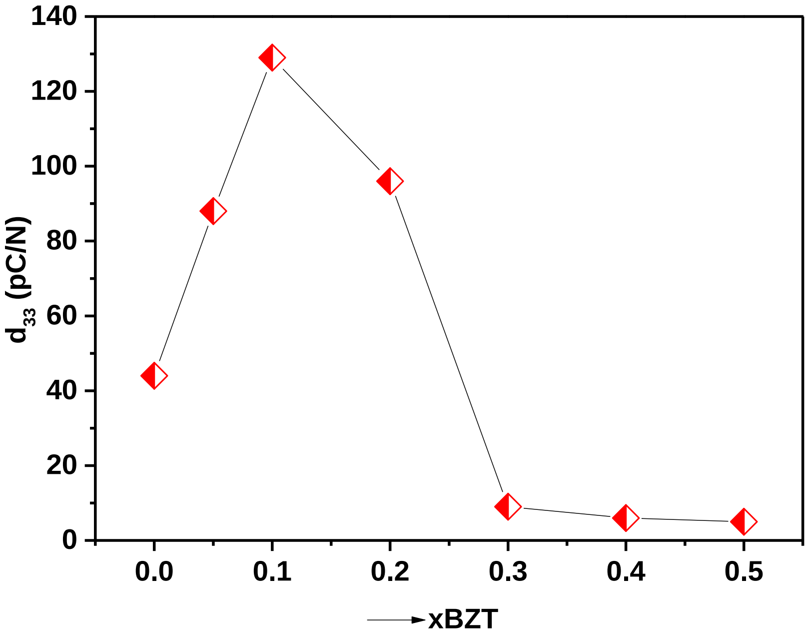

Figure 5.12 Variation of piezoelectric charge coefficient, d_{33} versus *x*BZT (x = 0-0.5).

5.2.7 Electromechanical coupling factor (k_p)-Temperature

Figure 5.13 shows the electromechanical coupling coefficient, k_p as a function of temperature for samples $x = 0$, 0.1 and 0.2. Values of k_p at room temperature were ~ 0.16 for samples $x = 0$ and 0.1, and $k_p = 0.12$ for $x = 0.2$. On increasing temperature, a slight increase in the k_p values occurred up to temperature of ~ 100 °C for $x = 0$ and ~ 70 °C for $x = 0.1$, then decreased progressively with increase of temperature reaching zero at a temperature ~ 220 °C. The variation of k_p versus temperature for this (1-

x)KBT-*x*BZT samples indicated a similar trend and depolarisation temperature ~ 210-220 ºC as observed for (1-*x*)KBT-*x*BMT system [Chapter 4] but had higher depolarization temperature (T_d) than $Na_{0.5}Bi_{0.5}TiO_3$-$BaTiO_3$ (NBT-BT) (T_d ~ 100 ºC) and $Na_{0.5}Bi_{0.5}TiO_3$-$K_{0.5}Bi_{0.5}TiO_3$ (NBT-KBT) (T_d ~ 170 ºC) MPB compositions [Rödel et al. (2009)].

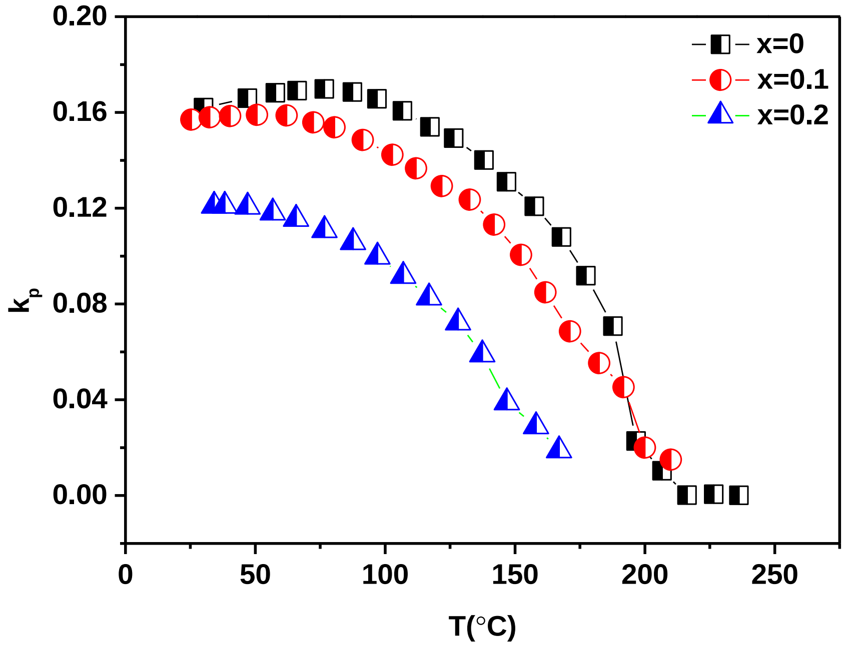

Figure 5.13 Variation of electromechanical coupling factor k_p versus temperature for compositions *x* = 0, 0.1 and 0.2.

Table 5.1 Dielectric, ferroelectric and piezoelectric properties of the (1-*x*)KBT-*x*BZT ceramic system.

Parameters	$x = 0$	0.05	0.1	0.2	0.3	0.4	0.5	0.6	0.7	0.8	0.9	1
T_m (ºC, 1 kHz)	380	370	310	240	220	160	130	90	30	-10	-50	T_c~55
ε_r (25 ºC, 1 kHz)	620	750	780	1040	1080	1240	1510	1790	1540	1140	450	3150
$\varepsilon_{r\ max}$ (1 kHz)	4080	4100	4260	4560	3840	3140	3080	2070	1560	1190	482	16200
tanδ (25 ºC, 1 kHz)	0.04	0.05	0.07	0.07	0.08	0.09	0.1	0.08	0.031	0.003	0.003	0.03
P_r ($\mu C/cm^2$)	4.1	5.4	12.3	14.4	4.5	2.5	-	-	-	-	-	8
E_c (kV/cm)	-	-	30	20	13	8	-	-	-	-	-	5
d_{33} (pC/N)	44	88	130	100	10	-	-	-	-	-	-	-
k_p (25 ºC)	0.16	-	0.15	0.12	-	-	-	-	-	-	-	-
T_d (ºC) k_p-T	210	-	220	-	-	-	-	-	-	-	-	-
Bipolar Strain(%, 50 kV/cm)	0.04	0.06	0.13	0.14	0.08	0.08	0.06	0.06	0.05	0.03	-	-
d_{33}^*(pm/V)	87	100	200	230	-	-	-	-	-	-	-	-

5.2.8 Microstructural analysis

The microstructure of polished and thermally etched ceramic samples was analysed by using SEM. The average grain size was estimated by linear intercept method. The grain size was of the order of ~ 0.5 μm for KBT ($x = 0$), Figure 5.14, increased slightly to ~ 0.7 μm for $x = 0.1$ and then increased to ~ 1 μm for compositions $0.2 \leq x \leq 0.9$. However, an average grain size of ~ 30 μm was observed for BZT ($x = 1$). The densities of sintered ceramic pellets were 90-92% of theoretical. Values of geometrical density were measured for at least three pellets, summarised in Table 5.2.

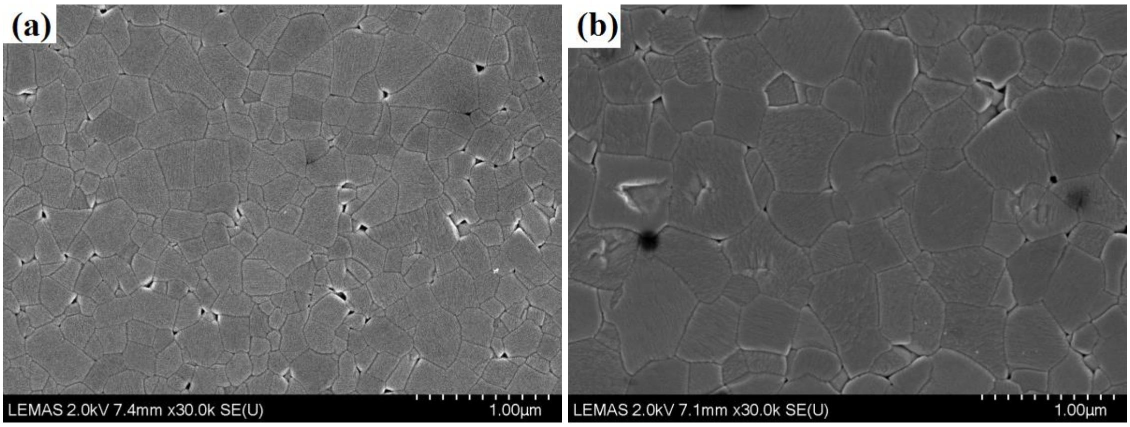

Figure 5.14 SEM micrographs of polished and thermally etched samples for (a) $x = 0$ (b) $x = 0.1$.

Table 5.2 Average grain size and geometrical density for the (1-*x*)KBT-*x*BZT system.

Composition (*x*)	Average grain size (µm)	Density, ρ (g/cm^3)
$x = 0$	0.5	4.9
$x = 0.1$	0.7	5.4
$x = 0.2$	1	5.5
$x = 0.3$	1	5.1
$x = 0.4$	1	5.5
$x = 0.5$	1	5.4
$x = 0.6$	1	5.3
$x = 0.7$	1	5.5
$x = 0.8$	1	5.4
$x = 1$	30	5.1

5.2.9 Conclusions

The solid solution system, (1-*x*)KBT-*x*BZT has been investigated. XRD patterns at room temperature revealed a tetragonal structure for composition $x = 0$. Compositions $0.05 \leq x \leq 0.4$ exhibited a mixed phase tetragonal+cubic. A single phase cubic was obtained for samples $x \geq 0.5$. The temperature of peak relative permittivity, T_m, decreased with increasing levels of BZT, with T_m ~ 380 ºC for $x = 0$, decreasing to T_m ~ -10 ºC for $x = 0.8$.

A narrow range of compositions, $x = 0.1$ and 0.2, were ferroelectric with remanent P_r ~ 12 µC/cm^2 and ~ 14 µC/cm^2, respectively. The maximum piezoelectric charge coefficient, d_{33} was 130 pC/N with bipolar strain 0.13% (S_{max}/E_{max} = 200 pm/V) for $x = 0.1$. The corresponding values for $x = 0.2$ were 100 pC/N and 0.14% (S_{max}/E_{max} = 230 pm/V). Values of k_p were ~ 0.16 for compositions *x* 0 and $x = 0.1$. Based on the k_p-T data, the depolarisation occurred at a temperature (T_d) ~ 220 ºC for composition $x = 0.1$, in contrast to other lead-free NBT-BT piezoelectrics (T_d ~ 100 ºC).

Chapter 6

Dielectric and Ferroelectric Properties of the $(1-x)Ba_{0.8}Ca_{0.2}TiO_3-xBi(Mg_{0.5}Ti_{0.5})O_3$ Ceramic System

6.1 Summary

This chapter describes the dielectric and ferroelectric properties of the $(1-x)Ba_{0.8}Ca_{0.2}TiO_3-xBi(Mg_{0.5}Ti_{0.5})O_3$ ceramic system, abbreviated as $(1-x)$BCT-xBMT. X-ray diffraction data revealed single phase perovskite patterns for compositions $x < 0.6$. Compositions $x = 0$ (BCT) and $x = 0.05$ were tetragonal; a change to single-phase cubic X-ray patterns occurred for $x \geq 0.1$. Compositions $x = 0$ and $x = 0.05$ exhibited typical ferroelectric polarisation-electric field loops, with remanent polarisation, $P_r \sim 12$ μC/cm^2, coercive field, $E_c \sim 7$ kV/cm and ~ 16 kV/cm, respectively.

Dielectric measurements indicated sharp Curie peak at $T_c \sim 130$ ºC for $x = 0$ and a broad peak at ~ 110 ºC for $x = 0.05$. A relaxor behaviour occurred for compositions $x \geq 0.1$. Increasing the BMT content improved the temperature stability of relative permittivity, ε_r at high temperatures. For composition $x = 0.5$, a near plateau in the ε_r-T plot occurred; $\varepsilon_r = 800\pm15\%$, across the temperature range, 40 ºC to 550 ºC, the corresponding loss tangent, tanδ, was ≤ 0.02 for temperatures between 100 ºC and 400 ºC. Composition $x = 0.55$ gave $\varepsilon_r = 950\pm15\%$ over a temperature range from 70 ºC to 600 ºC and loss tangent, tanδ ≤ 0.02 from 160-550 ºC.

Values of dc resistivity for $x = 0.5$ and $x = 0.55$ were ~ 10^9 Ω m at a temperature of 300 ºC, and ~ 10^6 Ω m at 500 ºC. The $(1-x)$BCT-xBMT ($x = 0.5$ and 0.55) ceramic

materials, indicated electrical breakdown to occur at an electric field 258±30 kV/cm for $x = 0.5$ and 204±14 kV/cm for $x = 0.55$.

6.2 Results and discussion

6.2.1 Phase analysis

Room temperature X-ray diffraction patterns for the crushed sintered pellets of the (1-x)BCT-xBMT ceramic system are shown in Figure 6.1. The $x = 0$ (BCT) and $x = 0.05$ compositions were tetragonal perovskite. Further incorporation of BMT content $x \geq 0.1$, induced a change to cubic single-phase XRD patterns with no clear evidence of {200} peak splitting in the peak at ~ 45 °2θ. Secondary peaks of similar d-spacings belong to bismuth oxide [ICDD card number 00-029-0236, Figure A2, Appendix] began to appear for $x = 0.6$ and increased in relative intensity at higher xBMT content.

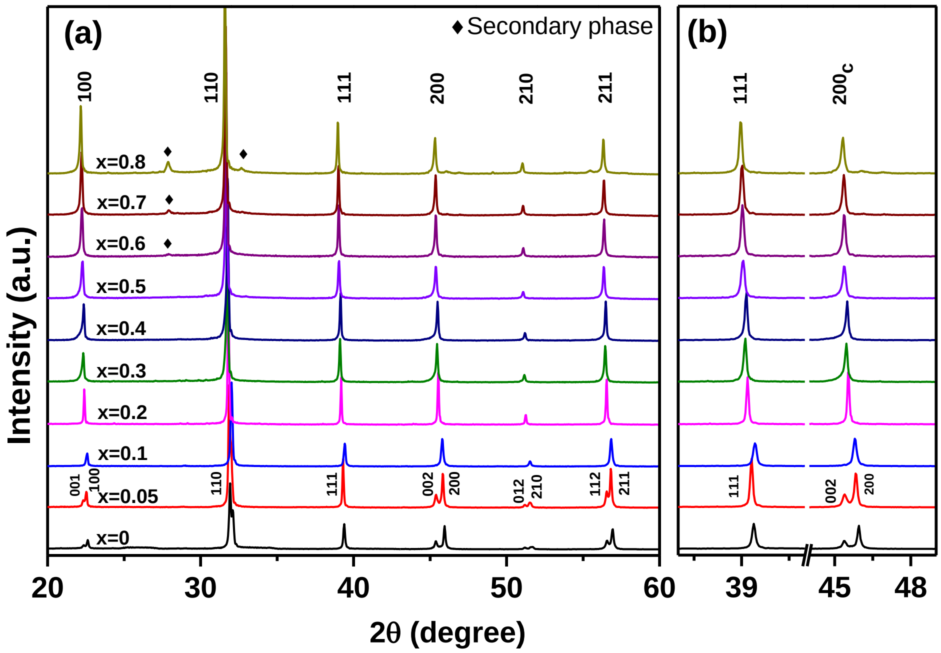

Figure 6.1(a) Room temperature XRD patterns for the crushed sintered pellets of (1-x)BCT-xBMT and (b) highlighted 111_c and 200_c reflections.

Lattice parameters are plotted as a function of *x*BMT content in Figure 6.2. It can be seen from the plot that a slight contraction in tetragonal ***c*** and increase in ***a*** lattice parameters occurred between $x = 0$ and $x = 0.05$, giving overall decrease of ***c/a*** ratio from 1.013±0.003 at $x = 0$ to 1.010±0.003 for $x = 0.05$. For cubic compositions $x \geq 0.1$, a progressive increase in cubic ***a*** lattice parameters from 3.972±0.002 Å at $x = 0.1$ to 3.988±0.003 Å for $x = 0.5$ was observed.

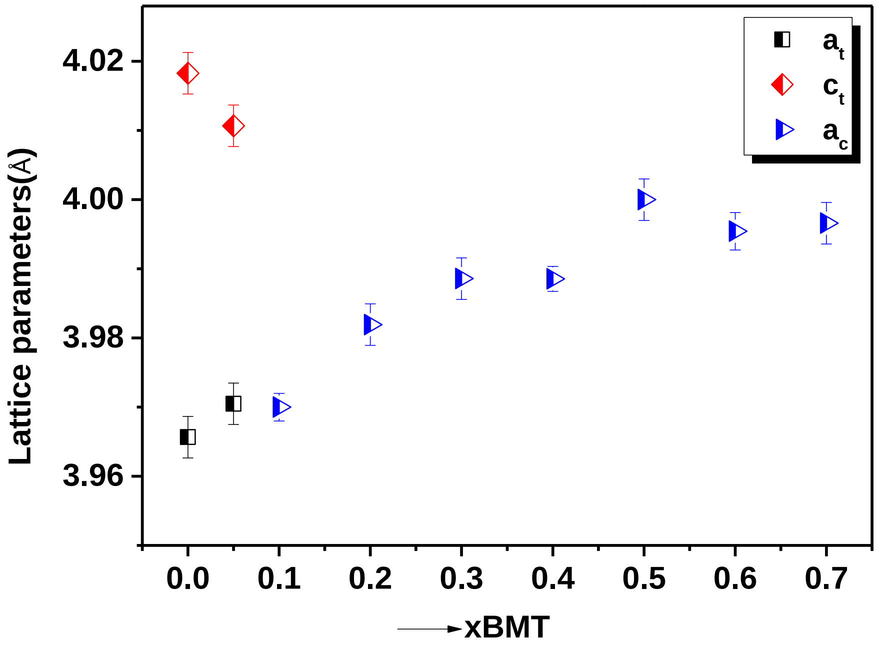

Figure 6.2 Variation of lattice parameters for the (1-*x*)BCT-*x*BMT ceramic system as a function of *x*BMT.

The data from the following sections are summarized in Table 6.1.

6.2.2 Relative Permittivity

Plots of relative permittivity, ε_r and loss tangent (tanδ) versus temperature at various frequencies are shown in Figure 6.3. Composition $x = 0$ (BCT) showed a sharp Curie peak, typical of a normal ferroelectric with Curie point, T_c ~ 130 ºC, Figure 6.3(a). The ε_r peak become more broad, and T_c decreased to ~ 110 ºC for composition $x = 0.05$, Figure 6.3(b). A change over to relaxor dielectric behaviour occurred for $x =$

0.1, with a frequency-dependent dielectric response below the temperature of peak permittivity, T_m with T_m at ~ 0 ºC. Further incorporation of BMT content, depressed the peak values of relative permittivity and a gradual decrease in the temperature-sensitivity of relative permittivity at $T > T_m$, occurred for compositions $x \geq 0.2$, with a minimum temperature-dependence for $x \geq 0.5$, Figure 6.3.

For $x = 0.5$, the relative permittivity values were ε_r = 800±15% in the temperature range 40 ºC to 550 ºC. Relative permittivity was found slightly greater with less variability with temperature for composition $x = 0.55$, for which ε_r = 950±15% over the temperature range 70 ºC-600 ºC. For $x = 0.6$, the maximum ε_r values (at > T_m) were higher, 2270, with an overall consistency, ε_r = 2100±15%, for temperatures from 120 ºC to 450 ºC. The peak values of relative permittivity, $\varepsilon_{r\ max}$ decreased from ~ 2100 for $x = 0.1$ to 875 at $x = 0.5$, then $\varepsilon_{r\ max}$ increased to ~ 2270 for $x = 0.6$. Values of T_m increased from ~ 40 ºC to ~ 160 ºC for $x = 0.2$-0.6, Figure 6.4.

6.2.3 Loss Tangent

Values of loss tangent (tanδ) as a function of temperature for (1-x)BCT-xBMT are shown in Figure 6.3. For compositions $x \leq 0.1$, tanδ values were ≤ 0.05 in the temperature from 25 ºC to ~ 250 ºC at 1 kHz and then increased sharply above ~ 250-300 ºC. For higher BMT content, tanδ values remained low ≤ 0.02 across the temperature from ≥ 50 ºC to temperature ≤ 400 ºC for compositions $0.2 \leq x \leq 0.4$. At low temperature (≤ 50 ºC) tanδ values were higher due to dispersion in loss tangent peak at ~ T_m. A relatively constant and low tanδ values ≤ 0.02, were recorded across the temperature range ~ 100 ºC to 400 ºC for $x = 0.5$ and 160-550 ºC for $x = 0.55$. For composition $x = 0.6$ the loss tangent, tanδ ≤ 0.02 in the temperature range from 170 ºC to 300 ºC at 1 kHz. Above these upper limiting temperatures, tanδ rose sharply in the manner usually associated with lattice defects arising from loss of bismuth oxide during high temperature calcination/sintering.

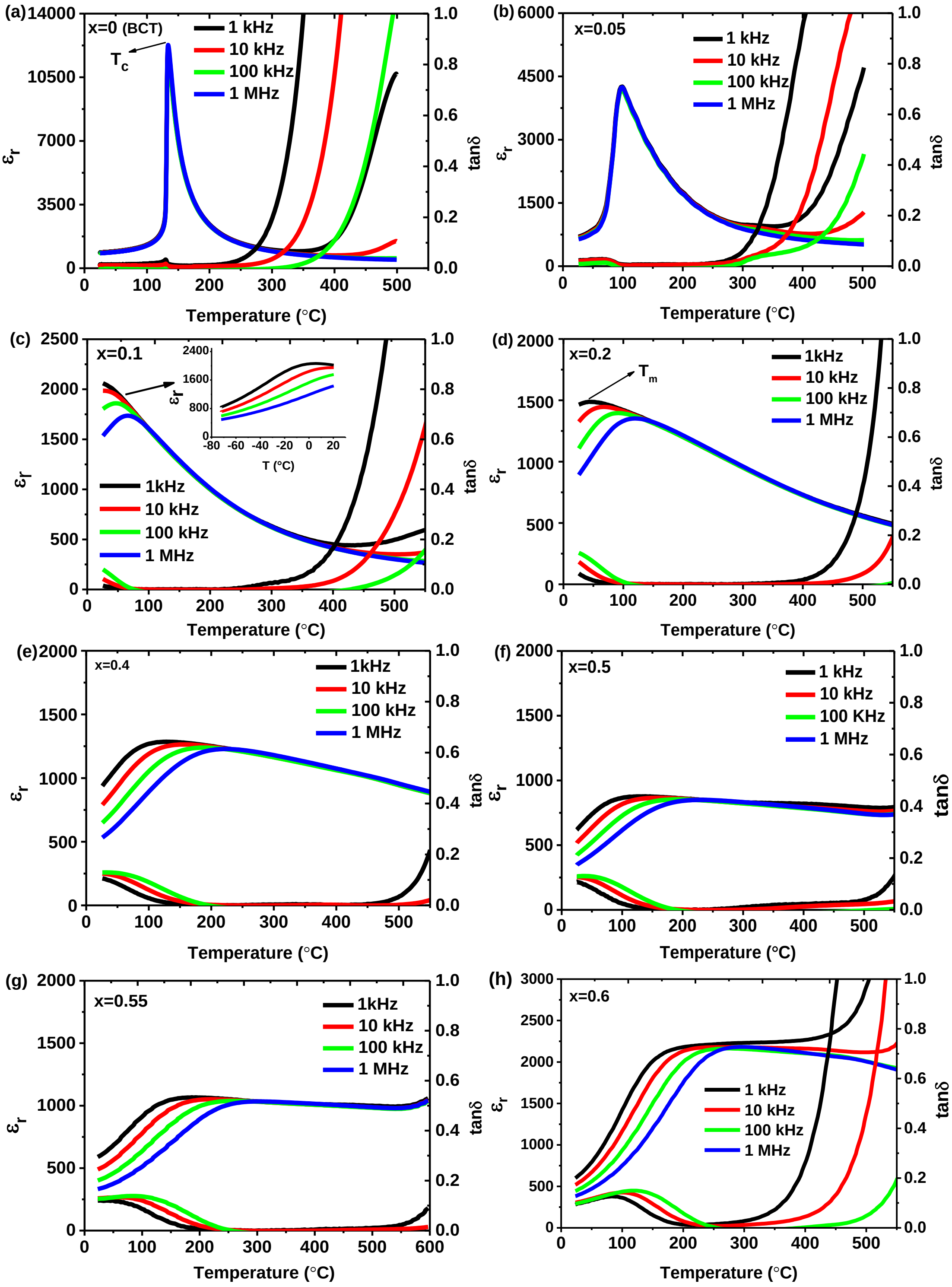

Figure 6.3 Relative permittivity and tanδ versus temperature for: (a) *x* = 0, (b) *x* = 0.05 (c) *x* = 0.1; (d) *x* = 0.2; (e) *x* = 0.4; (f) *x* = 0.5. (g) *x* = 0.55 and (h) *x* = 0.6.

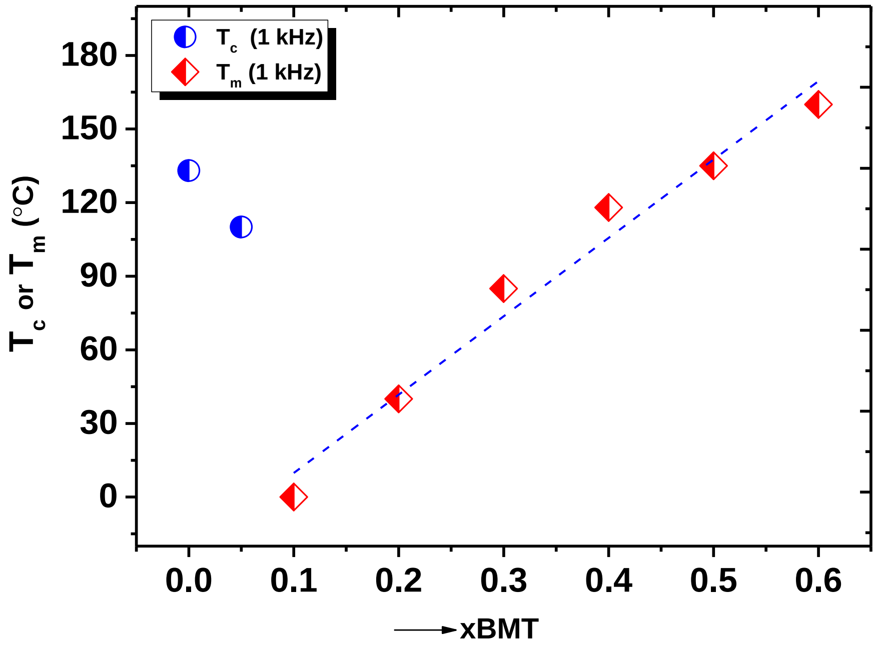

Figure 6.4 Variation of temperature corresponds to maximum relative permittivity versus *x*BMT.

6.2.4 Ferroelectric Properties

Figure 6.5, shows the polarisation-electric field response for the ceramic samples x = 0-0.5, measured at room temperature (50 kV/cm, 1 Hz). The samples x = 0 and 0.05 exhibited typical ferroelectric behaviour. Both compositions gave rise to similar values of remnant polarisation, $P_r \sim 11\ \mu C/cm^2$ but with different coercive fields (E_c) of ~ 8 kV/cm for x = 0 and ~ 16 kV/cm for x = 0.05. Composition x = 0.1 exhibited slim P-E loop with little or no indication of ferroelectric behaviour. Further addition of BMT to the solid solution gave a linear P-E response typical of a low loss dielectric, Figure 6.5(b).

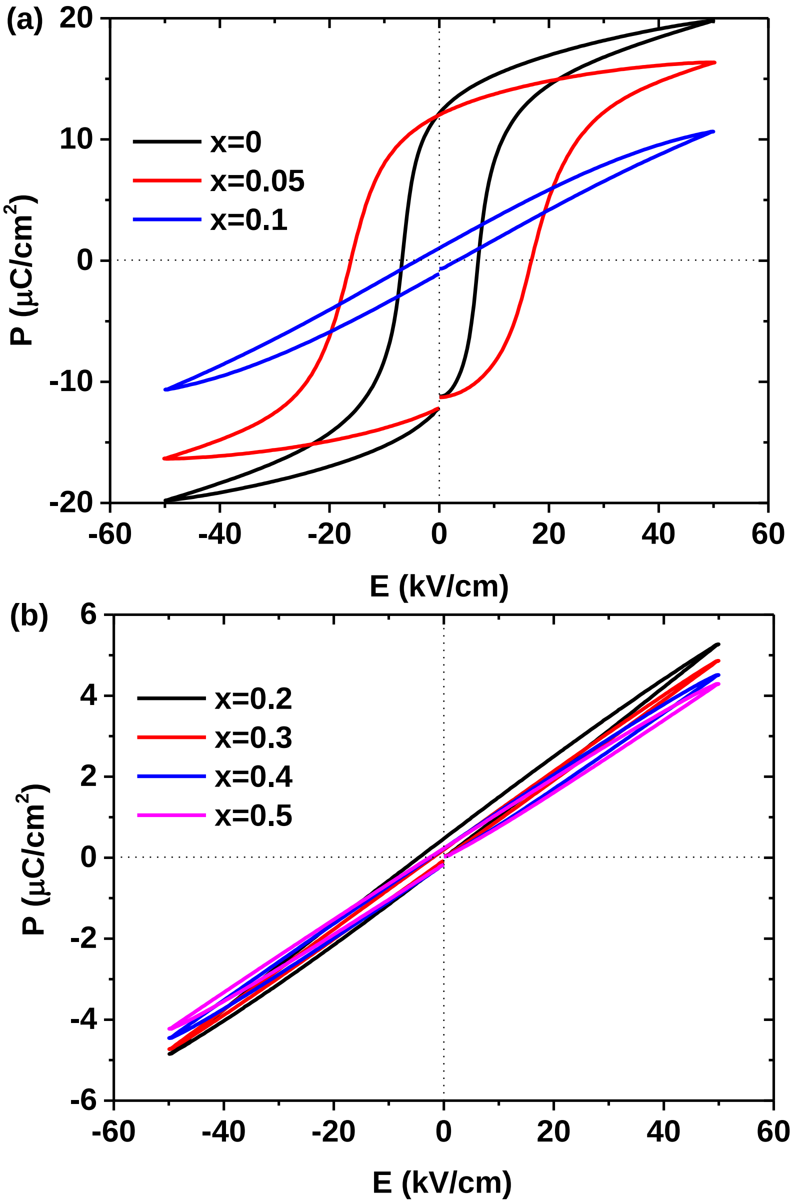

Figure 6.5 Polarisation-electric field response for ceramic compositions: (a) *x* = 0-0.1 and (b) *x* = 0.2-0.5.

6.2.5 Piezoelectric Properties

The values of piezoelectric charge coefficient, d_{33} were measured by using Berlincourt method for compositions $x \leq 0.3$, are presented in Figure 6.6. All these ceramic samples were poled for a period of 20 min at an applied electric field of ~ 40 kV/cm at a temperature of 30 °C. Poling at higher fields led to the breakdown of ceramic samples. For BCT (x = 0), value of piezoelectric charge coefficient, d_{33} was 116 pC/N. Incorporation of 5 mol% BMT to the solid solution led to decrease of d_{33} value to 92 pC/N and then very small values of $d_{33} \leq 10$ pC/N were obtained for relaxor compositions $x \geq 0.1$, Figure 6.6.

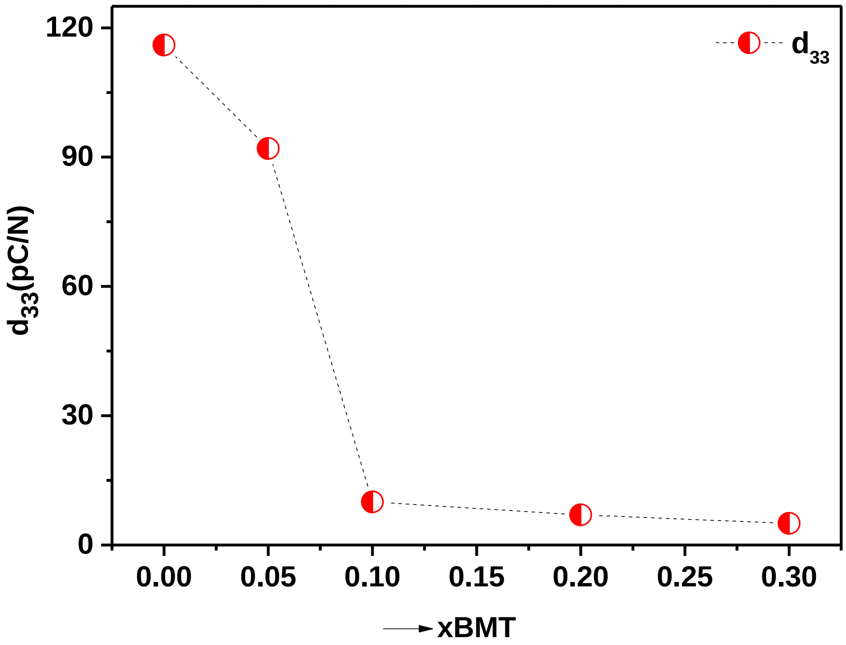

Figure 6.6 Variation of piezoelectric charge coefficient, d_{33} versus xBMT for compositions $x \leq 0.3$.

The strain-electric field response for the (1-x)BCT-xBMT system was recorded at room temperature (E ~ 50 kV/cm, 1 Hz) as presented in Figure 6.7. Typical butterfly like strain-field loops were observed for compositions x = 0 and 0.05. The maximum strain values were ~ 0.12% for x = 0 and 0.14% for x = 0.05 at an applied electric field of 50 kV/cm. Samples $x \geq 0.1$ revealed an electrostrictive behavior with strain values ≤ 0.11%.

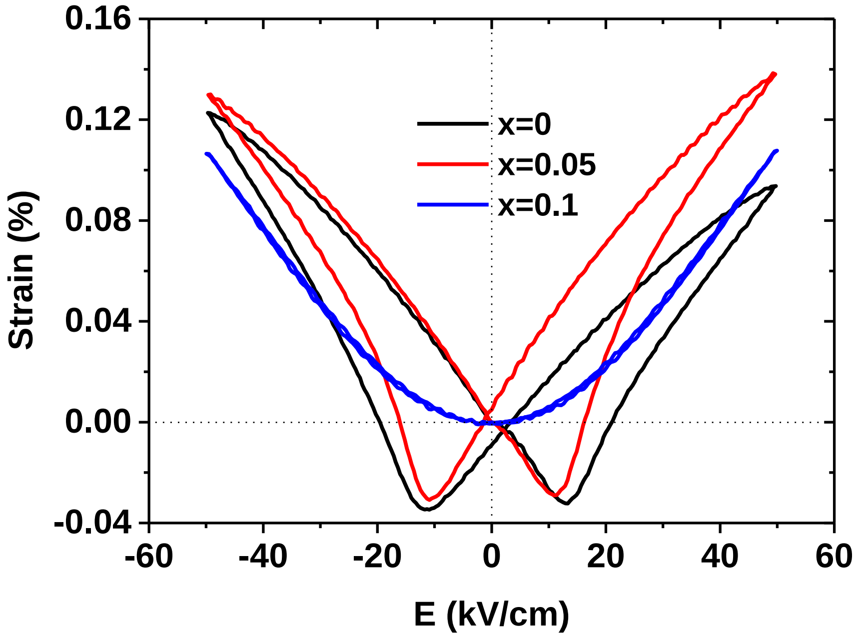

Figure 6.7 Electric field induced strain curves for compositions *x* = 0, 0.05 and 0.1, measured at room temperature (1 Hz).

Table 6.1 Summary of dielectric (1 kHz) and ferroelectric and piezoelectric properties of (1-*x*)BCT-*x*BMT ceramic system ($x \leq 0.6$).

Measured Parameters	x = 0	0.05	0.1	0.2	0.3	0.4	0.5	0.55	0.6
T_c or T_m (ºC)	130	110	0	40	85	118	135	160	160
$\varepsilon_{r\ max}$ (1 kHz)	12060	4230	2090	1485		1280	875	1060	2270
P_r (μC/cm^2) at RT	11	12	-	-	-	-	-	-	-
E_c (kV/cm)	8	16	-	-	-	-	-	-	-
d_{33} (pC/N)	116	92	10	8	5	-	-	-	-
Strain(%, 50 kV/cm)	0.12	0.14	0.11	0.08	-	-	-	-	-
T-range (ºC), $\varepsilon_r \leq \pm 15\%$	-	-	-	-	-	-	(40-550) 800±15%	(70-600) 950±15%	(120-450) 2100±15%
T-range (ºC), $\tan\delta \leq 0.02$	-	-	-	-	-	-	100-400	160-550	170-300

6.2.6 Dielectric Breakdown Strength

Dielectric breakdown strength was measured at room temperature for compositions $x = 0.5$ and 0.55. Ten pellets of each composition with thickness of ≤ 500 μm were tested in silicon oil. A high triangular electric field was applied with ramp rate of 500 V/s. The dielectric breakdown strength was recorded by detecting the spike in current displayed on the cathode ray oscilloscope. The estimated average dielectric breakdown strength with mean standard deviation for composition $x = 0.5$ was 258±30 kV/cm and 204±14 kV/cm for composition $x = 0.55$. Details of the estimated breakdown strength are given in Table 6.2.

Table 6.2 Estimated dielectric breakdown strength for compositions *x* = 0.5 and *x* = 0.55.

Pellet Number	Estimated dielectric breakdown (kV/cm) $x = 0.5$	Estimated dielectric breakdown (kV/cm) $x = 0.55$
1	280	220
2	230	210
3	210	190
4	275	195
5	283	180
6	250	210
7	233	180
8	333	220
9	216	220
10	267	210

6.2.7 Energy Density and dc bias Relative Permittivity

The high electric field polarisation response was studied at a maximum electric field of ~ 90 kV/cm (20 Hz), for compositions $x = 0.5$ and 0.55 over the temperature from 20 ºC to 150 ºC, Figure 6.8. Composition x = 0.5 exhibited a nearly temperature independent linear dielectric response with low loss. However, the P-E response for composition x = 0.55 was little lossy at room temperature and then change to linear dielectric with low loss at high temperatures.

Values of energy density as a function of applied electric field at various temperature are presented in Figure 6.8(c) and 6.8(d). Energy density values were calculated by integrating the area enclosed by the decreasing field part polarisation-electric field as described in the literature [Wang et al. (2014), Hao (2013)]. The trend of increasing energy density for both compositions was nearly the same up to a field of ~ 50 kV/cm at all temperatures. Increasing field further, values of energy density were increased but became temperature dependent. Peak values of energy density were 0.44 J/cm^3 for composition x = 0.5 and 0.5 J/cm^3 for x = 0.55 at room temperature (E ~ 90 kV/cm, 20 Hz). This difference in energy density was due to the difference in values of relative permittivity and polarisation. The values of energy density decreased to 0.38 J/cm^3 for x = 0.5 and 0.36 J/cm^3 for x = 0.55 at temperature 150 ºC.

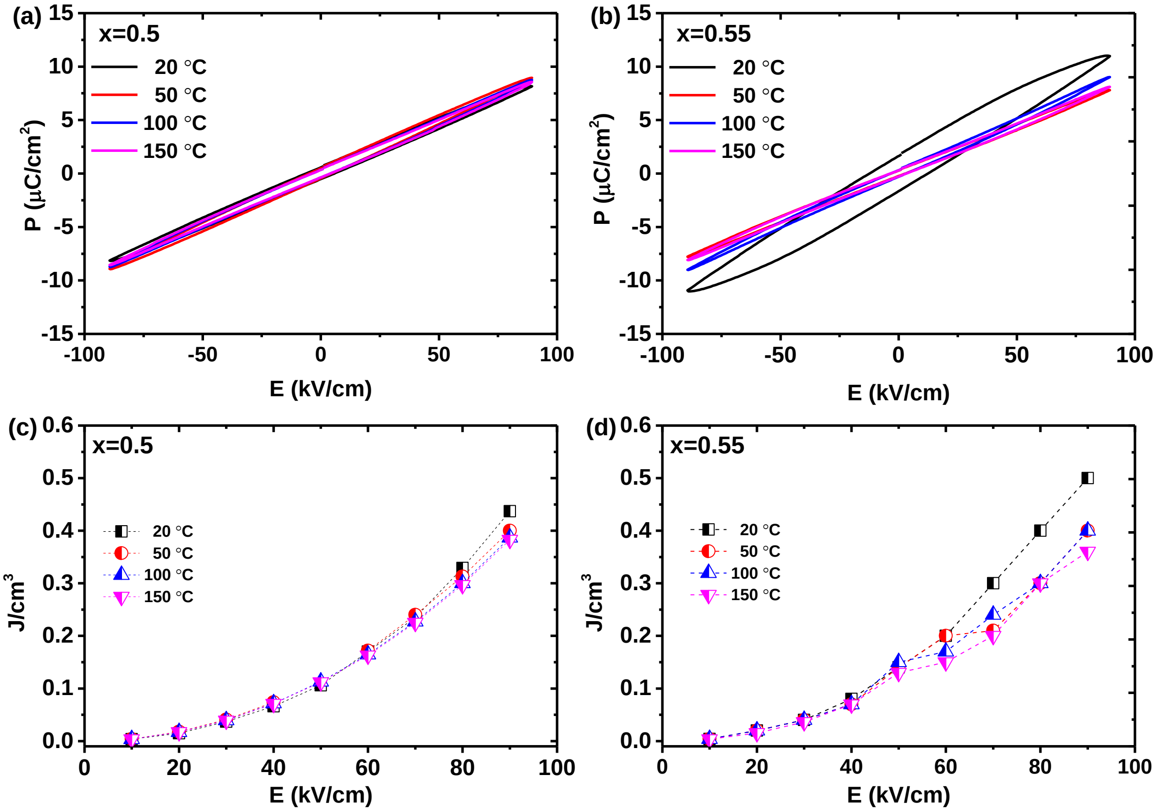

Figure 6.8 Temperature dependent polarisation-electric field response (E ~ 90 kV/cm) for: (a) *x* = 0.5 and (b) *x* = 0.55, and variation of energy density versus electric field over the temperature from 20-150 ºC for: (c) *x* = 0.5 and (d) *x* = 0.55.

Figure 6.9, shows the relative permittivity and loss tangent (tanδ) as a function of dc bias field for *x* = 0.55 across the temperature from 20 ºC to 150 ºC. Values of relative permittivity and loss tangent were abstracted from the polarisation-electric field loops (~ 20 kV/cm, 20 Hz) at dc bias field of 40 kV/cm. Relative permittivity with dc bias field exhibited a nearly stable behaviour with no significant change, in contrast to other $BaTiO_3$ and $Na_{0.5}Bi_{0.5}TiO_3$-based materials [Yu et al. (2002), Spreitzer et al. (2007)].

Under dc bias field (40 kV/cm), values of relative permittivity were similar and temperature dependent as in the absence of dc field with ε_r ~ 930 at room temperature increased to ~ 1070 at 140 ºC and 180 ºC. Values of loss tangent, tanδ (20 Hz) were high ~ 0.15 at room temperature and then decreased to ~ 0.003 at 180 ºC, Figure 6.9.

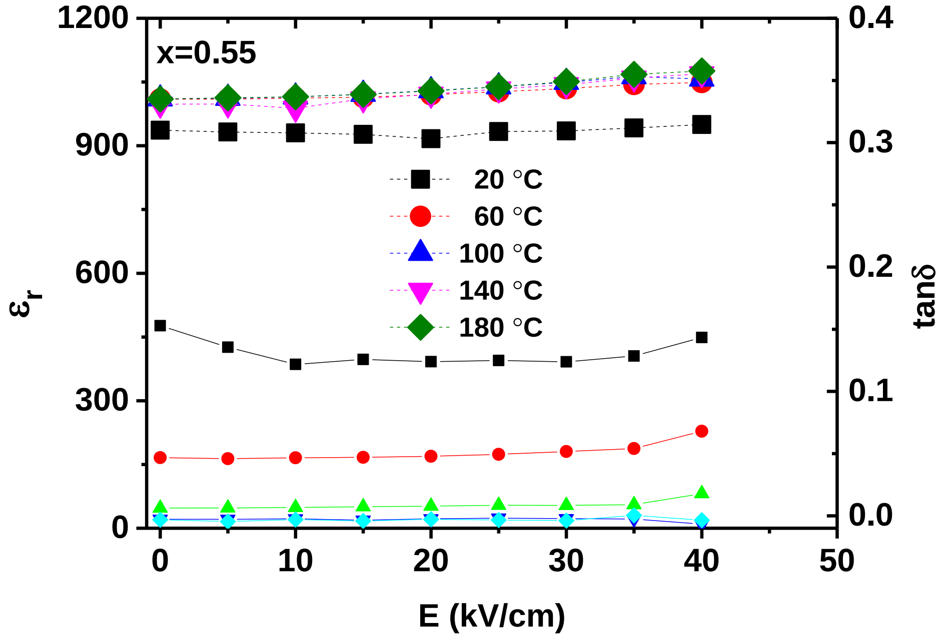

Figure 6.9 Relative permittivity and dielectric loss, tanδ as function of dc bias fields (20 Hz) over temperature range 20-150 ºC for *x* = 0.55.

6.2.8 dc resistivity

Values of dc resistivity for temperature stable dielectric compositions *x* = 0.5, 0.55 and 0.6 were recorded as a function of temperature at fixed dc voltage ~ 80 V. Values of dc resistivity are presented in the plots over the temperature range from 250 ºC to 550 ºC, Figure 6.10. For compositions *x* = 0.5 and 0.55, values of dc resistivity were ~ 10^9 Ω m at a temperature of 300 ºC, and ~ 10^6 Ω m at 500 ºC. A slight decrease in resistivity was recorded for sample *x* = 0.6, may be attributed to the charge carriers concentration rather than different conduction mechanisms compared to *x* = 0.5 and 0.55. The activation energy abstracted from conductivity data for *x* = 0.5 and 0.55 was ~ 0.6 eV consistent with an oxygen vacancy migration mechanism [Selvamani et al. (2012), Morrison et al. (1999)].

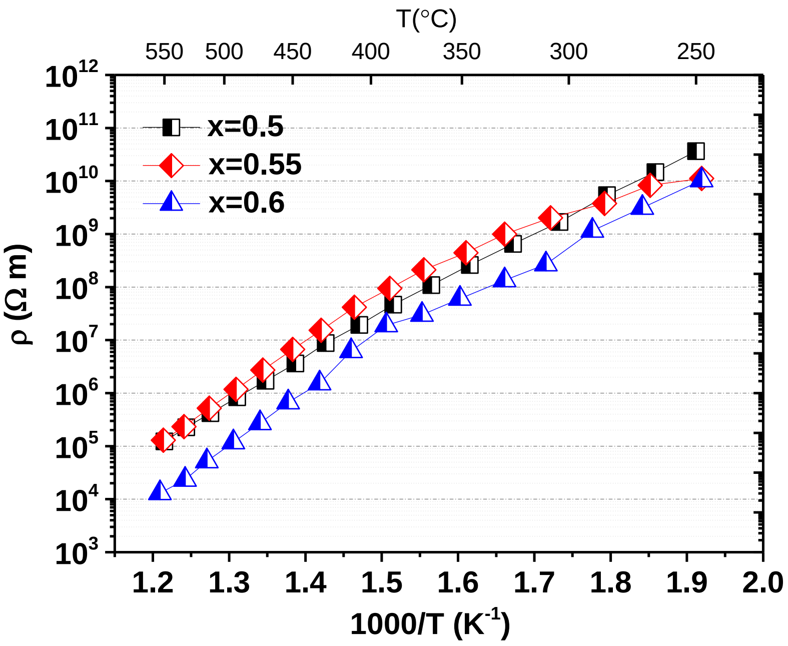

Figure 6.10 Variation of dc resistivity as a function of inverse of absolute temperature (1/T) for *x* = 0.5, 0.55 and 0.6.

6.2.9 Microstructural analysis

SEM micrographs for polished and chemically etched surfaces for samples *x* = 0, 0.1, 0.2 and 0.3 are presented in Figure 6.11. The grain size for each composition was estimated by using the linear intercept method. For composition *x* = 0, SEM micrograph revealed a domain structure and estimated average grain size of ~ 7 µm. A decrease in grain size occurred with the addition of BMT with average size of ~ 3 µm for *x* = 0.1 and ~ 2 µm for *x* ≥ 0.3. The geometrical density estimated for at least three pellets was 5.4 g/cm^3 for *x* = 0 increased to 6.1 g/cm^3 for *x* = 0.6, Table 6.3. Relative densities of all samples were in the range of 90 to 95% of the theoretical.

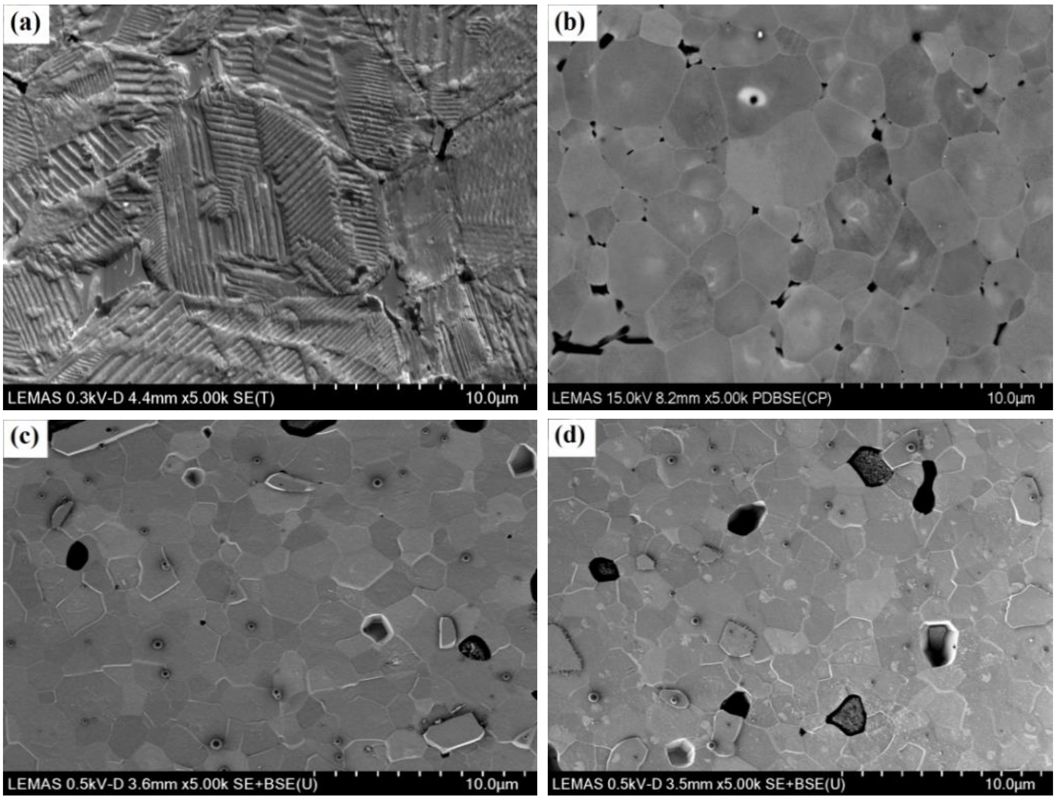

Figure 6.11 SEM micrographs of chemically etched surfaces for: (a) x = 0, (b) x = 0.1, (c) x = 0.2 and (d) x = 0.3.

Table 6.3 Summary of the average grain size and geometrical densities for the (1-x)BCT-xBMT system.

Composition (x)	Ave. grain size (μm)	Density, ρ (g/cm^3)
x = 0	7	5.4
x = 0.05	7	5.5
x = 0.1	3	5.2
x = 0.2	2	5.5
x = 0.3	2	5.7
x = 0.4	2	5.9
x = 0.5	2	6.1
x = 0.6	2	6.1

6.2.10 SEM-EDX analysis

As a preliminary study, SEM-EXD was performed for selected samples x = 0.05, 0.1, 0.8 and 0.5 to examine any compositional variation inside the grains. Figure 6.12 shows the SEM micrograph and EDX elemental mapping for x = 0.05. A domain structure in several grains was evident from the SEM micrograph. A careful analysis by SEM-EDX mapping showed that there was no detectable chemical non-uniformity in the grains for composition x = 0.05.

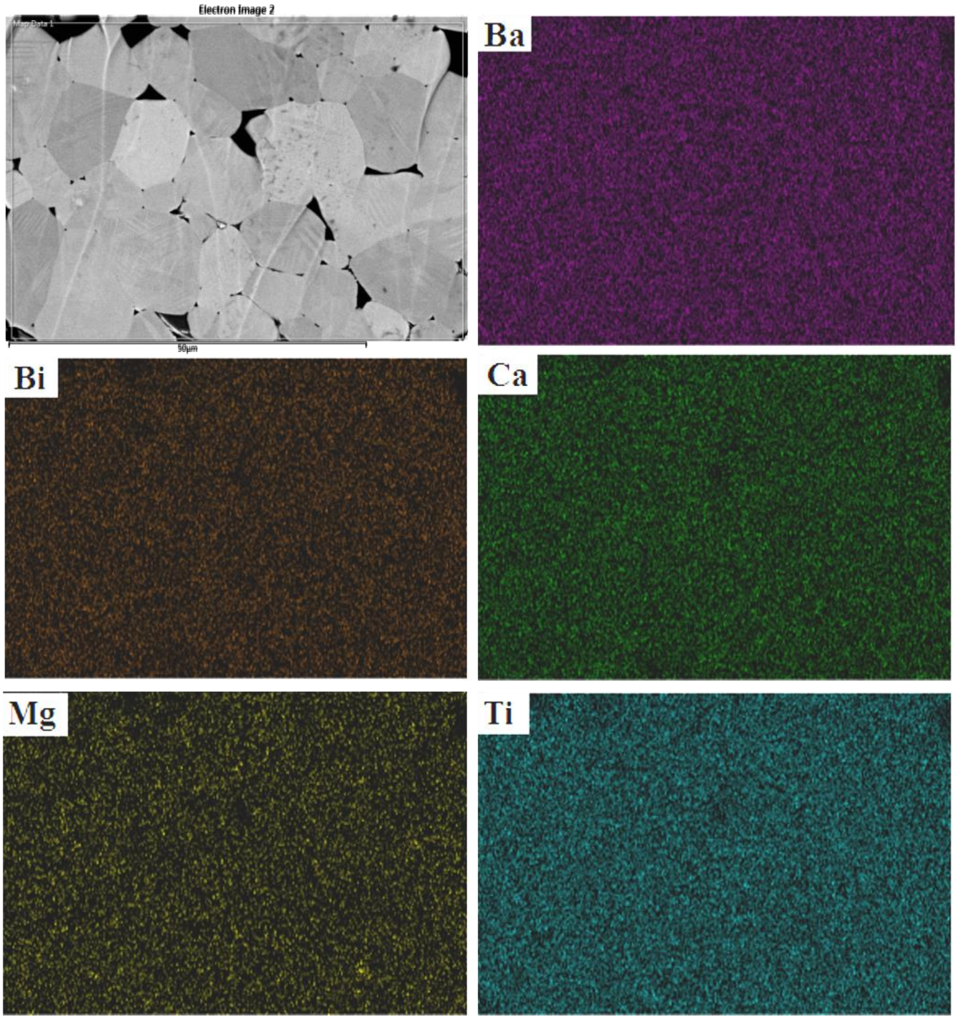

Figure 6.12 Illustration of SEM-EDX elemental mapping for composition x = 0.05.

Figure 6.13 and 6.14, shows the elemental mapping by SEM-EDX for samples $x = 0.1$ and 0.2. Examination of composition $x = 0.1$ revealed a compositional contrast in the grains. EDX mapping showed a segregation of Bi^{3+} and Ca^{2+} in several grains. However, there was little or no evidence of Mg^{2+} non-uniformity in the grains of the examined sample. Other elements Ba^{2+} and Ti^{4+} were uniformly distributed throughout the grains.

For composition $x = 0.2$, the SEM-EDX results demonstrated the existence of all elements with appropriate concentration in all grains except for one grain in which a slight difference in Bi^{3+}, Ca^{2+} and Mg^{2+} proportion was identified, Figure 6.14.

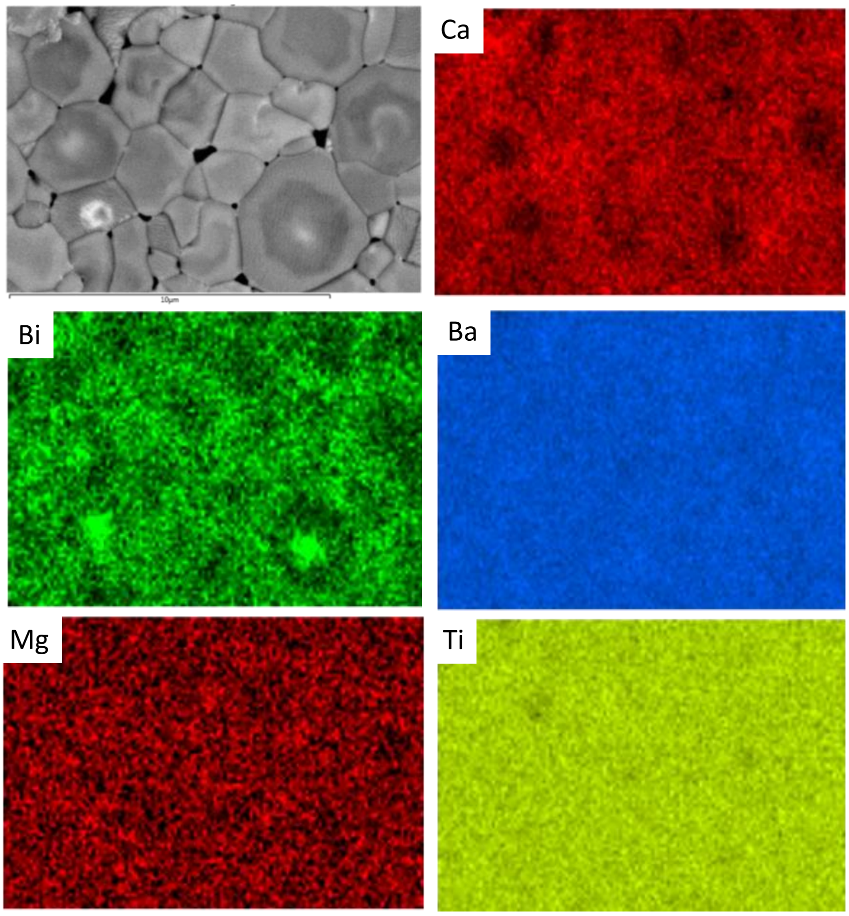

Figure 6.13 SEM-EDX scan and elemental mapping showing the segregation of Bi^{3+} and Ca^{2+} for composition $x = 0.1$.

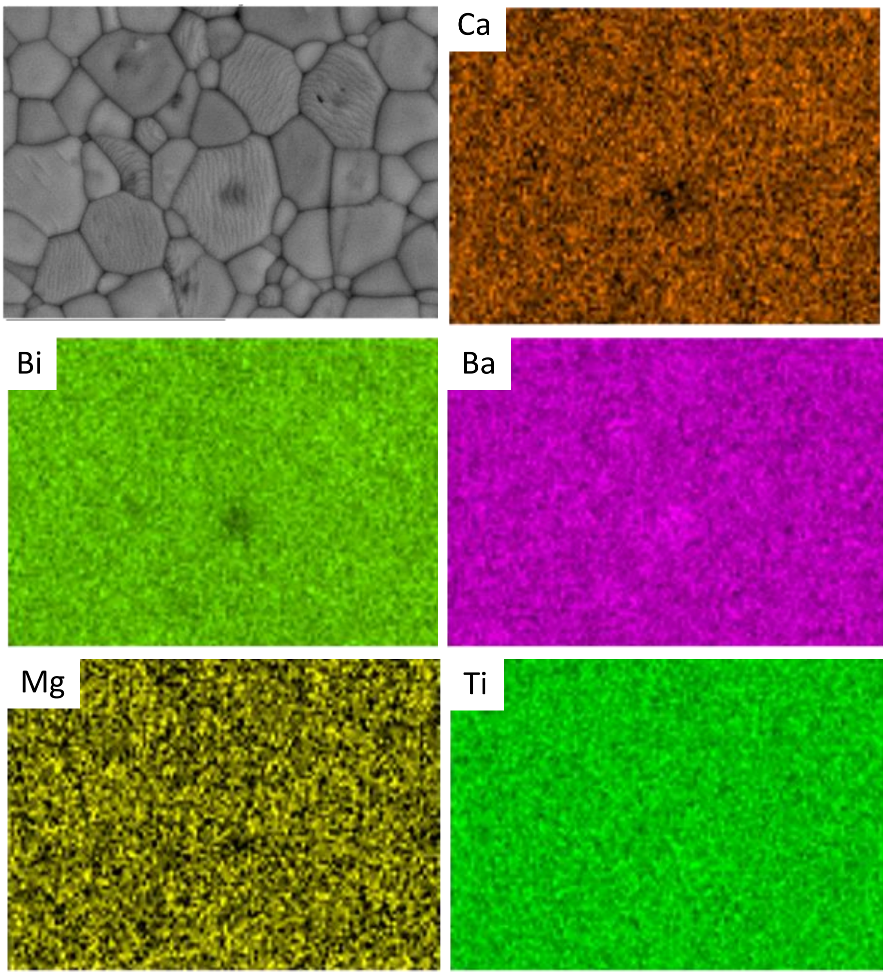

Figure 6.14 SEM-EDX elemental mapping for composition *x* = 0.2.

SEM-EDX analysis of the pre-sintered powders and polished ceramic pellet was also conducted for $x = 0.5$. Figure 6.15 shows the SEM micrograph and EDX elemental mapping for pre-sintered powder for composition $x = 0.5$. The SEM image revealed an agglomerated and irregularly shape particles. The examination of elemental distribution by EDX-mapping revealed a slight Ca^{2+} and Mg^{2+} rich concentration regions. However, the distribution for other elements was uniform.

Figure 6.16 shows the SEM image and elemental map for polished and thermally etched sample $x = 0.5$. The SEM-EDX mapping confirmed little evidence of Bi^{3+} non-uniformity in the grains. However, unlike the composition $x = 0.1$, there was no apparent deficiency of Ca^{2+} in the grains with the detectable limit of SEM-EDX. Other elements distribution was uniform throughout the grains.

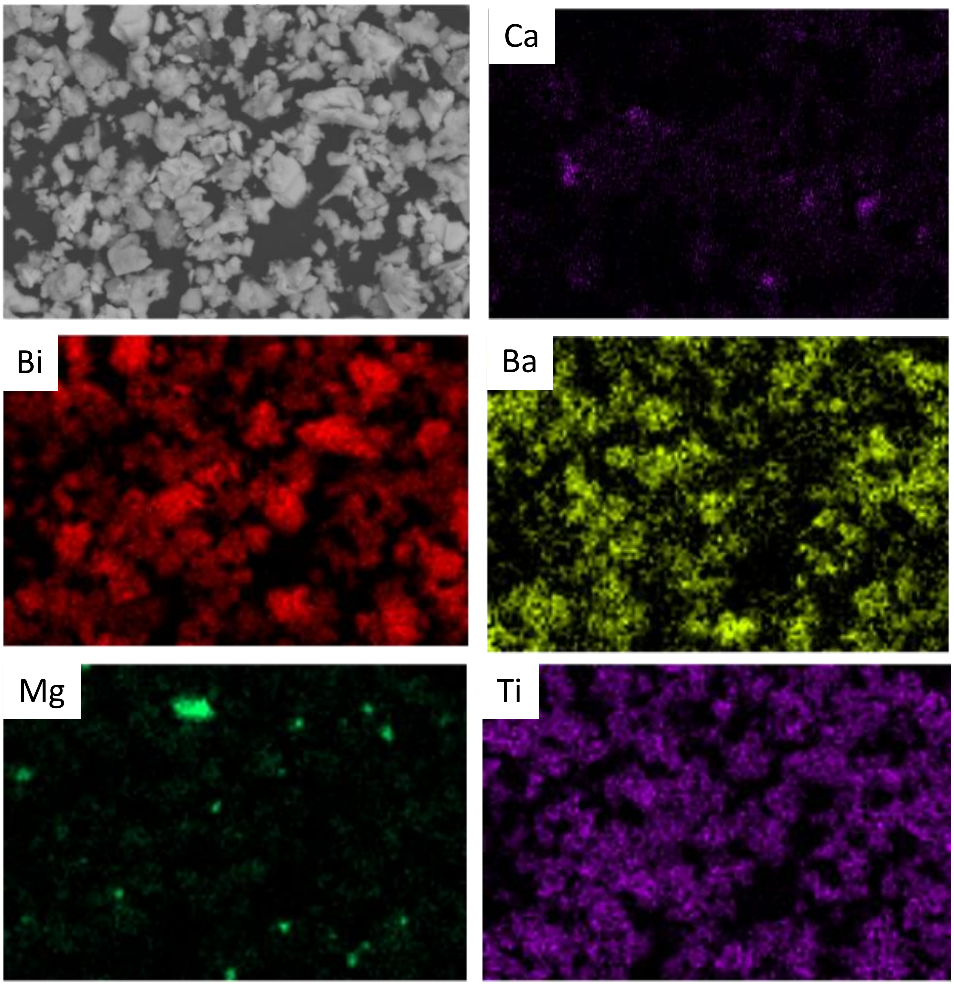

Figure 6.15 SEM-EDX of pre-sintered powders for composition *x* = 0.5.

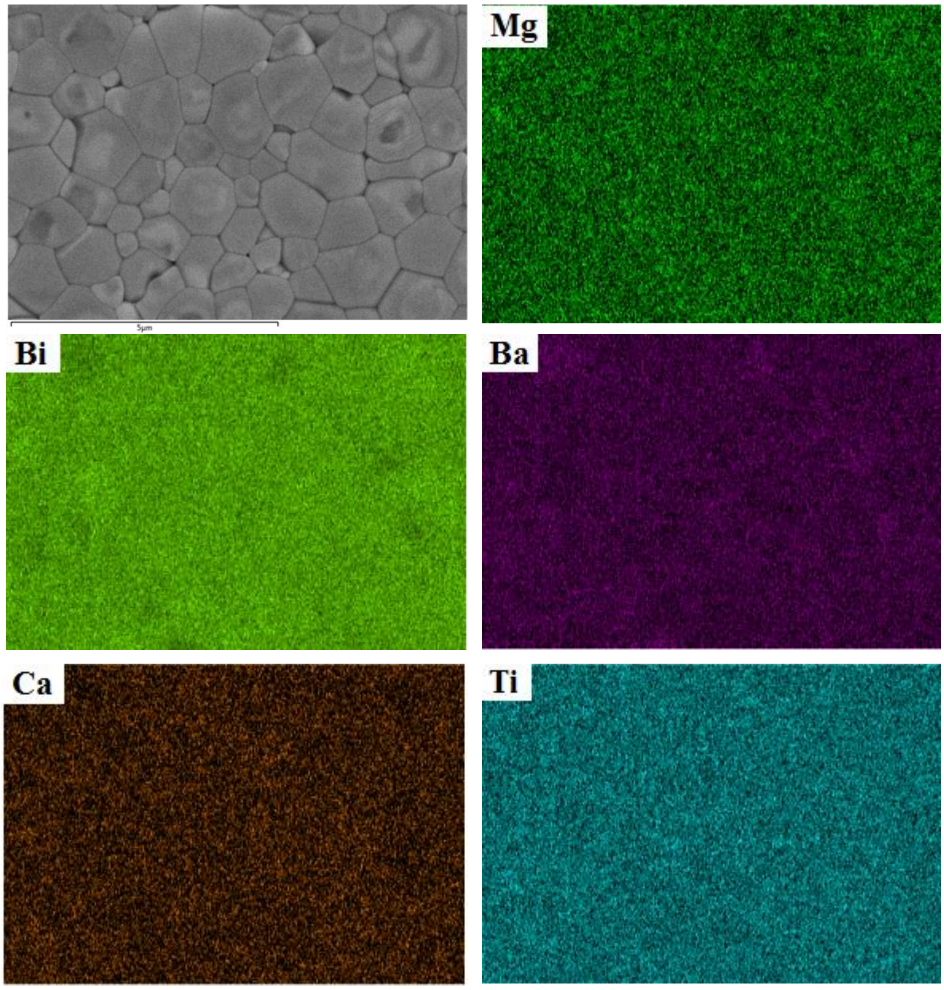

Figure 6.16 SEM-EDX elemental mapping indicating Bi^{3+} segregation in the grains for composition $x = 0.5$.

6.2.11 TEM/EDX analysis

Composition $x = 0.05$ was also examined by TEM-EDX after preparation by standard method; cutting, grinding, dimpling and ion beam polishing. Microstructural information was obtained by using transmission electron microscopy (TEM; Philips, CM200) as mentioned in section 3.37. A domain structure was evident from the TEM micrographs, Figure 6.17. Elemental mapping by STEM-EDX confirmed that there was no detectable elemental variation in the grains, Figure 6.18.

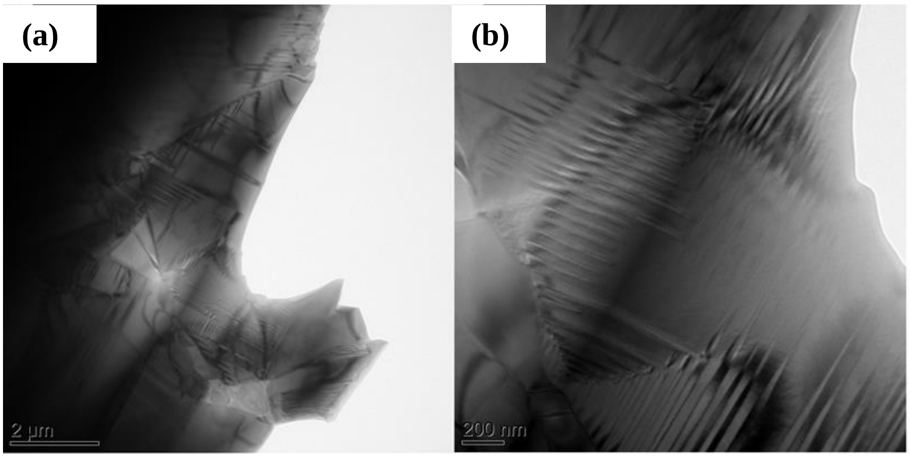

Figure 6.17 STEM micrographs for: (a) several grains and (b) single grain for sample *x* = 0.05, indicating domain structure.

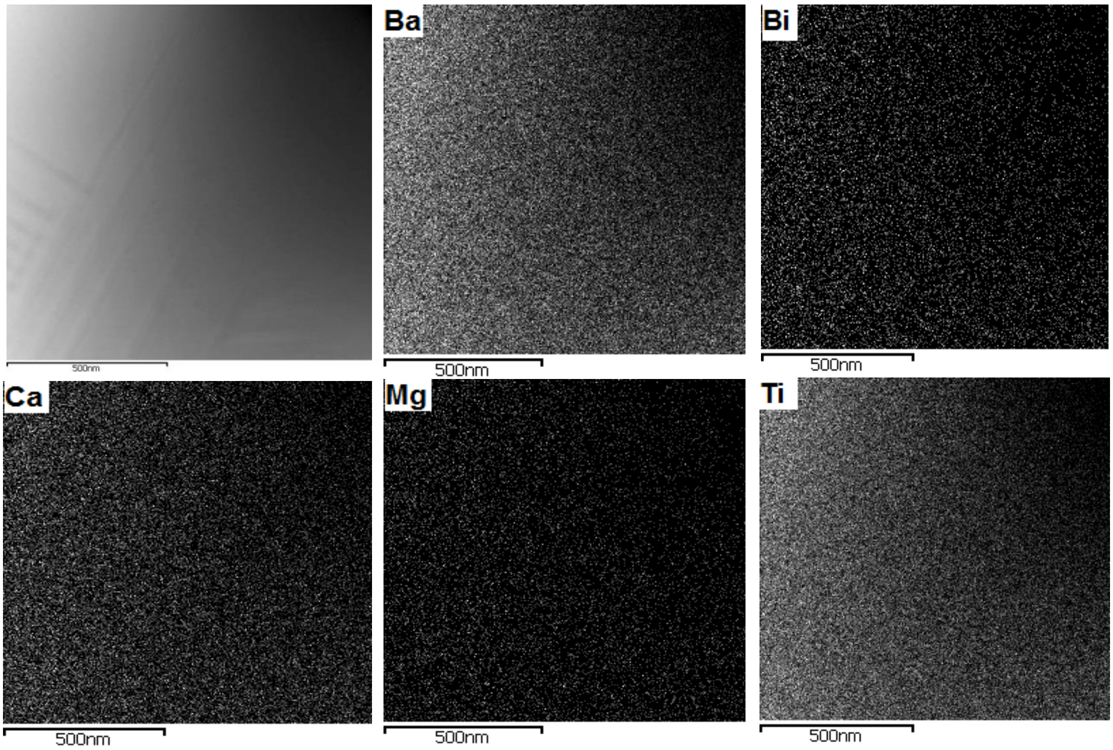

Figure 6.18 STEM-EDX elemental mapping showing no detectable elemental variation in grain for composition *x* = 0.05.

6.2.12 Conclusions

Ceramics in the system (1-x)BCT-xBMT have been fabricated and analysed. Single-phase perovskite-type X-ray diffraction patterns were observed for $x < 0.6$, with tetragonal structure for $x \leq 0.05$, changed to single phase cubic for $0.1 \leq x < 0.6$. For compositions $x \leq 0.05$, no frequency dispersion in relative permittivity was observed, although $x = 0.05$ peaks were more diffuse than for a normal ferroelectric.

A change to relaxor dielectric behaviour occurred for the cubic ceramics, $0.1 \leq x \leq 0.6$. Diffuse, frequency-dependent permittivity-temperature plots exhibited near flat responses in the frequency independent region $T > T_m$ for compositions $x = 0.5$, 0.55 and 0.6. For $x = 0.5$, relative permittivity (1 kHz) was 800±15% for temperatures extending from 40 ºC to 550 ºC.

A more stable temperature dependent relative permittivity response was found for $x = 0.55$, 950±15% in a wide range of temperature from 70 ºC to 600 ºC. Permittivity values were much higher for $x = 0.6$, in the range 2100±15% for temperatures 120 ºC to 450 ºC. The loss tangent (1 kHz) values were ≤ 0.02 for temperatures 100 ºC-400 ºC for composition $x = 0.5$ and from 160-550 ºC for $x = 0.55$. Values of dc resistivities were in the range of 10^9 Ω m at a temperature of 300 ºC, and ~ 10^6 Ω m at 500 ºC.

Chapter 7

Dielectric Properties of the $NaNbO_3$-modified $(Ba_{0.8}Ca_{0.2})TiO_3$-$Bi(Mg_{0.5}Ti_{0.5})O_3$ Ceramic System

7.1 Summary

This chapter deals with the dielectric properties of the $0.45Ba_{0.8}Ca_{0.2}TiO_3$-(0.55-*x*)$Bi(Mg_{0.5}Ti_{0.5})O_3$-*x*$NaNbO_3$ ($x < 0.3$) system, abbreviated as 0.45BCT-(0.55-*x*)BMT-*x*NN. XRD patterns were indexed as cubic perovskite for all studied compositions. Compositions in the solid solution system: 0.45BCT-(0.55-*x*)BMT-*x*NN, displayed a relaxor character with temperature-stable dielectric properties. Ceramics of composition $x = 0$ [Chapter 6] have a relative permittivity, $\varepsilon_r = 950 \pm 15\%$ over a wide temperature range from +70 ºC to 600 ºC. For $x = 0.1$, the stability of relative permittivity, within ±15% occurred over the temperature range ≤ 20 ºC to 550 ºC.

Modification with $NaNbO_3$, $x = 0.2$ decreased the lower limiting temperature to -70 ºC, but also decreased relative permittivity such that $\varepsilon_r = 600 \pm 15\%$ over the temperature range -70 ºC to 500 ºC. For composition $x = 0.3$, $\varepsilon_r = 550 \pm 15\%$ occurred across the temperature range, ≤ -70 ºC to 300 ºC and tanδ values ≤ 0.02, from -60 ºC to 300 ºC. This stability in ε_r allied to low loss occurred over a temperature range that extends from below the military specification lower temperature limit for a capacitor, -55 ºC, to an upper limit of 300 °C, making the $x = 0.2$ and 0.3 sample relevant for proposed aerospace and other applications.

Relative permittivity values under dc bias up to ~ 40 kV/cm was retained for all compositions. The values of energy storage density for composition $x = 0$, were ~ 0.5

J/cm^3 at an electric field of ~ 90 kV/cm and ~ 0.2 J/cm^3 and ~ 0.17 J/cm^3 for $x = 0.2$ and $x = 0.3$ respectively. Values of dc resistivity for all samples were of the order of 10^{10} Ω m at 250 ºC and 10^7 Ω m at 400 ºC.

7.2 Results and discussion

7.2.1 Phase analysis

X-ray powder diffraction patterns of the crushed sintered ceramics for the 0.45BCT-(0.55-x)BMT-xNN system are presented in Figure 7.1. The XRD patterns of all studied compositions, x = 0-0.30, appeared cubic perovskite with no evidence of {200} peak splitting. Minor second-phase XRD peaks suggested bismuth titanate in some samples. The unit cell cubic lattice parameter decreased slightly from $\boldsymbol{a}$ = 3.983±0.001 Å for x = 0 to $\boldsymbol{a}$ = 3.978±0.003 Å for x = 0.3, shown in Figure 7.2.

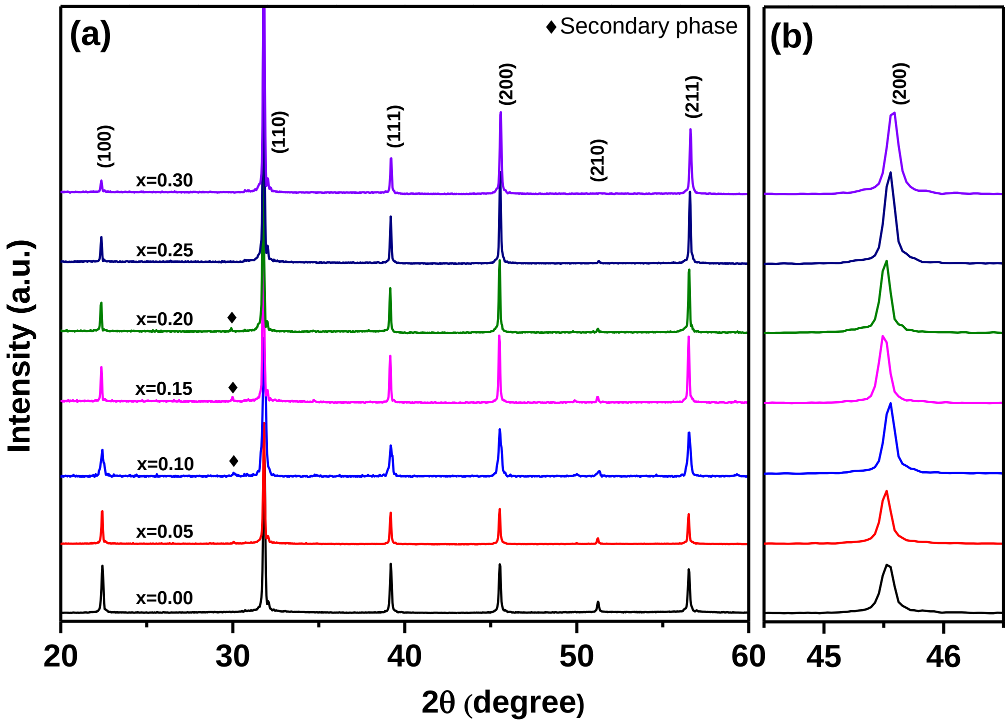

Figure 7.1(a) XRD patterns of crushed ceramic pellets for the 0.45BCT-(0.55-x)BMT-xNN system ($x \leq 0.3$) and (b) expanded scale for {200} reflection.

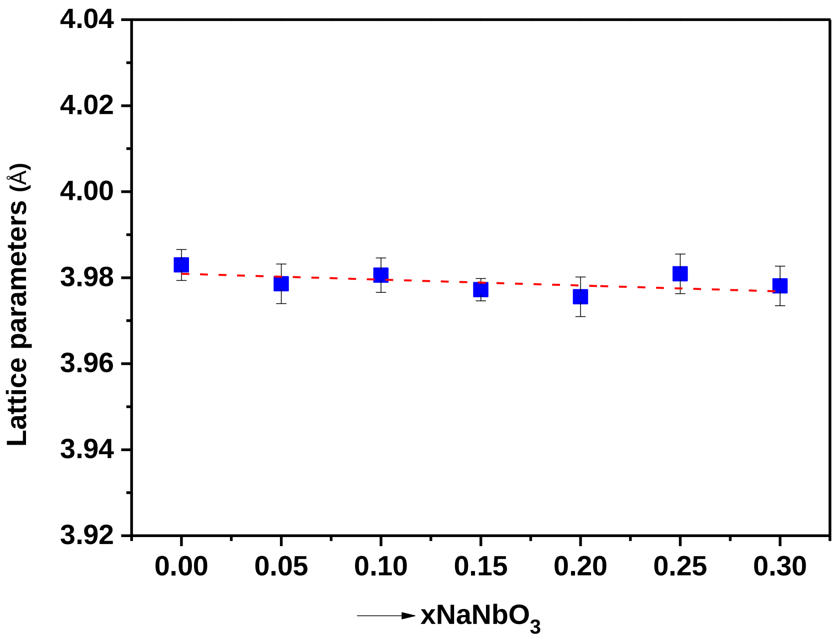

Figure 7.2 Lattice parameters as a function of *x*NaNbO$_3$ content for 0.45BCT-(0.55-*x*)BMT-*x*NN compositions, $x \leq 0.3$.

7.2.2 Relative Permittivity and Loss Tangent

The temperature dependent relative permittivity (ε_r) and loss tangent (tanδ) are plotted at various frequencies (1 kHz-1 MHz), Figure 7.3 and 7.4. All compositions displayed a strong frequency dispersion in ε_r(T) plots at $T \leq T_m$ and corresponding dispersion in tanδ data, typical of a relaxor dielectric. The temperature of maximum relative permittivity, T_m, was ~ 160 °C for $x = 0$: adding NN content to the solid solution resulted in decrease of T_m to ~ 0 °C for $x = 0.2$ and -55 °C for $x = 0.3$, Figure 7.5 (all values in text refer to 1 kHz data, unless otherwise stated).

The least temperature-dependence of relative permittivity occurred for composition $x = 0$ (0.45BCT-0.55BMT), for which $\varepsilon_r = 950 \pm 15\%$ over the temperature range 70 °C-600 °C. For $x = 0.1$, relative permittivity, $\varepsilon_r = 580 \pm 15\%$ in the temperature range ≤ 20-550 °C. Achieving temperature-stability down to -55 °C and below was accomplished by the incorporation of $NaNbO_3$ at a level $x \geq 0.2$. For composition $x = 0.2$, $\varepsilon_r = 600\pm15\%$ over the temperature range -70 ºC to 500 ºC, thus achieving the goal of producing a temperature-stable relaxor dielectric with the potential to operate in a range of harsh environments down to < -55 ºC. Modification with $x = 0.3$, led to the temperature stability in relative permittivity, with $\varepsilon_r = 550\pm15\%$ across the temperature range -70 ºC-300 ºC.

For $x = 0$, values of $\tan\delta \leq 0.02$, were in the temperature range 160-550 ºC and 40 ºC to 420 ºC for $x = 0.1$. Further incorporation of NN content extended the temperature range of $\tan\delta \leq 0.02$ from -20 ºC to 400 ºC for $x = 0.2$. For composition $x = 0.3$, the dispersion in tanδ (1 kHz) shifted to lower temperatures (-60 ºC), such that a combination of $\tan\delta \leq 0.02$ and $\varepsilon_r = 550\pm15\%$ occurred across the temperature range, -60 ºC to 300 ºC. This combination of low tanδ and stable ε_r from ≤ -55 ºC to 300ºC makes $x = 0.3$ promising for future development as a capacitor material, although the moderate permittivity would require compensating dimensional engineering, for example thin layers to achieve high capacitance. A sharp rise in loss tangent, tanδ at ≥ 500 ºC under low field ac signal may be attributed to electrical conduction mechanisms.

A summary of the dielectric properties of all studied 0.45BCT-(0.55-x)BMT-xNN compositions are presented in Table 7.1.

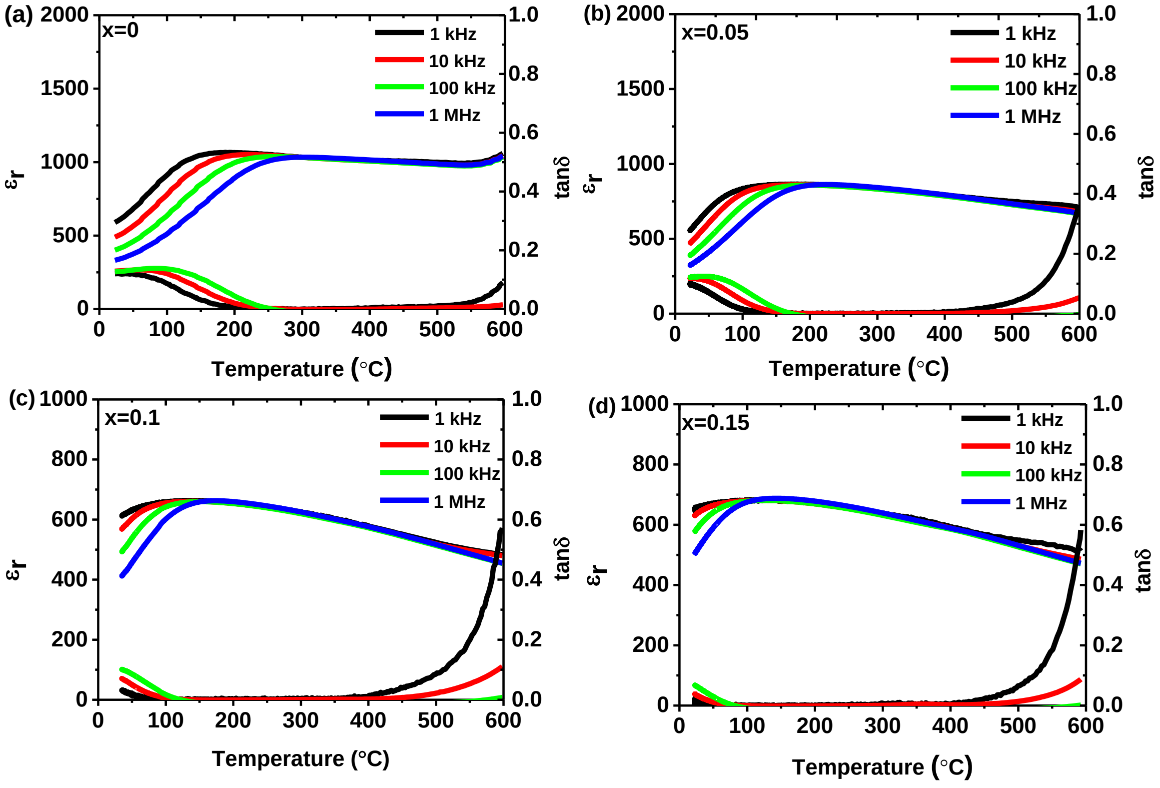

Figure 7.3 Temperature dependent relative permittivity and tanδ for: (a) *x* = 0 and (b) *x* = 0.05 (c) *x* = 0.1 and (d) *x* = 0.15 over the temperature range 25 °C to 600 °C (data set continued).

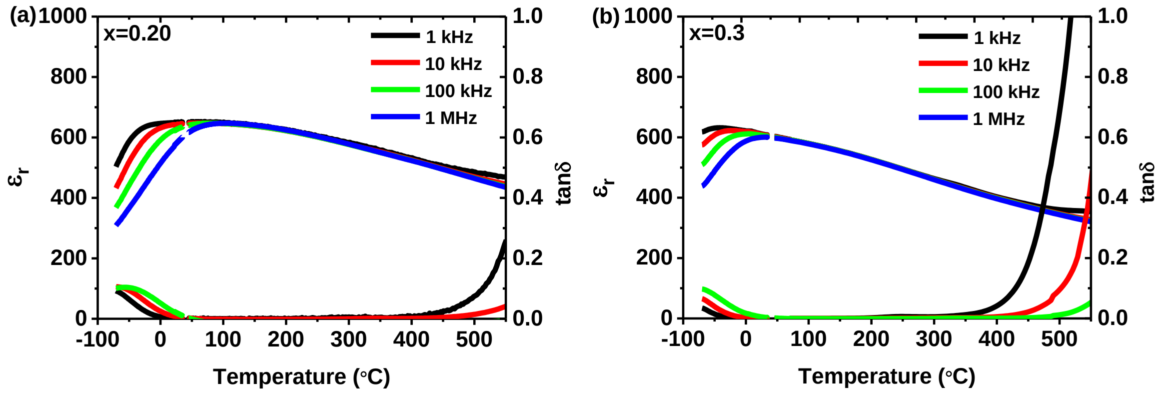

Figure 7.4 Temperature dependent relative permittivity and tanδ for (a) *x* = 0.20 and (b) *x* = 0.3, over the temperature range -70 °C to 550 °C (break indicates the changeover of low and high temperature instruments).

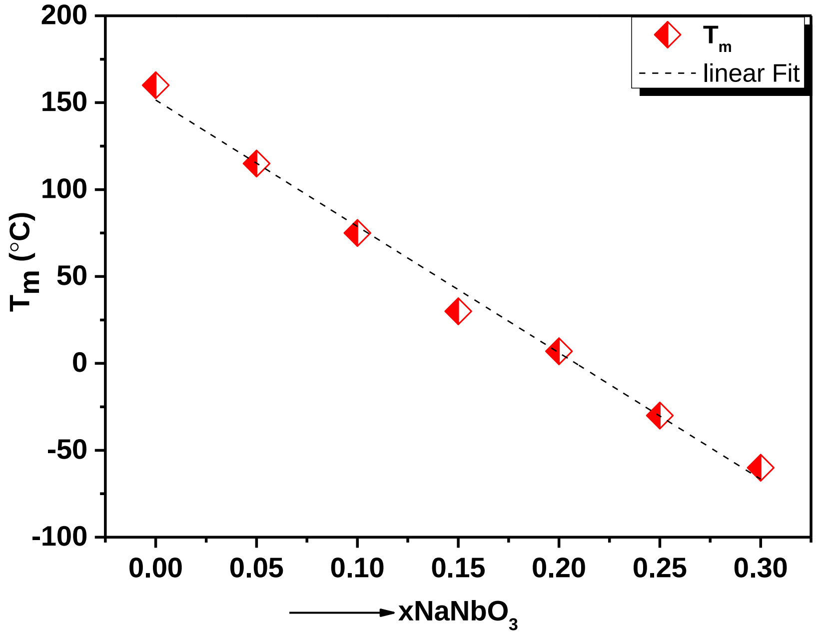

Figure 7.5 Trend of falling of temperature corresponds to maximum relative permittivity, T_m as a function of $NaNbO_3$ content.

Table 7.1 Summary of the dielectric properties of 0.45BCT-(0.55-*x*)BMT-*x*NN; ε_r and tanδ values measured at 1 kHz.

Sample	T_m (°C)	$\varepsilon_{r\ max}$	T-range (°C) ε_r±15%	T-range (°C) tanδ ≤ 0.02
x = 0	160	1060	70-600 950±15%	160-550
0.05	115	850	50-600 830±15%	80-490
0.10	75	665	~ 20-550 580±15%	40-420
0.15	30	685	~ 20-500 585±15%	25-450
0.20	0	650	-70-500 600±15%	-20-400
0.25	-30	620	-70-330 565±15%	-40-400
0.30	-55	630	-70-300 550±15%	-60-390

7.2.3 dc resistivity and RC constant

The dc resistivity values estimated using a Keithley electrometer were plotted as a function of inverse absolute temperature, Figure 7.6. Values of dc resistivity were similar in the high temperature regime for all studied compositions while different at low temperatures. This difference in resistivity at low temperature, may be attributed to the difference in charge carriers concentration rather than different conduction mechanism which become similar by thermal assistance in the high temperature region [El-Mallah (2004)].

The recorded dc resistivity values were ~ 10^{10} Ω m at 250 ºC, and 10^{7} Ω m at 400 ºC. The activation energy deduced from conduction data was ~ 0.6 eV consistent with an oxygen vacancy migration mechanism [Acosta et al. (2012), Selvamani et al. (2012), Morrison et al. (1999)].

Values of RC constant were calculated from dc resistance and capacitance (1 kHz). For unmodified composition $x = 0$, value of RC constant was 10.4 s, decreased to ~ 4 s for compositions $x = 0.2$ and $x = 0.3$. These values of RC constant were comparable to reported other high temperature dielectric ceramics [Acosta et al. (2012), Raengthon et al. (2012)].

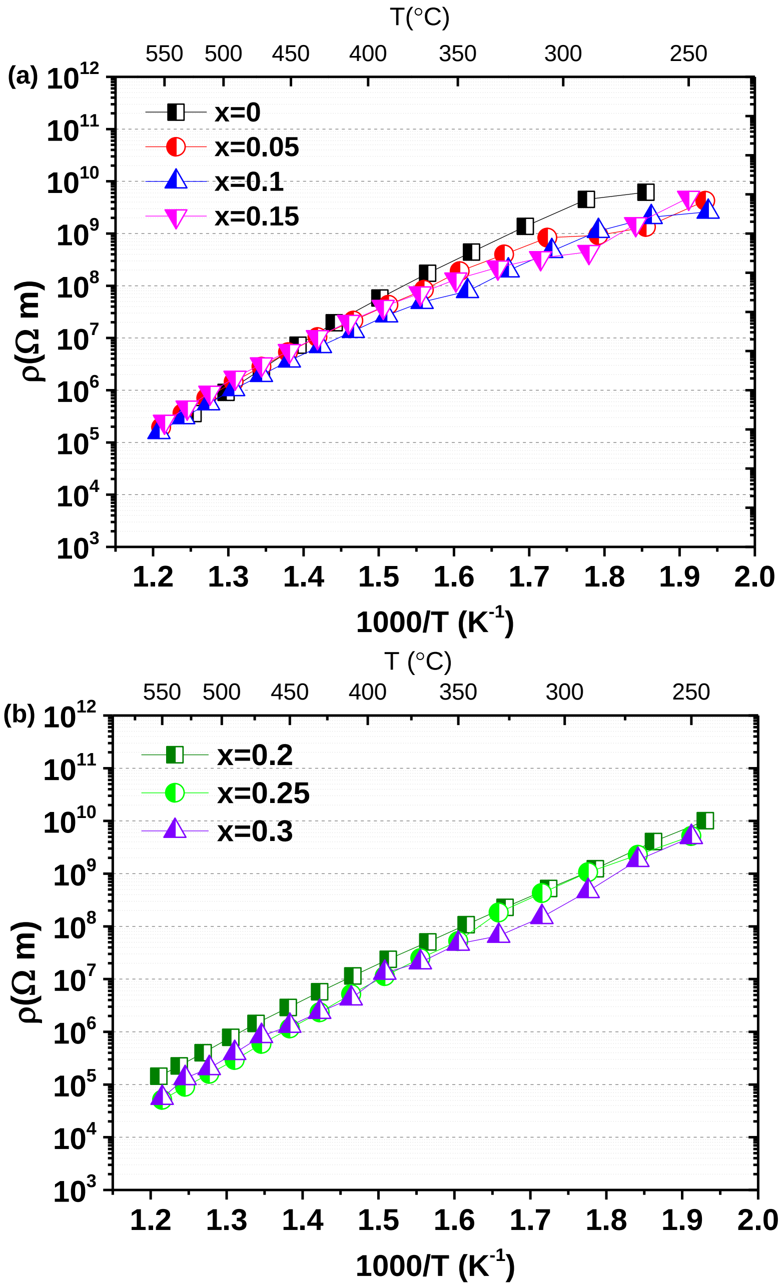

Figure 7.6 Logarithmic plot of dc resistivity as a function of 1/T for:(a) *x* = 0, 0.05, 0.1 and 0.15, and (b) 0.20, 0.25 and 0.30.

7.2.4 Polarisation-Electric Field analysis

Figure 7.7, displays the polarisation-electric field response measured at room temperature for an electric field of ~ 50 kV/cm (1 Hz). There was no evidence of ferroelectric character in any sample. For compositions $x \leq 0.1$, P-E plots were narrow indicating low but significant leakage current. This may be due to the high dispersion peak in tanδ around room-temperature. In the case of compositions $x \geq 0.15$, the P-E response was linear and typical of a capacitor with negligible dielectric loss.

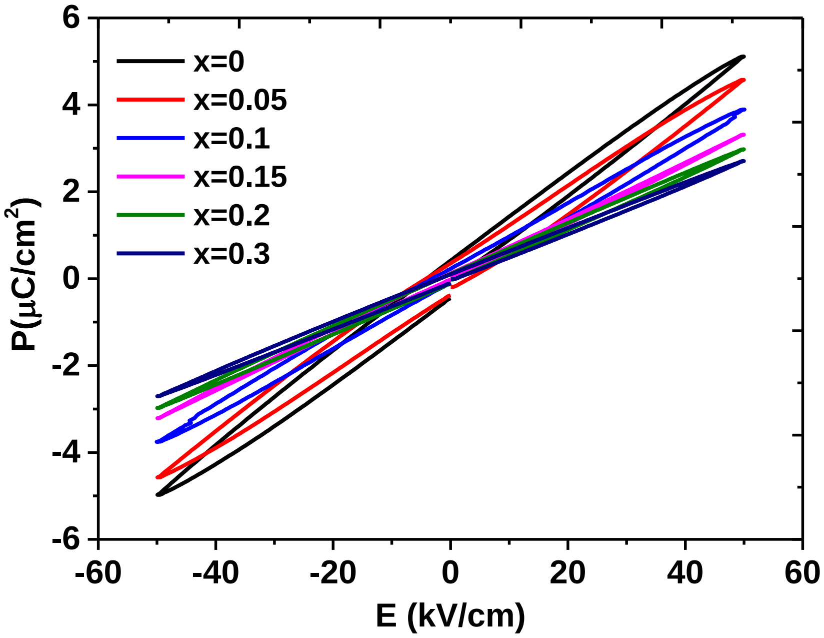

Figure 7.7 Polarisation-electric field response for the 0.45BCT-(0.55-*x*)BMT-*x*NN ceramic system ($x \leq 0.3$).

7.2.5 Relative Permittivity and Loss Tangent under dc Bias Field

Figure 7.8, shows the relative permittivity and loss tangent (tanδ) measured at 20 Hz as a function of dc bias fields over the temperature range from 20 ºC to 180 ºC for x = 0, 0.1, 0.2 and 0.3. All ceramic compositions, under dc bias field up to 40 kV/cm (maximum studied), retained stability in relative permittivity with no significant variation. This behaviour was in contrast to other ferroelectric materials, where a severe decrease in relative permittivity occurred under dc bias [Yu et al. (2002)]. Values of relative permittivity were consistent with the values of unbiased relative permittivity.

The values of loss tangent, tanδ (20 Hz) were high ~ 0.15 at room temperature significantly decreased to a value of 0.003 at 180 ºC for composition *x* = 0. A similar decreasing trend was also observed for compositions *x* ≥ 0.1, Figure 7.8.

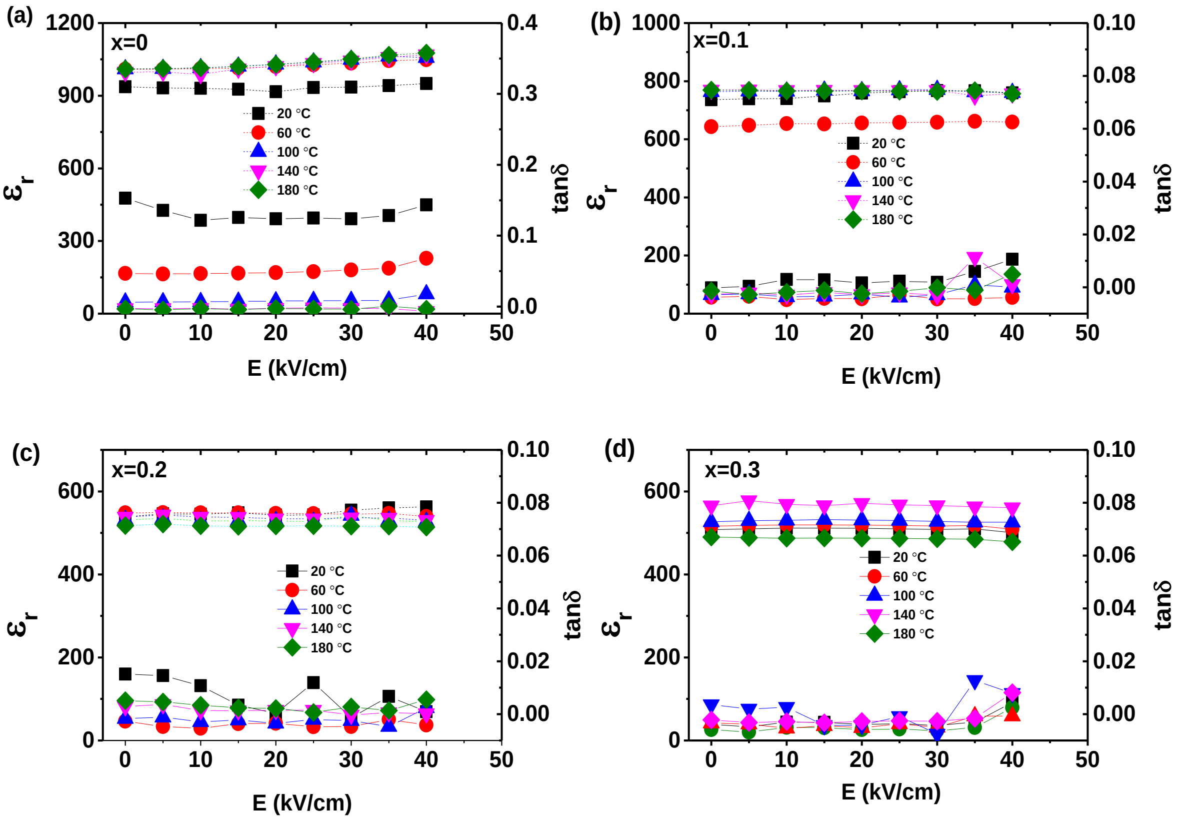

Figure 7.8 Relative permittivity and dielectric loss, tanδ under dc bias fields (20 Hz) at different temperature for:(a) *x* = 0, (b) *x* = 0.1, (c) *x* = 0.2 and (d) *x* = 0.3.

7.2.6 High Field P-E analysis and Energy Storage Density

The polarisation-electric field (P-E) behaviour was evaluated under high electric field ~ 90 kV/cm (20 Hz) over the temperature range from 20 ºC to 150 ºC, Figure 7.9. All studied ceramic compositions exhibited a linear behaviour and values of maximum polarisation decreased with the addition of NN content.

Plots of electric field dependent energy density over the temperature from 20 ºC to 150 ºC are presented in Figure 7.10. For unmodified composition *x* = 0, the energy density was temperature independent with a field up to ~ 50 kV/cm and then became temperature dependent with further increase of electric field (> 50 kV/cm) [Chapter 6]. However, for compositions $x \geq 0.1$, the energy density up to maximum field (90 kV/cm) was nearly the same at all temperatures. The energy density at room temperature for composition $x = 0$ was ~ 0.5 J/cm^3 at a maximum field of 90 kV/cm decreased to 0.36 J/cm^3 at temperature of 150 ºC. For $x = 0.2$, maximum values of energy density were ~ 0.2 J/cm^3 decreased to ~ 0.17 J/cm^3 for $x = 0.3$, Table 7.2. This decrease in energy density may be attributed to decrease of electric field induced polarisation in these samples. Higher fields would needed to achieve higher energy density for energy storage applications.

Table 7.2 Summary of the energy density (90 kV/cm) at different temperatures for *x* = 0-0.3.

Sample	Density(J/cm^3) (20 ºC)	Density(J/cm^3) 50 °C	Density(J/cm^3) 100 °C	Density(J/cm^3) 150 °C
0	0.5	0.4	0.4	0.36
0.1	0.3	0.28	0.26	0.27
0.2	0.21	0.2	0.2	0.19
0.3	0.17	0.16	0.15	0.157

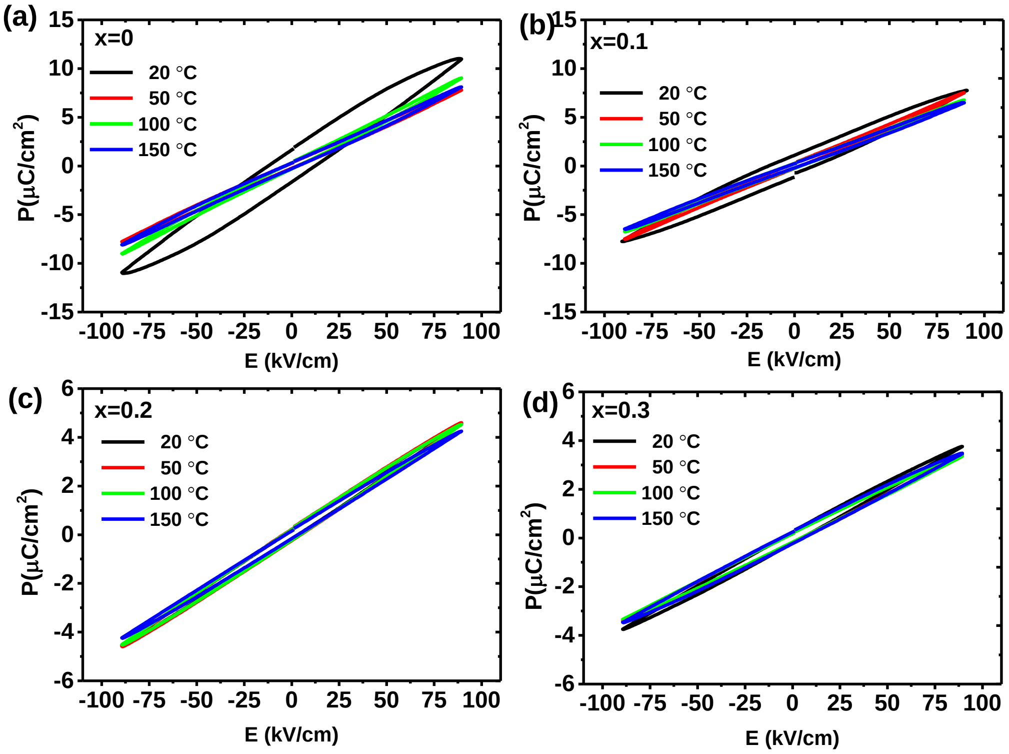

Figure 7.9 P-E response at a field of 90 kV/cm over the temperature range 20-150 °C for: (a) *x* = 0, (b) *x* = 0.1 (c) *x* = 0.2 and (d) *x* = 0.3.

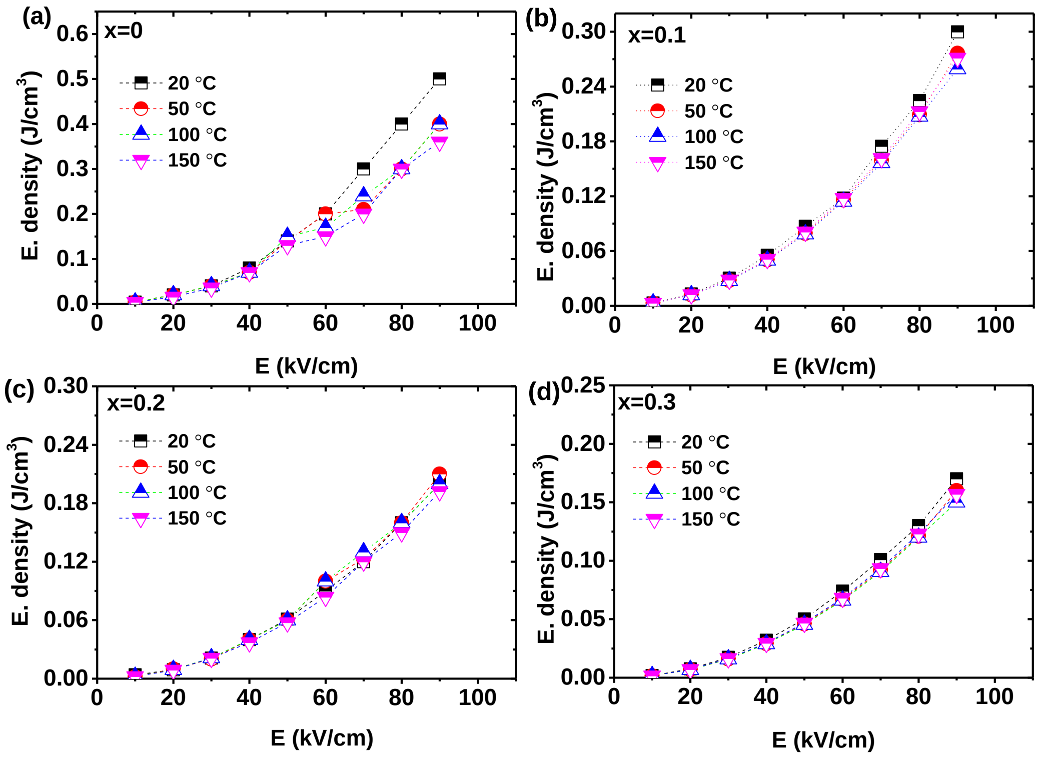

Figure 7.10 Energy storage density up to a field of 90 kV/cm over temperature from 20 °C to 150 °C for: (a) *x* = 0, (b) *x* = 0.1 (c) *x* = 0.2 and (d) *x* = 0.3.

7.2.7 Microstructural analysis

The grain microstructure of polished and chemically etched samples are shown in Figure 7.11. The grain size was estimated by using linear intercept method. All samples had relative densities of 91-94%. Values of the estimated average grain sizes increased with $NaNbO_3$ ($x > 0.1$) content from ~ 3 µm for $x = 0$ to ~ 7 µm for $x = 0.3$, Table 7.3. A minor second phase was also evident for compositions $x = 0$ and 0.1, whereas, the tiny white spots on grains for $x = 0.1$ and 0.3 correspond to some contamination during polishing or etching.

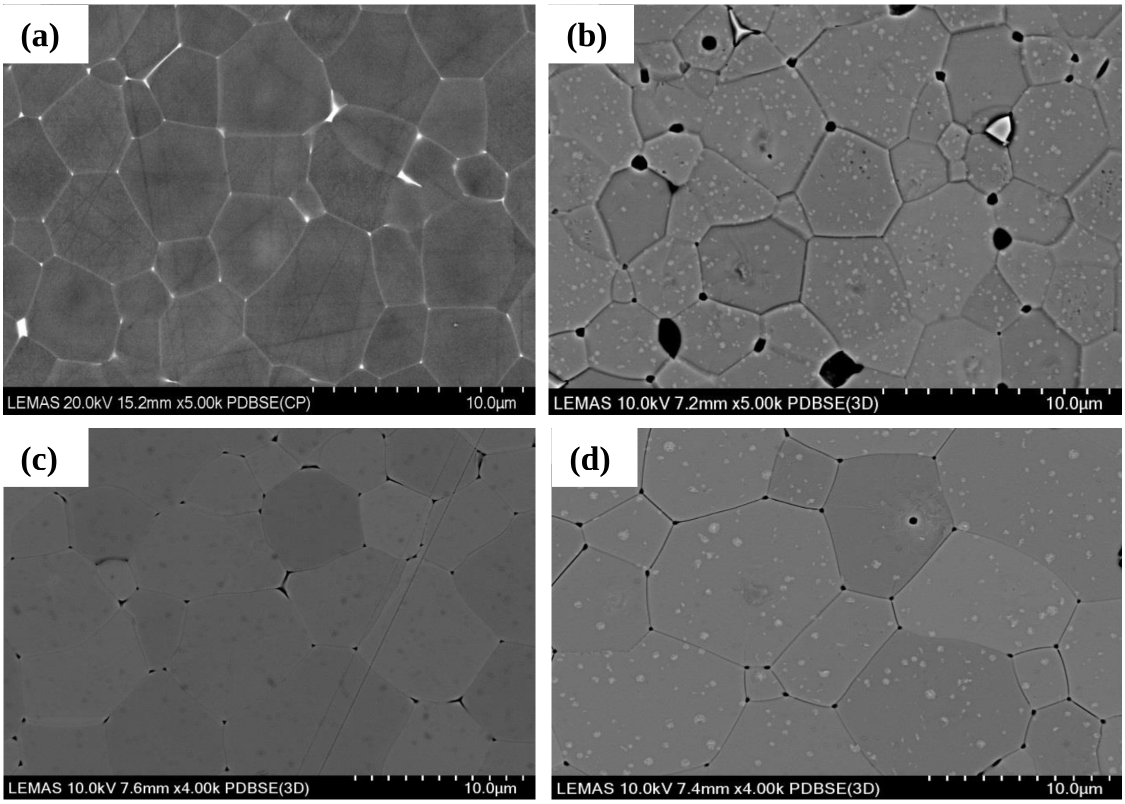

Figure 7.11 SEM micrographs of chemically etched polished surfaces for: (a) $x = 0$, (b) $x = 0.1$, (c) $x = 0.2$ and (d) $x = 0.3$.

Table 7.3 Average grain size, absolute and relative densities for the 0.45BCT-(0.55-*x*)BMT-*x*NN system.

Sample (*x*)	Average grain size (μm)	Density (g/cm^3)	% relative density
0	3	5.4	91
0.05	3	5.9	93
0.1	3	5.8	93
0.15	4	5.9	94
0.2	6	5.6	91
0.25	6	5.8	93
0.3	7	5.7	91

7.2.8 Conclusions

A series of temperature-stable perovskite relaxor dielectrics have been developed with wide operating temperature ranges. The temperature-dependence of relative permittivity for composition $x = 0$, was $\varepsilon_r = 950\pm15\%$ over the temperature range 70 ºC-600 ºC. A composition $x = 0.2$ exhibited a variation in relative permittivity within ±15% from -70 ºC to 500 ºC, along with low dielectric loss. Composition $x = 0.3$ shifted T_m to even lower temperatures, extending the temperature range of $\tan\delta \leq 0.02$ to -60 ºC and remain below 0.02 up to 300 ºC, maintaining $\varepsilon_r = 550\pm15\%$ from -70 ºC to 300 ºC.

The loss tangent values were far lower, and the relative permittivity values slightly higher than the reported $CaZrO_3$-modified $Na_{0.5}Bi_{0.5}TiO_3$ ceramics which have similar operational temperature ranges to the new materials: for example $CaZrO_3$-modified $Na_{0.5}Bi_{0.5}TiO_3$ have loss tangent up to 10% at ≤ 400 ºC compared to only 2%

for the new BCT-BMT-NN compositions [Acosta et al. (2012)]; the upper temperature in the ε_r±15% specification range is also higher for 0.45BCT-(0.55-x)BMT-xNN.

Relative permittivity under dc bias up to maximum field tested 40 kV/cm retained similar values as zero bias for all studied compositions. The values of energy storage density for composition $x = 0$ were ~ 0.5 J/cm^3 at a field of 90 kV/cm but decreased to 0.2 J/cm^3 and ~ 0.17 J/cm^3 for $x = 0.2$ and $x = 0.3$, respectively.

The dc resistivity values were of the order of 10^{10} Ω m at 250 ºC and 10^7 Ω m at 400 ºC, with activation energy of conduction estimated at ~ 0.6 eV, and RC constants of 10.4 s for $x = 0$ and ~ 4 s for compositions $x = 0.2$ and 0.3 (at 300 ºC).

Chapter 8

Dielectric and Ferroelectric Properties of the (1-x)$BaTiO_3$-$x$$Bi(Mg_{0.5}Zr_{0.5})O_3$ Ceramic System

8.1 Summary

This chapter outlines the dielectric and ferroelectric properties of the (1-x)$BaTiO_3$-$x$$Bi(Mg_{0.5}Zr_{0.5})O_3$ ceramic system, abbreviated as (1-x)BT-xBMZ. Ceramics in the solid solution series (1-x)BT-xBMZ, for $x \leq 0.5$, were fabricated by solid state processing. A single-phase was confirmed by X-ray powder diffraction for compositions $x < 0.5$. Ceramic samples $x \leq 0.05$ were indexed as tetragonal perovskite; a change to cubic perovskite occurred for compositions $x \geq 0.1$.

Plots of relative permittivity (ε_r), versus temperature exhibited a sharp Curie peak for $x = 0$, which changed to double peaks in the compositions $x = 0.03$ and 0.05. A single frequency-dependent peak occurred for compositions $x \geq 0.1$. A progressive decline in $\varepsilon_{r\ max}$ for compositions $x > 0.1$ led to near temperature-stable dielectric properties over a wide temperature range. Composition $x = 0.3$, exhibited a temperature dependent variation in $\varepsilon_r = 570$ within ±15% from -20 ºC to 430 ºC, and tanδ values ≤ 0.02 across the temperature range 30 ºC to 420 ºC. At $x = 0.4$, $\varepsilon_r = 600 \pm 15\%$ from 25 ºC-420 ºC with loss tangent, tanδ ≤ 0.02 from 55 ºC to 280 ºC (at 1 kHz). Values of dc resistivity were ~ 10^{10} Ω m at 250 ºC and ~ 10^{6} Ω m at 400 ºC.

Compositions $x = 0$ and $x = 0.03$ exhibited ferroelectric behaviour with similar remnant polarization, $P_r \sim 10$ μC/cm^2 but different coercive fields of ~ 5 kV/cm and ~ 8

kV/cm respectively. TEM-EDX analysis for the composition $x = 0.05$, which showed double peaks in relative permittivity-temperature plots revealed a core-shell grain structure.

8.2 Results and discussion

8.2.1 Phase analysis

The room temperature XRD patterns of the (1-x)BT-xBMZ crushed sintered samples, are presented in Figure 8.1 for the compositions studied, $0 \leq x \leq 0.5$. Compositions $x \leq 0.03$ were tetragonal perovskite. Composition $x = 0.05$ appeared to be cubic but with broadening to the {100} and {200} reflections (with no clear evidence of peak splitting to confirm a tetragonal distortion). All (cubic) peaks were sharper in $x \geq 0.1$ sample compositions. Peaks associated to secondary phase (bismuth titanate, Figure A3, Appendix) appeared in the composition $x = 0.5$, implying a solid solution at $0.4 < x < 0.5$.

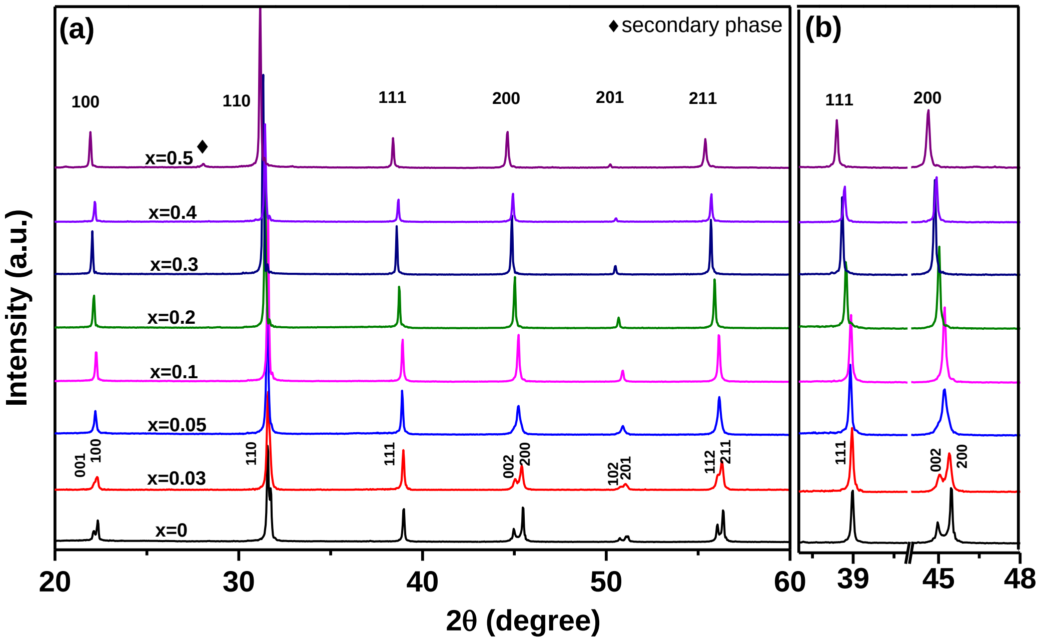

Figure 8.1 (a) XRD patterns at room temperature for (1-x)BT-xBMZ compositions $x \leq 0.5$ (b) highlighted {111} and {200} peaks.

The lattice parameters measured from the XRD data by least square refined method are plotted as a function of xBMZ in Figure 8.2. For tetragonal composition x = 0, the unit cell lattice parameters were $\boldsymbol{a}$ = 3.986±0.002 Å and $\boldsymbol{c}$ = 4.028±0.002 Å, and $\boldsymbol{a}$ = 3.996±0.001 Å and $\boldsymbol{c}$ = 4.022±0.003 Å for x = 0.03, illustrating a slight decrease in tetragonal distortion ($\boldsymbol{c/a}$) between x = 0 and 0.03. An increase in the cubic $\boldsymbol{a}$-lattice parameter was observed with increasing BMZ content for compositions $x \geq 0.1$.

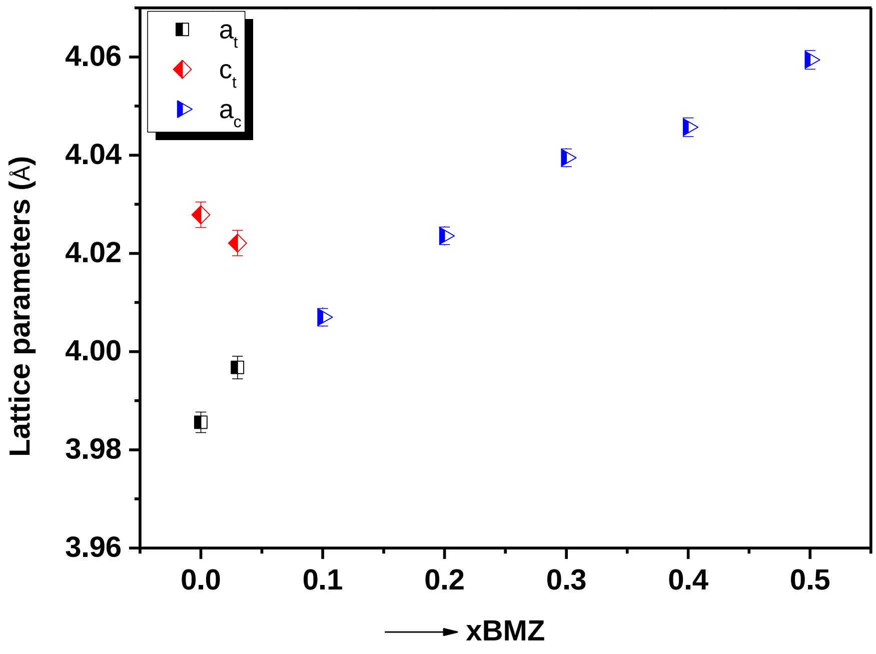

Figure 8.2 Variation of lattice parameters as a function of *x*BMZ content for the (1-*x*)BT-*x*BMZ ceramic system.

A summary of data presented in the following sections appears in Table 8.1.

8.2.2 Relative Permittivity-Temperature

Figure 8.3, shows the temperature dependence of relative permittivity and loss tangent (tanδ), measured at various single frequencies (1 kHz, 10 kHz, 100 kHz and 1 MHz) from room temperature (25 ºC) to 500 ºC. The end member $BaTiO_3$ (x = 0) displayed a sharp peak at a temperature of T_c ~ 130 ºC with a value of relative permittivity ~ 10,000, consistent with previous reports [Shvartsman and Lupascu (2012)].

The incorporation of x = 0.03 BMZ transformed the dielectric response from a ferroelectric with a sharp Curie peak to a broad peak with two maxima, with $\varepsilon_{r\ peak1}$ = 2900 at T_1 = 115 ºC and $\varepsilon_{r\ peak2}$ = 2700 at T_2 = 150 ºC, with a weak frequency dependence in T_1, Figure 8.3(b). The x = 0.05 sample also displayed twin peaks with an increased dispersion in T_1, and a decrease in T_1 to a 30 ºC, Figure 8.3(c). The temperature of the second peak, T_2, in $x = 0.05$ was similar to that of composition $x = 0.03$ (~ 150 ºC).

Increasing the BMZ content to $x = 0.1$ produced a single, broad relaxor dielectric peak, with T_m ~ -20 ºC (1 kHz) and a reduction in $\varepsilon_{r\ max}$ to ~ 1440, Figure 8.4(d). Further increase in xBMZ continued to decrease $\varepsilon_{r\ max}$ creating a drop in the rate of change in ε_r with temperature at $T > T_m$. At $x = 0.3$, the temperature dependent variation in $\varepsilon_r = 570$ occurred within ±15% from -20 ºC to 430 ºC and tanδ values were ≤ 0.02 across the temperature range 30 ºC to 420 ºC. For composition $x = 0.4$, $\varepsilon_r = 600 \pm 15\%$ from 25 ºC to 420 ºC, however, at temperature > 280 ºC dielectric losses increased sharply.

The reason for these higher dielectric losses is thought to relate to electrical conduction, which increases more sharply at high temperatures. Bismuth oxide volatilisation may be responsible for oxygen vacancy formation and thermally activated conduction [Skidmore et al. (2011), Bomlai et al. (2008), Bongkarn et al. (2008)].

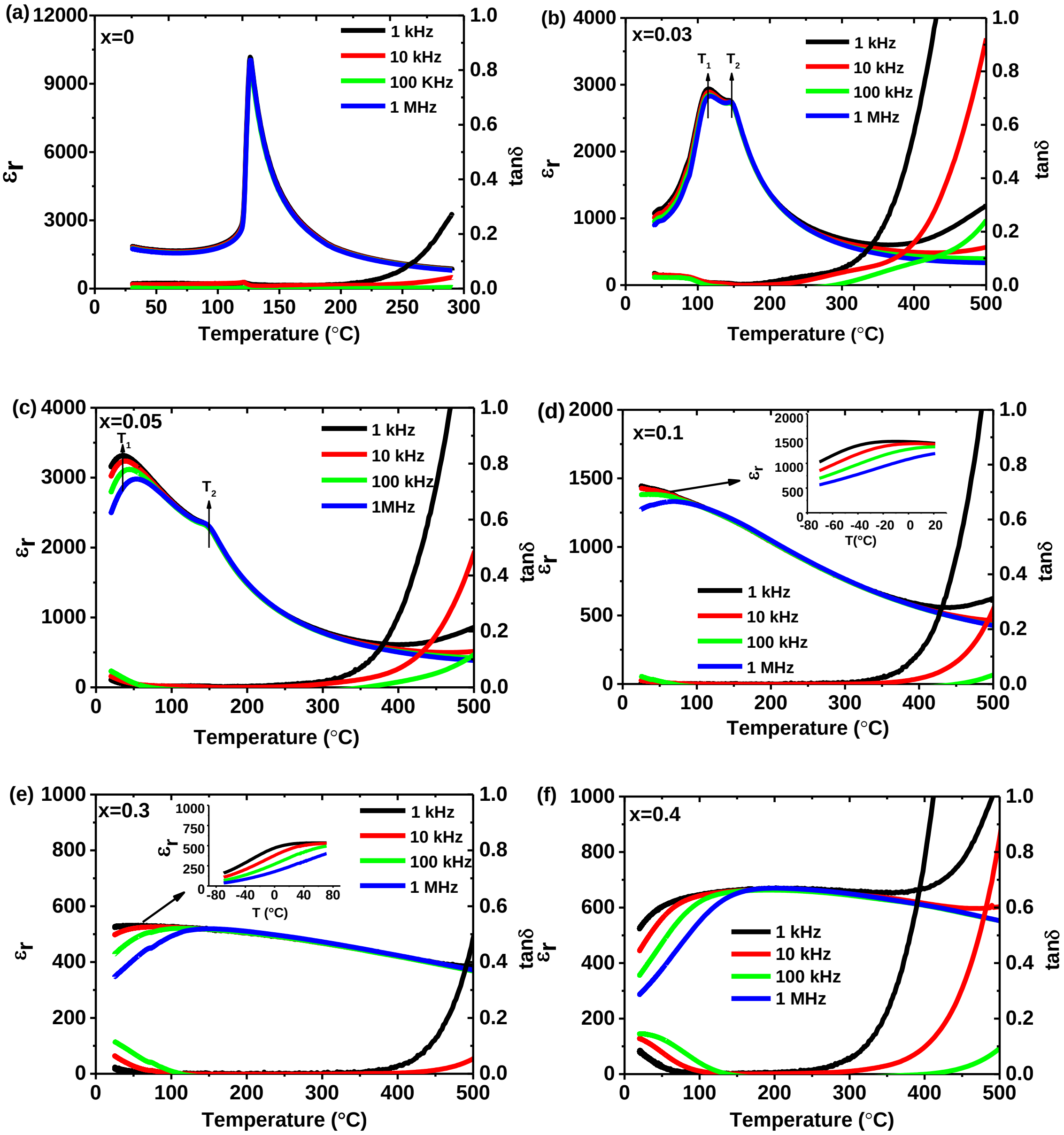

Figure 8.3 Temperature dependent relative permittivity (ε_r) and loss tangent (tanδ) for (1-*x*)BT-*x*BMZ compositions (a) *x* = 0, (b) *x* = 0.03, (c) *x* = 0.05, (d) *x* = 0.1, (e) *x* = 0.3, and (f) *x* = 0.4 (the inset shows ε_r-T plot from -70 ºC to 20-70 ºC.

Table 8.1 Summary of dielectric properties (1 kHz) of the (1-*x*)BT-*x*BMZ ceramic system ($x \leq 0.5$).

	Peak Temp (ºC)	$\varepsilon_{r\ max}$	T-rang (ºC) $\tan\delta \leq 0.02$	T-range (ºC) $\varepsilon_r \leq \pm 15\%$
$x = 0$	127	10,170	30-215	
0.03	$T_1 = 115$ $T_2 = 150$	$\varepsilon_{r1} = 2900$ $\varepsilon_{r2} = 2700$	100-220	
0.05	$T_1 = 30$ $T_2 = 150$	$\varepsilon_{r1} = 3300$ $\varepsilon_{r2} = 2300$	≤ 25-300	
0.1	-20	1440	-15-350	
0.2	10	680	5-380	
0.3	20	630	30-420	-20-430
0.4	60	650	55-280	25-420
0.5	70	570	75-250	50-420

8.2.3 dc resistivity

Figure 8.4 displays dc resistivity values as a function of temperature, measured at a fixed dc voltage of ~ 80 V for selected compositions $x = 0.05$ and $x = 0.4$ across the temperature span from 200 ºC to 550 ºC. A decrease in resistivity was observed with increasing x, most notably toward the lower range of temperatures. Composition $x = 0.05$ had a dc resistivity of ~ 10^{10} Ω m at 250 ºC and ~ 10^{6} Ω m at 400 ºC. The corresponding values of dc resistivity for $x = 0.4$ were of the order of 10^{9} Ω m at 250 ºC and 10^{6} Ω m at 400 ºC. There was an indication of a slight change in slope of resistivity plots was observed at ~ 320 ºC, corresponding to a change in activation energy of the electrical conduction process [Selvamani et al. (2012), Morrison et al. (1999)].

For composition $x = 0.05$, activation energy, $E_a = 0.54$ eV in the low temperature region (< 325 ºC) and 0.68 eV at higher temperatures. Values of low-temperature E_a, were 0.49 eV for $x = 0.4$ with corresponding high temperature E_a =

0.64. These values fall in the range normally associated with the migration of oxygen lattice vacancies [Selvamani et al. (2012), Morrison et al. (1999)].

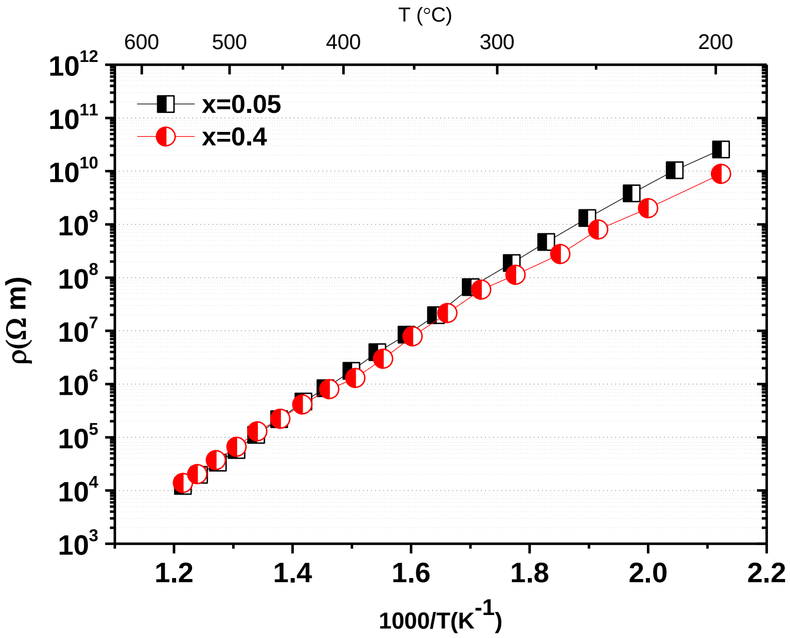

Figure 8.4 Variation of dc resistivity as a function of inverse of absolute temperature for compositions *x* = 0.05 and *x* = 0.4.

8.2.4 Ferroelectric Properties

Polarisation-electric field hysteresis loops measured at room temperature at 1 Hz are presented in Figure 8.5. Compositions *x* = 0 and *x* = 0.03 displayed ferroelectric behaviour with similar remnant polarization, $P_r \sim 10$ μC/cm^2 but with different coercive fields of ~ 5 kV/cm and ~ 8 kV/cm respectively. Sample *x* = 0.05 also displayed a P-E loop characteristic of a ferroelectric, but the loop was narrower than *x* = 0 and 0.03 and remanent polarisation was smaller, $P_r \sim 4$ μC/cm^2. It is noted therefore that the true symmetry of *x* = 0.05 cannot be centrosymmetric (at least under the application of a field). The XRD pattern in Figure 8.1 was cubic but with some broadening to the 100 and 200 peaks (but not 111); the P-E response gives weight to the premise that overlapping 200 and 002 tetragonal XRD peaks was responsible for this broadening.

For compositions $x \geq 0.1$, there was no evidence of ferroelectric character and the P-E response being that of a linear dielectric, Figure 8.5(b). The higher permittivity of the $x = 0.1$ compared to $x > 0.1$ samples was reflected in the respective P-E responses, Figure 8.5(b).

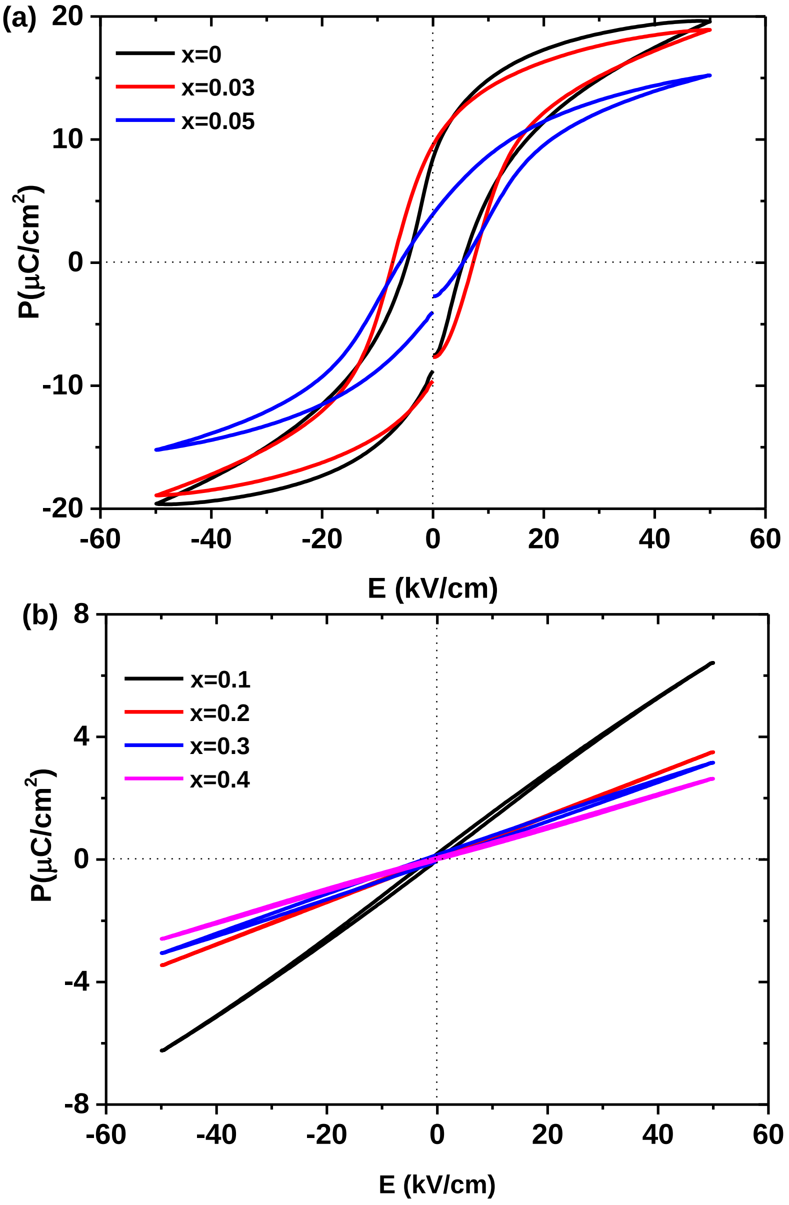

Figure 8.5 Polarisation-electric field loops for (1-*x*)BT-*x*BMZ compositions: (a) $x \leq 0.05$ and (b) $0.1 \leq x \leq 0.4$ at 50 kV/cm (1 Hz).

8.2.5 Piezoelectric Properties

The measurement of piezoelectric charge coefficient, d_{33} was carried out on poled samples by Berlincourt method. The ceramic samples were poled in silicon oil at a temperature of 30 °C for 20 min. The dc field was applied for all studied samples was ~ 40 kV/cm. The end member BT ($x = 0$) gave a peak value of d_{33} ~ 158 pC/N which decreased to ~ 55 pC/N for composition $x = 0.03$ and then ~ 30 pC/N for composition $x = 0.05$, Figure 8.6. Very small values of piezoelectric charge coefficients, $d_{33} \leq 10$ pC/N were recorded for compositions at $x \geq 0.1$.

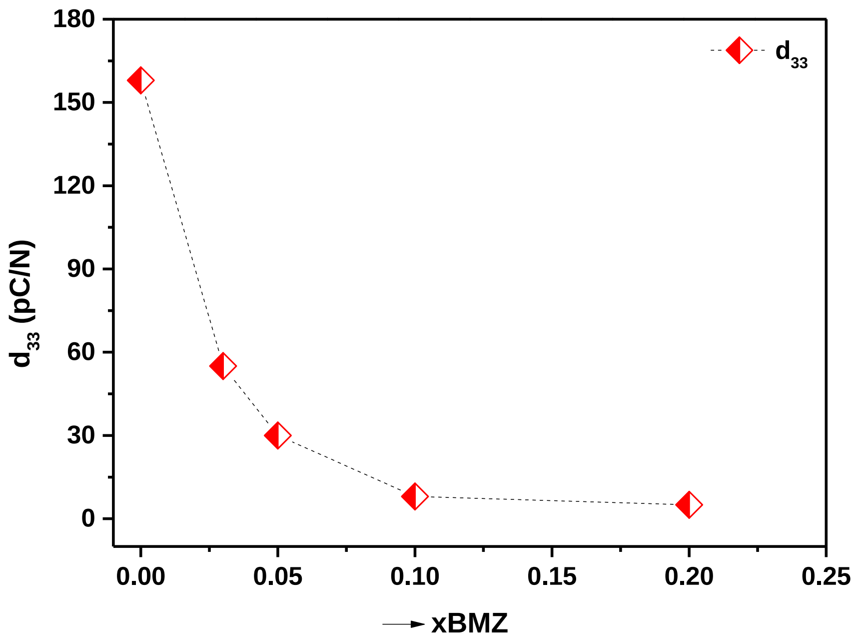

Figure 8.6 Variation of piezoelectric charge coefficient, d_{33} as a function of *x*BMZ ($x \leq 0.2$).

The electric field induced strain behaviour (1 Hz) at room temperature is shown in Figure 8.7. A typical butterfly S-E loop of a piezoelectric material was observed for composition $x = 0$ with maximum strain of ~ 0.25% at 50 kV/cm. The tetragonal ferroelectric composition $x = 0.03$ also gave a strain level at room-temperature of ~ 0.25% (at 50 kV/cm) but with an increase in negative strain compared to $x = 0$. These values were relatively high for a Pb-free piezoelectric [Skidmore et al. (2009), Royles et al. (2010), Zhu et al. (2011b), Coondoo et al. (2013)]. The *x* = 0.05 sample, gave a maximum strain of 0.32% (with little negative strain). Further incorporation of BMZ content into the solid solution drastically decrease the strain values to ≤ 0.03% with electrictrostictive nature for compositions $x \geq 0.1$.

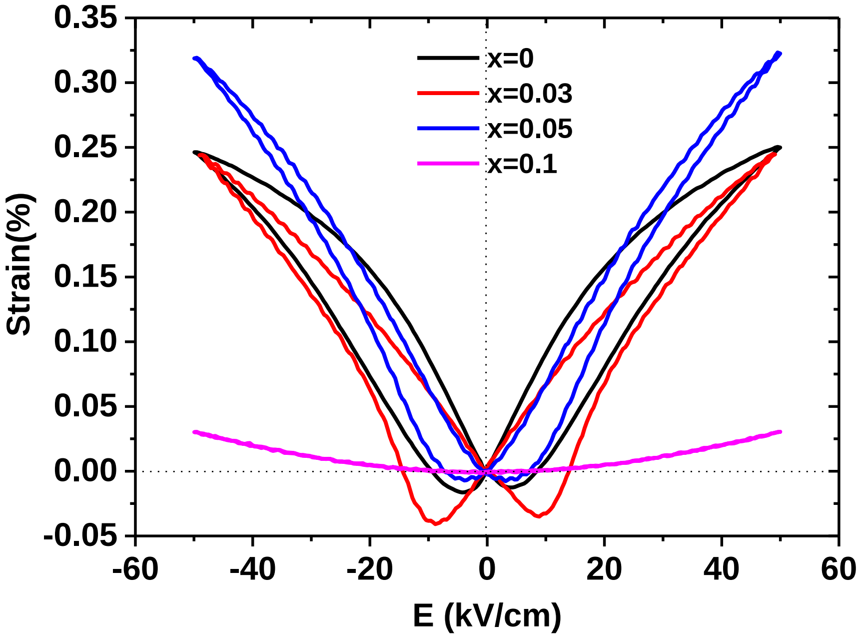

Figure 8.7 Electric field induced strain for (1-*x*)BT-*x*BMZ system, *x* ≤ 0.1 at room temperature (50 kV/cm, 1 Hz).

8.2.6 Microstructural analysis

Microstructural information on polished and chemically etched samples was obtained by using SEM. The grain size was estimated using the linear intercept method. SEM micrographs for selected compositions of sintered pellets are presented in Figure 8.8. For composition *x* = 0, the average grain size estimated of ~ 10 µm, but some grains were up to ~ 20 µm. A decreasing trend in grain size was observed by incorporation of BMZ content and the average reduced to ~ 5 µm for *x* = 0.4. For composition *x* = 0.2 and 0.3 some intergranular structure was evident in the SEM micrographs. The holes at the grain boundary may be due to over etching which destroyed the grain boundaries in composition *x* = 0.2. The grain size, geometrical and the relative density (based on the ratio of geometrical and theoretical density) are summarised in Table 8.3.

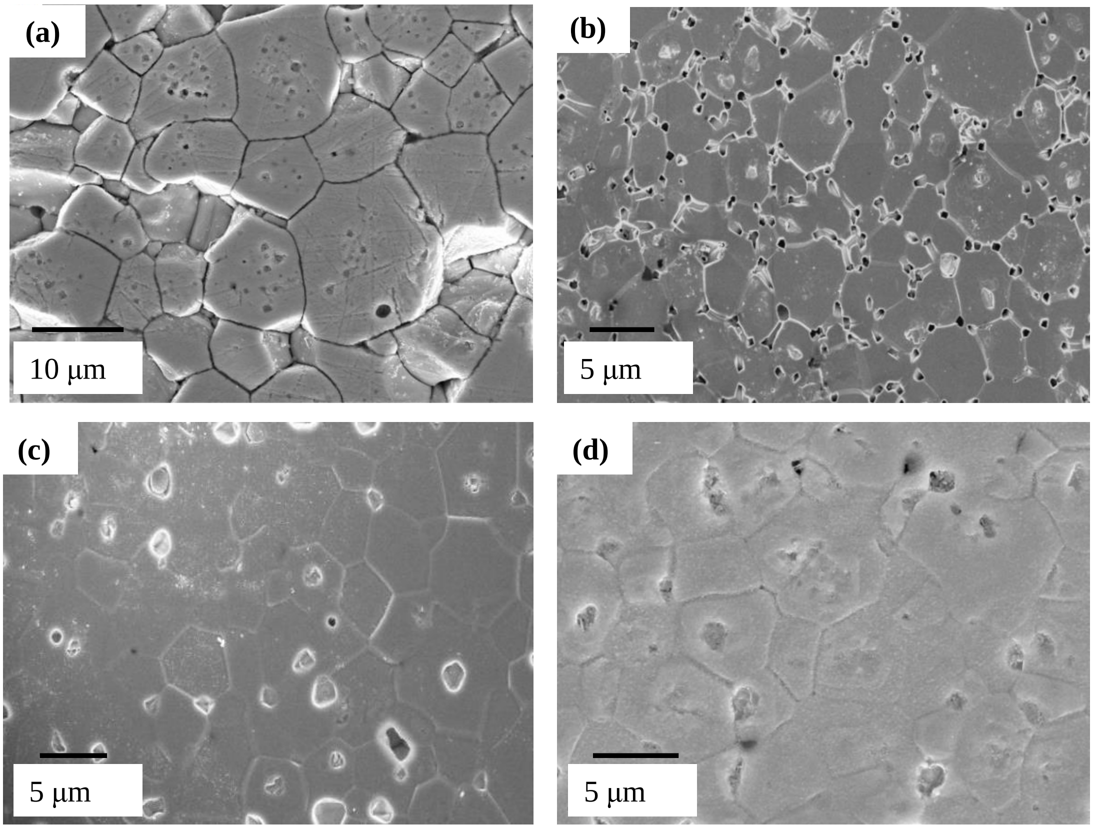

Figure 8.8 SEM micrographs for polished and chemically etched surfaces for: (a) *x* = 0, (b) *x* = 0.2, (c) *x* = 0.3 and (d) *x* = 0.4.

Table 8.2 Summary of the absolute, relative density and average grain size of the (1-*x*)BT-*x*BMZ ceramic system.

Sample(x)	Density (g/cm^3)	Relative density (%)	Average grain size(µm)
x = 0	5.7	95	9.7
0.03	5.6	93	-
0.05	5.5	95	3.0
0.1	5.4	90	4.0
0.2	6.0	94	7.0
0.3	6.1	94	5.8
0.4	6.2	93	5.0
0.5	6.1	90	4.8

8.2.7 TEM/EDX analysis

Transmission electron microscopy analysis was carried out for composition x = 0.05. Based on the previous reports, double peaks in ε_r-T plots were attributed to compositional variation in grains (core-shell structure) [Ogihara et al. (2009b), Zhu et al. (2011a)]. Therefore, composition x = 0.05 was selected for STEM-EDX analysis for such core shell structure investigation.

The sample was prepared from the sintered pellet by standard method; cutting, grinding, dimpling and ion beam polishing as described in section 3.37 [Chapter 3]. Analysis by STEM-EDX of x = 0.05 indicated a core-shell structure in many grains, Figure 8.9. Elemental mapping exhibited a core deficient in Bi and Zr and Mg relative to the grain shell, Figure 8.10. Hence, the double peaks in ε_r-T plots may be attributed to two different compositions, one from the core the other the outer regions of core-shell grains. Given that the T_2 anomaly was the minor peak in ε_r plots (Figure 8.3c), and that only a minor fraction of grains exhibited a core-shell structure, it is likely that T_2 corresponded to core material.

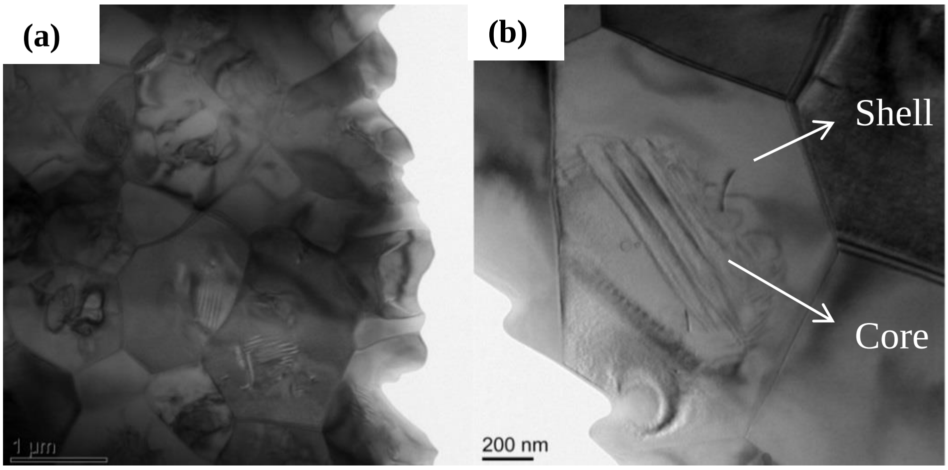

Figure 8.9 STEM micrographs for composition *x* = 0.05 (a) several grains and (b) single grain showing the core-shell structure.

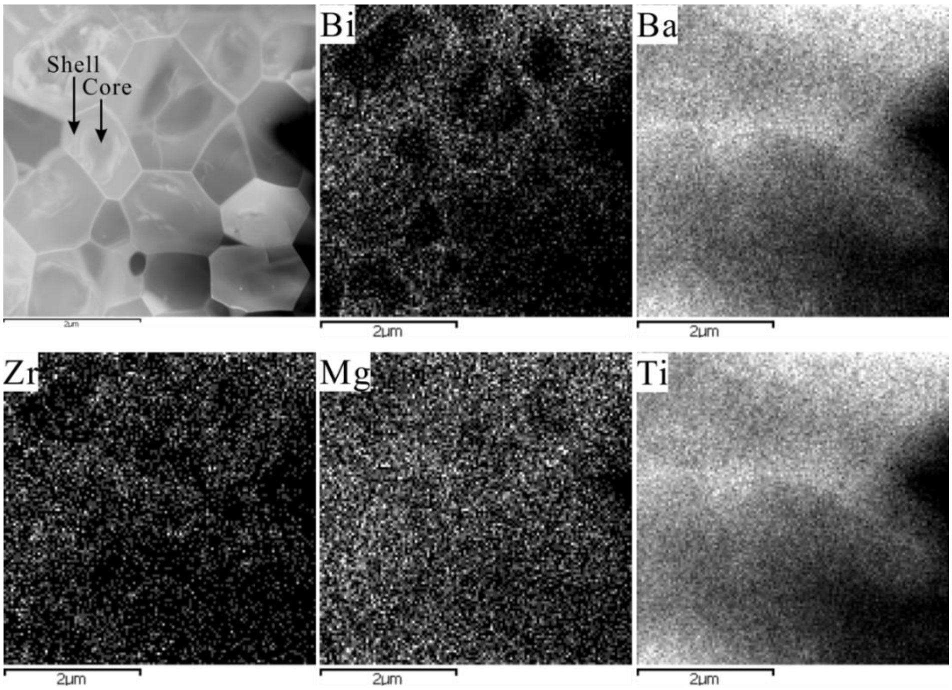

Figure 8.10 STEM dark field micrograph and EDX elemental mapping showing core-shell grain structures, with enhancement of Bi^{3+}, Mg^{2+}, Zr^{4+} in the outer shell for *x* = 0.05.

8.2.8 Conclusions

Ceramic compositions in the (1-x)BT-xBMZ system, for $0 \leq x \leq 0.5$ have been fabricated and studied. XRD data revealed a tetragonal structure for composition $x \leq 0.03$, changing to cubic for compositions ≥ 0.05. However, polarisation-electric field measurements indicated $x = 0.05$ was non-cubic (which may explain broadening to 100 and 200 XRD peaks).

At low levels of BMZ substitution, $x = 0.03$ and 0.05, a double peak was observed in plots of relative permittivity versus temperature. A change to normal relaxor dielectric plots, with a single, broad frequency dependent relative permittivity peak occurred for $x = 0.1$. For compositions $x = 0.3$ and 0.4 the peak relative permittivity value decreased such that a low variation in relative permittivity with temperature was observed over a wide temperature range. The values of ε_r were in the range ~ 600±15% from -20 ºC to 430 ºC for $x = 0.3$ and 25 ºC to 420 ºC for $x = 0.4$ (at 1 kHz).

The dc resistivity values recorded were of the order of 10^{10} Ω m at 250 ºC and 10^{6} Ω m at 400 ºC. Composition $x = 0.03$, close to the tetragonal-cubic phase boundary, with a ε_{r1} peak temperature of 115 ºC, gave a piezoelectric strain of ~ 0.25% (at 50 kV/cm). Composition $x = 0.05$ gave a strain of ~ 0.32%.

Chapter 9

Dielectric and Ferroelectric Properties of the (1-x)$Ba_{0.8}Ca_{0.2}TiO_3$-$x$$Bi(Zn_{0.5}Ti_{0.5})O_3$ Ceramic System

9.1 Summary

This chapter focusses on the study of dielectric and ferroelectric properties of the ceramic system (1-x)$Ba_{0.8}Ca_{0.2}TiO_3$-$x$$Bi(Zn_{0.5}Ti_{0.5})O_3$ for compositions $0 \leq x \leq 0.4$. The binary system is abbreviated as (1-x)BCT-xBZT hereafter for simplicity.

Based on X-ray powder diffraction analysis, the solubility range for this system was found at $x \sim 0.3$. The compositions $x = 0$ and 0.05 indicated tetragonal symmetry, which switched to cubic at $x \geq 0.1$. The temperature dependent relative permittivity plots exhibited a sharp Curie peak for $x = 0$, changing to a broad peak with no strong frequency dispersion for $x = 0.05$. A change to normal relaxor with frequency dependent peaks in plots of relative permittivity versus temperature occurred at $x \geq 0.1$. A significant reduction in the temperature dependence of relative permittivity occurred for $x = 0.3$, with $\varepsilon_r = 1030 \pm 15\%$ over the temperature range ~ 25 ºC-425 ºC, and loss tangent, $\tan\delta \leq 0.02$ from 90 ºC to 460 ºC. Values of dc resistivities at 300 ºC were of the order of 10^9 Ω m and decreased to ~ 10^6 Ω m at 450 ºC.

From polarisation-electric field responses, the $x = 0$ and 0.05 samples were ferroelectric with remanent polarisation, $P_r \sim 11$ μC/cm^2 and 10 μC/cm^2 at coercive fields, $E_c \sim 8$ kV/cm and 16 kV/cm, respectively. A change to a very narrow P-E loop occurred for composition $x = 0.1$ whilst linear dielectric behaviour was recorded for $x > 0.1$.

9.2 Results and Discussion

9.2.1 Phase analysis

For phase analysis, an X-ray powder diffractometer (Bruker D8, Cu, Kα~1.5406 Å); was used with scan speed, 1º/min, at room temperature.

Figure 9.1, shows the perovskite XRD patterns for powders of sintered pellets of (1-x)BCT-xBZT, x = 0-0.4 with highlighted {111} and {200} peaks. Single phase perovskite patterns were obtained for compositions $x \leq 0.3$. A secondary phase corresponding to the pattern of $Bi_4Ti_4O_{15}$ [Figure A4, Appendix], first appeared for $x = 0.34$, increasing in proportion at $x = 0.4$ indicating a solid solution limit at $x \sim 0.3$ (XRD detection limits are a few wt%). It is evident from the splitting of, for example the {100} and {200} peaks, that $x = 0$ and $x = 0.05$ samples showed tetragonal symmetry, with a slight decrease in tetragonal distortion between $x = 0$ and 0.05. The compositions $x \geq 0.1$ were indexed as a cubic perovskites with no evidence of peak splitting of {200} peaks, but the peak showed slight broadening relative to $x > 0.1$ samples.

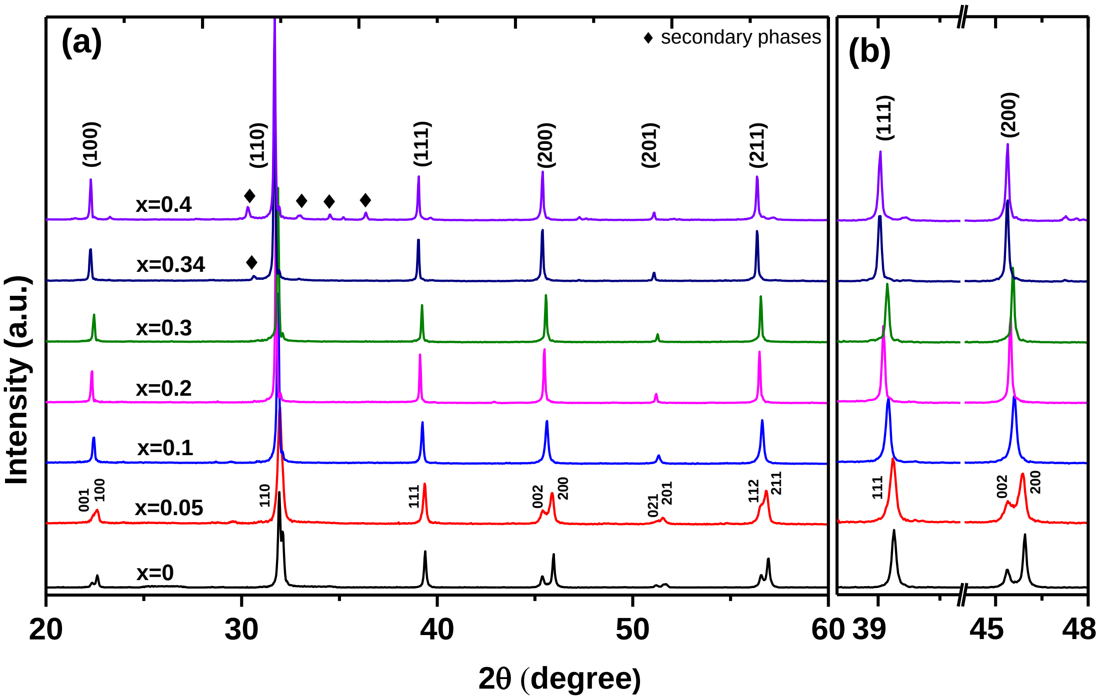

Figure 9.1 XRD patterns of crushed sintered ceramic pellets of (1-x)BCT-xBZT ceramic system, $x \leq 0.4$ (a) from 20-60 º2θ and (b) 38-48 º2θ.

Lattice parameters were deduced from d-spacing based on the XRD data using least square refinement method are plotted as function of xBZT, Figure 9.2.

Compositions x = 0 and x = 0.05 were of tetragonal symmetry with $\boldsymbol{a}$ = 3.948±0.002 Å, $\boldsymbol{c}$ = 3.996±0.002 Å, $\boldsymbol{c/a}$ = 1.012±0.002 for x = 0, whilst for x = 0.05, $\boldsymbol{a}$ = 3.962±0.002 Å, $\boldsymbol{c}$ = 3.994±0.003 Å and $\boldsymbol{c/a}$ = 1.008±0.003. The cubic compositions $x \geq 0.1$ showed little change in cubic lattice parameters: $\boldsymbol{a}$ = 3.976±0.001 Å for x = 0.1 and $\boldsymbol{a}$ = 3.978±0.001 Å for x = 0.3, Figure 9.2.

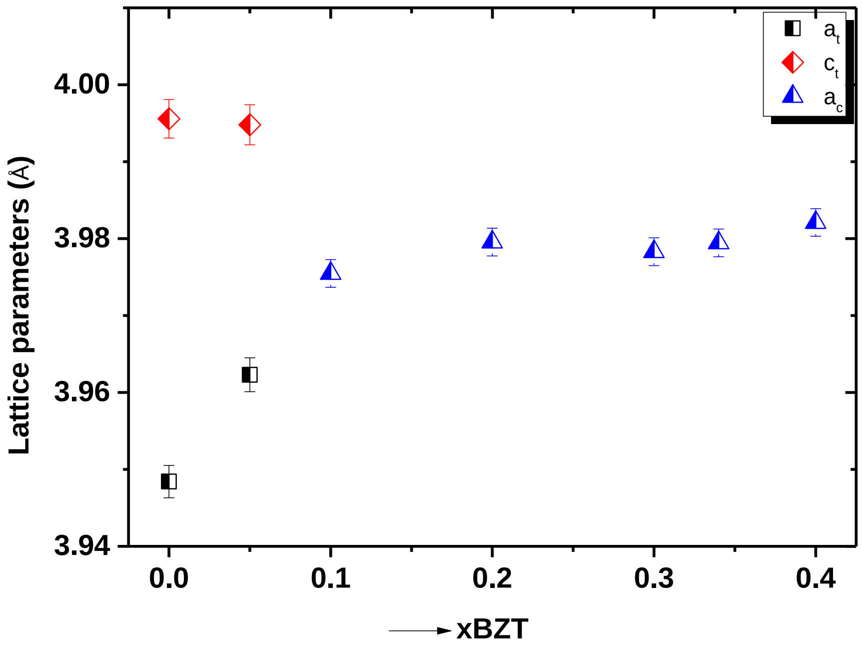

Figure 9.2 Variation of lattice parameters as function of *x*BZT content for (1-*x*)BCT-*x*BZT system.

The data from the following sections are summarized in Table 9.1.

9.2.2 Permittivity-Temperature and Loss Tangent

The relative permittivity, ε_r and loss tangent, tanδ, were plotted as a function of temperature at various frequencies (1 kHz-1 MHz), Figure 9.3. Composition $x = 0$, exhibited a reasonably sharp Curie peak, typical of a normal ferroelectric with Curie point, T_c ~ 130 ºC in the range reported for BCT at this composition [Levin et al. (2013)].

A change in relative permittivity to a broad peak, with little evidence of frequency dispersion, and peak temperature ~ 100 ºC occurred for $x = 0.05$. Further addition of BZT content into the solid solution, transformed the system to a typical relaxor at $x \geq 0.1$, with relative permittivity plots showing strong frequency dependence at temperatures, $T < T_m$. The temperature dependence of relative permittivity, ε_r at $T > T_m$ became less severe as the fractional substitution of Bi^{3+} and Zn^{2+} increased. The compositions $x = 0.3$ and 0.34 showing nearly temperature stable dielectric response and low loss tangent (tanδ).

Values of T_m (1 kHz) initially decreased from 130 ºC for $x = 0$ to 100 ºC for $x = 0.05$. The composition $x = 0.1$ exhibited the $\varepsilon_{r\,max}$ at ~ 25 ºC and then increased to 90 ºC for compositions $x = 0.3$ and $x = 0.34$, Figure 9.4. Values corresponding to maximum relative permittivity, $\varepsilon_{r\,max}$ decreased from ~ 12,000 for $x = 0$ to ~ 1180 at $x = 0.3$ (the limit of the single phase solid solution), Figure 9.4.

The temperature stable composition $x = 0.3$, gave $\varepsilon_r = 1030\pm15\%$ over the temperature range ≤ 25 ºC to 425 ºC measured at 1 kHz. Composition $x = 0.34$ exhibited a temperature stable relative permittivity $\varepsilon_r = 960\pm15\%$ over the temperature range ≤ 25 ºC to 440 ºC.

Low dielectric loss is important parameter for proposed capacitor applications. For composition $x = 0.3$, tanδ ≤ 0.02 over the temperature range 90-460 ºC; tanδ ≤ 0.01 over the range 110-420 ºC while tanδ ≤ 0.02 was remained across the temperature range from 90 ºC to 380 ºC for $x = 0.34$ (a biphasic composition).

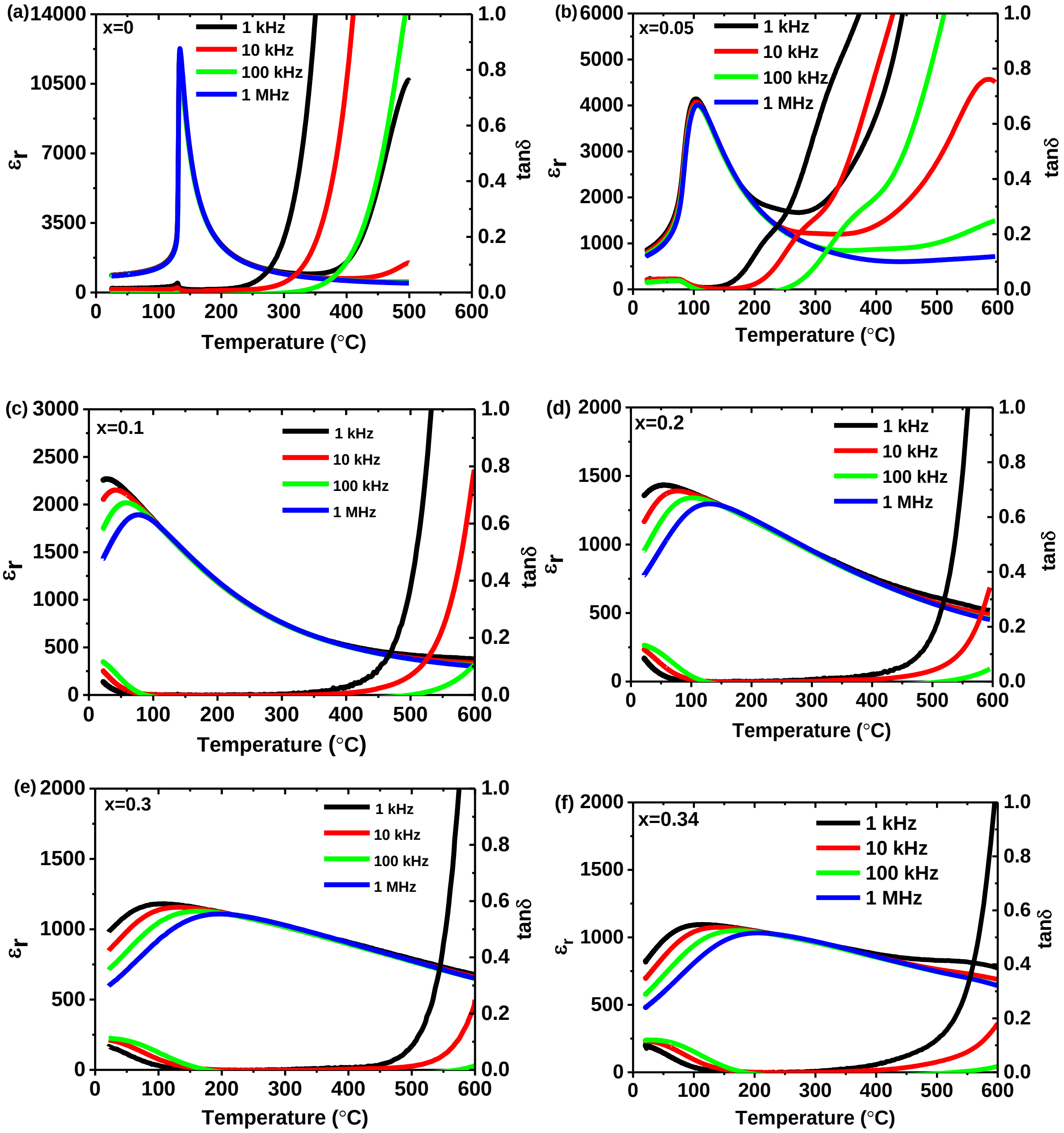

Figure 9.3 Relative permittivity and tanδ versus temperature at frequencies 1 kHz-1 MHz for: (a) *x* = 0 (b) *x* = 0.05 (c) *x* = 0.1 and (d) *x* = 0.2. (e) *x* = 0.3 and (f) *x* = 0.34.

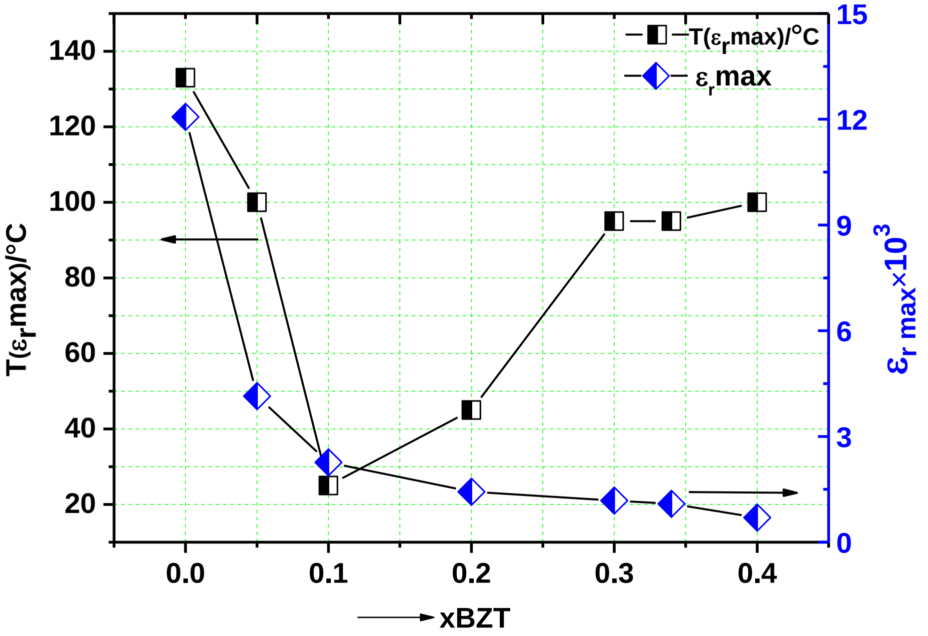

Figure 9.4 Variation of temperature corresponding to $\varepsilon_{r\ max}$ along with $\varepsilon_{r\ max}$ values as a function of *x*BZT content.

9.2.3 Relaxor behaviour and Curie-Weiss analysis

As mentioned above, composition $x = 0$ exhibited a sharp Curie peak while for $x = 0.05$ a broad permittivity peak with no clear evidence of frequency dispersion was observed. A Curie-Weiss analysis was carried out for the (1-*x*)BCT-*x*BZT system. For a typical ferroelectric, the relative permittivity above its Curie temperature obeys the Curie Weiss law, Equation 9.1 [Zhu et al. (2011a)];

$$\varepsilon_r = \frac{C}{T - T_\circ} \qquad \text{Equation 9.1}$$

where C is the Curie-Weiss constant; $T_\circ$ is the Curie-Weiss temperature. Figure 9.5 shows the plots of inverse of relative permittivity (ε_r^{-1}) versus T at 1 MHz for compositions $x = 0$ to $x = 0.3$. Curie Weiss analysis confirmed typical ferroelectric behaviour for $x = 0$ and $x = 0.05$ with a linear fit to plots of ε_r^{-1} versus T at $T > T_c$ or T_m. An alternative expression of the Curie Weiss law has proved popular for analysing ferroelectric and relaxor materials, Equation 9.2 [Zhu et al. (2011a), Morrison et al. (1999)]:

$$\frac{1}{\varepsilon_r}-\frac{1}{\varepsilon_{r\max}}=\frac{(T-T_{\varepsilon_r\,\max})^{\gamma}}{C} \qquad \text{Equation 9.2}$$

For an ideal ferroelectric, the γ coefficient is equal to unity, increasing to ~ 2 for a typical relaxor [Zhang et al. (2011), Bai et al. (2013)]. The experimental data for (1-x)BCT-xBZT are plotted in Figure 9.6: values of γ increased from γ = 1.28 for x = 0 to 1.32 for x = 0.05, and then to γ = 1.60-1.88 for the relaxor compositions x = 0.1-0.3.

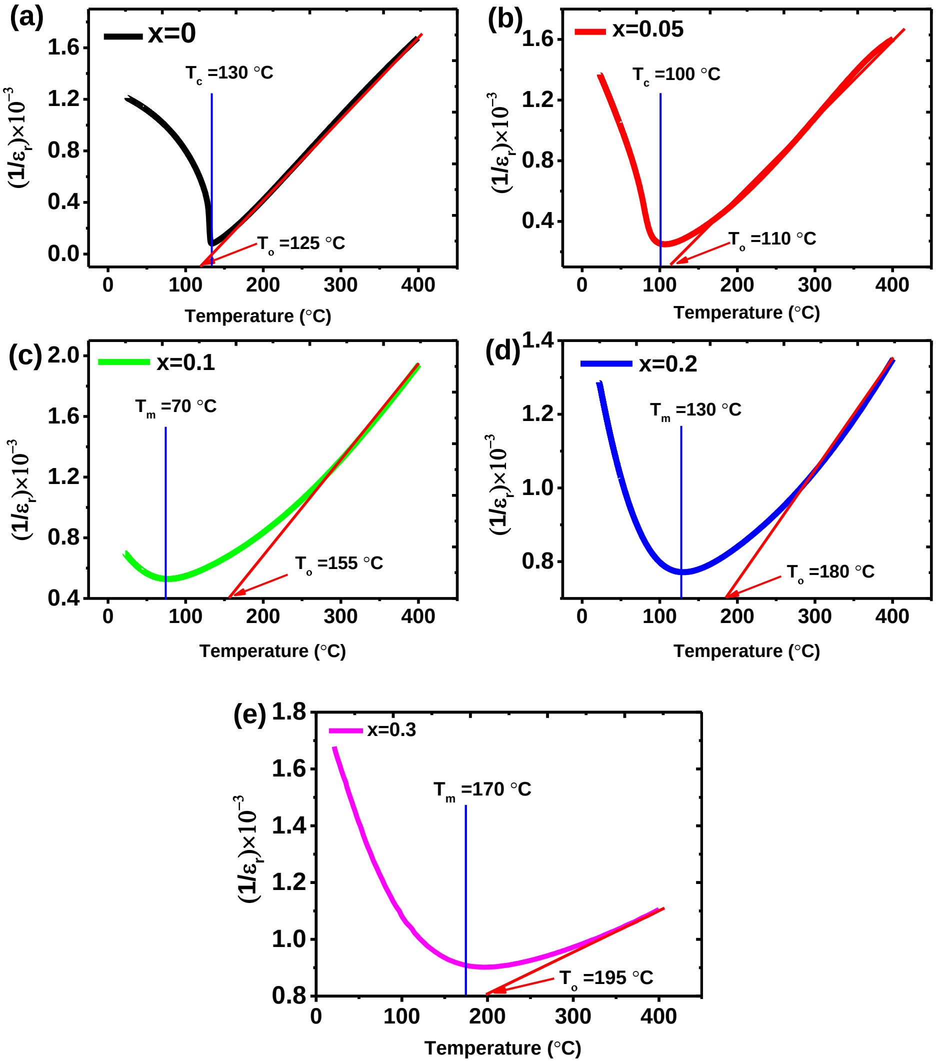

Figure 9.5 Plots of inverse of relative permittivity (1/εr) as function of temperature for x = 0-0.3 (1 MHz) (solid lines fitting to Curie-Weiss Law).

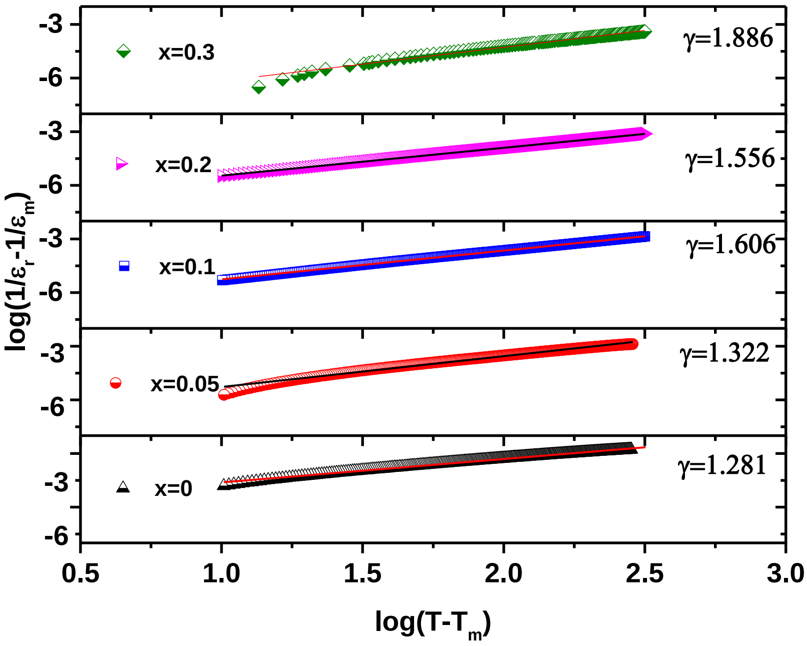

Figure 9.6 Values of log(1/ε_r-1/$\varepsilon_{r\ max}$) versus log (T-T_m) for *x* = 0-0.3, symbols represent the experimental data and solid line is the degree of fit.

9.2.4 dc resistivity

The values of dc resistivity were measured at fixed voltage of ~ 80 V for selected compositions *x* = 0.2 and *x* = 0.3 in the temperature range from ~ 250 ºC to ~ 550 ºC. Values of activation energies were deduced from the slope on conductivities-temperature versus 1/T (absolute temperature) plots. The logarithmic plots of dc resistivity for *x* = 0.2 and *x* = 0.3 as a function of 1/T (absolute temperature) are given in Figure 9.7.

Values of dc resistivities at 300 ºC were of the order of 10^9 Ω m and decreased to ~ 10^6 Ω m at 450 ºC. For sample *x* = 0.2, a discontinuity occurred at ~ 325 ºC; activation energies, E_a, from corresponding conductivities, were 0.58 eV in the low and 0.79 eV in the high temperature region. Both values fall in the range normally expected from oxygen ion migration in perovskites [Selvamani et al. (2012), Morrison et al. (1999), Raengthon and Cann (2012)], thus the discontinuity may signifies a change in carrier concentration/mobility, rather than a difference in charge carrier type. For x = 0.3, there was no discontinuity, with E_a being 0.79 eV across the temperature range measured.

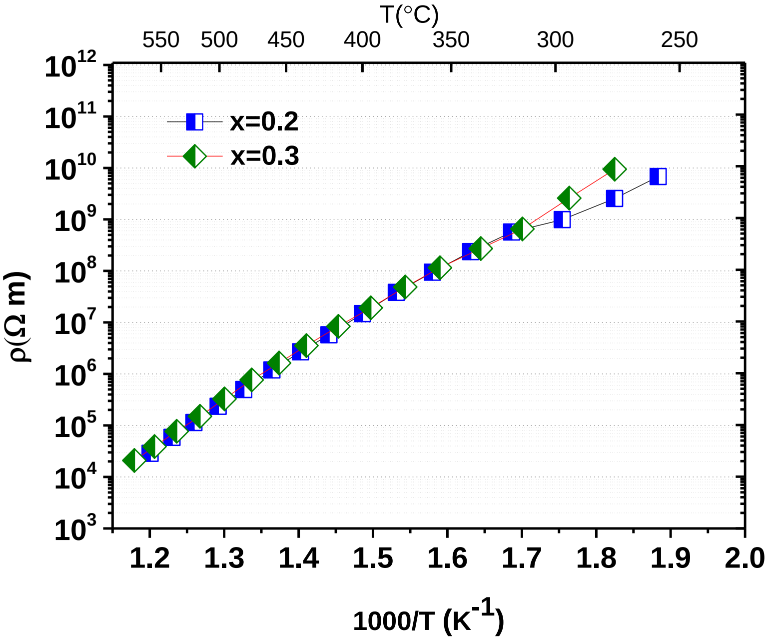

Figure 9.7 Logarithmic plot of dc resistivity versus inverse of absolute temperature (1000/T) for x = 0.2 and 0.3 measured at 80 V_{dc}.

9.2.5 Ferroelectric analysis

The polarization-electric field data for the (1-x)BCT-xBZT system for compositions x = 0-0.3 are shown in Figure, 9.8. The data were obtained at room temperature at a frequency of 1 Hz with maximum electric field of 50 kV/cm for each composition. The compositions x = 0 and x = 0.05 exhibited a typical ferroelectric hysteresis loops.

For x = 0, remnant polarisation was of the order P_r ~ 11 μC/cm^2 and coercive field, E_c ~ 8 kV/cm. For composition x = 0.05, P_r decreased slightly to 10 μC/cm^2 and coercive field, E_c increased to ~ 16 kV/cm indicating less facile ferroelectric domain switching. The hysteresis data for the composition x = 0.1 revealed a slight bending at high fields that may indicate a small ferroelectric contribution. Further increases in BZT content eliminated the ferroelectric properties, with a change to a low loss linear dielectric P-E response for compositions $x \geq 0.1$.

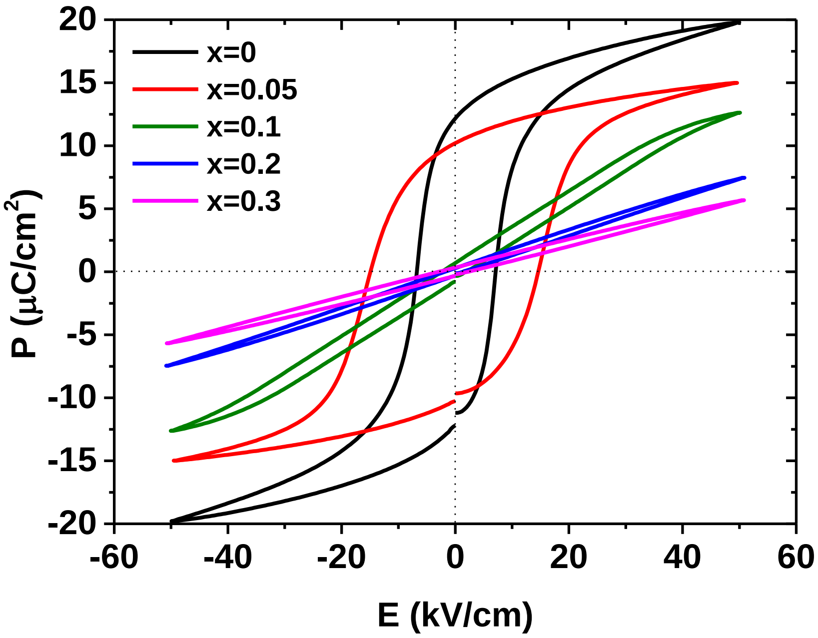

Figure 9.8 Room temperature P-E hysteresis response for (1-*x*)BCT-*x*BZT ceramic system for $x \leq 0.3$.

9.2.6 Piezoelectric Properties

The piezoelectric charge coefficient, d_{33} was measured by the Berlincourt technique. The samples were poled at ~ 60 kV/cm for 20 min in silicone oil at temperature of ~ 30 ºC. The piezoelectric charge coefficient, d_{33} for composition $x = 0$ was ~ 116 pC/N which decreased to a value of ~ 66 pC/N for $x = 0.05$, Figure 9.9. Further incorporation of BZT, led to a decrease in d_{33} to ~ 8 pC/N for relaxor compositions $x \geq 0.1$.

Figure 9.10 shows the bipolar strain-electric field response for compositions $x \leq 0.3$ measured at room temperature (50 kV/cm, 1 Hz). For $x = 0$ and 0.05, the strain-field curves exhibited butterfly loops and negative strains consistent with ferroelectric and piezoelectric behaviour. Other samples were electrostrictive in nature.

Values of maximum strain measured at 50 kV/cm were ~ 0.12% for *x* = 0, and ~ 0.10% for *x* = 0.05, with effective high-field $d_{33}^*(S_{max}/E_{max})$ ~ 240 pC/N and ~ 180 pC/N respectively. Compositions *x* = 0.1 exhibited electrostrictive maximum strain values of ~ 0.13% for sample *x* = 0.2 showed a very different S-E response, and a maximum strain of ≤ 0.04%.

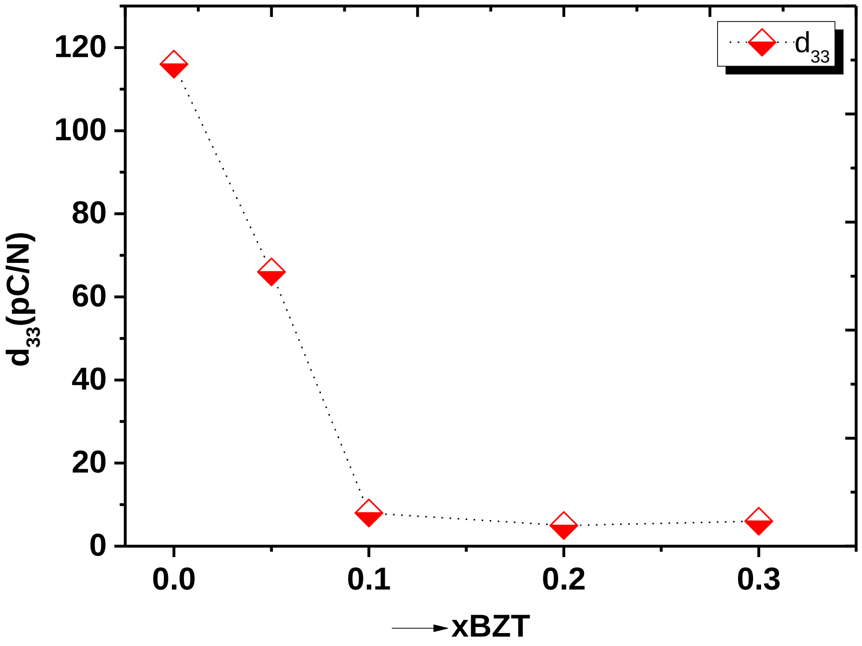

Figure 9.9 Variation of piezoelectric charge coefficients, d_{33} as a function of *x*BZT, *x* ≤ 0.3.

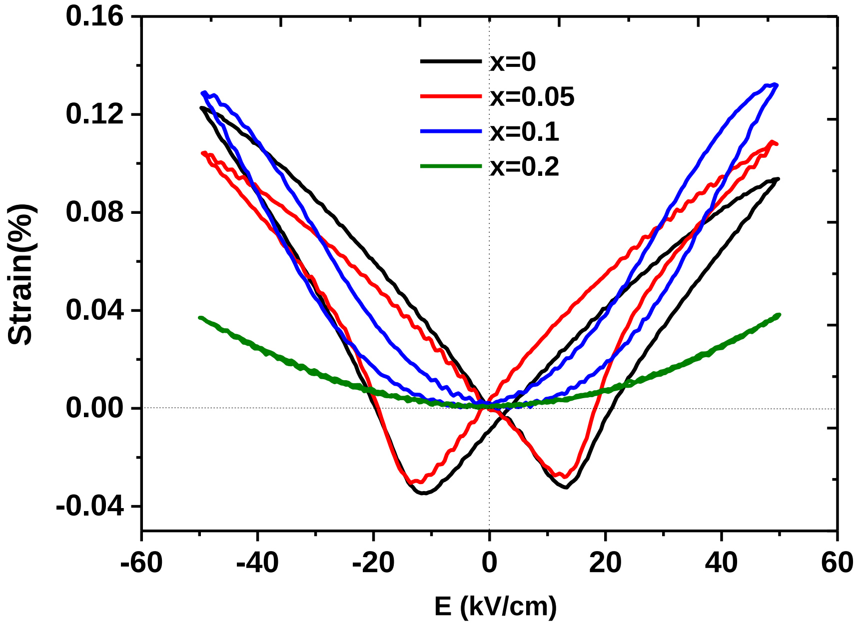

Figure 9.10 Strain-electric field response for compositions *x* ≤ 0.2 measured at 1 Hz.

Table 9.1 Summary of dielectric (1 kHz), ferroelectric and piezoelectric properties of (1-*x*)BCT-*x*BZT ceramic system (*x* ≤ 0.34).

Measured Parameters	*x* = 0	0.05	0.1	0.2	0.3	0.34
T_c or T_m (°C)	130	100	25	45	90	90
$\varepsilon_{r\ max}$ (1 kHz)	12060	4140	2260	1430	1180	1090
T-range (°C), $\varepsilon_r \leq \pm15\%$	-	-	-	-	25-425 (1030±15%)	25-440 (950±15%)
T-range(°C), tanδ ≤ 0.02	-	-	-	-	90-460	90-380
P_r (μC/cm^2) at RT	11	10	-	-	-	-
E_c (kV/cm)	8	16	-	-	-	-
d_{33} (pC/N)	116	66	8	-	-	-
Strain (%, 50 kV/cm)	0.12	0.11	0.13	0.04	-	-

9.2.7 Microstructural analysis

The SEM micrographs of polished and chemically etched samples are shown in Figure 9.11. A domain structure is evident for $x = 0$ (the ferroelectric sample). Microstructural analysis revealed that the incorporation of BZT content led to a decrease in grain size, Table 9.2. The average grain size estimated by the linear intercept method was ~ 7 µm for $x = 0$ (BCT) [Chapter 6] decreasing to ~ 2 µm for $x = 0.3$. For composition $x = 0.3$, the dark contrast grains may indicate a small amount of secondary phase which was not detected by XRD. The estimated average grain size and the values of geometrical densities are summarized in the Table 9.2.

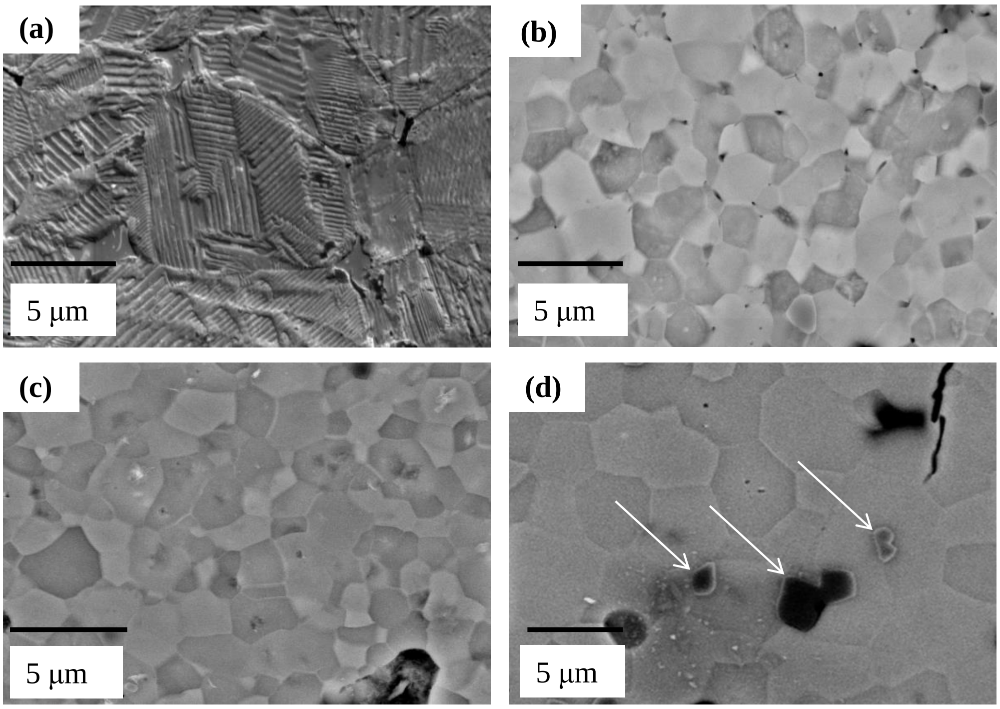

Figure 9.11 Back scattered electrons SEM micrographs for (a) $x = 0$ (b) $x = 0.1$ (c) $x = 0.2$ and (d) $x = 0.3$ (arrows indicate the second phase).

Table 9.2 Estimated average grain size and geometrical density for (1-*x*)BCT-*x*BZT ceramic system.

Composition (*x*)	Grain size (µm)	Density, ρ (g/cm^3)
$x = 0$	7	5.2
$x = 0.05$	5	5.3
$x = 0.1$	3	5.4
$x = 0.2$	3.5	5.7
$x = 0.3$	3.3	5.6
$x = 0.34$	2	5.2

It is appropriate to compare the present results to a closely related solid solution $(1-x)BaTiO_3-xBi(Zn_{0.5}Ti_{0.5})O_3$, (1-*x*)BT-*x*BZT [Huang and Cann (2008)]. The compositional range of tetragonal solid solution is more restricted and the cubic more extensive in (1-*x*)BCT-BZT, with a phase boundary at $0.05 < x < 0.1$ in (1-*x*)BCT-*x*BZT compared to $0.1< x < 0.2$ for (1-*x*)BT-*x*BZT [Huang and Cann (2008)].

Ferroelectric properties are comparable, with P_r ~ 10 µC/cm^2 for tetragonal 0.95BT-0.05BZT [Huang and Cann (2008)]. The Ca-modified ceramics displayed lower values of $\varepsilon_{r\ max}$ temperatures, T_m. For example T_m ~ 25 ºC for $x = 0.1$ in (1-*x*)BCT-*x*BZT, compared to ~ 45 ºC in (1-*x*)BT-*x*BZT for $x = 0.1$.

Importantly for proposed high temperature capacitor applications, the (1-*x*)BCT-*x*BZT system gives rise to a much wider range of temperatures with near-stable dielectric properties. In (1-*x*)BT-*x*BZT, the composition with least temperature variability $x = 0.34$, shows a change in ε_r from ~ 1600 to ~ 1200 in the temperature range of ~ 120-400 ºC; equivalent to a variation of 1400±15% about a mid-value. In contrast, the incorporation of Ca^{2+} generates a wider temperature range with low variability in permittivity, ≤ 25 ºC to 425 ºC, albeit with lower ε_r values.

9.2.8 Conclusions

Electrical properties of the solid solution (1-*x*)BCT-*x*BZT have been studied. The solid solution limit occurred for $x \sim 0.3$, as evidenced from XRD and SEM data. Dielectric measurements revealed a change from normal ferroelectric to relaxor behaviour for $x \geq 0.1$. Values of ε_r peak temperature decreased from ~ 130 ºC for $x = 0$ to ~ 25 ºC for $x = 0.1$ and then increased to 90 ºC for $x = 0.3$.

Polarisation-electric field measurement showed normal ferroelectric behaviour in $x = 0$ and 0.05 samples, with $P_r \sim 11$ µC/cm^2 for $x = 0$, and $P_r \sim 10$ µC/cm^2 for $x = 0.05$. Compositions $x > 0.1$ were linear dielectrics. Stability in relative permittivity over a wide temperature range was demonstrated for $x = 0.3$, with, $\varepsilon_r = 1030 \pm 15\%$ over the temperature range ≤ 25-425 ºC, and $\tan\delta \leq 0.02$ from 90 ºC to 420 ºC. The dc resistivity ranged from ~ 10^9 Ω m at 300 ºC to ~ 10^6 Ω m at 450 ºC.

Chapter 10

Dielectric Properties of the $(1\text{-}x)[0.5K_{0.5}Bi_{0.5}TiO_3\text{-}0.5Ba(Zr_{0.2}Ti_{0.8})O_3]\text{-}x Bi(Zn_{2/3}Nb_{1/3})O_3$ Ceramic System

10.1 Summary

The dielectric properties of ceramics in the relaxor system $(1\text{-}x)[0.5K_{0.5}Bi_{0.5}TiO_3\text{-}0.5Ba(Zr_{0.2}Ti_{0.8})O_3]\text{-}x Bi(Zn_{2/3}Nb_{1/3})O_3$, abbreviated as $(1\text{-}x)$[0.5KBT-0.5BZT]-xBZN were studied for compositions $x \leq 0.3$. X-ray powder diffraction patterns displayed a single phase cubic perovskite structure for $x < 0.3$ but secondary phases were present for $x = 0.3$.

The temperature corresponding to maximum relative permittivity, T_m, decreased from 150 ºC for $x = 0$ to 70 ºC for $x = 0.2$. Composition $x = 0.2$ exhibited the least temperature-dependence of relative permittivity, ε_r, with $\varepsilon_r = 805 \pm 15\%$ across a wide temperature range, from -20 ºC to 600 ºC; with $\tan\delta \leq 0.02$ from 50 ºC to 450 ºC. Values of dc resistivity were of the order of $\sim 10^9$ Ω m at 300 ºC for $x = 0.1$ and 0.2, and $\sim 10^8$ Ω m for $x = 0.3$.

10.2 Results and discussion

10.2.1 Phase analysis

Room temperature XRD patterns for crushed sintered ceramics are shown in Figure 10.1. Ceramic compositions $x \leq 0.2$ exhibited a single-phase cubic perovskite structure. Secondary phase of bismuth titanate appeared at composition $x = 0.3$.

Detailed analysis of XRD patterns revealed no evidence of peak splitting; hence all patterns were indexed according to cubic symmetry. Lattice parameters deduced by a peak profile fitting method indicated an increasing trend as a result of the incorporation of BZN.

The unit cell lattice parameters were found to be 3.990±0.002 Å for $x = 0$ increased to 4.019±0.004 Å for $x = 0.3$, Figure 10.2.

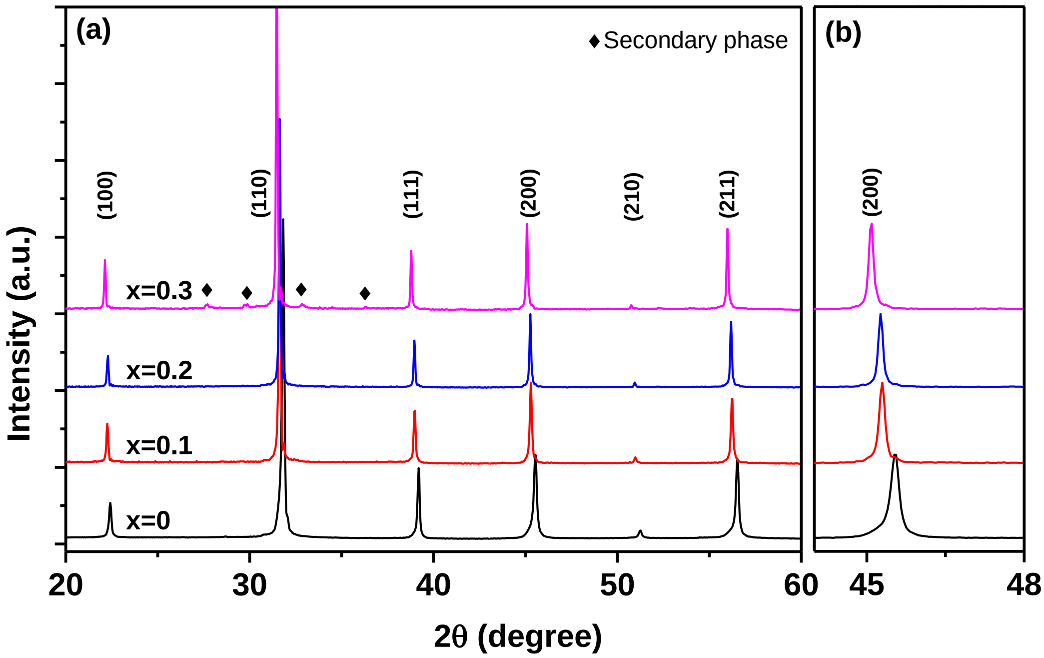

Figure 10.1 (a) XRD patterns for crushed sintered pellets of the (1-x)[0.5KBT-0.5BZT]-xBZN ceramic samples, $x \leq 0.3$ (b) Highlighted {200} reflection.

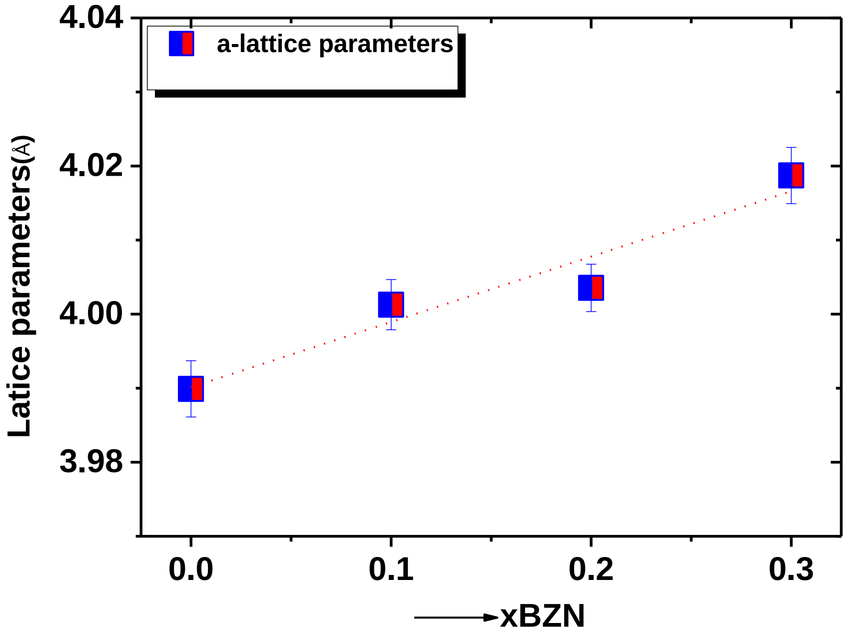

Figure 10.2 Variation of lattice parameters as a function of *x*BZN (*x* ≤ 0.3).

10.2.2 Relative Permittivity-Temperature

Plots of relative permittivity and tanδ as a function of temperature at various frequencies are shown in Figure 10.3 and 10.4. All compositions exhibited strong frequency dispersion below the temperature of maximum relative permittivity (T_m) consistent with relaxor characteristics. For the base composition 0.5KBT-0.5BZT (*x* = 0) the peak temperature T_m = 150 ºC [Chapter 5] and $\varepsilon_{r\ max}$ = 3080; in terms of its temperature range of stable permittivity, ε_r = 2750±15% occurred across a temperature range of 70-250 ºC. Incorporating 10 mol% BZN (*x* = 0.1) supressed the ε_r peak somewhat ($\varepsilon_{r\ max}$ = 1330) and T_m decreased to 90 ºC, Figure 10.3(b). The temperature range of stable ε_r values was broader, 20-400 ºC with a lower ε_r value of 1160 (i.e. ε_r = 1160±15%) from 20-400 ºC. Increasing the BZN level to *x* = 0.2 and 0.3, further supressed the ε_r peak; T_m was ~ 70 ºC for both compositions. Dielectric measurements were carried out to temperatures of -70 ºC for *x* = 0.2 and 0.3, revealing ε_r = 805±15%

from -20 ºC to 600 ºC for x = 0.2, and ε_r = 680±15%, from -20 ºC to 380 ºC for x = 0.3, Figure 10.4 and Table 10.1.

10.2.3 Loss tangent-Temperature

As demonstrated throughout this thesis, for many temperature-stable dielectrics, the characteristic tanδ peak at $T \sim T_m$ is a hindrance to achieving low dielectric loss across the full temperature range of stable permittivity, and the (1-x)[0.5KBT-0.5BZT]-xBZN system is no exception.

As a result of the tanδ dispersion, the temperature ranges of low loss, taken as tanδ < 0.02 (1 kHz), was restricted to 70-350 ºC for x = 0.2, and to 50-450 ºC for x = 0.3, Table 10.1. At the other extreme of the temperature range, the sharp increase in tanδ at above 300-400 ºC, Figure 10.3 and 10.4, is most probably due to the effects of mobile lattice defects which are introduced as a result of the loss of some of the volatile oxide components during calcination and sintering, as described in earlier chapters.

These presumed process-related increases in tanδ were most pronounced in the x = 0.3 data, to the extent that measured values of permittivity were affected above ~ 300 ºC, Figure 10.4(b). However, a detailed analysis of charge transport mechanisms would be required to conform this interpretation (it is possible that defect chemistry may involve electronic conduction).

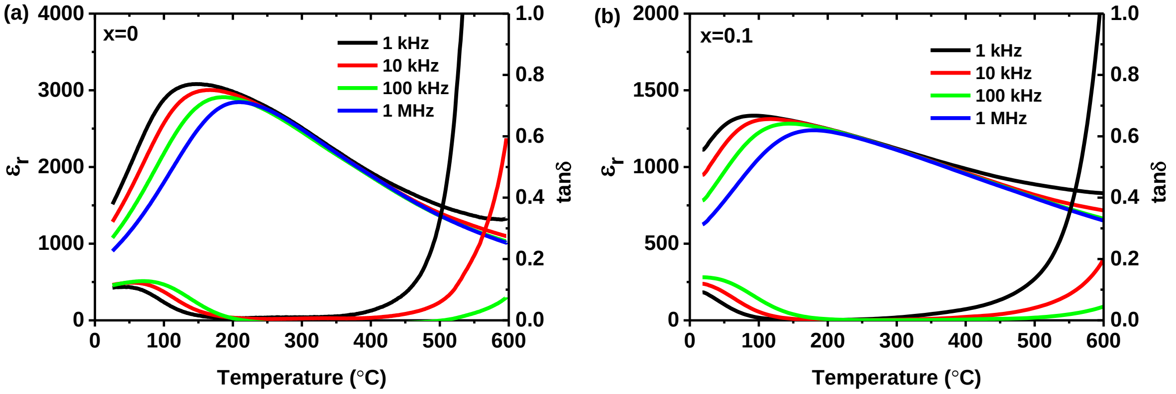

Figure 10.3 Temperature dependent relative permittivity and loss tangent (tanδ) for:(a) *x* = 0 and (b) *x* = 0.1 across the temperature range 25-600 ºC.

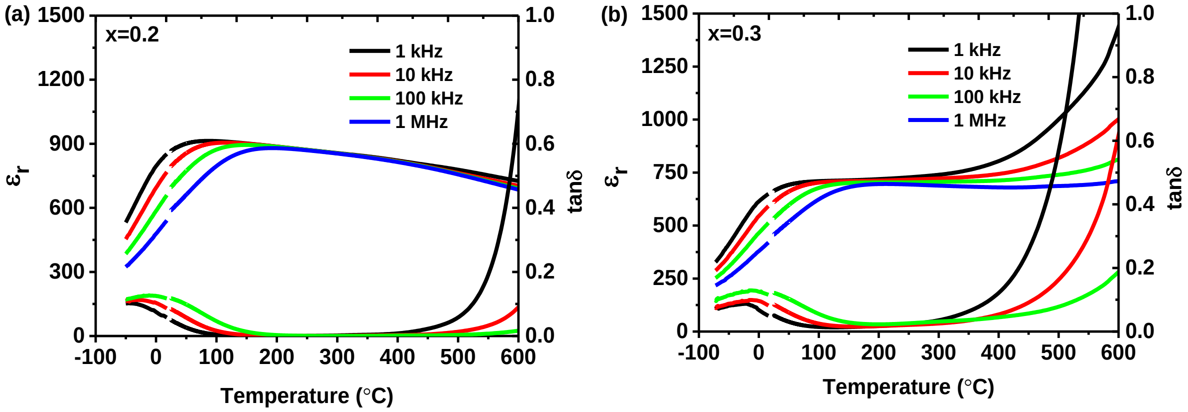

Figure 10.4 Temperature dependent relative permittivity and tanδ for:(a) *x* = 0.2 and (b) *x* = 0.3 over the temperature range -70 ºC to 600 ºC (break indicating the changeover of low and high temperature instruments).

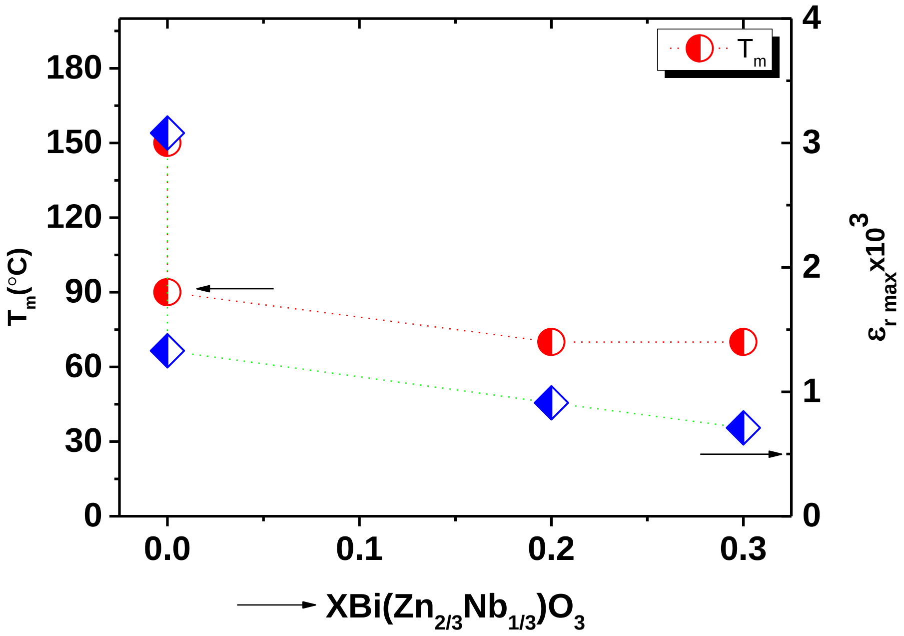

Figure 10.5 Variation of temperature corresponding to peak permittivity, T_m and the value of peak relative permittivity, $\varepsilon_{r\ max}$ as a function of *x*BZN ($x \leq 0.3$).

Table 10.1 Summary of dielectric properties for (1-*x*)[0.5KBT-0.5BZT]-*x*BZN ceramic system (1 kHz data).

Sample(*x*)	T_m (°C)	$\varepsilon_{r\ max}$	T-range (°C) $\varepsilon_r \leq 15\%$	T-range (°C), tanδ ≤ 0.02
x = 0	150	3080	70-250 (2750)	130-380
x = 0.1	90	1330	≤ 20-400 (1160)	70-350
x = 0.2	70	910	-20-600 (805)	50-450
x = 0.3	70	710	-20-380 (680)	65-240

10.2.4 dc resistivity

Figure 10.6 shows the temperature dependent dc resistivity measured at fixed dc voltage of 80 V across the temperature range of 250-550 °C. As in other systems, a discontinuity in slope of the plot of resistivity was observed, on this occasion at temperature ~ 350-400 ºC. Compositions *x* = 0.1 and 0.2 exhibited slightly higher resistivity than *x* = 0 and 0.3.

Values of dc resistivity were of the order of ~ 10^9 Ω m at a temperature of 300 ºC for *x* = 0.1 and 0.2, compared to ~ 10^8 Ω m for *x* = 0; the multiphase composition *x* = 0.3 also had a resistivity of ~ 10^8 Ω m at 300 ºC. Activation energy values based on the conduction data were in the range of 0.5-0.7 eV consistent with oxygen vacancies migration [Selvamani et al. (2012), Morrison et al. (1999), Zeb and Milne (2014a)].

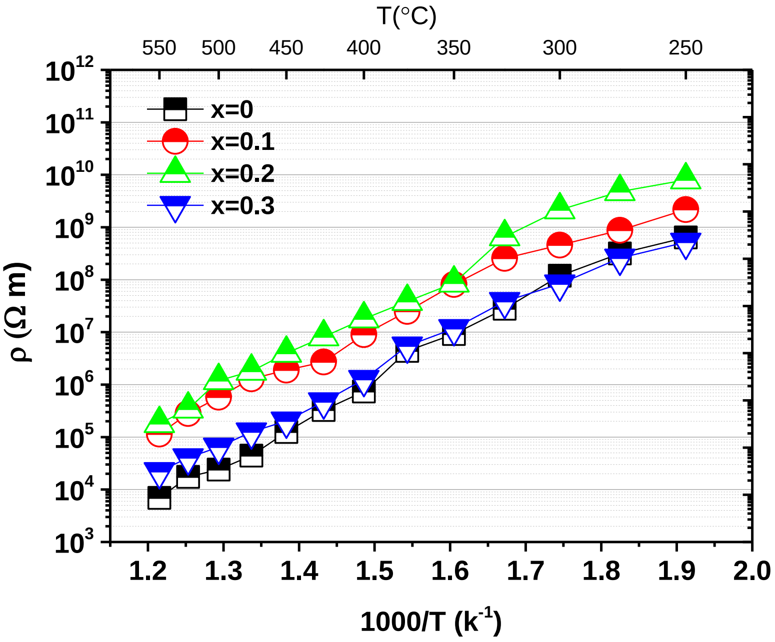

Figure 10.6 Variation of dc resistivity versus 1/T (absolute temperature) for (1-*x*)[0.5KBT-0.5BZT]-*x*BZN system.

10.2.5 Polarisation-Electric Field analysis

Polarisation-electric field responses for (1-*x*)[0.5KBT-0.5BZT]-*x*BZN ceramics were evaluated at room temperature and frequency of 1 Hz, Figure 10.7. A slim P-E loop with a little evidence of ferroelectric nature was evident for composition *x* = 0 (E

= 50 kV/cm, 1 Hz), Figure 10.7. Compositions *x* ≥ 0.1, revealed a highly linear P-E responses consistent with low loss capacitor.

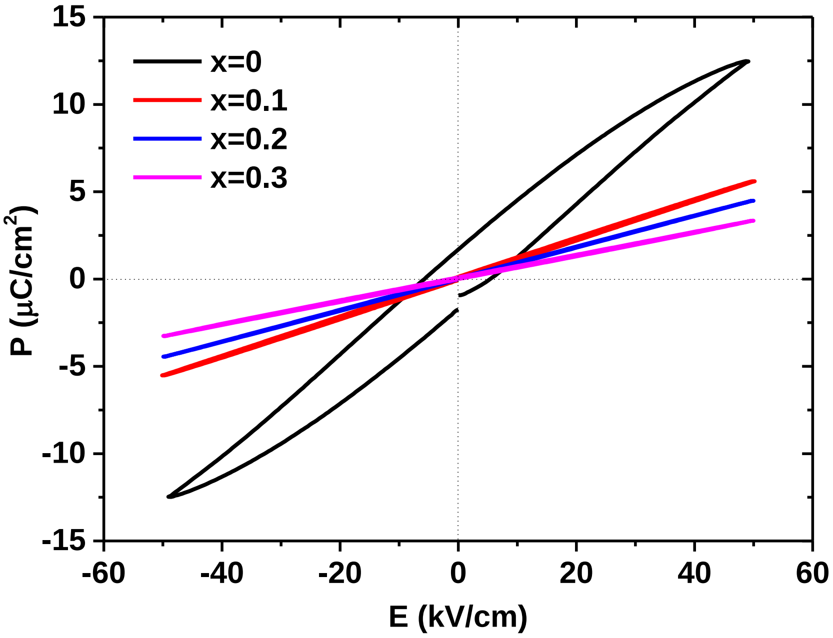

Figure 10.7 Polarisation-Electric field responses for *x* = 0-0.3 measured at field of 50 kV/cm (1 Hz).

10.2.6 Microstructural analysis

Figure 10.8 shows SEM micrographs of polished and thermally etched pellet surfaces for *x* = 0-0.3. All SEM micrographs revealed a relatively dense microstructure, except for composition *x* = 0.1, where higher levels of porosity were evident. The rounded grains and intergranular material present in sample *x* = 0.3 (this sample contained secondary phases by XRD, Figure 10.1) suggests liquid phase had formed during sintering, which points to a decrease in melting temperature for this sample to below the uniform sintering temperature of 1040 °C.

The average grain sizes estimated by the linear intercept method were ≤ 1 μm for samples *x* = 0 and 0.1, increasing to ~ 2 μm for sample *x* = 0.2. The estimated relative densities from the geometrical method were estimated in the range 91-94%.

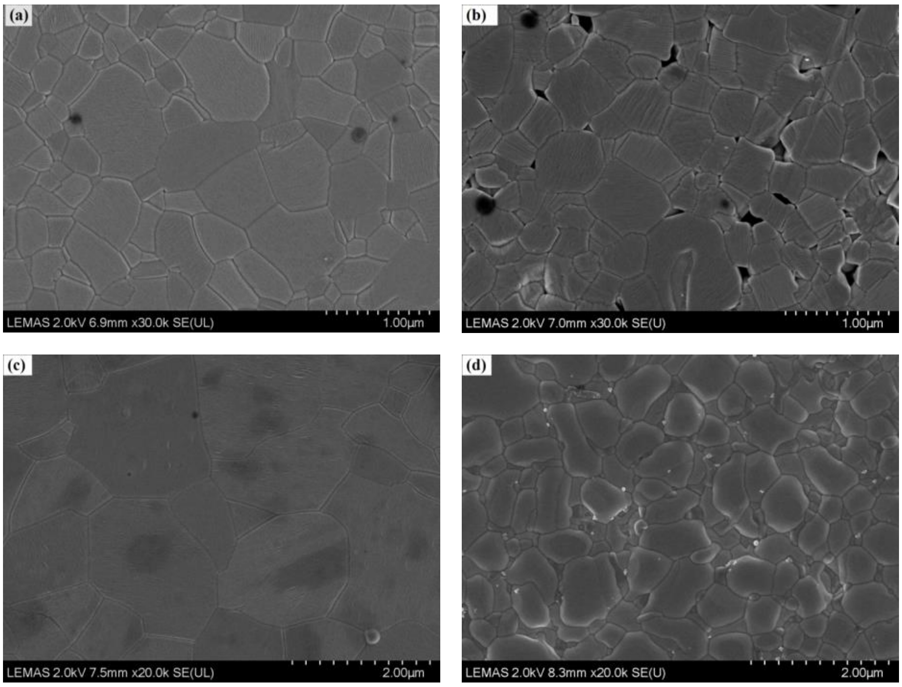

Figure 10.8 SEM micrographs for polished and thermally etched surfaces for (a) $x = 0$, (b) $x = 0.10$ (c) $x = 0.2$ and (d) $x = 0.3$.

10.3 Conclusions

Electrical properties of the relaxor system (1-x)[0.5KBT-0.5BZT]-xBZN, were studied. X-ray powder diffraction analysis revealed a cubic structure for all compositions studied, $x \leq 0.3$. Incorporation of BZN led to an improvement in the temperature stability of relative permittivity, relative to the base 0.5KBT-0.5BZT material. Composition $x = 0.2$ exhibited permittivity values of $\varepsilon_r = 805$ within ±15% across a wide temperature range from -20 ºC to 600 ºC; with corresponding loss tangent, $\tan\delta \leq 0.02$, over the temperature range from 50-450 ºC.

Values of dc resistivity were of the order of ~ 10^9 Ω m at temperature of 300 ºC for compositions for $x = 0.1$ and 0.2. The results suggest the new material has merit in the context of developing dielectrics for capacitors operating from high (>> 200 ºC) to sub-zero temperatures.

Chapter 11

Summary and Property Comparisons with Pb-free Piezoelectric and High Temperature Dielectric Materials Published by Other Research Groups

11.1 Summary

A number of novel lead-free ceramic systems have been examined during this research. Their structural, dielectric, ferroelectric and piezoelectric properties were presented.

The study of $(1-x)K_{0.5}Bi_{0.5}TiO_3-xBi(Mg_{0.5}Ti_{0.5})O_3$ ceramic system ($0 \leq x \leq 0.12$) [Chapter 4], revealed distinctive piezoelectric features. Based on the high temperature XRD data, a phase boundary between tetragonal and tetragonal+cubic phases was located at $0.025 < x < 0.03$ (at room-temperature). A peak value of piezoelectric charge coefficient, d_{33} = 150 pC/N was obtained for MPB composition $x = 0.03$ and bipolar strain of ~ 0.25% (50 kV/cm, 1 Hz). The mixed phase compositions $x = 0.04$ and 0.06, exhibited high bipolar strains of ~ 0.35% and ~ 0.3%, respectively (50 kV/cm, 1 Hz).

Low hysteresis was present in unipolar strain-field loops: room-temperature S_{max} (measured in Leeds) was ~ 0.14% for $x = 0.03$ (50 kV/cm, 1 Hz). Values of unipolar strain of up to 0.18% for $x = 0.03$ were retained up to relatively high temperature ~ 185 ºC (measured at Tsinghua University).

Room temperature polarisation data for compositions $x = 0.03$ and 0.04 exhibited ferroelectric characteristics with peak value of remanent polarisation at room temperature, P_r of ~ 14 μC/cm^2 (E_c ~ 25 kV/cm) and ~ 18 μC/cm^2 (E_c ~ 28 kV/cm), respectively. Temperature dependent polarisation analysis for these compositions demonstrated no strong evidence of pinch shape P-E loops up to a temperature of 180 ºC, but it is likely that 180 ºC is the upper limit of normal P-E loops. Thermally stimulated charge decay and k_p-T measurements indicated full depolarisation (P = 0) at T_d ~ 220 ºC for $x = 0.03$ and ~ 200 ºC for $x = 0.04$. This is similar to unmodified KBT but higher than many other leading Pb-free piezoelectrics.

Taking all dielectric and ferroelectric results into account, the T_d values can represent a change from ferroelectric < ~ 200 ºC to relaxor > ~ 200 ºC ($x = 0.03$). These temperatures are ~ 100 ºC lower than the high temperature boundary on the phase diagram.

A study of (1-x)$K_{0.5}Bi_{0.5}TiO_3$-xBa($Zr_{0.2}Ti_{0.8}$)O_3 solid solutions was also carried out and revealed reasonable ferroelectric and piezoelectric properties for composition $x = 0.1$, with d_{33} = 130 pC/N and bipolar strain 0.13%.

11.2 Property Comparisons

11.2.1 Dielectric, Ferroelectric and Piezoelectric Properties

A comparison of dielectric, ferroelectric and piezoelectric properties of (1-x)KBT-xBMT (x = 0.03, 0.04) with widely studied other potential lead-free materials is given in Table 11.1 for: $Na_{0.5}Bi_{0.5}TiO_3$-$BaTiO_3$ (NBT-BT); $Na_{0.5}Bi_{0.5}TiO_3$-$K_{0.5}Bi_{0.5}TiO_3$ (NBT-KBT); $Na_{0.5}Bi_{0.5}TiO_3$-$BaTiO_3$-$K_{0.5}Na_{0.5}NbO_3$ (NBT-BT-KNN), and some of the best KNN-based materials

Table 11.1 Comparison of dielectric, ferroelectric and piezoelectric properties of (1-x)KBT-xBMT (x = 0.03, x = 0.04) with lead-free 94NBT-6BT [Xu et al. (2008), Guo et al.(2011)], 80NBT-20KBT [Yoshii et al. (2006)], 93NBT-5BT-2KNN [Zhang et al.(2008a), Zhang et al.(2008b)], 95LKNNT-5CZ [Ke Wang et al. (2013)] and $0.92K_{0.5}Na_{0.5}NbO_3$-$0.02Bi_{0.5}Li_{0.5}TiO_3$-$0.06BaZrO_3$ (92KNN-2BLT-6BZ) [Wang et al. (2015)] systems.

Parameters	x = 0.03	x = 0.04	94NBT-6BT	80NBT-20KBT	93NBT-5BT-2KNN	95LKNNT-5CZ	92KNN-2BLT-6BZ
T_c or T_m (ºC)	334	336	288	~ 275	260	192	243
ε_r (20 ºC), 1 kHz	1050	1050	826	884	2060	1735	2000 (1 kHz)
$\varepsilon_{r\ max}$, 1 kHz	5970	6240	~ 6500	~ 7000	~ 4800	~ 7000	~ 10, 000
tanδ (20 ºC),1 kHz	0.05	0.06	0.025	0.02	0.054	0.014	0.02 (1 kHz)
P_r (µC/cm^2)	13.5	18	38	38	32	16	-
E_c (kV/cm)	25	28	34	38	31	10	-
d_{33} (pC/N)	150	133	155	157	98	320	348
k_p, RT	0.18	0.15	0.36	0.27	0.27	-	0.58
T_d (ºC) (k_p-T)	220	200	105	174 (k_{33}-T)	117 (ε_r-T)	-	-
Bipolar Strain (%)	0.25(50kV/cm, 1 Hz)	0.35(50 kV/cm, 1 Hz)	0.25 (60 kV/cm, 1 Hz)	0.19 (80 kV/cm, 0.1 Hz)	0.29 (60 kV/cm, 0.05 Hz)	~ 0.13 (40 kV/cm, 1 Hz)	-
Bipolar d_{33}^*(pm/V)	520	760	-	240	276	-	-

11.2.2 Temperature-dependent ferroelectric properties

Temperature-dependent P-E loops for (1-*x*)KBT-*x*BMT, $x = 0.03$ and 0.04 are compared with leading Pb-free piezoelectric materials at various temperatures in Figure 11.1.

For compositions $x = 0.03$ and 0.04, an increase in temperature resulted in an increase of remanent polarisation and decrease in coercive field. Values of remanent polarisation, P_r ~ 14 μC/cm^2 at 25 ºC increases to ~ 18 μC/cm^2 at 150 ºC for $x = 0.03$, with decrease of coercive field, E_c from ~ 25 kV/cm to ~ 17 kV/cm. Similarly, for composition $x = 0.04$, remanent polarisation P_r was ~ 18 μC/cm^2 25 ºC increases to ~ 20 μC/cm^2. This indicates increased realignment of polar domains with increasing temperature, consistent with other ferroelectric materials. However, for composition $x = 0.04$, a slight constriction in P-E loop was evident at a temperature of 180 ºC.

The published literature for 94NBT-6BT [Guo et al. (2011)], 80NBT-20KBT [Seifert et al. (2010)] and 93NBT-5BT-2KNN [Zhang et al.(2008b)] ceramic materials exhibited higher remanent polarisations, $P_r \leq 30$ μC/cm^2 with higher coercive fields, $E_c \leq 30$ kV/cm at room temperature, compared to KBT-BMT, Figure 11.1(c), (d) and (e). However, an increase in temperature for 94NBT-6BT led to the pinched shape P-E loops at a temperature between 60 and 100 ºC, whilst loops were pinched at 75 ºC for 80NBT-20KBT and 93NBT-5BT-2KNN with notable decrease in remanent polarisation (≤ 10 μC/cm^2).

There is much interest in the piezoceramic composition 95$(Na_{0.49}K_{0.49}Li_{0.02})(Nb_{0.8}Ta_{0.2})O_3-5CaZrO_3$+2 wt% MnO_2 (95LKNNT-5CZ) [Wang et al. (2013)]. It shows remanent polarisation, P_r ~ 16 μC/cm^2 and E_c = 40 kV/cm at room temperature but P_r decayed above room temperature, although no pinching was observed up to 175 ºC (P_r ~ 7 μC/cm^2 at 175 ºC), Figure 11.1(f).

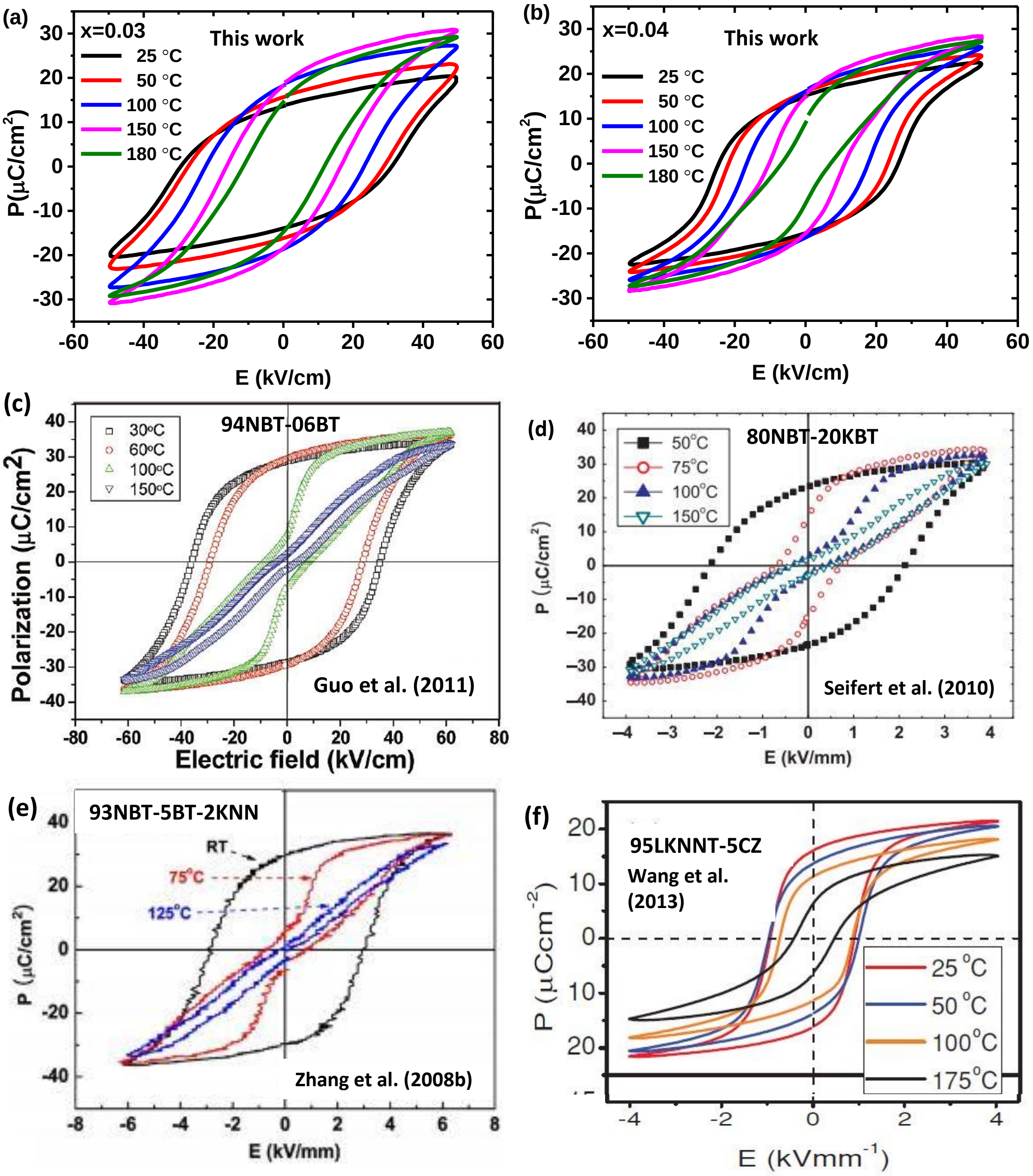

Figure 11.1 Comparison of temperature dependent P-E loops for (1-*x*)KBT-*x*BMT (a) *x* = 0.03, (b) *x* = 0.04, with (c) 94NBT-6BT, (d) 80NBT-20KBT, (e) 93NBT-5BT-2KNN and (f) 95LKNNT-5CZ.

11.2.3 Room temperature unipolar strain comparison

Figure 11.2(a) and (b) shows unipolar strain curves for (1-x)KBT-xBMT (x = 0.03 and 0.04) ceramic samples at room temperature. For (1-x)KBT-xBMT ceramic samples, a near-linear increase of unipolar strain (S_{max}) was observed with the increasing electric fields (E_{max} = 50 kV/cm, f = 1 Hz). Slim strain curves were retained at all drive fields indicating low hysteresis, Table 11.2. This is important for actuator applications since it allows accurate positioning and reduces self-heating which can lead to partial or full depolarisation. Values of unipolar strain at fields 50 kV/cm were ~ 0.14% for x = 0.03 and ~ 0.16% for x = 0.04.

For NBT-BT system (at 6 mol% BT), the reported unipolar strain values was of ~ 0.1% at a field of ~ 60 kV/cm [Guo et al. (2011), Zhang et al.(2008)] which are lower than the values (~ 0.16%, 50 kV/cm) for (1-x)KBT-xBMT (x = 0.04) materials. However, it is noted that KBT-BMT samples sent to Tsinghua showed strains of ~ 0.12% using their test facility. Calibration of the rigs requires further consideration in future.

Comparison of unipolar strain for KBT-BMT with the lead free KNN-based: [$0.92(Na_{0.535}K_{0.48})NbO_3$-$0.08LiNbO_3$] (KNNL8) [Wang et al. (2011)], showed nearly similar values (~ 0.17%) at 50 kV/cm, Figure 11.2(b). However, for composition: $0.965K_{0.45}Na_{0.55}Nb_{0.96}Sb_{0.04}O_3$-$0.035Bi_{0.5}Na_{0.5}HfO_3$ (KNNS-BNH) [Tao et al. (2015)], the values of unipolar strain were higher (~ 0.30%, 50 kV/cm) than KBT-BMT. Other KNN-based materials; $0.96(K_{0.5}Na_{0.5})NbO_3$-$0.04CaZrO_3$+0.03Zr (KNN-CZ-2), revealed a moderate unipolar strain (~ 0.10%) at low field of ~ 30 kV/cm [Kawada et al. (2009)]. The shape of the S-E loops (and developed strains) are the closest to KBT-BMT of any of these materials, but slightly more curved (non-linear).

Ceramic materials based on the ternary system: 0.92NBT-0.06BT-0.02KNN (NBT-BT-KNN) [Zhang et al. (2007)] exhibited a ‘giant’ electromechanical unipolar strain ~ 0.45% (E = 80 kV/cm) arising from an electric field induced relaxor-ferroelectric phase transition, Figure 11.2(f) [Wang et al. (2013)].

It is noted the measurement frequency was 0.05 Hz (which seems not to be relevant test conditions for rapid response actuators). However, such high unipolar strain suffers from high hysteresis (~ 69%), Table 11.2 [Zheng and Zuo (2015)].

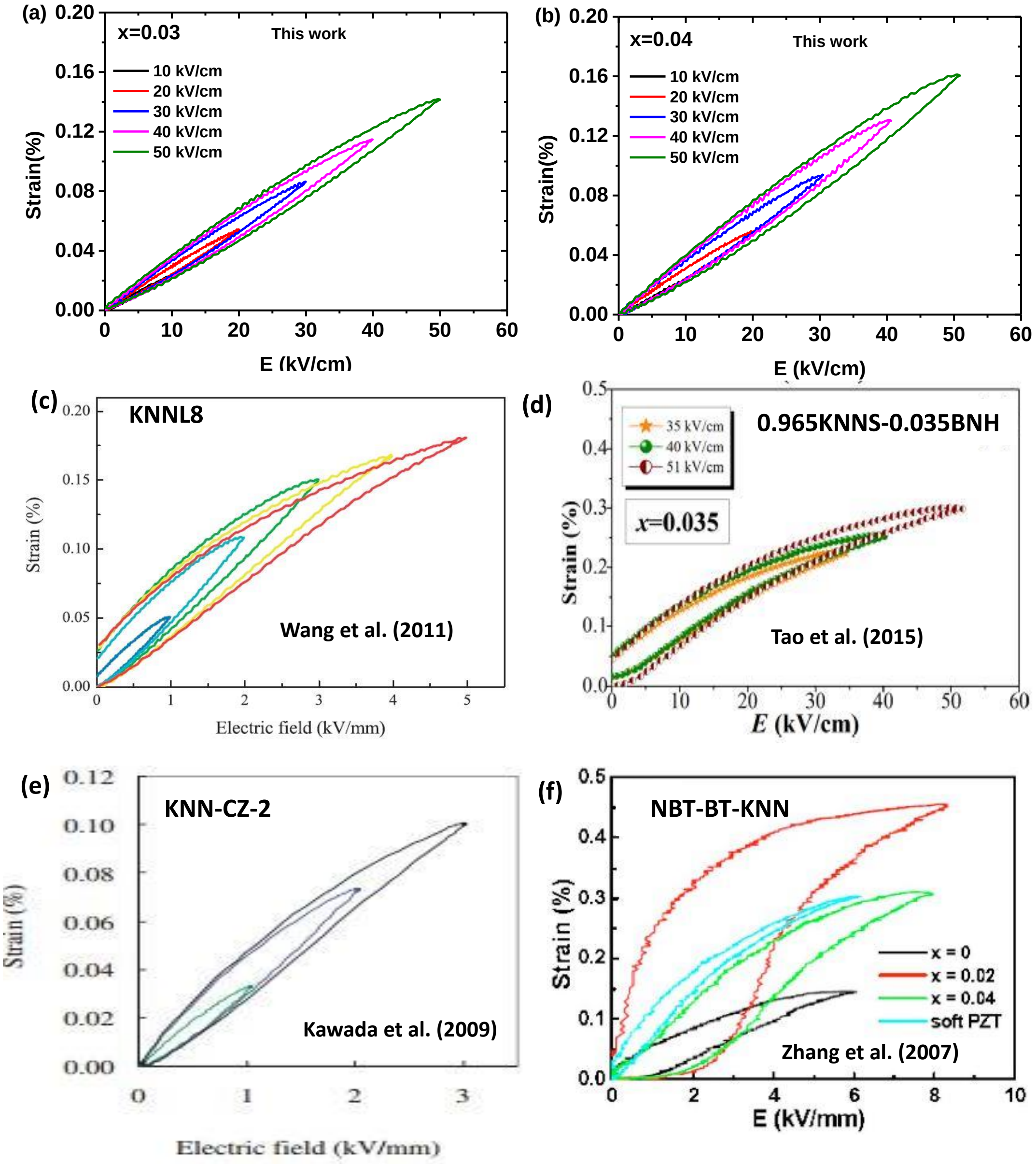

Figure 11.2 Comparison of room temperature unipolar strain for: (a) (1-*x*)KBT-*x*BMT, *x* =0.03 (b) *x* = 0.04, (c) $0.965K_{0.45}Na_{0.55}Nb_{0.96}Sb_{0.04}O_3$-$0.035Bi_{0.5}Na_{0.5}HfO_3$ (KNNS-BNH) [Tao et al. (2015)], (d) $0.92(Na_{0.535}K_{0.48})NbO_3$–$0.08LiNbO_3$ (KNNL8) [Wang et al. (2011)], (e) $0.96(K_{0.5}Na_{0.5})NbO_3$–$0.04CaZrO_3$+0.03Zr (KNN-CZ-2) [Kawada et al. (2009)] and (f) NBT-BT-KNN [Zhang et al. (2007)] (Note: Unipolar strain scale is different for this comparison).

Table 11.2 Comparison of unipolar strain (%), d_{33}* (S_{max}/E_{max}) and hysteresis (%) for *x* = 0.03 and 0.04 with other lead-free piezoelectric materials.

Materials	Unipolar S_{max} (%) (RT)	Unipolar d_{33}* (S_{max}/E_{max})	Hysteresis (%)	References
x = 0.03	0.14 (50 kV/cm, 1 Hz) (0.11% Tsinghua) (50 kV/cm, 1 Hz)	320	13	This work
x = 0.04	0.16 (50 kV/cm (1 Hz)	340	11	This work
94NBT-6BT	0.10 (60 kV/cm, 0.05 Hz)	180	69	Zhang et al. (2008)
0.92NBT-0.06BT-0.02KNN	0.45 (80 kV/cm, 0.05 Hz)	560	69	Zhang et al. (2007), Zheng and Zuo (2015)
95LKNNT-5CZ	0.16 (60 kV/cm, 1 Hz)	320	-	Wang et al. (2013)
0.8928KNN-0.0672LN-0.04CZ	0.16 (50 kV/cm, 10 Hz)	320	25 (estimated)	Zhang et al. (2015)
KNNS-BNH	0.31 (51 kV/cm, 10 Hz)	608	16 (estimated)	Tao et al.(2015)
92KNN-6BLT-2BZ	0.069 (20 kV/cm, 0.1 Hz)	530	28 (estimated)	Wang et al.(2015)

11.2.4 Unipolar strain temperature stability

The temperature dependent unipolar strains curves were also compared with lead free NBT and KNN-based materials, Figure 11.3 and 11.4.

For (1-*x*)KBT-*x*BMT (*x* = 0.03 and 0.04) ceramic samples, the values of unipolar strain at a field of 50 kV/cm increased gradually from ~ 0.11% (Tsinghua values for both samples) at room temperature to ~ 0.18% for *x* = 0.03 and 0.16% for *x* = 0.04 at a temperature of 185 ºC. The change in S_{max} with temperature was approximately linear for both samples with relatively low hysteresis in the loops (Hys ~ 13-25%).

For NBT-BT at 6 mol% BT, the reported values of the unipolar strain at a field of ≥ 60 kV/cm increased from 0.10% at room temperature to peak value of ~ 0.40% at a temperature of 100 ºC, Figure 11.3(e). This high strain value is correlated with the ferroelectric-relaxor induced phase transition near its T_d (~ 100 ºC). However, further increase of temperature resulted in the decay of strain values to ~ 0.35% at maximum test temperature of 150 ºC [Guo et al. (2011)].

The ternary 93NBT-5BT-2KNN system, with ‘giant electrostrictive strain’ Figure 11.3(f), exhibited a unipolar strain of ~ 0.15% at room temperature at a field of ~ 60 kV/cm. Values of unipolar strain reached to maximum of 0.40% at 75 ºC and then decayed to 0.30% at 125 ºC. Both NBT-BT and NBT-BT-KNN systems exhibited large electromechanical strain curves revealed similar large hysteresis ~ 69% [Zheng and Zuo (2015) which is higher than the KBT-BMT system (13-25%).

In KNN-based ceramic materials, the maximum values of unipolar strain obtained for composition: 95LKNNT-5CZ, Figure 11.4(c) [Wang et al. (2013)] was ~ 0.12% (E_{max} = 30 kV/cm) at room temperature, then slightly increased to ~ 0.14% up to

50 ºC. Above a temperature of > 50 ºC, a gradual decrease in strain values was evident but retained high as ~ 0.12% till 175 ºC and then decreased to ~ 0.09% at 200 ºC, Figure 11.4(c).

The other popular reported compositional systems based on KNN: $Li_{0.02}(K_{0.45}Na_{0.55})_{0.98}(Nb_{0.77}Ta_{0.18}Sb_{0.05})O_3$ (KNNLTS) [Yao et al. (2014)] and $0.04Bi_{0.5}K_{0.5}Zr_{0.85}Sn_{0.15}O_3$ (KNNS-BKZS) [Zhou et al. (2015)], exhibited maximum unipolar strain values ~ 0.12% (E_{max} = 30 kV/cm) and ~ 0.14% (E_{max} = 30 kV/cm) at room temperature. On heating above the room temperature, values of S_{max} gradually decreased to ~ 0.10% for both system up to ~120 ºC and then become relatively stable till 190 ºC for the latter system.

In conclusion, the temperature stability in unipolar strain for (1-*x*)KBT-*x*BMT samples was notably comparable to the best of KNN-based piezoelectric materials; 95LKNNT-5CZ, unipolar strain [Ke Wang et al. (2013)] and $0.92(Na_{0.535}K_{0.48})NbO_3$-$0.08LiNbO_3$ (KNNL8) [Wang et al. (2011)].

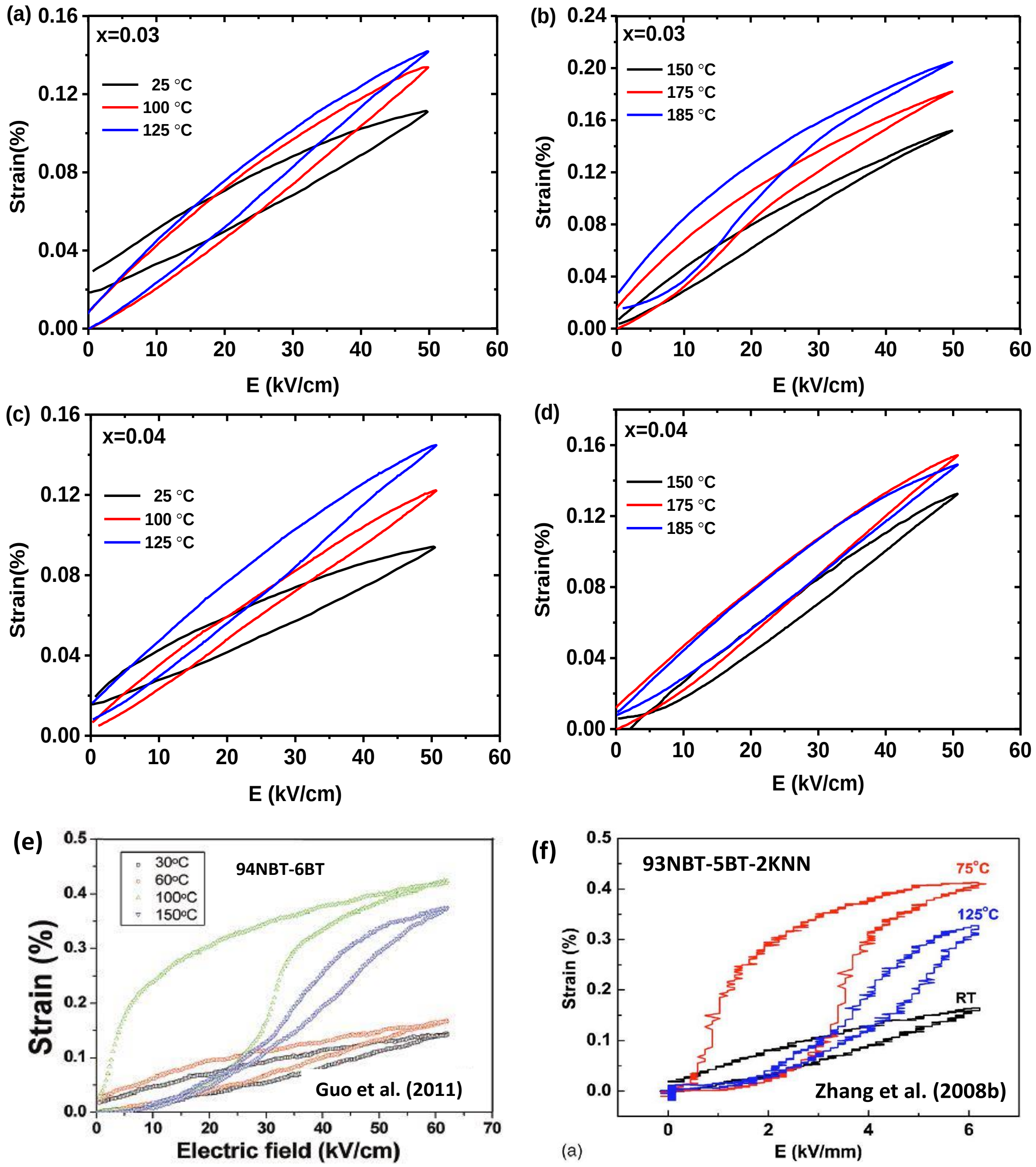

Figure 11.3 Comparison of unipolar strain for(1-*x*)KBT-*x*BMT: (a-b) *x* = 0.03 (c-d) *x* = 0.04, with NBT-based materials (e) 94NBT-06BT [Guo et al. (2011)], (f) 93NBT-05BT-02KNN [Zhang et al.(2008b)] (Note: Unipolar strain scale is different for this comparison).

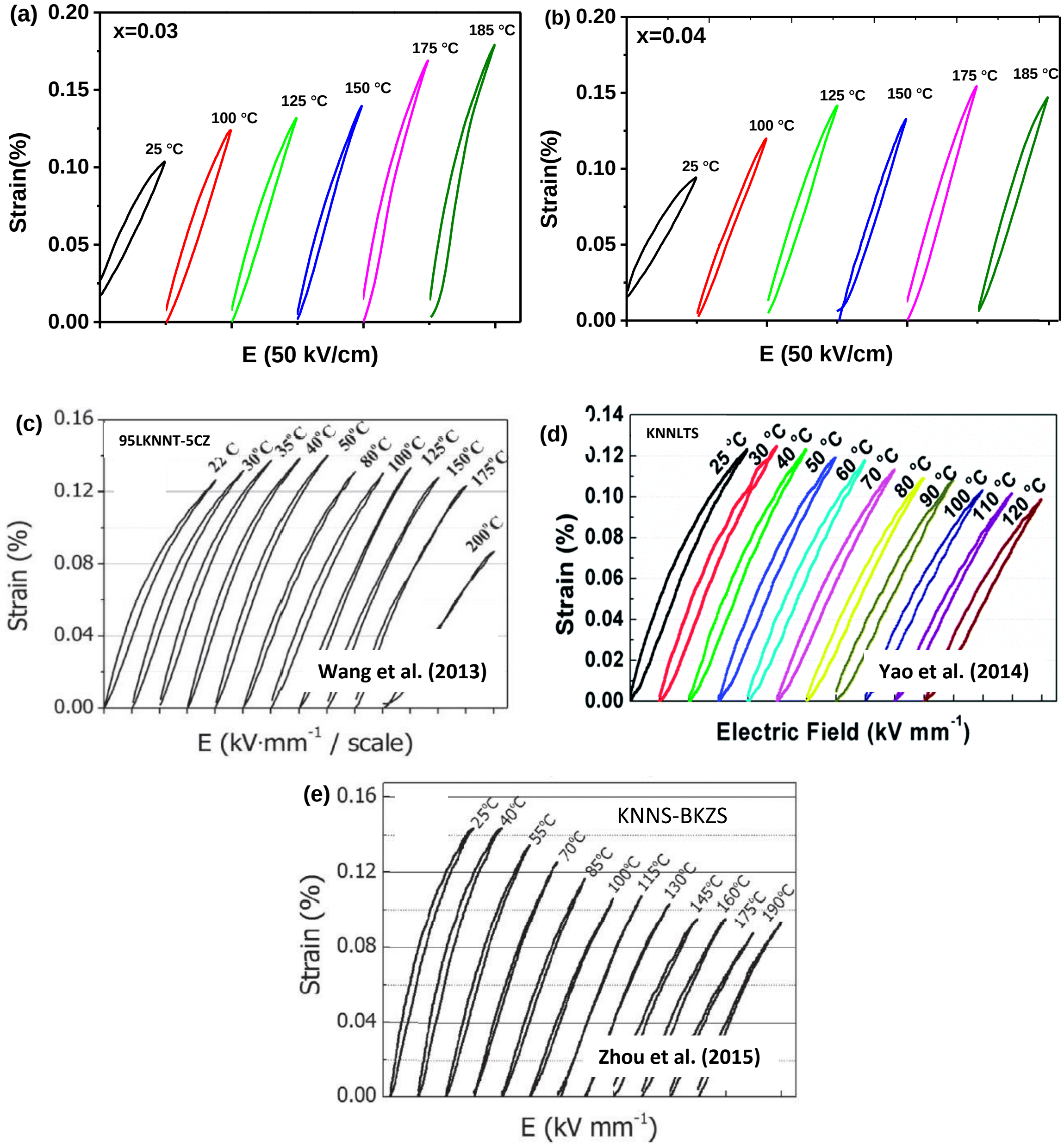

Figure 11.4 Comparison of unipolar strain for: (a) (1-x)KBT-xBMT (x = 0.03 (b) x = 0.04, with KNN-based materials (c) 95LKNNT-5CZ [Ke Wang et al. (2013)], (d) KNNLTS [Yao et al. (2014)], (e) 0.96 $(K_{0.4}Na_{0.6})(Nb_{0.96}Sb_{0.04})O_3$-$0.04Bi_{0.5}K_{0.5}Zr_{0.85}Sn_{0.15}O_3$ (KNNS-BKZS) [Zhou et al. (2015)].

Figure 11.5 and 11.6 show the temperature dependence of d_{33}* (S_{max}/E_{max}) and S_{max} (%) for compositions *x* = 0.03 and 0.04 along with comparison of other lead free materials. At room temperature, both compositions *x* = 0.03 and 0.04 exhibited a d_{33}* values of ~ 220 pm/V, increases to 283 pm/V at 150 ºC. On heating further, values of d_{33}* reached to 381 pm/V for *x* = 0.03 and 328 pm/V for *x* = 0.04 at 185 ºC.

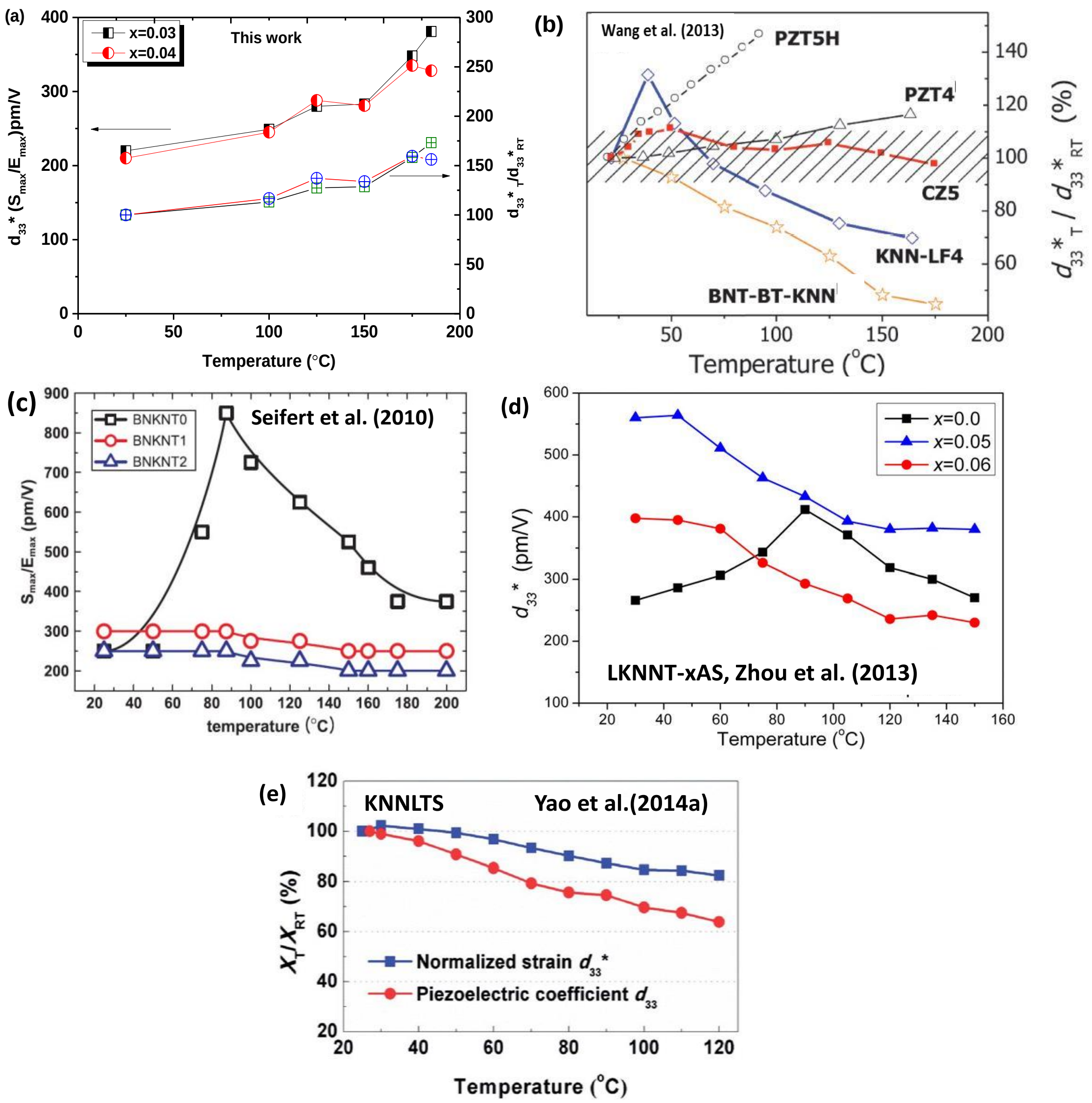

Figure 11.5 Comparison of temperature dependent d_{33}* (S_{max}/E_{max}) for: (a) *x* = 0.03, 0.04, with (b) 95LKNNT-5CZ (c) NBT-KBT0, NBT-KBT10 and NBT-KBT20 (d) $(1-x)Li_{0.02}(Na_{0.53}K_{0.48})_{0.98}Nb_{0.8}Ta_{0.2}O_3-xAgSbO_3$ (e) $Li_{0.02}(K_{0.45}Na_{0.55})_{0.98}(Nb_{0.77}Ta_{0.18}Sb_{0.05})O_3$.

The temperature stability in d_{33}* for KBT-BMT compositions are comparable to the NBT-BT-KNN, LKNN-5CZ, Figure 11.5(b) and NBT-KBT, Figure 11.5(c), in which d_{33}* values showed stability over a broad range of temperature (linear from 20-150 ºC for KBT-BMT).

A comparison of maximum unipolar strain (%), S_{max} for *x* = 0.03 and 0.04 with 94NBT-6BT [Zhang et al.(2008)], (1-*x*-*y*)NBT-*x*BT-*y*KNN [Zhang et al.(2008b)] and $Na_{0.5}K_{0.5}NbO_3-Bi_{0.5}Li_{0.5}TiO_3-BaZrO_3$ (NKN-BLT-BZ) [Wang et al. (2015)] over the temperature range 25 ºC to ≤ 200 ºC is presented in Figure 11.6.

For compositions *x* = 0.03 and 0.04, the maximum unipolar strain increases from ~ 0.11% at room temperature to ~ 0.18% at 185 ºC for *x* = 0.03 and ~ 0.16% for *x* = 0.04. For NBT-BT (6 mol% BT) and 94NBT-5BT-01KNN, Figure 11.6(b) and (c), the S_{max} increased first from ≥ 0.1% at room temperature to a high value of > 0.40% at 100 ºC and the decayed to value of S_{max} ~ 0.20% at 200 ºC. However, for NKN-BLT-BZ, a gradual decrease in S_{max} values was evident above room temperature, 11.6(d).

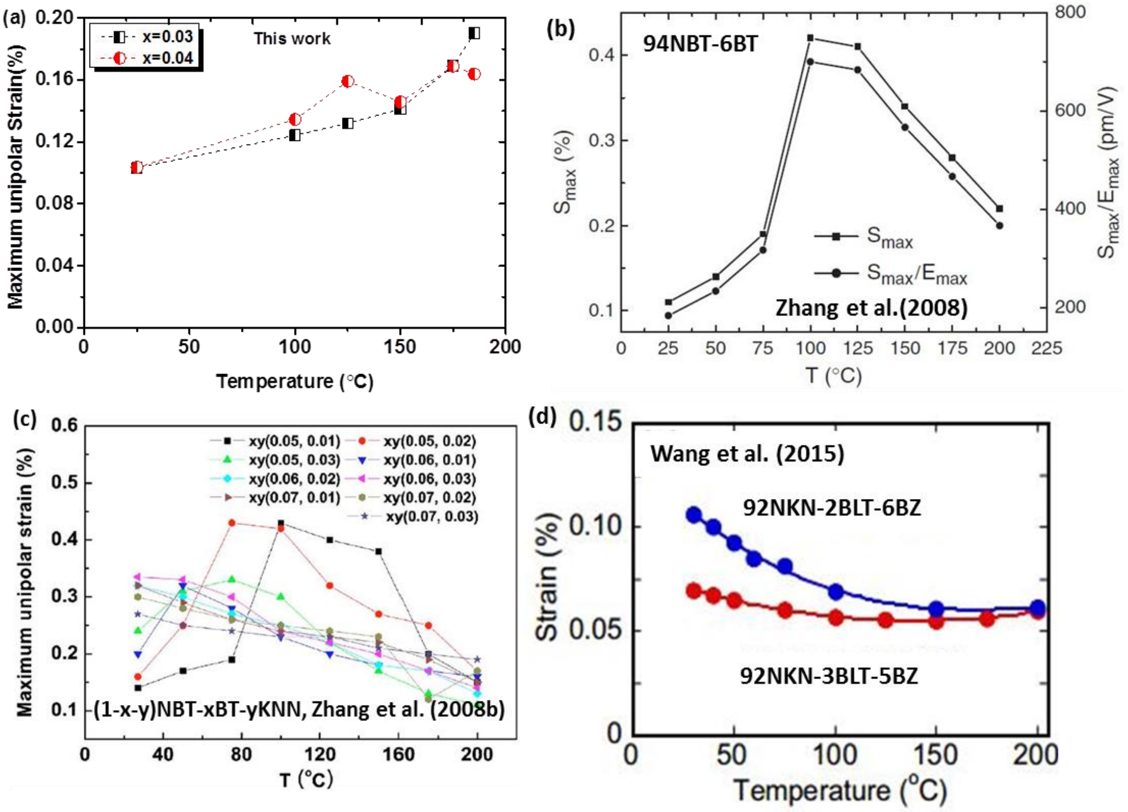

Figure 11.6 Maximum unipolar strain, S_{max} (%) versus temperature for: (a) x = 0.03, x = 0.04, (b) 94NBT-6BT, (c) (1-x-y)NBT-xBT-yKNN and (d) NKN-BLT-BZ.

The recorded k_p-T data for (1-x)KBT-xBMT, revealed k_p values of ~ 0.18 for x = 0.0.3 and 0.16 for x = 0.04. The trend in k_p values versus temperature was nearly-similar for all studied samples, with a slight increase up to ~ 100 ºC, Figure 11.7(a). Above 100 ºC, k_p started to decrease, the rate of decrease increasing above 150 ºC and then values approached zero at ~ 200-220 ºC, which signifies similarly high depolarisation temperature T_d for all three samples.

The trend of variation in k_p versus temperature for KBT-BMT was comparable with the trend in k_{33}-T data, for (1-x)NBT-xKBT (MPB) [Yoshii et al. (2006)], Figure 11.7(b). However, for 80NBT-20KBT, the depolarisation temperature, T_d was around ~ 170 ºC, some 50 ºC smaller than KBT-BMT system.

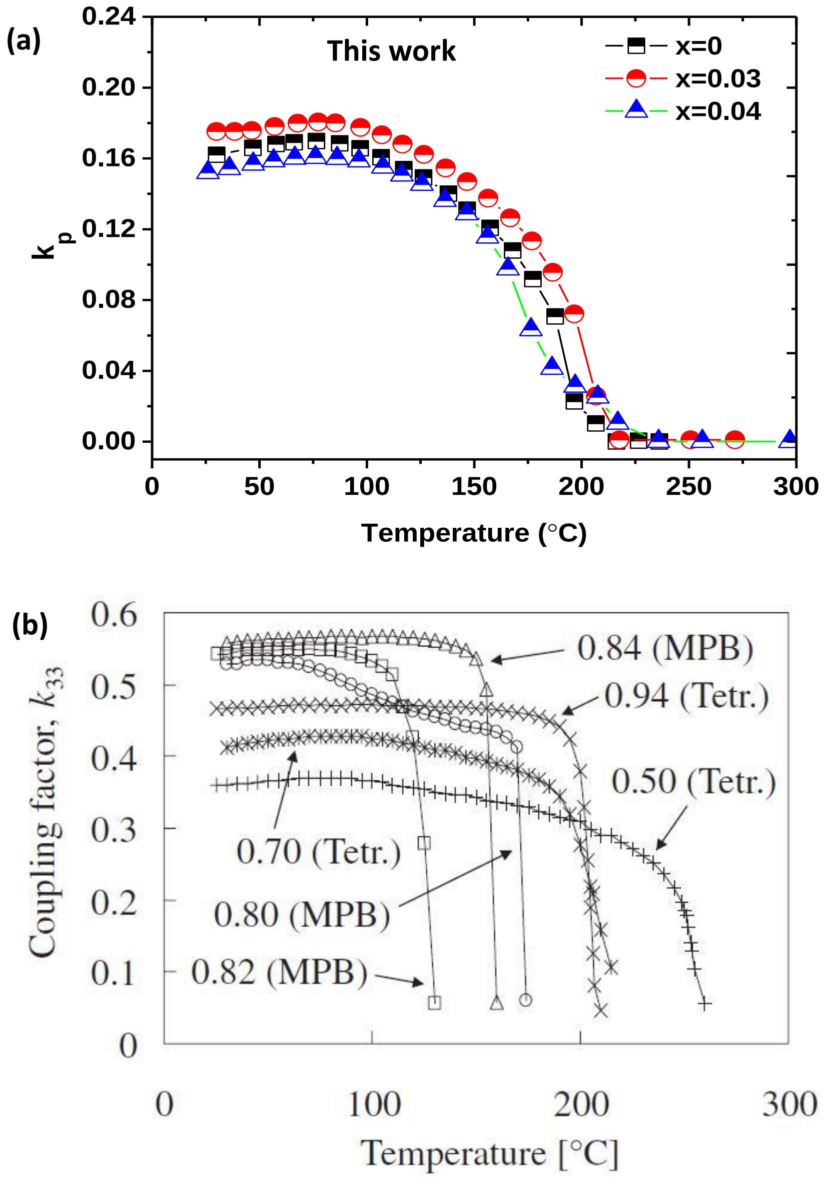

Figure 11.7 Variation of k_p versus temperature for (a) (1-x)KBT-xBMT and (b) K_{33} versus temperature for (1-x)NBT-xKBT ceramic materials [Yoshii et al. (2006)].

Unipolar strains for (1-x)KBT-xBMT, x = 0, 0.03, 0.04 and PZT806 from 10 kV/cm to higher fields up to 50 kV/cm (1 Hz) are shown in Figure 11.8. The PZT806 ceramic is a ‘hard’, low loss piezoelectric and provides a testing comparison for this new lead-free KBT-BMT system. For this comparison, lower level of unipolar strain values for $x = 0$, 0.03 and 0.04 were considered with hard PZT806 as mentioned in chapter 4 due to instrumental error.

Unmodified KBT ($x = 0$) gave a strain of 0.02 % at 20 kV/cm Hys ~ 4%), and of ~ 0.06% strain at 50 kV/cm (Hys ~ 8%). For compositions $x = 0.03$ and 0.04, a unipolar strain of ≤ 0.02% at 10 kV/cm and ≤ 0.16% at 50 kV/cm was observed.

The level of S-E hysteresis for samples $x = 0.03$ and $x = 0.04$ was low ~ 7-13%, at low-moderate drive fields, slightly higher than the hard PZT806 ceramic sample (Hys ~ 3-7%). However, against other high strain lead-free ceramics, KBT-BMT gave narrow S-E loops than the best NBT-BT-KNN materials (hysteresis ~ 69%) which is advantageous for device applications.

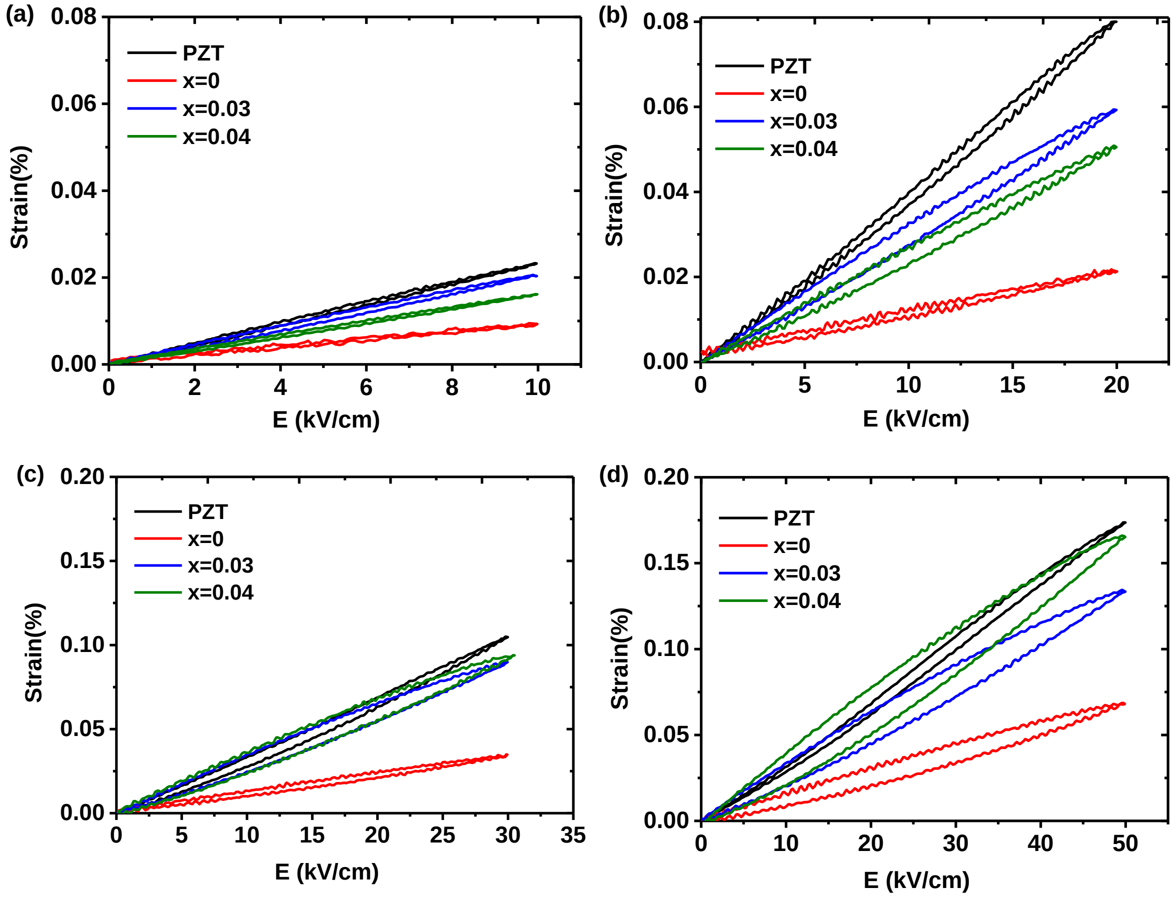

Figure 11.8 Comparison of unipolar strain (%) for *x* = 0, 0.03 and 0.04 with hard PZT806 (Courtesy Dr. James Bennet, Morgan ceramics, UK, for providing PZT806 samples).

11.3 Temperature stable dielectric systems

Solid solutions: (1-x)$B_{0.8}Ca_{0.2}TiO_3$-xBi($Mg_{0.5}Ti_{0.5}$)O_3, 0.45$Ba_{0.8}Ca_{0.2}TiO_3$-(0.55-x)Bi($Mg_{0.5}Ti_{0.5}$)O_3-$x$$NaNbO_3$, (1-$x$)$BaTiO_3$-$x$Bi($Mg_{0.5}Zr_{0.5}$)$O_3$, (1-$x$)$Ba_{0.8}Ca_{0.2}TiO_3$-$x$Bi($Zn_{0.5}Ti_{0.5}$)$O_3$ and (1-x)[0.5$K_{0.5}Bi_{0.5}TiO_3$-0.5Ba($Zr_{0.2}Ti_{0.8}$)O_3]-xBi($Zn_{2/3}Nb_{1/2}$)O_3 have been explored which exhibited temperature stable dielectric characteristics over a wide range of temperature within ±15% variation in the relative permittivity, ε_r. Values of dc resistivity were of the order of ~ 10^9 Ω m at temperature of ~ 300 ºC for the best ceramic compositions in these systems.

The best temperature stable dielectric characteristics were found in the systems: (1-x)BCT-xBMT, at $x = 0.5$ and 0.55 [Chapter 6]; (1-x)BCT-xBZT at , $x = 0.3$ [Chapter 9] and (1-x)[0.5KBT-0.5BZT]-xBZN, at $x = 0.2$ [Chapter 10]. For example, values of relative permittivity, ε_r were in the range 800-1000, with the upper limit temperature 400-600 ºC within ±15% of ε_r for (1-x)BCT-xBMT, $x = 0.5$ and 0.55. However, the lower limit of temperature for these compositions was above room temperature with the exception of (1-x)[0.5KBT-0.5BZT]-xBZN, $x = 0.2$ composition (-20 ºC).

Stability to lower temperatures, -70 ºC was achieved for 0.45BCT-(0.55-x)BMT-xNN, $x = 0.2$ and 0.3 [Chapter 7], but relative permittivity values were lower than the BCT-BMT system, $\varepsilon_r \sim 500$.

A preliminary study of the breakdown strength of (1-x)BCT-xBMT ceramic materials ($x = 0.5$ and 0.55) indicated electrical breakdown to occur at an electric field 258±30 kV/cm for $x = 0.5$, and 204±14 kV/cm for $x = 0.55$.

A graphical comparison of these promising ceramic materials in terms of temperature stability in ε_r±15% and $\tan\delta \leq 0.02$ are presented in Figure 11.9.

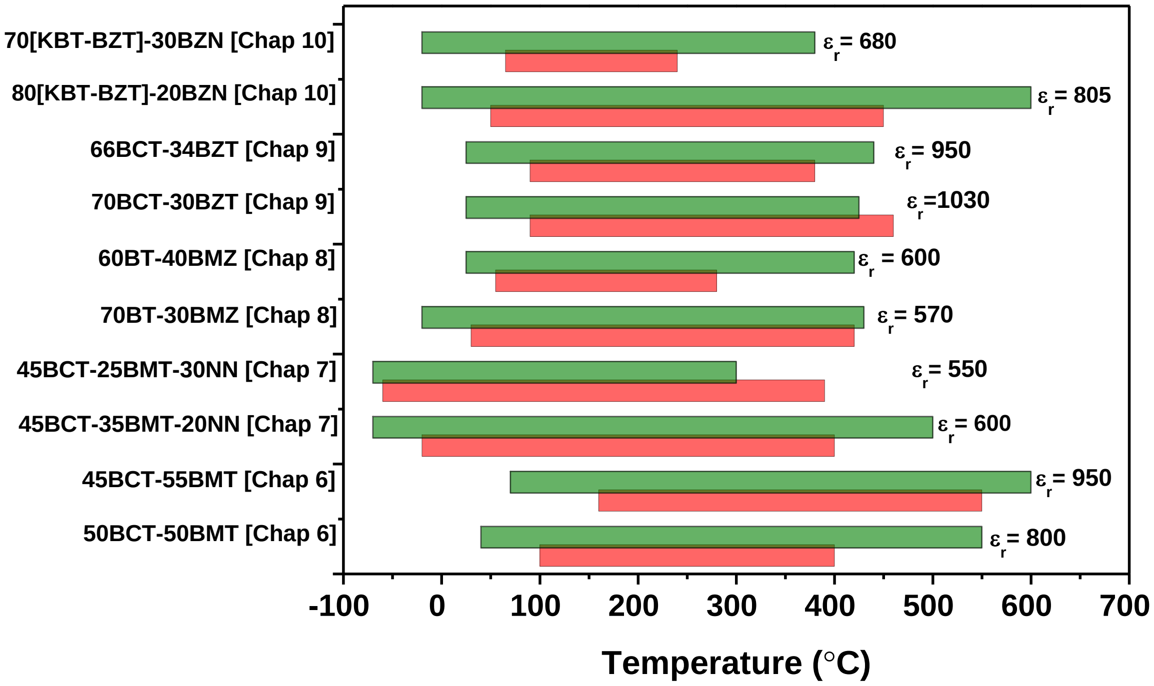

Figure 11.9 Comparison of temperature stable dielectric materials of the ceramic systems developed during this research (green bars indicate temperature range within ±15% in ε_r and red bars for tanδ ≤ 0.02).

The best temperature-stable high-temperature dielectric ceramics reported by other laboratories include $BaTiO_3$-$BiScO_3$ [Ogihara et al. (2009] and $BaTiO_3$-$Bi(Zn_{1/2}Ti_{1/2})O_3$-$BiScO_3$ [Raengthon et al. (2012)]. These offer temperature-stability in relative permittivity to a maximum temperature of ~ 300-450 ºC, and with a lower limit of ~ 20 ºC for $70BaTiO_3$-$30BiScO_3$, and ~ 80 ºC for $50BaTiO_3$-$25Bi(Zn_{1/2}Ti_{1/2})O_3$-$25BiScO_3$. The $BaTiO_3$-$Bi(Zn_{1/2}Ti_{1/2})O_3$-$BiScO_3$ materials exhibit similar performance to BCT-BMT (this work) but the Leeds' material avoids costly raw materials: the high price of Sc_2O_3 would limit commercial use.

Other complex solid solution perovskites with minimal temperature variation in relative permittivity include: $Na_{0.5}Bi_{0.5}TiO_3$-$BaTiO_3$-$K_{0.5}Na_{0.5}NbO_3$ [Dittmer et al. (2011)], $Na_{0.5}Bi_{0.5}TiO_3$-$K_{0.5}Bi_{0.5}TiO_3$-$K_{0.5}Na_{0.5}NbO_3$ [Dittmer et al. (2012)], $Na_{0.5}Bi_{0.5}TiO_3$-$BaTiO_3$-$CaZrO_3$ [Acosta et al. (2012)]; and $Na_{0.5}Bi_{0.5}TiO_3$-$BaTiO_3$-

$K_{0.5}Na_{0.5}NbO_3$-$CaZrO_3$ [Acosta et al. (2012)]. However, dielectric losses increase sharply above ~ 300 ºC for this family of ceramic materials, limiting the working temperature to ~ 300 ºC for practical uses. They achieve temperature-stability in permittivity by compositional variation of the temperatures of T_m and a lower temperature inflection (of NBT), as well as changes to the relative magnitude and breadth of the dielectric anomalies.

A detailed comparison of the dielectric properties of the aforementioned materials explored during this research against the best alternative high-temperature dielectrics are presented in the bar plot, Figure 11.10 and Table 11.3.

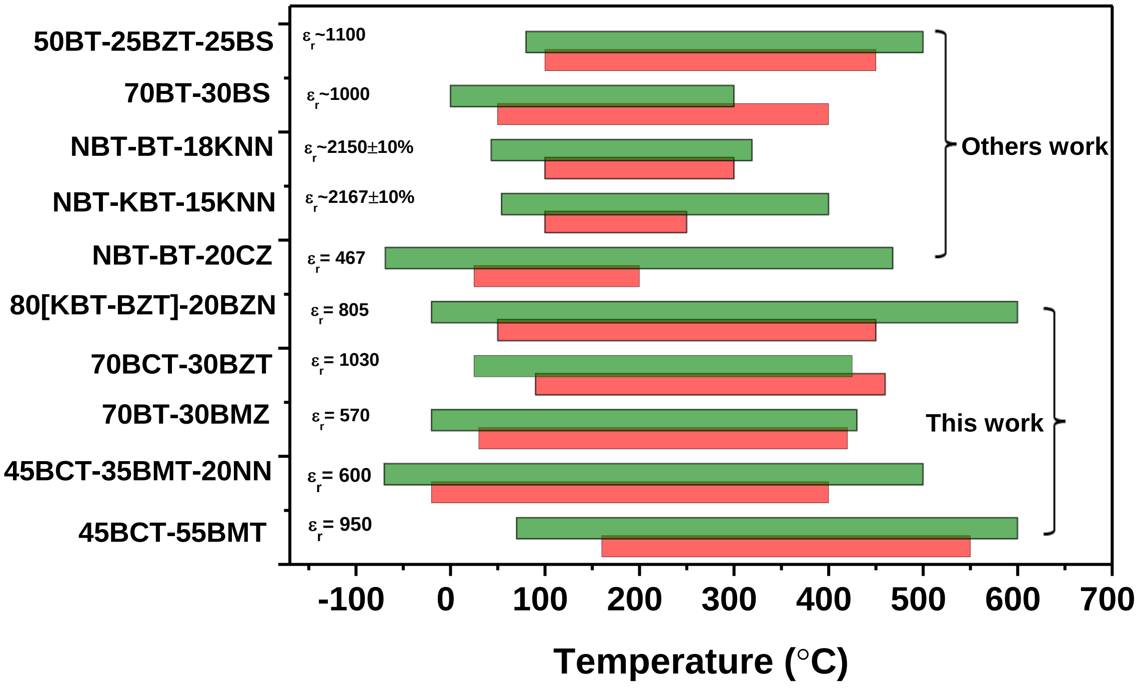

Figure 11.10 Comparison of temperature stable dielectric materials of the ceramic systems developed during this research with the others potential systems: NBT-BT-20CZ [Acosta et al. (2012)], BNT-KBT-15KNN [Dittmer et al. (2012)], NBT-BT-18KNN [Dittmer et al. (2011)], 70BT-30BS [Ogihara et al. (2009a)] and 50BT-25BZT-25BS [Raengthon et al. (2012)] (green bars indicate temperature range in ε_r±15% or less and red bars for tanδ ≤ 0.02).

Table 11.3 Comparison of the temperature stable dielectric properties for the ceramic materials developed during this research, relative permittivity within ±15% variation at 1 kHz and tanδ ≤ 0.02 (1 kHz), with other lead free potential temperature stable dielectric materials.

Material system	T-range, ε_r ±15% (ºC)	T-range (ºC) tanδ ≤ 0.02 (1 kHz)	References
$0.5Ba_{0.8}Ca_{0.2}TiO_3$-$0.5Bi(Mg_{0.5}Ti_{0.5})O_3$	800±15% (40-600)	(100-400)	This work
$0.45Ba_{0.8}Ca_{0.2}TiO_3$-$0.55Bi(Mg_{0.5}Ti_{0.5})O_3$	950±15% (70-600)	160-550	This work
$0.45Ba_{0.8}Ca_{0.2}TiO_3$-$0.35Bi(Mg_{0.5}Ti_{0.5})O_3$-$0.2NaNbO_3$	600±15% (-70-+500)	-20-+400	This work
$0.7BaTiO_3$-$0.3Bi(Mg_{0.5}Zr_{0.5})O_3$	570±15% (-20-+430)	30-420	This work
$0.8[0.5K_{0.5}Bi_{0.5}TiO_3$-$0.5Ba(Zr_{0.2}Ti_{0.8})O_3$-$0.2Bi(Zn_{2/3}Nb_{1/3})O_3$	805±15% (-20-+600)	50-450	This work
$0.7Ba_{0.8}Ca_{0.2}TiO_3$-$0.3Bi(Zn_{0.5}Ti_{0.5})O_3$	1030±15% (25-425)	85-460	This work
$0.7BaTiO_3$-$0.3BiScO_3$	1000±15% (0-300)	50-400	Ogihara et al. (2009a)
$0.5BaTiO_3$-$0.5Bi(Mg_{0.5}Ti_{0.5})O_3$	2400±15% (167-400)	238-400 (100 kHz)	Zhang et al. (2011)
$0.8BaTiO_3$-$0.2Bi(Zn_{0.5}Ti_{0.5})O_3$ (Ba-deficient	1150±15% (100-350)	tanδ ~ 0.05(100-460)	Raengthon and Cann (2011)
$0.5BaTiO_3$-$0.25Bi(Zn_{0.5}Ti_{0.5})O_3$-$0.25BiScO_3$ (Ba-deficient)	1100±15% (80-500)	~ 100-450	Raengthon et al. (2012)
$0.82(0.94Na_{0.5}Bi_{0.5}TiO_3$-$0.06BaTiO_3)$-$0.18K_{0.5}Na_{0.5}NbO_3$	2151±10% (43-319)	tanδ ≤ 0.025(50-300)	Dittmer et al. (2011)
$0.85[0.6Na_{0.5}Bi_{0.5}TiO_3$-$0.4K_{0.5}Bi_{0.5}TiO_3]$-$0.15K_{0.5}Na_{0.5}NbO_3$	2167±10% (54-400)	~ 100-250	Dittmer et al. (2012)
$0.8[0.82(0.94Na_{0.5}Bi_{0.5}TiO_3$-$0.06BaTiO_3)$-$0.18K_{0.5}Na_{0.5}NbO_3]$-$0.2CaZrO_3$	467±15% (-69-+468)	-	(Acosta et al. (2012))

Future Work

(1-*x*)KBT-*x*BMT and (1-*x*)KBT-*x*BZT Piezoelectrics

Understanding the mechanisms behind the properties described in this thesis would require further work.

- For piezoelectric (1-*x*)KBT-*x*BMT and (1-*x*)KBT-*x*BZT ceramic systems, high resolution diffraction experiments, including *in situ* synchrotron and neutron experiments, would be important to understand the nature of the 'cubic' phase and its response to an applied electric field, for example, the evidence of ferroelectric character in the composition $x = 0.08$ [(1-*x*)KBT-*x*BMT], which is single phase cubic by XRD.
- High temperature XRD on poled samples will useful to correlate the depolarisation temperature with the phase transitions.
- Local structure analysis by X-ray absorption techniques (EXAFS, XANES), as well as high resolution TEM (including atomic resolution imaging and chemical analysis) to explore polar length scales and compositions of polar regions (especially at MPB region of KBT-BMT) would be invaluable to formulating mechanistic understanding.
- The piezoelectric materials developed exhibited useful features, for example the favourable electromechanical strain make these systems compositions as a potential candidate for the actuator applications. However, for durable actuator applications, fatigue analysis at different temperatures must be carried out at different temperatures (software problems with the Radiant prevented this within the thesis).
- To further elucidate electrical properties of the piezoelectric systems, PFM (Piezoresponse Force Microscopy) would be utilised to try to resolve polar nano domains.

- Synthesis of single crystals for (1-*x*)KBT-*x*BMT system would be highly useful, to have superior properties compared to polycrystalline ceramics because of the absence of grain boundaries.
- A detailed impedance spectroscopy analysis would be useful to understand the defect chemistry and its effect on dielectric losses.
- Thermally stimulated charge decay measurements for the end member KBT will be useful as a future work.
- Modification of the MPB compositions with other dopants like Li^{1+}, Ta^{5+} etc will be helpful to enhance the piezoelectric properties.

(1-*x*)BCT-*x*BMT and other temperature stable dielectric systems

Further improvements in basic dielectric properties and working temperature ranges are required for practical applications. Capacitor-grade testing is also essential to fully evaluate the materials.

- A fundamental study is also required to correlate the temperature stable dielectric parameters with the nano/lattice scale by the use of high resolution transmission electron microscopy (TEM) and elemental variation in the grains by electron probe microscopy analysis (EPMA). Local structure analysis by EXAFS, XANES also would be useful.
- Optimise densification of the ceramic samples by the incorporation of glass additives (e.g. B_2O_3, SiO_2 and ZnO) may be useful to produce dense ceramics and to enhance relative permittivity for capacitor applications.
- Energy storage density measurements under high electric field at different temperatures is important (thin layer samples are required to replicate real-life applications and achieve high electric fields to be tested).
- High insulation resistance and dielectric breakdown strength under high electric fields at different temperatures are the key figures for capacitors applications. Manganese (Mn) doping could be useful to increase the electrical resistivity and thus increasing the

RC time constant (as may other variations of composition e.g. Ba vacancies and excess volatile oxides).

- Analysis at high field by standard equipment using thin layers made by tape casting may be beneficial to minimise any defect in the samples and to enhance the dielectric breakdown strength.
- A detailed analysis by impedance spectroscopy in different environments (air, oxygen and nitrogen) will be helpful to understand the defect chemistry and its correlation to electrical properties.

Appendix

The figures presented below consist of selected XRD patterns containing secondary phases with closely possible matched ICCD patterns for different systems. XRD profiles and peak fitting by WinPlotr and X'pert Highscore plus for (1-*x*)KBT-*x*BMT system (*x* = 0.04) along with the deduced unit cell parameters are also presented below. Calculation of theoritical and geometrical density as an example for ceramics in the (1-*x*)KBT-*x*BMT system are given in the Tables A1 and A2.

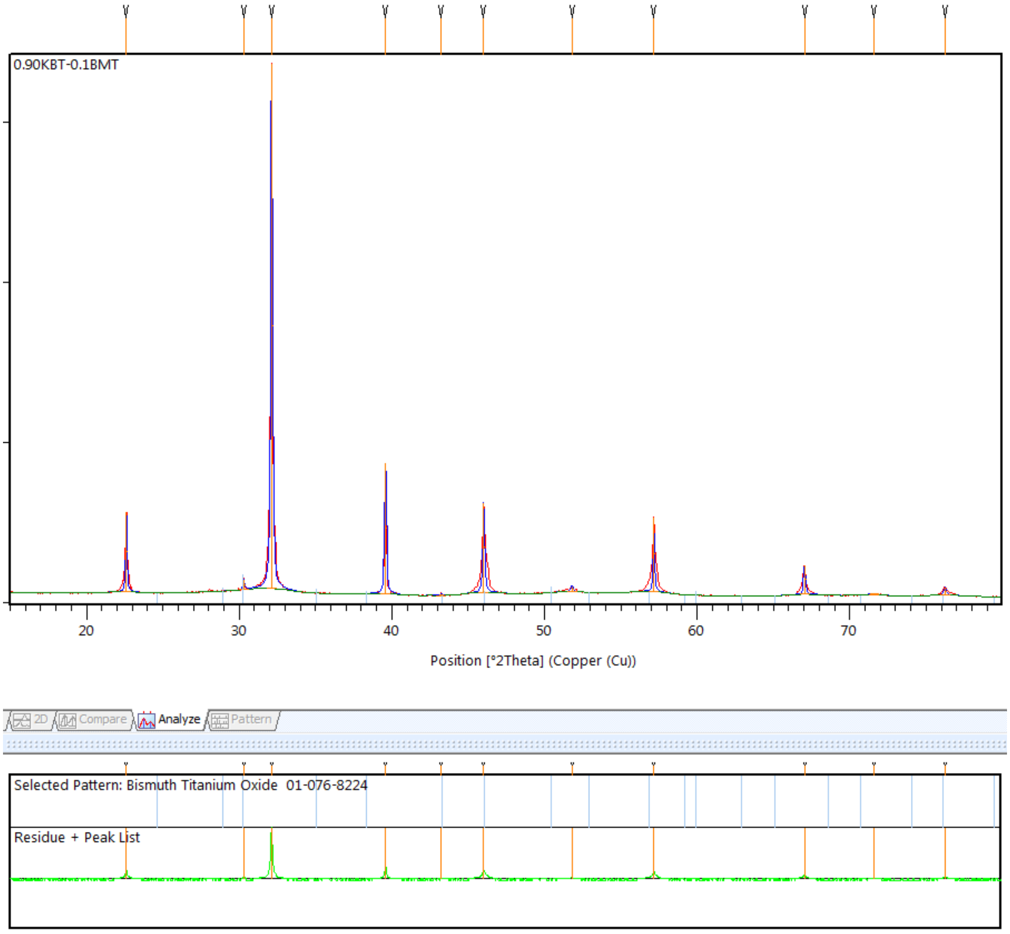

Figure A1 XRD pattern for 0.9KBT-0.1BMT ceramic crush powder indicating secondary phase of bismuth titanate.

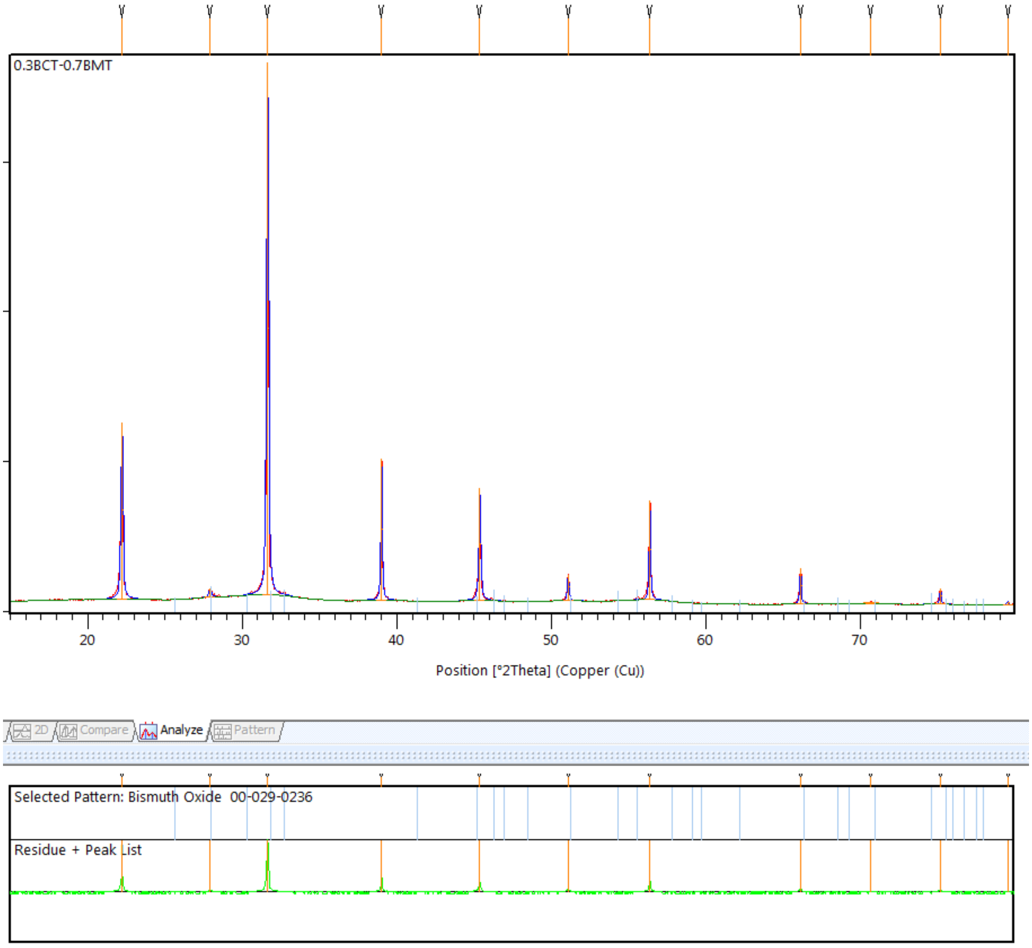

Figure A2 Room temperature XRD pattern for 0.3BCT-0.7BMT ceramic crush powder with the secondary phase of bismuth oxide.

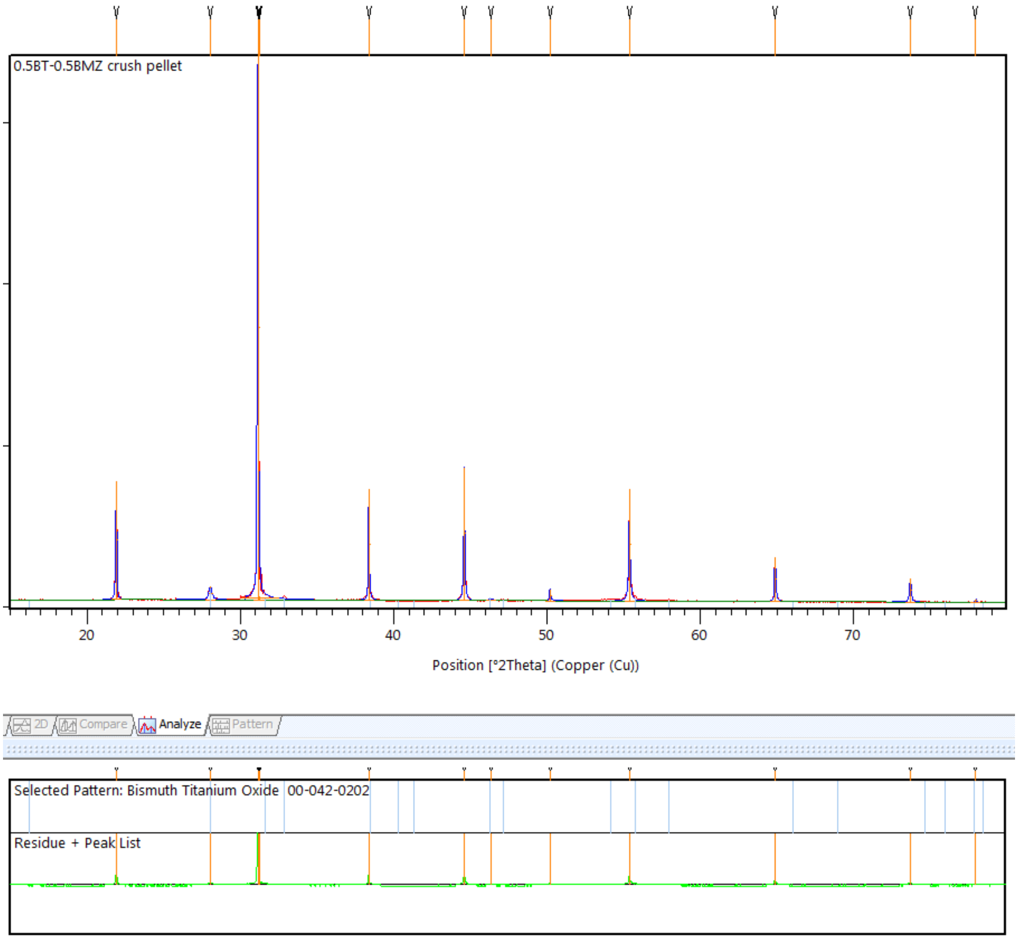

Figure A3 XRD pattern for 0.5BT-0.5BMZ ceramic crush powder with the secondary phase of bismuth titanate.

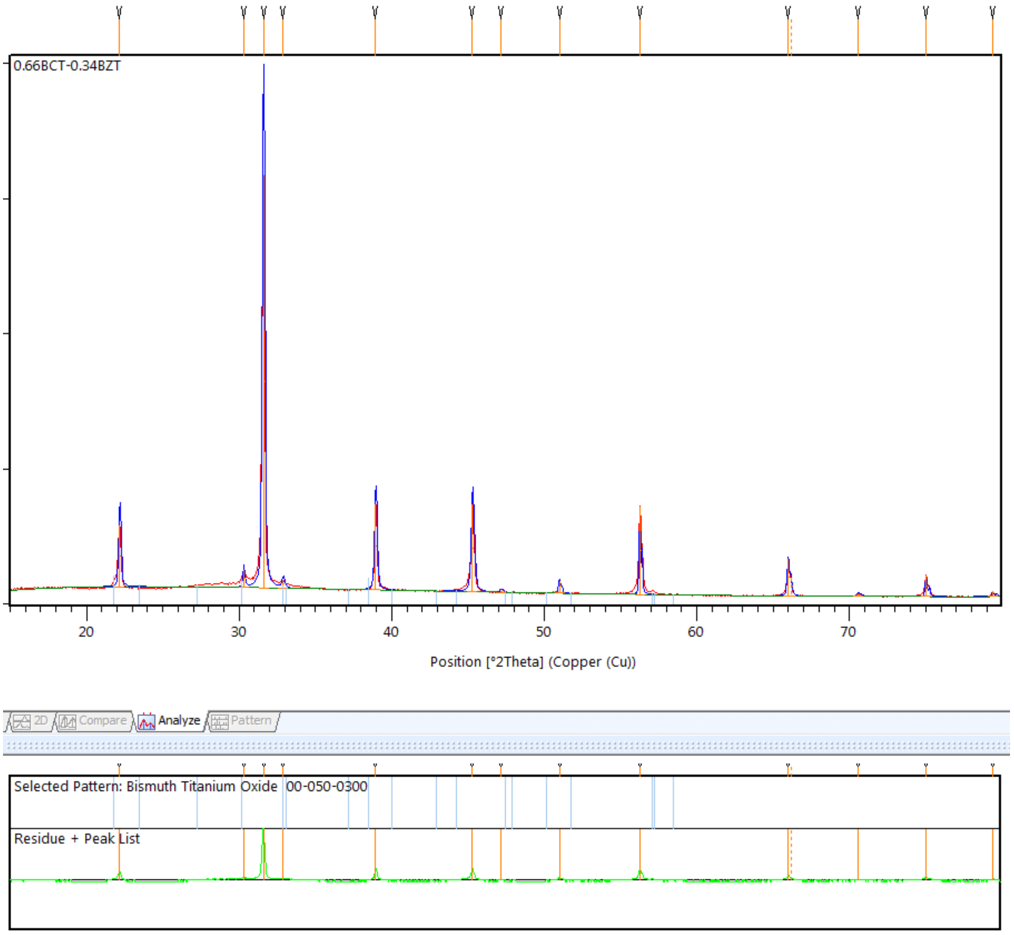

Figure A4 XRD pattern for 0.66BCT-0.34BZT ceramic crush powder with the secondary phase of bismuth titanate.

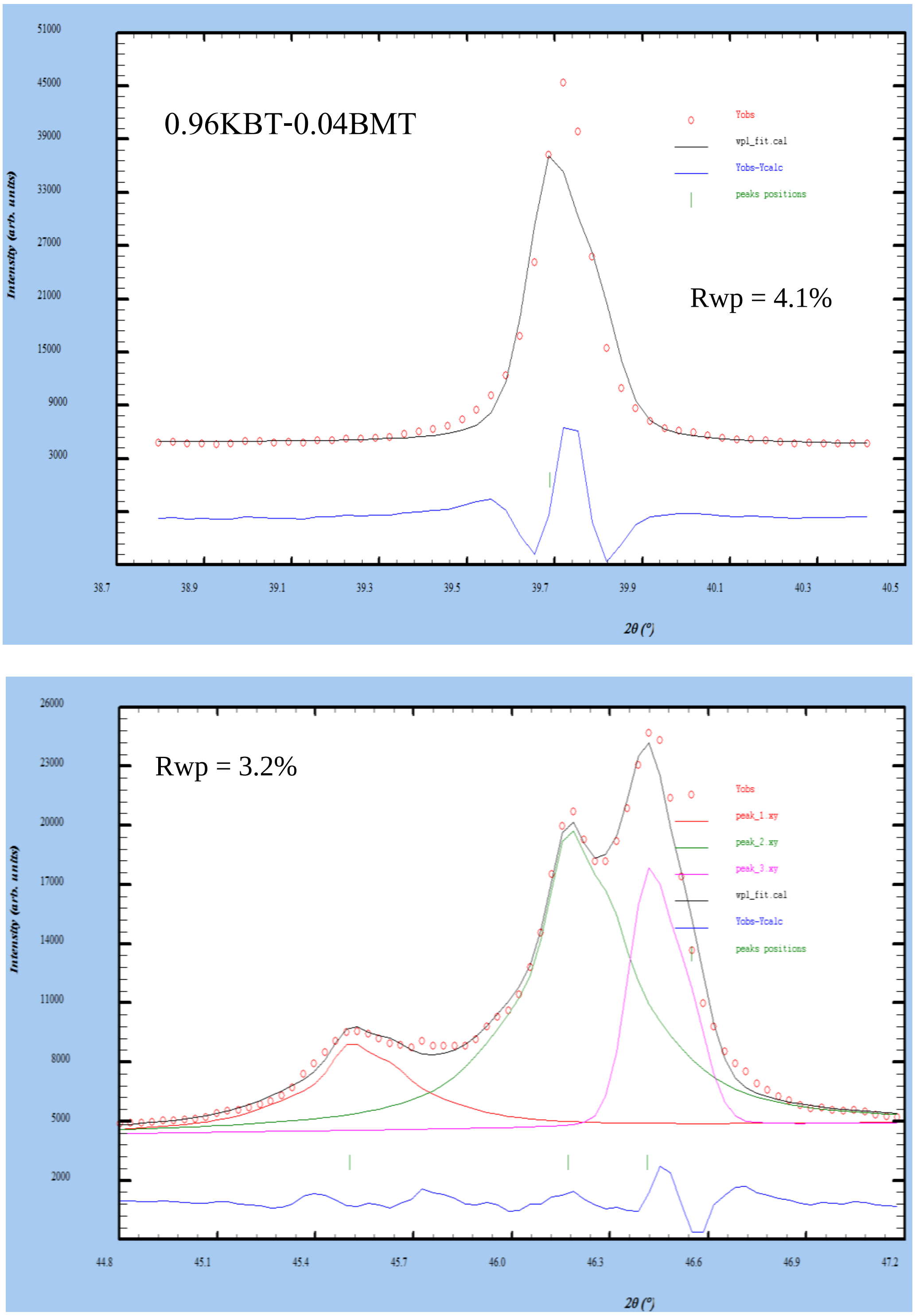

Figure A5 Illustration of XRD peak profile fitting by WinPlotr for 0.96KBT-0.04BMT composition with 111 and 200 peaks (Rwp is the quality of fit, as an example).

Table A1 Unit cell parameters deduced from XRD peak profile fitting by WinPlotr for (1-*x*)KBT-*x*BMT, *x* = 0.04 (as an example).

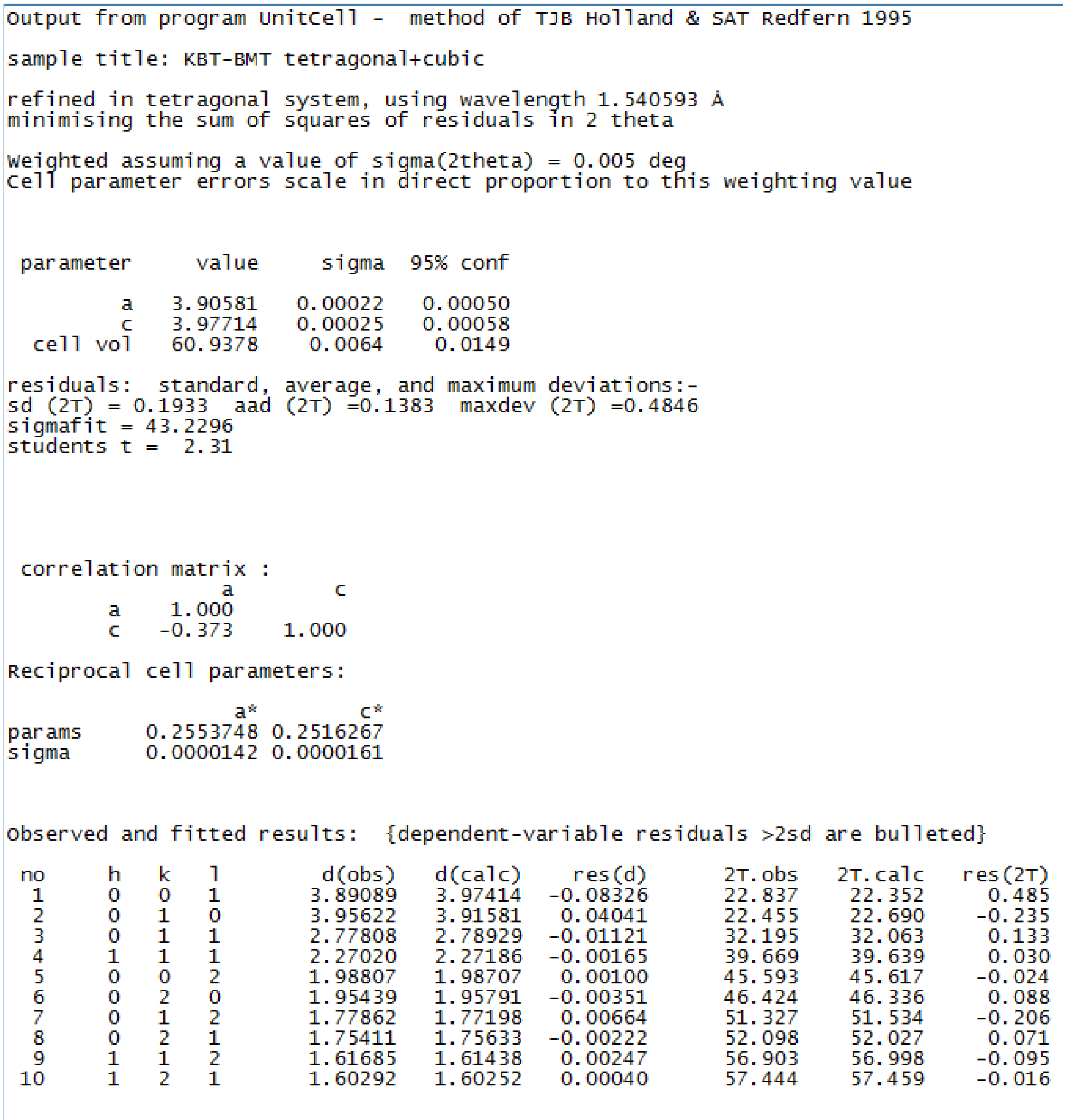

```
Output from program UnitCell -  method of TJB Holland & SAT Redfern 1995

sample title: KBT-BMT tetragonal+cubic

refined in tetragonal system, using wavelength 1.540593 Å
minimising the sum of squares of residuals in 2 theta

weighted assuming a value of sigma(2theta) = 0.005 deg
Cell parameter errors scale in direct proportion to this weighting value



 parameter     value     sigma   95% conf

         a    3.90581   0.00022   0.00050
         c    3.97714   0.00025   0.00058
  cell vol   60.9378     0.0064    0.0149

residuals:  standard, average, and maximum deviations:-
sd (2T) = 0.1933  aad (2T) =0.1383  maxdev (2T) =0.4846
sigmafit = 43.2296
students t =  2.31





 correlation matrix :
                 a        c
        a    1.000
        c   -0.373    1.000

Reciprocal cell parameters:

                   a*         c*
params      0.2553748 0.2516267
sigma       0.0000142 0.0000161



Observed and fitted results:  {dependent-variable residuals >2sd are bulleted}

 no      h   k   l         d(obs)   d(calc)    res(d)      2T.obs   2T.calc    res(2T)
  1      0   0   1        3.89089   3.97414  -0.08326      22.837    22.352      0.485
  2      0   1   0        3.95622   3.91581   0.04041      22.455    22.690     -0.235
  3      0   1   1        2.77808   2.78929  -0.01121      32.195    32.063      0.133
  4      1   1   1        2.27020   2.27186  -0.00165      39.669    39.639      0.030
  5      0   0   2        1.98807   1.98707   0.00100      45.593    45.617     -0.024
  6      0   2   0        1.95439   1.95791  -0.00351      46.424    46.336      0.088
  7      0   1   2        1.77862   1.77198   0.00664      51.327    51.534     -0.206
  8      0   2   1        1.75411   1.75633  -0.00222      52.098    52.027      0.071
  9      1   1   2        1.61685   1.61438   0.00247      56.903    56.998     -0.095
 10      1   2   1        1.60292   1.60252   0.00040      57.444    57.459     -0.016
```

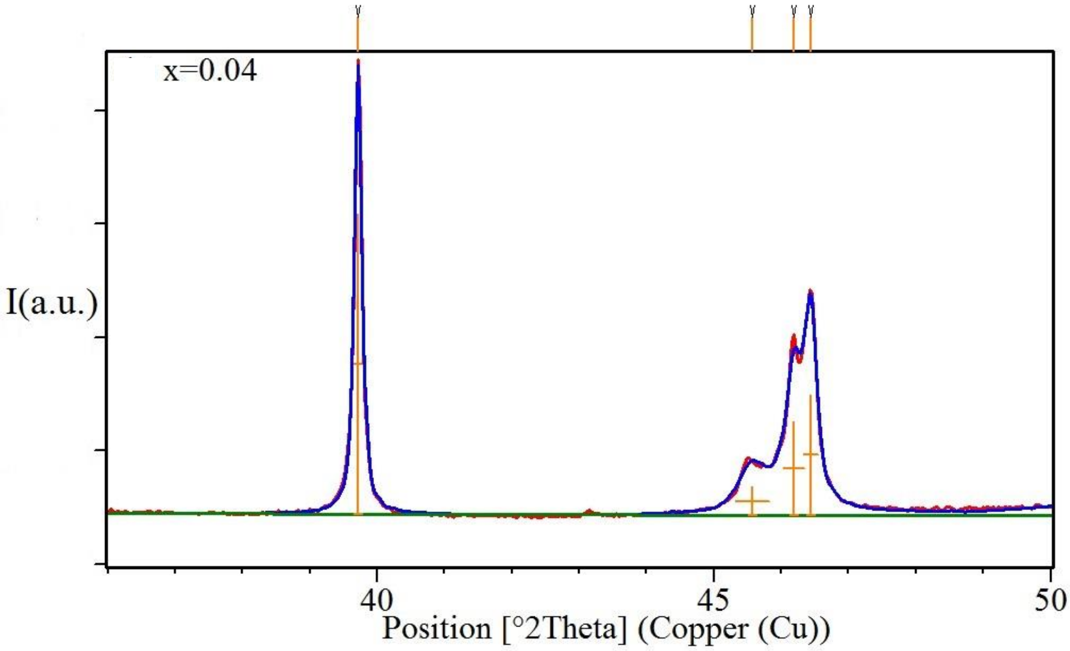

Figure A6 XRD profile and peak fitting by X'pert Highscore plus for (1-*x*)KBT-*x*BMT, *x* = 0.04 at room-temperature (as an example).

Table A2 Peaks position and d-spacing based on peak profile fitting by X'pert Highscore plus for (1-*x*)KBT-*x*BMT, *x* = 0.04 (as an example).

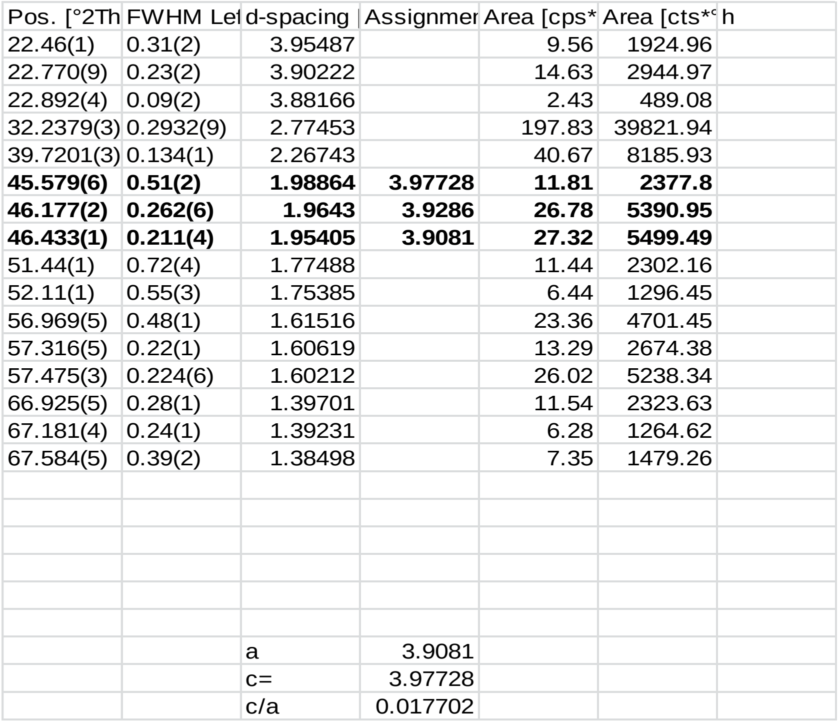

Pos. [°2Th	FWHM Le	d-spacing	Assignmen	Area [cps*	Area [cts*	h
22.46(1)	0.31(2)	3.95487		9.56	1924.96	
22.770(9)	0.23(2)	3.90222		14.63	2944.97	
22.892(4)	0.09(2)	3.88166		2.43	489.08	
32.2379(3)	0.2932(9)	2.77453		197.83	39821.94	
39.7201(3)	0.134(1)	2.26743		40.67	8185.93	
45.579(6)	**0.51(2)**	**1.98864**	**3.97728**	**11.81**	**2377.8**	
46.177(2)	**0.262(6)**	**1.9643**	**3.9286**	**26.78**	**5390.95**	
46.433(1)	**0.211(4)**	**1.95405**	**3.9081**	**27.32**	**5499.49**	
51.44(1)	0.72(4)	1.77488		11.44	2302.16	
52.11(1)	0.55(3)	1.75385		6.44	1296.45	
56.969(5)	0.48(1)	1.61516		23.36	4701.45	
57.316(5)	0.22(1)	1.60619		13.29	2674.38	
57.475(3)	0.224(6)	1.60212		26.02	5238.34	
66.925(5)	0.28(1)	1.39701		11.54	2323.63	
67.181(4)	0.24(1)	1.39231		6.28	1264.62	
67.584(5)	0.39(2)	1.38498		7.35	1479.26	
		a	3.9081			
		c=	3.97728			
		c/a	0.017702			

Table A3 Theoretical density calculations for (1-*x*)KBT-*x*BMT system (unit cell volumes measured from lattice parameters based on XRD data).

(x)	$(1-x)K_{0.5}Bi_{0.5}TiO_3$- $xBi(Mg_{0.5}Ti_{0.5})O_3$	ΣA	ρ = ΣA/NV (g/cm^3)
0	$K_{0.5}Bi_{0.5}TiO_3$	39.0983×0.5+208.9804×0.5 +47.867+15.9994×3 = 219.905	219.905/(6.023×10^{23}×60.907×10^{-24}) = 5.7
0.02	$K_{0.49}Bi_{0.51}Mg_{0.01}Ti_{0.99}O_3$	221.368	5.8
0.04	$K_{0.48}Bi_{0.52}Mg_{0.02}Ti_{0.98}O_3$	222.831	6.0
0.06	$K_{0.47}Bi_{0.53}Mg_{0.03}Ti_{0.97}O_3$	224.294	6.1
0.08	$K_{0.46}Bi_{0.54}Mg_{0.04}Ti_{0.96}O_3$	225.757	6.2

ΣA= sum of the atomic weights of the atoms in the unit cell, N = Avogadro number (6.023×10^{23} atoms/mol) and V is the volume of the unit cell.

Table A4 Calculation of geometrical density, ρ (based on the dimension of the disc) and % density for (1-*x*)KBT-*x*BMT system.

x	Pellet thickness, t (mm)	Pellet diameter, D (mm)	Pellet mass, m (g)	Density, ρ= 4m/3.14×D^2×t (g/cm^3)	Ave. density (g/cm^3)	% density
0	1.069	8.453	0.305	5.09	5.13	90
	1.075	8.387	0.302	5.12		
	1.040	8.394	0.297	5.17		
0.02	1.043	8.236	0.318	5.73	5.52	90
	1.026	8.236	0.304	5.56		
	1.051	8.255	0.317	5.64		
0.04	0.995	8.220	0.305	5.76	5.74	94
	1.065	8.166	0.313	5.60		
	1.015	8.246	0.323	5.96		
0.06	0.992	8.278	0.320	5.96	5.80	94
	1.005	8.268	0.313	5.81		
	1.003	8.321	0.316	5.78		
0.08	1.059	8.354	0.339	5.83	5.82	93
	1.034	8.396	0.336	5.85		
	1.062	8.379	0.342	5.81		

ρ = mass/volume = m/V= m/area×length = m/ πr^2×t = 4m/3.14×D^2×t.

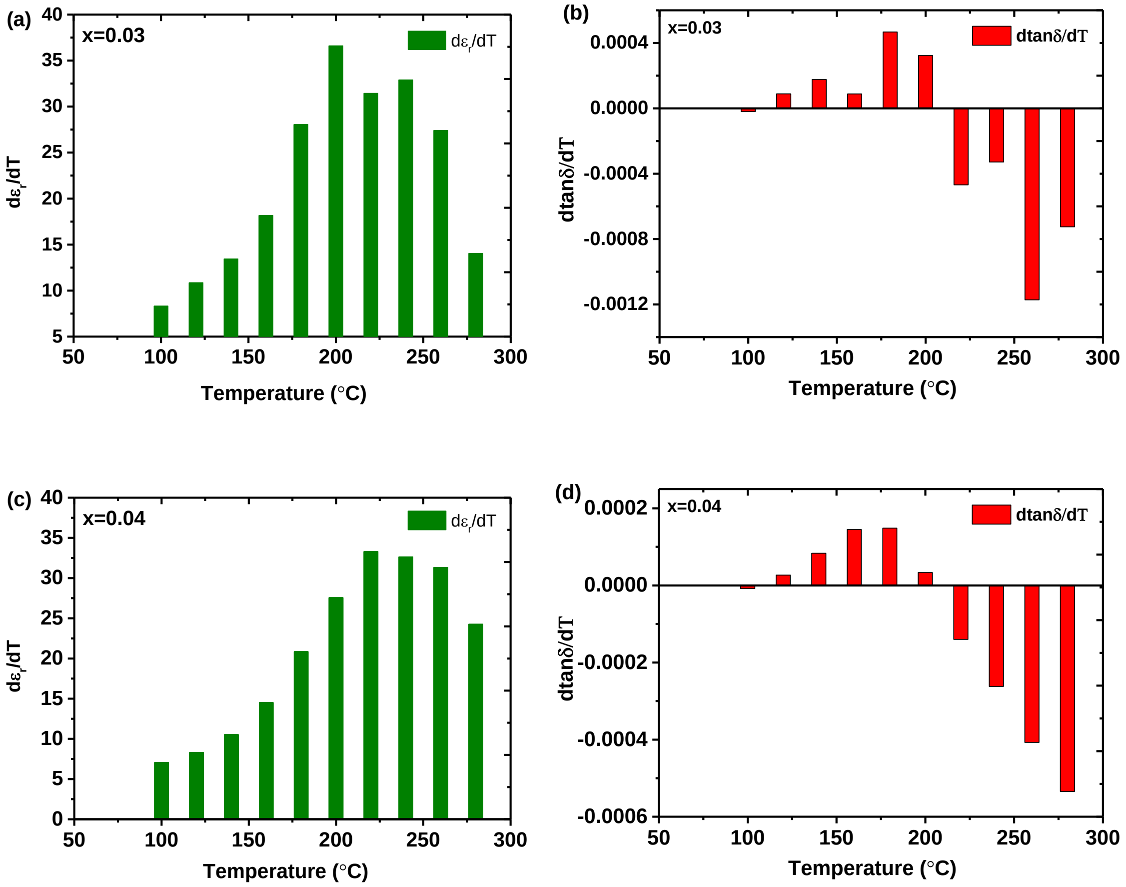

Figure A7 Temperature dependent differential plots of relative permittivity and tanδ for poled samples (a-b) x = 0.03 and (c-d) x = 0.04. This broadly confirms the interpretation of inflection temperatures in ε_r-T and tanδ plots quoted in in Chapter 4.

Tolerance Factor Considerations for Future Work

A plot of tolerance factor versus *x*BMT content for the temperature-stable relative permittivity system (1-*x*)BCT-*x*BMT is shown in Figure A8. The tolerance factor decreases with increasing *x*, as the ε_r-T peak becomes progressively supressed. However, during the research project, compositional disorder was the main selection criteria when exploring new high-temperature dielectric solid solutions. For example, in the (1-*x*)BCT-*x*BMT system increasing amount of BMT(*x*) led to the increase in entropy and hence increased disorder on both A and B sites. In future it may be useful to use tolerance factor, or more sensitive mathematical correlation using temperature dependent ionic radii and polarisabilities to predict structures [Miller and Tidrow (2015)].

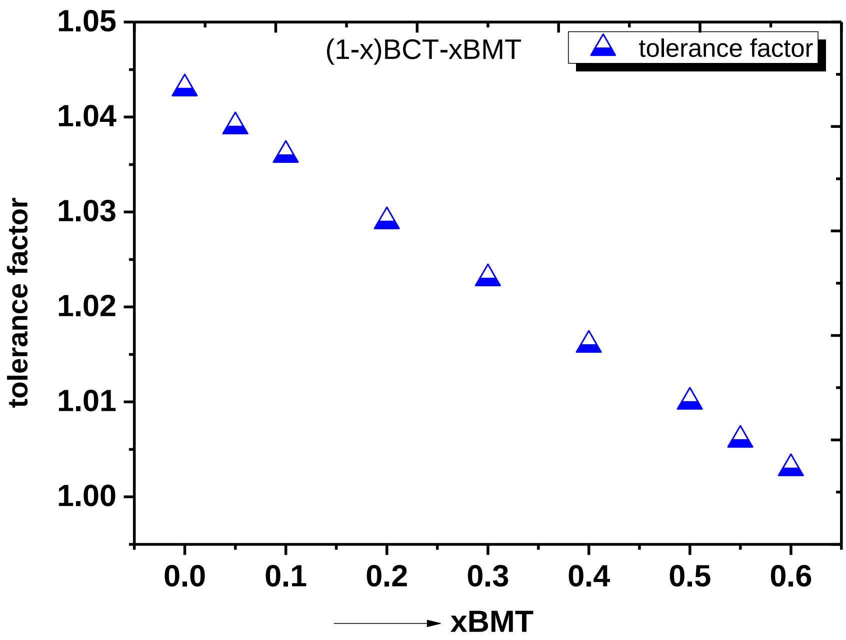

Figure A8 Variation of tolerance factor with *x*BMT for the ceramic system (1-*x*)BCT-*x*BMT.

References

Acosta, M., Zang, J., Jo, W. and Rödel, J. (2012) High-temperature dielectrics in $CaZrO_3$-modified $Bi_{1/2}Na_{1/2}TiO_3$-based lead-free ceramics. *Journal of the European Ceramic Society, 32*(16), pp. 4327-4334.

Ahart, M., Somayazulu, M., Cohen, R., Ganesh, P., Dera, P., Mao, H.-k., Hemley, R. J., Ren, Y., Liermann, P. and Wu, Z. (2008) Origin of morphotropic phase boundaries in ferroelectrics. *Nature, 451*(7178), pp. 545-548.

Ahn, C., Rabe, K. and Triscone, J.-M. (2004) Ferroelectricity at the nanoscale: local polarization in oxide thin films and heterostructures. *Science, 303*(5657), pp. 488-491.

Ansell, T. Y., Cann, D. P., Sapper, E. and Rödel, J. (2014) Thermal Depolarization in the High-Temperature Ternary Piezoelectric System xPbTiO$_3$–yBiScO$_3$–zBi(Ni$_{1/2}$Ti$_{1/2}$)O$_3$. *Journal of the American Ceramic Society*.

Anton, E.-M., Jo, W., Damjanovic, D. and Rödel, J. (2011) Determination of depolarization temperature of $(Bi_{1/2}Na_{1/2})TiO_3$-based lead-free piezoceramics. *Journal of applied physics, 110*(9), pp. 094108.

Argast, A. a. T., Clarence F., (2004) A web resource for the study of alkali feldspars and perthitic textures using light microscopy, scanning electron microscopy and energy dispersive X-ray spectroscopy. *Journal of Geoscience Education, 52*(3), pp. 213-217.

Badapanda, T., Rout, S., Cavalcante, L., Sczancoski, J., Panigrahi, S., Longo, E. and Li, M. S. (2009) Optical and dielectric relaxor behaviour of $Ba(Zr_{0.25}Ti_{0.75})O_3$ ceramic explained by means of distorted clusters. *Journal of Physics D: Applied Physics, 42*(17), pp. 175414.

Bai, W., Hao, J., Shen, B. and Zhai, J. (2013) Dielectric properties and relaxor behavior of high Curie temperature $(Ba_{0.85}Ca_{0.15})(Zr_{0.1}Ti_{0.9})O_3$–$Bi(Mg_{0.5}Ti_{0.5})O_3$ Lead-free ceramics. *Ceramics International, 39*(Supplement 1), pp. S19-S23.

Barsoum, M. and Barsoum, M. (2003) *Fundamentals of ceramics,* Taylor & Francis group, New York, NY 10016.

Bengagi, M., Morini, F., El Maaoui, M. and Marchet, P. (2012) Structure and electrical properties in the $K_{1/2}Bi_{1/2}TiO_3$–$K_{1/2}Bi_{1/2}ZrO_3$ solid solution (KBT–KBZ). *physica status solidi (a), 209*(10), pp. 2063-2072.

Bokov, A. (1992) Recent advances in diffuse ferroelectric phase transitions. *Ferroelectrics, 131*(1), pp. 49-55.

Bokov, A. and Ye, Z.-G. (2006) Recent progress in relaxor ferroelectrics with perovskite structure. in *Frontiers of Ferroelectricity*: Springer. pp. 31-52.

Bokov, A. and Ye, Z.-G. (2007) Recent progress in relaxor ferroelectrics with perovskite structure. in *Frontiers of Ferroelectricity*: Springer. pp. 31-52.

Bokov, A. A. and Ye, Z. G. (2000) Phenomenological description of dielectric permittivity peak in relaxor ferroelectrics. *Solid state communications, 116*(2), pp. 105-108.

Bomlai, P., Sinsap, P., Muensit, S. and Milne, S. J. (2008) Effect of MnO on the phase development, microstructures, and dielectric properties of $0.95Na_{0.5}K_{0.5}NbO_3$–$0.05LiTaO_3$ ceramics. *Journal of the American Ceramic Society, 91*(2), pp. 624-627.

Bongkarn, T., Rujijanagul, G. and Milne, S. (2008) Antiferroelectric-ferroelectric phase transitions in $Pb_{1-x}Ba_xZrO_3$ ceramics: Effect of PbO content. *Applied Physics Letters, 92*(9), pp. 092905-092905-3.

Bonneau, P., Garnier, P., Calvarin, G., Husson, E., Gavarri, J., Hewat, A. and Morell, A. (1991) X-ray and neutron diffraction studies of the diffuse phase transition in $PbMg_{1/3}Nb_{2/3}O_3$ ceramics. *Journal of Solid State Chemistry, 91*(2), pp. 350-361.

Bonneau, P., Garnier, P., Husson, E. and Morell, A. (1989) Structural study of PMN ceramics by X-ray diffraction between 297 and 1023 K. *Materials Research Bulletin, 24*(2), pp. 201-206.

Bridger, K., Cooke, A. V. and Schulze, W. A. (2008) High-Temperature Dielectric Materials and Capacitors Made Therefrom. in: US patent 2008/0239627 A1.

Buhrer, C. F. (1962) Some properties of bismuth perovskites. *The Journal of Chemical Physics, 36*(3), pp. 798-803.

Cai, W., Fan, Y., Gao, J., Fu, C. and Deng, X. (2011) Microstructure, dielectric properties and diffuse phase transition of barium stannate titanate ceramics. *Journal of Materials Science: Materials in Electronics, 22*(3), pp. 265-272.

Chen, X., Chen, J., Ma, D., Huang, G., Fang, L. and Zhou, H. (2015) High relative permittivity, low dielectric loss and good thermal stability of novel $(K_{0.5}Na_{0.5})NbO_3$–$Bi(Zn_{0.75}W_{0.25})O_3$ solid solution. *Materials Letters, 145*, pp. 247-249.

Cheng, X., Wu, J., Lou, X., Wang, X., Wang, X., Xiao, D. and Zhu, J. (2014) Achieving Both Giant d_{33} and High T_C in Patassium-Sodium Niobate Ternary System. *ACS applied materials & interfaces, 6*(2), pp. 750-756.

Cheng, Y., Bi, Z., Huq, A., Feygenson, M., Bridges, C., Paranthaman, M. and Sumpter, B. (2014) An integrated approach for structural characterization of complex solid state electrolytes: the case of lithium lanthanum titanate. *Journal of Materials Chemistry A, 2*(7), pp. 2418-2426.

Choi, D. H., Baker, A., Lanagan, M., Trolier-McKinstry, S. and Randall, C. (2013) Structural and Dielectric Properties in $(1\text{-}x)BaTiO_3–xBi(Mg_{1/2}Ti_{1/2})O_3$ Ceramics ($0.1 \leq x \leq 0.5$) and Potential for High-Voltage Multilayer Capacitors. *Journal of the American Ceramic Society, 96*(7), pp. 2197-2202.

Chu, B.-J., Chen, D.-R., Li, G.-R. and Yin, Q.-R. (2002) Electrical Properties of $Na_{1/2}Bi_{1/2}TiO_3–BaTiO_3$ Ceramics. *Journal of the European Ceramic Society, 22*(13), pp. 2115-2121.

Coondoo, I., Panwar, N. and Kholkin, A. (2013) Lead-free piezoelectrics: Current status and perspectives. *Journal of Advanced Dielectrics, 3*(02).

Cullity, B. D. and Stock, S. R. (2001) *Elements of X-ray Diffraction,* Pearson Prentice-Hall, Inc. New Jersey 07458.

Damjanovic, D. (1998) Ferroelectric, dielectric and piezoelectric properties of ferroelectric thin films and ceramics. *Reports on Progress in Physics, 61*(9), pp. 1267.

Daniels, J. E., Jo, W., Rödel, J., Honkimäki, V. and Jones, J. L. (2010) Electric-field-induced phase-change behavior in $(Bi_{0.5}Na_{0.5})TiO_3–BaTiO_3–(K_{0.5}Na_{0.5})NbO_3$: A combinatorial investigation. *Acta Materialia, 58*(6), pp. 2103-2111.

Directive (2003a) Directive 2002/95/EC of the European Parliament and of the Council on the restriction of the use of certain hazardous substances in electrical and electronic equipment. *Official Journal of the European Union, 1*(27), pp. 19-23.

Directive (2003b) EU-Directive 2002/96/EC: Waste Electrical and Electronic Equipment (WEEE)

Official Jounal of the European Union, 46(L37), pp. 24-38.

Dittmer, R., Anton, E. M., Jo, W., Simons, H., Daniels, J. E., Hoffman, M., Pokorny, J., Reaney, I. M. and Rödel, J. (2012) A High-Temperature-Capacitor Dielectric Based on $K_{0.5}Na_{0.5}NbO_3$-Modified $Bi_{1/2}Na_{1/2}TiO_3–Bi_{1/2}K_{1/2}TiO_3$. *Journal of the American Ceramic Society, 95*(11), pp. 3519-3524.

Dittmer, R., Jo, W., Damjanovic, D. and Rödel, J. (2011) Lead-free high-temperature dielectrics with wide operational range. *Journal of applied physics, 109*(3), pp. 034107.

Dorcet, V., Trolliard, G. and Boullay, P. (2008) Reinvestigation of phase transitions in $Na_{0.5}Bi_{0.5}TiO_3$ by TEM. Part I: First order rhombohedral to orthorhombic phase transition. *Chemistry of Materials, 20*(15), pp. 5061-5073.

Egerton, L. and Dillon, D. M. (1959) Piezoelectric and dielectric properties of ceramics in the system potassium—sodium niobate. *Journal of the American Ceramic Society, 42*(9), pp. 438-442.

Eitel, R. E., Randall, C. A., Shrout, T. R., Rehrig, P. W., Hackenberger, W. and Park, S.-E. (2001) New high temperature morphotropic phase boundary piezoelectrics based on $Bi(Me)O_3$–$PbTiO_3$ ceramics. *Japanese Journal of Applied Physics, 40*(10R), pp. 5999.

El-Mallah, H. M. (2004) D.C. conduction mechanisms of certain perovskite ceramics. *Journal of materials science, 39*(5), pp. 1711-1715.

Feng, L., Jiang, L., Zhu, M., Liu, H., Zhou, X. and Li, C. (2008) Formability of ABO_3 cubic perovskites. *Journal of Physics and Chemistry of Solids, 69*(4), pp. 967-974.

Glaum, J., Simons, H., Acosta, M. and Hoffman, M. (2013) Tailoring the piezoelectric and relaxor properties of $(Bi_{1/2}Na_{1/2})TiO_3$–$BaTiO_3$ via zirconium doping. *Journal of the American Ceramic Society, 96*(9), pp. 2881-2886.

Goodhew, P. J., Humphreys, J. and Beanland, R. (2001) *Electron microscopy and analysis,* Taylor & Francis London.

Guo, Y., Kakimoto, K.-i. and Ohsato, H. (2004) Phase transitional behavior and piezoelectric properties of $(Na_{0.5}K_{0.5})NbO_3$–$LiNbO_3$ ceramics. *Applied Physics Letters, 85*(18), pp. 4121-4123.

Guo, Y., Liu, Y., Withers, R. L., Brink, F. and Chen, H. (2010) Large Electric Field-Induced Strain and Antiferroelectric Behavior in $(1-x)(Na_{0.5}Bi_{0.5})TiO_3$-$xBaTiO_3$ Ceramics. *Chemistry of Materials, 23*(2), pp. 219-228.

Guo, Y., Liu, Y., Withers, R. L., Brink, F. and Chen, H. (2011) Large Electric Field-Induced Strain and Antiferroelectric Behavior in $(1-x)(Na_{0.5}Bi_{0.5})TiO_3$-$xBaTiO_3$ Ceramics. *Chemistry of Materials, 23*(2), pp. 219-228.

Haertling, G. H. (1999) Ferroelectric ceramics: history and technology. *Journal of the American Ceramic Society, 82*(4), pp. 797-818.

Hammond, C. (2001) *The basics of crystallography and diffraction,* 2nd edition, Oxford University Press, Oxford.

Hao, H., Liu, H., Zhang, S., Xiong, B., Shu, X., Yao, Z. and Cao, M. (2012) Fabrication, structure and property of $BaTiO_3$-based dielectric ceramics with a multilayer core–shell structure. *Scripta Materialia, 67*(5), pp. 451-454.

Hao, X. (2013) A review on the dielectric materials for high energy-storage application. *Journal of Advanced Dielectrics, 3*(01).

Hass, D. and Wadley, H. (2011) A Dielectric Sensing Approach for Controlling Matrix Composition During Oxide-Oxide Ceramic Composite Processing. *Journal of Nondestructive Evaluation, 30*(2), pp. 81-90.

Hiruma, Y., Aoyagi, R., Nagata, H. and Takenaka, T. (2004) Piezoelectric properties of $BaTiO_3$–$(Bi_{1/2}K_{1/2})TiO_3$ ferroelectric ceramics. *Japanese Journal of Applied Physics, 43*(11R), pp. 7556.

Hiruma, Y., Aoyagi, R., Nagata, H. and Takenaka, T. (2005) Ferroelectric and piezoelectric properties of $(Bi_{1/2}K_{1/2})TiO_3$ ceramics. *Japanese Journal of Applied Physics, 44*(7R), pp. 5040.

Hiruma, Y., Nagata, H. and Takenaka, T. (2007a) Grain-size effect on electrical properties of $(Bi_{1/2}K_{1/2})TiO_3$ ceramics. *Japanese Journal of Applied Physics, 46*(3R), pp. 1081.

Hiruma, Y., Nagata, H. and Takenaka, T. (2009) Thermal depoling process and piezoelectric properties of bismuth sodium titanate ceramics. *Journal of applied physics, 105*(8), pp. 4112.

Hiruma, Y., Watanabe, Y., Nagata, H. and Takenaka, T. (2007b) Phase transition temperatures of divalent and trivalent ions substituted $(Bi_{1/2}Na_{1/2})TiO_3$ ceramics. *Key Engineering Materials, 350*, pp. 93-96.

Huang, C.-C. and Cann, D. P. (2008) Phase transitions and dielectric properties in $Bi(Zn_{1/2}Ti_{1/2})O_3$-$BaTiO_3$ perovskite solid solutions. *Journal of applied physics, 104*(2), pp. 024117-024117-4.

Huang, C.-C., Vittayakorn, N. and Cann, D. P. (2009) Structure and ferroelectric properties of $Bi(Zn_{1/2}Ti_{1/2})O_3$-$(Bi_{1/2}K_{1/2})TiO_3$ perovskite solid solutions. *Ultrasonics, Ferroelectrics, and Frequency Control, IEEE Transactions on, 56*(7), pp. 1304-1308.

Isupov, V. (2005) Ferroelectric $Na_{0.5}Bi_{0.5}TiO_3$ and $K_{0.5}Bi_{0.5}iTO_3$ perovskites and their solid solutions. *Ferroelectrics, 315*(1), pp. 123-147.

Jaffe, B., Cook, W. R. & Jaffe, H. (1971) *Piezoelectric Ceramics* Academic Press, London.

Jarupoom, P., Patterson, E., Gibbons, B., Rujijanagul, G., Yimnirun, R. and Cann, D. (2011) Lead-free ternary perovskite compounds with large electromechanical strains. *Applied Physics Letters, 99*(15), pp. 152901.

Kamei, H., Fujii, I., Nakashima, K., Kuroiwa, Y., Minemoto, H. and Wada, S. (2014) Preparation of $(Bi_{1/2}K_{1/2})TiO_3$-$Bi(Mg_{1/2}Ti_{1/2})O_3$-$BiFeO_3$ Ceramics with nanodomain Structure and their Piezoelectric Properties. *Key Engineering Materials, 582*, pp. 88-91.

Kawada, S., Kimura, M., Higuchi, Y. and Takagi, H. (2009) (K, Na) NbO_3-based multilayer piezoelectric ceramics with nickel inner electrodes. *Applied physics express, 2*(11), pp. 111401.

Kim, J., Sung, Y., Cho, J., Song, T., Kim, M., Chong, H., Park, T., Do, D. and Kim, S. (2010) Piezoelectric and Dielectric Properties of Lead-Free (1-x)$(Bi_{0.5}K_{0.5})TiO_3$-x$BiFeO_3$ Ceramics. *Ferroelectrics, 404*(1), pp. 88-92.

Kleemann, W. (2012) Random fields in relaxor ferroelectrics—a jubilee review. *Journal of Advanced Dielectrics, 2*(02), pp. 1241001.

König, J., Spreitzer, M. and Suvorov, D. (2011) Influence of the synthesis conditions on the dielectric properties in the $Bi_{0.5}Na_{0.5}TiO_3$–$KTaO_3$ system. *Journal of the European Ceramic Society, 31*(11), pp. 1987-1995.

Kruea-In, C., Rujijanagul, G., Zhu, F. Y. and Milne, S. J. (2012) Relaxor behaviour of $K_{0.5}Bi_{0.5}TiO_3$-$BiScO_3$ ceramics. *Applied Physics Letters, 100*(20), pp. 202904.

Lee, S., Randall, C. A. and Liu, Z. K. (2007) Modified phase diagram for the barium oxide–titanium dioxide system for the ferroelectric barium titanate. *Journal of the American Ceramic Society, 90*(8), pp. 2589-2594.

Lee, W.-C., Huang, C.-Y., Tsao, L.-K. and Wu, Y.-C. (2009) Chemical composition and tolerance factor at the morphotropic phase boundary in $(Bi_{0.5}Na_{0.5})TiO_3$-based piezoelectric ceramics. *Journal of the European Ceramic Society, 29*(8), pp. 1443-1448.

Leontsev, S. O. and Eitel, R. E. (2010) Progress in engineering high strain lead-free piezoelectric ceramics. *Science and Technology of Advanced Materials, 11*(4), pp. 044302.

Levin, I., Krayzman, V. and Woicik, J. C. (2013) Local-structure origins of the sustained Curie temperature in (Ba,Ca)TiO_3 ferroelectrics. *Applied Physics Letters, 102*(16), pp. 162906.

Li, M., Zhang, H., Cook, S. N., Li, L., Kilner, J. A., Reaney, I. M. and Sinclair, D. C. (2015) Dramatic Influence of A-Site Nonstoichiometry on the Electrical Conductivity and Conduction Mechanisms in the Perovskite Oxide $Na_{0.5}Bi_{0.5}TiO_3$. *Chemistry of Materials, 27*(2), pp. 629-634.

Li, W., Xu, Z., Chu, R., Fu, P. and Zang, G. (2011) High piezoelectric d_{33} coefficient of lead-free $(Ba_{0.93}Ca_{0.07})(Ti_{0.95}Zr_{0.05})O_3$ ceramics sintered at optimal temperature. *Materials Science and Engineering: B, 176*(1), pp. 65-67.

Li, Y., Chen, W., Zhou, J., Xu, Q., Sun, H. and Xu, R. (2004) Dielectric and piezoelecrtic properties of lead-free $(Na_{0.5}Bi_{0.5})TiO_3$–$NaNbO_3$ ceramics. *Materials Science and Engineering: B, 112*(1), pp. 5-9.

Lim, J. B., Zhang, S., Kim, N. and Shrout, T. R. (2009) High-Temperature Dielectrics in the $BiScO_3$–$BaTiO_3$–$(K_{1/2}Bi_{1/2})TiO_3$ Ternary System. *Journal of the American Ceramic Society, 92*(3), pp. 679-682.

Liu, G., Zhang, S., Jiang, W. and Cao, W. (2015) Losses in ferroelectric materials. *Materials Science and Engineering: R: Reports, 89*, pp. 1-48.

Liu, M., Hao, H., Zhen, Y., Wang, T., Zhou, D., Liu, H., Cao, M. and Yao, Z. (2015) Temperature stability of dielectric properties for $xBiAlO_3$–$(1-x)BaTiO_3$ ceramics. *Journal of the European Ceramic Society, 35*(8), pp. 2303-2311.

Liu, W. and Ren, X. (2009) Large piezoelectric effect in Pb-free ceramics. *Physical Review Letters, 103*(25), pp. 257602.

Ma, C., Tan, X., Dul'Kin, E. and Roth, M. (2010) Domain structure-dielectric property relationship in lead-free $(1-x)(Bi_{1/2}Na_{1/2})TiO_3$-$xBaTiO_3$ ceramics. *Journal of applied physics, 108*(10), pp. 104105.

Ma, D., Chen, X., Huang, G., Chen, J., Zhou, H. and Fang, L. (2015) Temperature stability, structural evolution and dielectric properties of $BaTiO_3$–$Bi(Mg_{2/3}Ta_{1/3})O_3$ perovskite ceramics. *Ceramics International, 41*(5), pp. 7157-7161.

Martín-Arias, L., Castro, A. and Algueró, M. (2012) Ferroelectric phases and relaxor states in the novel lead-free (1-x)$Bi_{1/2}K_{1/2}TiO_3$-$x$$BiScO_3$ system ($0 \leq x \leq 0.3$). *Journal of materials science, 47*(8), pp. 3729-3740.

Matsuo, H., Noguchi, Y., Miyayama, M., Suzuki, M., Watanabe, A., Sasabe, S., Ozaki, T., Mori, S., Torii, S. and Kamiyama, T. (2010) Structural and piezoelectric properties of high-density ($Bi_{0.5}K_{0.5}$)TiO_3–$BiFeO_3$ ceramics. *Journal of applied physics, 108*(10), pp. 104103-104103-6.

Maurya, D., Murayama, M., Pramanick, A., Reynolds Jr, W., An, K. and Priya, S. (2013) Origin of high piezoelectric response in A-site disordered morphotropic phase boundary composition of lead-free piezoelectric 0.93($Na_{0.5}Bi_{0.5}$)TiO_3–0.07$BaTiO_3$. *Journal of applied physics, 113*(11), pp. 114101.

Miller, V. and Tidrow, S. (2015) Perovskites: Some Polarization Induced Structural Phase Transitions Using "Effective" Temperature and Coordination Dependent Radii and Polarizabilities of Ions. *Integrated Ferroelectrics, 166*(1), pp. 206-224.

Mitchel, B. (2003) An introduction to materials engineering and science. in: Wiley, New York. pp. 31.

Morozov, M. I., Einarsrud, M.-A., Grande, T. and Damjanovic, D. (2012) Lead-Free Relaxor-Like 0.75$Bi_{0.5}K_{0.5}TiO_3$–0.25$BiFeO_3$ Ceramics with Large Electric Field-Induced Strain. *Ferroelectrics, 439*(1), pp. 88-94.

Morrison, F. D., Sinclair, D. C. and West, A. R. (1999) Electrical and structural characteristics of lanthanum-doped barium titanate ceramics. *Journal of applied physics, 86*(11), pp. 6355-6366.

Moulson, A. J. and Herbert, J. M. (2003) *Electroceramics: materials, properties, applications*, 2nd Ed, John Wiley & Sons Ltd., New York.

Nagata, H., Tabuchi, K. and Takenaka, T. (2013) Fabrication and Electrical Properties of Multilayer Ceramic Actuator Using Lead-Free ($Bi_{1/2}K_{1/2}$)TiO_3. *Japanese Journal of Applied Physics, 52*(9S1), pp. 09KD05.

Nagata, H., Yoshida, M., Makiuchi, Y. and Takenaka, T. (2003) Large piezoelectric constant and high Curie temperature of lead-free piezoelectric ceramic ternary system based on bismuth sodium titanate-bismuth potassium titanate-barium titanate near the morphotropic phase boundary. *Japanese Journal of Applied Physics, 42*(12R), pp. 7401.

Nemoto, M., Hiruma, Y., Nagata, H. and Takenaka, T. (2008) Fabrication and piezoelectric properties of grain-oriented $(Bi_{1/2}K_{1/2})TiO_3$–$BaTiO_3$ ceramics. *Japanese Journal of Applied Physics, 47*(5S), pp. 3829.

Nemoto, M., Hiruma, Y., Nagata, H. and Takenaka, T. (2009) Electrical Properties of Textured $(Bi_{1/2}K_{1/2})TiO_3$–$BaTiO_3$ Lead-Free Piezoelectric Ceramics. *Japanese Journal of Applied Physics, 48*(7S), pp. 07GA04.

Noheda, B., Cox, D., Shirane, G., Gonzalo, J., Cross, L. and Park, S.-E. (1999) A monoclinic ferroelectric phase in the $Pb(Zr_{1-x}Ti_x)O_3$ solid solution. *Applied Physics Letters, 74*(14), pp. 2059-2061.

Ogihara, H., Randall, C. A. and Trolier-McKinstry, S. (2009a) Weakly Coupled Relaxor Behavior of $BaTiO_3$–$BiScO_3$ Ceramics. *Journal of the American Ceramic Society, 92*(1), pp. 110-118.

Ogihara, H., Randall, C. A. and Trolier-McKinstry, S. (2009b) Weakly coupled relaxor behavior of $BaTiO_3$–$BiScO_3$ ceramics. *Journal of the American Ceramic Society, 92*(1), pp. 110-118.

Otoničar, M., Škapin, S. D., Jančar, B., Ubic, R. and Suvorov, D. (2010) Analysis of the phase transition and the domain structure in $K_{0.5}Bi_{0.5}TiO_3$ perovskite ceramics by in situ XRD and TEM. *Journal of the American Ceramic Society, 93*(12), pp. 4168-4173.

Paik, D.-S., Park, S.-E., Shrout, T. and Hackenberger, W. (1999) Dielectric and piezoelectric properties of perovskite materials at cryogenic temperatures. *Journal of materials science, 34*(3), pp. 469-473.

Panda, P. and Sahoo, B. (2015) PZT to Lead Free Piezo Ceramics: A Review. *Ferroelectrics, 474*(1), pp. 128-143.

Popper, P., Ruddlesden, S. and Ingles, T. (1957) Double oxides with layer structures related to perovskite. I. Structure and electrical properties of $Bi_4Ti_3O_{12}$ and its application in dielectrics. *Trans. Br. Ceram. Soc, 56*, pp. 9.

Prasatkhetragarn, A., Yotburut, B., Triamnak, N., Yimnirun, R. and Cann, D. (2012) Synthesis and electrical properties of lead free $(Bi_{0.5}K_{0.5})TiO_3$–$BaTiO_3$–$Bi(Zn_{0.5}Ti_{0.5})O_3$ ceramics. *Ceramics International, 38*(1), pp. 827-830.

Prukop, S. and Barron, A. R. (2011) SEM and its Applications for Polymer Science.

Raengthon, N., Brown-Shaklee, H. J., Brennecka, G. L. and Cann, D. P. (2013) Dielectric properties of $BaTiO_3$–$Bi(Zn_{1/2}Ti_{1/2})O_3$–$NaNbO_3$ solid solutions. *Journal of materials science, 48*(5), pp. 2245-2250.

Raengthon, N. and Cann, D. P. (2011) High-K $(Ba_{0.8}Bi_{0.2})(Zn_{0.1}Ti_{0.9})O_3$ ceramics for high-temperature capacitor applications. *Ultrasonics, Ferroelectrics, and Frequency Control, IEEE Transactions on, 58*(9), pp. 1954-1958.

Raengthon, N. and Cann, D. P. (2012) Dielectric relaxation in $BaTiO_3$–$Bi(Zn_{1/2}Ti_{1/2})O_3$ ceramics. *Journal of the American Ceramic Society, 95*(5), pp. 1604-1612.

Raengthon, N., Sebastian, T., Cumming, D., Reaney, I. M. and Cann, D. P. (2012) $BaTiO_3$–$Bi(Zn_{1/2}Ti_{1/2})O_3$–$BiScO_3$ Ceramics for High-Temperature Capacitor Applications. *Journal of the American Ceramic Society, 95*(11), pp. 3554-3561.

Ramadass, N. (1978) ABO_3-type oxides—Their structure and properties—A bird's eye view. *Materials Science and Engineering, 36*(2), pp. 231-239.

Ranjan, R. and Dviwedi, A. (2005) Structure and dielectric properties of $(Na_{0.50}Bi_{0.50})_{1-x}Ba_xTiO_3$: $0 \leq x \leq 0.10$. *Solid state communications, 135*(6), pp. 394-399.

Ravez, J. and Simon, A. (2001) Some solid state chemistry aspects of lead-free relaxor ferroelectrics. *Journal of Solid State Chemistry*, *162*(2), pp. 260-265.

Reaney, I. M., Colla, E. L. and Setter, N. (1994) Dielectric and structural characteristics of Ba-and Sr-based complex perovskites as a function of tolerance factor. *Japanese Journal of Applied Physics, 33*(7R), pp. 3984.

Rödel, J., Jo, W., Seifert, K. T. P., Anton, E.-M., Granzow, T. and Damjanovic, D. (2009) Perspective on the Development of Lead-free Piezoceramics. *Journal of the American Ceramic Society, 92*(6), pp. 1153-1177.

Royles, A., Bell, A., Jephcoat, A., Kleppe, A., Milne, S. and Comyn, T. (2010) Electric-field-induced phase switching in the lead free piezoelectric potassium sodium bismuth titanate. *Appl. Phys. Lett, 97*(13), pp. 132909.

Saito, Y., Takao, H., Tani, T., Nonoyama, T., Takatori, K., Homma, T., Nagaya, T. and Nakamura, M. (2004) Lead-free piezoceramics. *Nature*, *432*(7013), pp. 84-87.

Sasaki, A., Chiba, T., Mamiya, Y. and Otsuki, E. (1999) Dielectric and piezoelectric properties of $(Bi_{0.5}Na_{0.5})TiO_3$–$(Bi_{0.5}K_{0.5})TiO_3$ systems. *Japanese Journal of Applied Physics, 38*(9S), pp. 5564.

Seifert, K. T., Jo, W. and Rödel, J. (2010) Temperature-Insensitive Large Strain of $(Bi_{1/2}Na_{1/2})TiO_3$–$(Bi_{1/2}K_{1/2})TiO_3$–$(K_{0.5}Na_{0.5})NbO_3$ Lead-Free Piezoceramics. *Journal of the American Ceramic Society*, *93*(5), pp. 1392-1396.

Selvamani, R., Singh, G., Tiwari, V. and Gupta, P. (2012) Oxygen vacancy related relaxation and conduction behavior in (1-x)NBT-xBiCrO$_3$ solid solution. *physica status solidi (a), 209*(1), pp. 118-125.

Shi, H., Chen, J., Wang, R. and Dong, S. (2016) Full set of material constants of (Na$_{0.5}$K$_{0.5}$)NbO$_3$–BaZrO$_3$–(Bi$_{0.5}$Li$_{0.5}$)TiO$_3$ lead-free piezoelectric ceramics at the morphotropic phase boundary. *Journal of Alloys and Compounds, 655*, pp. 290-295.

Shi, J., Fan, H., Liu, X., Ma, Y. and Li, Q. (2015) Bi deficiencies induced high permittivity in lead-free BNBT–BST high-temperature dielectrics. *Journal of Alloys and Compounds, 627,* pp. 463-467.

Shvartsman, V. V. and Lupascu, D. C. (2012) Lead-Free Relaxor Ferroelectrics. *Journal of the American Ceramic Society, 95*(1), pp. 1-26.

Skidmore, T. A. (2009) *Fabrication and Characterisation of Lead-Free Piezoelectric Ceramics. PhD thesis, University of Leeds, UK.*

Skidmore, T. A., Comyn, T. P., Bell, A. J., Zhu, F. and Milne, S. J. (2011) Phase diagram and structure-property relationships in the lead-free piezoelectric system: Na$_{0.5}$K$_{0.5}$NbO$_3$-LiTaO$_3$. *Ultrasonics, Ferroelectrics and Frequency Control, IEEE Transactions on, 58*(9), pp. 1819-1825.

Skidmore, T. A., Comyn, T. P. and Milne, S. J. (2009) Temperature stability of ([Na$_{0.5}$K$_{0.5}$NbO$_3$]$_{0.93}$–[LiTaO$_3$]$_{0.07}$) lead-free piezoelectric ceramics. *Applied Physics Letters, 94*(22), pp. 222902-222902-3.

Skidmore, T. A., Comyn, T. P. and Milne, S. J. (2010) Dielectric and piezoelectric properties in the system:(1-x)[(Na$_{0.5}$K$_{0.5}$NbO$_3$)$_{0.93}$–(LiTaO$_3$)$_{0.07}$]–x[BiScO$_3$]. *Journal of the American Ceramic Society, 93*(3), pp. 624-626.

Smith, M. B., Page, K., Siegrist, T., Redmond, P. L., Walter, E. C., Seshadri, R., Brus, L. E. and Steigerwald, M. L. (2008) Crystal structure and the paraelectric-to-ferroelectric phase transition of nanoscale BaTiO$_3$. *Journal of the American Chemical Society, 130*(22), pp. 6955-6963.

Smolenskii, G., Isupov, V., Agranovskaya, A. and Krainik, N. (1961) new ferroelectrics of complex composition, iv. *Soviet Physics-Solid State, 2*(11), pp. 2651-2654.

Smolenskii, G. (1984) Ferroelectrics with diffuse phase transition. *Ferroelectrics, 53*(1), pp. 129-135.

Snel, M., Groen, W. and de With, G. (2005) Investigation of the new piezoelectric system (1-x)Bi$(MgTi)_{0.5}O_3$–xPbTiO$_3$. *Journal of the European Ceramic Society, 25*(13), pp. 3229-3233.

Spreitzer, M., König, J., Jančar, B. and Suvorov, D. (2007) Enhanced tunable characteristics of the $Na_{0.5}Bi_{0.5}TiO_3$-$NaTaO_3$ relaxor-type system. *Ultrasonics, Ferroelectrics, and Frequency Control, IEEE Transactions on, 54*(12), pp. 2617-2622.

Stevenson, T. J. (2010) Magnetic and electric properties of bismuth ferrite lead titanate ceramics. in: PhD thesis, University of Leeds, UK.

Stock, S. and Cullity, B. (2001) Elements of X-ray diffraction. *Prentice Hall, Upper Saddle River, New Jersey,* (3rd), pp. 45.

Takenaka, T., Maruyama, K.-i. and Sakata, K. (1991a) $(Bi_{1/2}Na_{1/2})TiO_3$-$BaTiO_3$ system for lead-free piezoelectric ceramics. *Japanese Journal of Applied Physics, Part 1: Regular Papers and Short Notes and Review Papers, 30*(9 B), pp. 2236-2239.

Takenaka, T., Maruyama, K.-i. and Sakata, K. (1991b) $(Bi_{1/2}Na_{1/2})TiO_3$-$BaTiO_3$ system for lead-free piezoelectric ceramics. *Japanese Journal of Applied Physics, 30*(9S), pp. 2236.

Tao, H., Wu, J., Zheng, T., Wang, X. and Lou, X. (2015) New (1-x)$K_{0.45}Na_{0.55}Nb_{0.96}Sb_{0.04}O_3$-$x$$Bi_{0.5}Na_{0.5}HfO_3$ lead-free ceramics: Phase boundary and their electrical properties. *Journal of applied physics, 118*(4), pp. 044102.

Tinberg, D. S. and Trolier-McKinstry, S. (2007) Structural and electrical characterization of xBiScO$_3$–(1-x)BaTiO$_3$ thin films. *Journal of applied physics, 101*(2), pp. 024112-024112-4.

Turner, R., Fuierer, P. A., Newnham, R. and Shrout, T. (1994) Materials for high temperature acoustic and vibration sensors: a review. *Applied Acoustics, 41*(4), pp. 299-324.

Wada, S., Yamato, K., Pulpan, P., Kumada, N., Lee, B.-Y., Iijima, T., Moriyoshi, C. and Kuroiwa, Y. (2010) Piezoelectric properties of high Curie temperature barium titanate–bismuth perovskite-type oxide system ceramics. *Journal of applied physics, 108*(9), pp. 094114.

Wada, T., Fukui, A. and Matsuo, Y. (2002) Preparation of $(K_{0.5}Bi_{0.5})TiO_3$ ceramics by polymerized complex method and their properties. *Japanese Journal of Applied Physics, 41*(11S), pp. 7025.

Wang, K., Li, J.-F. and Zhou, J.-J. (2011) High normalized strain obtained in Li-modified (K, Na) NbO_3 lead-free piezoceramics. *Applied physics express, 4*(6), pp. 061501.

Wang, K., Yao, F. Z., Jo, W., Gobeljic, D., Shvartsman, V. V., Lupascu, D. C., Li, J. F. and Rödel, J. (2013) Temperature-Insensitive (K, Na)NbO_3-Based Lead-Free Piezoactuator Ceramics. *Advanced Functional Materials, 23*(33), pp. 4079-4086.

Wang, R., Wang, K., Yao, F., Li, J. F., Schader, F. H., Webber, K. G., Jo, W. and Rödel, J. (2015) Temperature Stability of Lead-Free Niobate Piezoceramics with Engineered Morphotropic Phase Boundary. *Journal of the American Ceramic Society*.

Wang, T., Jin, L., Li, C., Hu, Q. and Wei, X. (2014) Relaxor Ferroelectric $BaTiO_3$–$Bi(Mg_{2/3}Nb_{1/3})O_3$ Ceramics for Energy Storage Application. *Journal of the American Ceramic Society*.

Wang, X., Chan, H. L.-W. and Choy, C.-l. (2003) Piezoelectric and dielectric properties of CeO_2-added $(Bi_{0.5}Na_{0.5})_{0.94}Ba_{0.06}TiO_3$ lead-free ceramics. *Solid state communications, 125*(7), pp. 395-399.

Wang, Y., Chen, X., Zhou, H., Fang, L., Liu, L. and Zhang, H. (2013) Evolution of phase transformation behavior and dielectric temperature stability of $BaTiO_3$-$Bi(Zn_{0.5}Zr_{0.5})O_3$ ceramics system. *Journal of Alloys and Compounds, 551*, pp. 365-369.

Watson, J. and Castro, C. (2012) "High-Temperature Electronics Pose Design and Reliability Challenges “. *Analog Dialogue, 46*(4), pp. 3-9.

Wefring, E. T., Morozov, M. I., Einarsrud, M. A. and Grande, T. (2014) Solid-State Synthesis and Properties of Relaxor (1-*x*)BKT–*x*BNZ Ceramics. *Journal of the American Ceramic Society, 97*(9), pp. 2928-2935.

West, A. R. (2007) *Solid state chemistry and its applications*, John Wiley & Sons.

Xiong, B., Hao, H., Zhang, S., Liu, H. and Cao, M. (2011) Structure, dielectric properties and temperature stability of $BaTiO_3$–$Bi(Mg_{1/2}Ti_{1/2})O_3$ perovskite solid solutions. *Journal of the American Ceramic Society, 94*(10), pp. 3412-3417.

Xiong, B., Hao, H., Zhang, S., Liu, H., Cao, M. and Yu, Z. (2012) Dielectric behaviors of Nb_2O_5–Co_2O_3 doped $BaTiO_3$–$Bi(Mg_{1/2}Ti_{1/2})O_3$ ceramics. *Ceramics International, 38*, pp. S45-S48.

Xu, C., Lin, D. and Kwok, K. (2008) Structure, electrical properties and depolarization temperature of $(Bi_{0.5}Na_{0.5})TiO_3$–$BaTiO_3$ lead-free piezoelectric ceramics. *Solid State Sciences, 10*(7), pp. 934-940.

Xue, D., Zhou, Y., Bao, H., Gao, J., Zhou, C. and Ren, X. (2011a) Large piezoelectric effect in Pb-free $Ba(Ti,Sn)O_3$-$x(Ba,Ca)TiO_3$ ceramics. *Applied Physics Letters, 99*(12), pp. 122901.

Xue, D., Zhou, Y., Bao, H., Zhou, C., Gao, J. and Ren, X. (2011b) Elastic, piezoelectric, and dielectric properties of $Ba(Zr_{0.2}Ti_{0.8})O_3$-$50(Ba_{0.7}Ca_{0.3})TiO_3$ Pb-free ceramic at the morphotropic phase boundary. *Journal of applied physics, 109*(5), pp. 054110.

Yao, F.-Z., Yu, Q., Wang, K., Li, Q. and Li, J.-F. (2014) Ferroelectric domain morphology and temperature-dependent piezoelectricity of $(K,Na,Li)(Nb,Ta,Sb)O_3$ lead-free piezoceramics. *RSC Advances, 4*(39), pp. 20062-20068.

Yoshii, K., Hiruma, Y., Nagata, H. and Takenaka, T. (2006) Electrical properties and depolarization temperature of $(Bi_{1/2}Na_{1/2})TiO_3$–$(Bi_{1/2}K_{1/2})TiO_3$ lead-free piezoelectric ceramics. *Japanese Journal of Applied Physics, 45*(5S), pp. 4493.

Yu, J., Wang, L., Wang, Y., Peng, G., Liu, F. and Gao, J. (2005) A compact model for the simulation of ferroelectric capacitor. *Integrated Ferroelectrics, 75*(1), pp. 35-45.

Yu, Z., Ang, C., Guo, R. and Bhalla, A. (2002) Dielectric properties and high tunability of $Ba(Ti_{0.7}Zr_{0.3})O_3$ ceramics under dc electric field. *Applied Physics Letters, 81*(7), pp. 1285-1287.

Zang, J., Li, M., Sinclair, D. C., Frömling, T., Jo, W. and Rödel, J. (2014) Impedance Spectroscopy of $(Bi_{1/2}Na_{1/2})TiO_3$–$BaTiO_3$ Based High-Temperature Dielectrics. *Journal of the American Ceramic Society, 97*(9), pp. 2825-2831.

Zeb, A. and Milne, S. (2015) High temperature dielectric ceramics: a review of temperature-stable high-permittivity perovskites. *Journal of Materials Science: Materials in Electronics*, pp. 1-13.

Zeb, A. and Milne, S. J. (2014a) Low variation in relative permittivity over the temperature range 25–450 °C for ceramics in the system $(1\text{-}x)[Ba_{0.8}Ca_{0.2}TiO_3]$–$x[Bi(Zn_{0.5}Ti_{0.5})O_3]$. *Journal of the European Ceramic Society, 34*(7), pp. 1727-1732.

Zeb, A. and Milne, S. J. (2014b) Temperature-stable dielectric properties from -20°C to 430°C in the system $BaTiO_3$–$Bi(Mg_{0.5}Zr_{0.5})O_3$. *Journal of the European Ceramic Society, 34*(13), pp. 3159-3166.

Zhang, Q., Li, Z., Li, F. and Xu, Z. (2011) Structural and Dielectric Properties of $Bi(Mg_{1/2}Ti_{1/2})O_3$–$BaTiO_3$ Lead-Free Ceramics. *Journal of the American Ceramic Society, 94*(12), pp. 4335-4339.

Zhang, S.-T., Kounga, A. B., Aulbach, E., Ehrenberg, H. and Rödel, J. (2007) Giant strain in lead-free piezoceramics $Bi_{0.5}Na_{0.5}TiO_3$–$BaTiO_3$–$K_{0.5}Na_{0.5}NbO_3$ system. *Applied Physics Letters, 91*(11), pp. 112906.

Zhang, S.-T., Kounga, A. B., Aulbach, E., Granzow, T., Jo, W., Kleebe, H.-J. and Rödel, J. (2008a) Lead-free piezoceramics with giant strain in the system $Bi_{0.5}Na_{0.5}TiO_3$–$BaTiO_3$–$K_{0.5}Na_{0.5}NbO_3$. I. Structure and room temperature properties. *Journal of applied physics, 103*(3), pp. 034107.

Zhang, S.-T., Kounga, A. B., Aulbach, E., Jo, W., Granzow, T., Ehrenberg, H. and Rödel, J. (2008b) Lead-free piezoceramics with giant strain in the system $Bi_{0.5}Na_{0.5}TiO_3$-$BaTiO_3$-$K_{0.5}Na_{0.5}NbO_3$. II. Temperature dependent properties. *Journal of applied physics, 103*(3), pp. 034108.

Zhang, S. and Yu, F. (2011) Piezoelectric materials for high temperature sensors. *Journal of the American Ceramic Society, 94*(10), pp. 3153-3170.

Zhang, S. T., Kounga, A. B., Aulbach, E. and Deng, Y. (2008) Temperature-Dependent Electrical Properties of $0.94Bi_{0.5}Na_{0.5}TiO_3$–$0.06BaTiO_3$ Ceramics. *Journal of the American Ceramic Society, 91*(12), pp. 3950-3954.

Zhao, W. and Zuo, R. (2013) Morphotropic phase boundary and electrical properties of lead-free $(K_{0.5}Bi_{0.5})TiO_3$–$Bi(Ni_{0.5}Ti_{0.5})O_3$ relaxor ferroelectric ceramics. *Ceramics International, 39*(8), pp. 9121-9124.

Zheng, D. and Zuo, R. (2015) A Novel $BiFeO_3$–$BaTiO_3$–$BaZrO_3$ Lead-Free Relaxor Ferroelectric Ceramic with Low-Hysteresis and Frequency-Insensitive Large Strains. *Journal of the American Ceramic Society*.

Zhou, C., Liu, W., Xue, D., Ren, X., Bao, H., Gao, J. and Zhang, L. (2012) Triple-point-type morphotropic phase boundary based large piezoelectric Pb-free material—$Ba(Ti_{0.8}Hf_{0.2})O_3$-$(Ba_{0.7}Ca_{0.3})TiO_3$. *Applied Physics Letters, 100*(22), pp. 222910.

Zhou, J.-S., Wang, K., Yao, F.-Z., Zheng, T., Wu, J., Xiao, D., Zhu, J. and Li, J.-F. (2015) Multi-scale thermal stability of niobate-based lead-free piezoceramics with large piezoelectricity. *Journal of Materials Chemistry C, 3*(34), pp. 8780-8787.

Zhu, F., Skidmore, T., Bell, A., Comyn, T., James, C., Ward, M. and Milne, S. (2011a) Diffuse dielectric behaviour in $Na_{0.5}K_{0.5}NbO_3$–$LiTaO_3$–$BiScO_3$ lead-free ceramics. *Materials Chemistry and Physics, 129*(1), pp. 411-417.

Zhu, F., Ward, M. B., Comyn, T. P., Bell, A. J. and Milne, S. J. (2011b) Dielectric and piezoelectric properties in the lead-free system $Na_{0.5}K_{0.5}NbO_3$-$BiScO_3$-$LiTaO_3$. *Ultrasonics, Ferroelectrics and Frequency Control, IEEE Transactions on, 58*(9), pp. 1811-1818.

Zhu, F., Ward, M. B., Li, J.-F. and Milne, S. J. (2015) Core–shell grain structures and dielectric properties of $Na_{0.5}K_{0.5}NbO_3$–$LiTaO_3$–$BiScO_3$ piezoelectric ceramics. *Acta Materialia, 90*, pp. 204-212.

Zuo, R., Rödel, J., Chen, R. and Li, L. (2006) Sintering and Electrical Properties of Lead-Free $Na_{0.5}K_{0.5}NbO_3$ Piezoelectric Ceramics. *Journal of the American Ceramic Society, 89*(6), pp. 2010-2015.

Zuo, W., Zuo, R. and Zhao, W. (2013) Phase transition behavior and electrical properties of lead-free $(Bi_{0.5}K_{0.5})TiO_3$–$LiNbO_3$ relaxor ferroelectric ceramics. *Ceramics International, 39*(1), pp. 725-730.

Zushi, J., Ariizumi, T., Kojima, S., Wang, R. and Bando, H. (2013) Formation of Morphotropic Phase Boundary in $(Na_{0.5}K_{0.5})NbO_3$–$BaZrO_3$–$(Bi_{0.5}Li_{0.5})TiO_3$ Lead-Free Piezoelectric Ceramics. *Japanese Journal of Applied Physics, 52*(7S), pp. 07HB02.